Investigations into Ion Beam Emittance and Profile Monitoring

UNIVERSITY OF LIVERPOOL

Thesis submitted in accordance with the requirements of the University of Liverpool for the degree of Doctor in Philosophy

By

Vasileios Tzoganis

November 2016

Abstract

Beam diagnostics systems are essential constituents of any particle accelerator; they reveal the properties of a beam and how it behaves in the machine. This includes: synchrotron light sources and free-electron lasers; high energy accelerators for particle physics experiments; high-intensity hadron accelerators for the generation of exotic beams and spallation sources; much smaller accelerator facilities where cooled beams of specific (exotic) particles are provided for precision experiments and fundamental Physics studies. Without an appropriate set of diagnostic elements, it would simply be impossible to operate any accelerator complex, let alone optimise its performance.

This thesis covers investigations into two different beam diagnostics methods. The first part describes work carried out at RIKEN Radioactive Isotope Beam Factory (RIBF) in Japan during October 2013 – January 2016. It deals with the development of an online emittance monitor for an ECR ion source that produces low energy beams of various species ranging from protons up to heavier ions such as krypton. The monitor was initially based on an earlier RIKEN prototype which had insufficient performance. After four design iterations and multiple experimental tests the final prototype was integrated at the ion source and experimental measurements were carried out. One of the major challenges was to identify suitable scintillating materials that do not heavily degrade after irradiation with low energy ion beams. Additionally to the emittance monitor, work also focused on optimising the ECR ion source and increasing the beam current by improving the ion extraction.

The first and the last year of this PhD were spent at the Cockcroft Institute, UK. Work done there is presented in the second part of this thesis which delves into a non-invasive real-time beam profile monitor based on a supersonic gas jet. This monitor was originally conceived and developed by at the Cockcroft Institute but was never operated successfully in the gas jet mode but only as a residual gas monitor. During this PhD, the monitor was commissioned in gas jet mode, alignment issues that prevented previous operation were identified and addressed and the first experimental results were obtained. Moreover, the vacuum dynamics of the system were explored and additional diagnostics instrumentation for the measurement of the gas jet properties was developed and installed.

This thesis presents the design of both beam diagnostics methods, for transverse emittance and transverse profile determination, results from measurements with various beam species and a detailed analysis of their performance. Furthermore, it highlights the challenges of the design, integration, optimisation and real time operation for both instruments.

Acknowledgements

I would first like to acknowledge my supervisor Prof. Dr.Carsten Welsch for offering me the opportunity to become a member of the Quasar group and pursue my PhD. I greatly appreciate his support on both an academic and personal level.

I am very grateful to our colleagues from RIKEN in Japan, my local supervisor and leader of the accelerator group Dr Osamu Kamigaito, Dr Takashi Nagatomo as well as the entire ion source and beam diagnostics group members for their support and assistance in designing and performing the beam experiments.

I would like to thank all the Quasar group members and especially Dr Massimiliano Putignano for his time introducing me to the gas jet test stand, Dr Adam Jeff and Dr Hao Zhang for their help in performing the experiments at the Cockcroft Institute and Alexandra Alexandrova as our laser expert for her valuable advice in keeping us safe when working with lasers.

I appreciate the invaluable help of my office colleague Sam Jones who shared his knowledge in programming whenever i needed him and Dr Kei Sunouchi from RIKEN's mechanical workshop for his expert advice in mechanical design and device integration.

I would like to thank all the friends i made in the UK and Japan during the 2 years I have spent in each country and in particular my friend Andre in Liverpool for the long discussions during late hours on all aspects of personal and academic life.

Finally, I would like to thank my parents and family for their support and understanding throughout this journey.

Table of Contents

List of figures

List of tables

Acronyms

ADC	Analog to Digital Converter
ALPHA	Antihydrogen Laser PHysics Apparatus
ASACUSA	Atomic Spectroscopy And Collisions Using Slow Antiprotons
BA	Bayard Alpert
BNC	Bayonet Neill–Concelman
CCD	Charge-Coupled Device
CMOS	Complementary Metal Oxide Semiconductor
CNS	Center of Nuclear Science
ECR	Electron Cyclotron Resonance
EPICS	Experimental Physics and Industrial Control System
FETS	Front End Test Stand
FLAIR	Facility for Low-energy Antiproton and Ion Research
FLASH	Free electron LASer at Hamburg
fps	frames per second
FWHM	Full Width at Half Maximum
GigE	Gigabit Ethernet
GSI	Gesellschaft für Schwerionenforschung
GUI	Graphical User Interface
HIMAC	Heavy Ion Medical ACcelerator
HL-LHC	High Luminosity Large Hadron Collider
IPM	Ionisation Profile Monitor
J-PARC	Japan Proton Accelerator Research Complex
LEBT	Low Energy Beam Transport
Linac	Linear Accelerator
MCP	Micro Channel Plate
PIC	Particle In Cell
PoE	Power over Ethernet
PSF	Point Spread Function
QE	Quantum Efficiency
QUASAR	Quantum Systems and advanced Accelerator Research
RAL	Rutherford Appleton Laboratory
ReMi	Reaction Microscope
RF	Radio Frequency

RHIC	Relativistic Heavy Ion Collider
RIBF	Radioactive Isotope Beam Factory
RIKEN	RIkagaku KENkyūsho The institute of Physical and Chemical research
RMS	Root Mean Square
ROI	Region Of Interest
SEM	Secondary Emission Monitor
SNS	Spallation Neutron Source
TMP	Turbo Molecular Pump
UHV	Ultra-High Vacuum
USR	Ultra-low-energy Storage Ring

1. Introduction

The purpose of this chapter is to introduce the main concepts discussed in this thesis which are transverse beam emittance measurements and transverse beam profile measurements. Section 1.1 of this chapter is an introduction to beam diagnostics techniques. Section 1.2 presents a method for absolute beam current measurement. Section 1.3 discusses transverse beam profile monitors and focuses on least invasive methods introducing the idea of Ionisation Profile Monitors (IPM) which are relevant to the supersonic gas jet based beam profile monitor presented in chapter 3. Finally, the chapter introduces the concept of beam emittance and presents various methods for emittance measurements focusing more on pepperpot based systems.

1.1 Background

It has been said that "*an accelerator is as good as its diagnostics*". This sentence reveals the importance of beam diagnostics for the operation of particle accelerators. Beam diagnostics deal with the real beam conditions including any imperfections that have not been foreseen during the design phase. Without adequate diagnostics, it would simply be impossible to operate a large scale accelerator facility let alone to optimise it. The following section is based on an overview of beam diagnostics lectures from JUAS and CAS schools [1]–[3].

There are four quasi-discrete categories of diagnostics needs in particle accelerator facilities:

1. Complex instrumentation for the commissioning phases of an accelerator, for accelerator optimisation to solve more complex issues in case of a malfunction. Devices in this category may be destructive for the beam and complex to use in comparison with a single knob operation from category 2. They should allow a clear interpretation of a complex phenomenon and provide reliable information. An example here is the determination of beam emittance for the commissioning phase or for beam tuning.
2. Instrumentation for a daily check of accelerator performance and stability or the control of specific parameters. An example would be a beam profile monitor usually (but not limited to) operating in a destructive way by intercepting and stopping the particle beam.
3. Active influence of the particle beam after the beam properties are defined by the diagnostics. In this category, we find active or passive feedback systems where the value of the measured parameter is used to make adjustments. The example

here is a beam position monitor that provides a reading useful for the correction of the beam orbit.

4. Fast and reliable measurements to determine operating parameters of the accelerators by means of a quick check of its functionality. Such methods usually provide a single number as a reading or a simple plot. They should be non-invasive in order to allow for online operation without disturbing the beam. One example is a beam current measurement using an Integrating Current Transformer (ICT) or Fast Current transformer (FCT) [4].

It should be noted that there are no solid frontiers among these categories rather than smooth transitions from one category to the other and overlaps between them. There are a large number of beam parameters to be measured which also differ for different machines. To showcase this with an example, in a linear accelerator or a transfer line the beam passes only once but at a synchrotron or storage ring, it passes several times. For synchrotrons or storage rings, non-invasive methods are preferred for beam monitoring. Electron beams are quite different than proton or ion beams as they become relativistic at quite lower energies. Therefore, at the first stages of an electron linac, one has to deal with relativistic electrons while protons or ions would still be moving much slower. Table 1 shows an overview of some beam parameters and diagnostics for different types of machines. Diagnostics usually require about 3% to 10% of the total cost of an accelerator and usually about 10% to 20 % of the available manpower.

Figure 1 illustrates a selection of various beam diagnostics assembled on a test stand that has been used for commissioning of the high current RFQ at GSI. This setup allows for the measurement of all the relevant beam parameters. Quantities of interest here are: current, transverse profile, transverse emittance, energy, bunch position and structure, in dependence on a range of operating parameters settings. Table 1 summarises various particle beam parameters and traditionally used diagnostics methods. Table 2 lists the physical processes involved in specific diagnostics methods.

Table 1: Beam parameters and traditionally used diagnostics. Methods more relevant to the work covered in this thesis are in bold.

Beam parameter	Linac, transfer line	Synchrotron
Beam current	Faraday cup	ICT (integrating current transformer) WCM (wall current monitor)
Beam position	Cavity BPM	Cavity BPM (beam position monitor)
Beam profile	SEM grid Wire scanner Viewing screen OTR screen Laser wire	**Residual gas monitor** Synchrotron radiation Wire scanner Laser wire
Transverse emittance	Slit grid Quadrupole scan **Pepperpot**	Residual gas monitor Wire scanner

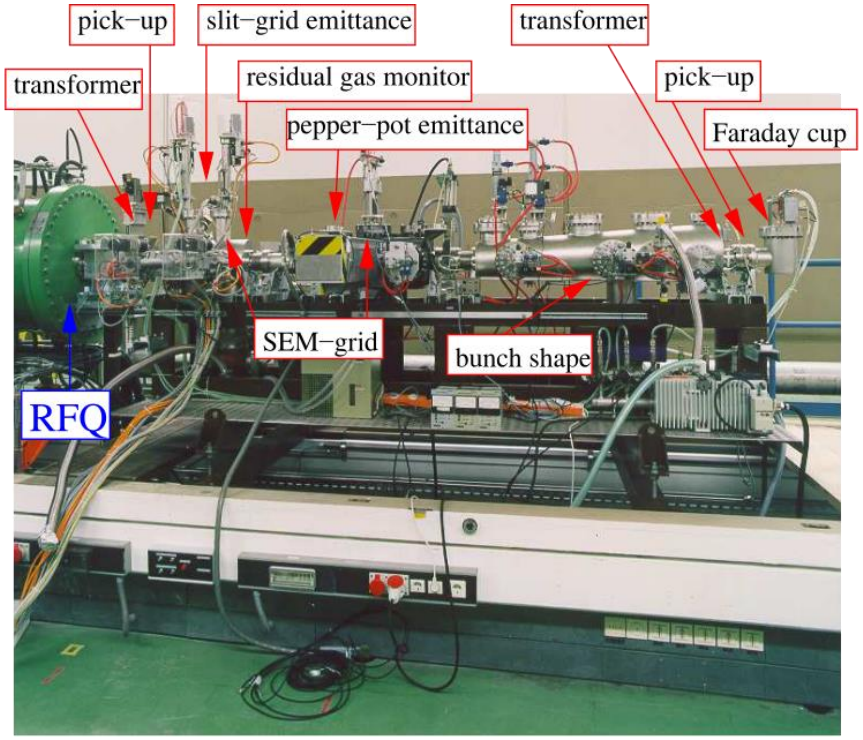

Figure 1: Movable test bench with diagnostics for commissioning of the high current RFQ at GSI [3], [5].

Table 2: Relevant physical processes for beam diagnostics.

Phenomenon	Physics	Quantity	Example
Electromagnetic influence by moving charges	Classical electrodynamics	Voltage Current frequencies	Beam transformers BPM's
Coulomb interaction of charged particles with matter	atomic and solid state physics	Current Optics Particle detectors	Scintillators Viewing screens Ionisation chambers Residual gas monitors
Interaction of particles with photons	optics, lasers	optical techniques, particle detectors	Laser scanners, polarimeters, photodetachment for H- beams
Emission of photon by accelerated charges: (mainly for electrons)	optics	optical techniques (from visible to x-ray)	Synchrotron radiation monitors
Nuclear- or elementary particle physics interactions	nuclear physics	particle detectors	beam loss monitors polarimeters luminosity monitors

In the rest of this chapter, some of the most widely used beam diagnostic methods will be discussed with emphasis on the diagnostics relevant to this work which are transverse beam profile monitors, beam emittance monitors and beam current monitors.

1.2 Beam current measurements

The total number of particles in a beam expressed as the beam current is a very important parameter in particle accelerator operation. An electric current measurement is a daily routine for all accelerator operators and users. One of the most popular methods to directly measure with precision the beam current even from the early days of accelerators is with a Faraday cup. For very high beam currents this destructive method can be scaled up in size resulting in massive water-cooled Faraday cups which can withstand very high power. A Faraday cup collects all primary and secondary charges generated by the beam and passes the electrical signal to a current meter or amplifier.

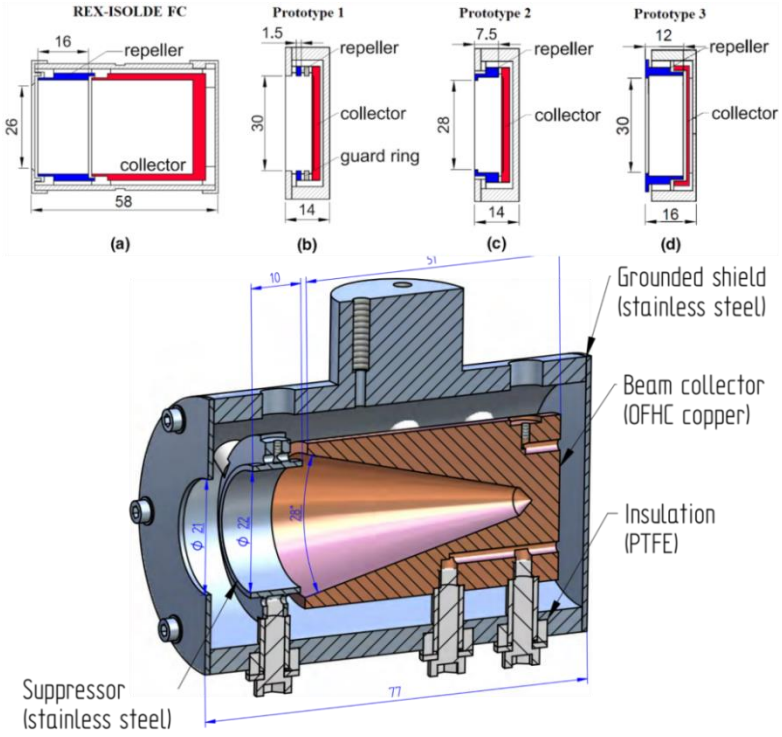

Figure 2: Two Faraday cup designs are shown here. Top: short Faraday cup optimised for low energy ion beams used at ISOLDE facility at CERN [6]. Bottom Faraday cup design for low energy low-intensity proton beams that will be used during the commissioning phase of the USR [7].

An important aspect of Faraday cup design is the secondary electron suppression. When a charged particle hits the surface, secondary electrons are generated. The electron flux is proportional to cos(θ), with θ being the angle between the impinging particle trajectory and the normal to the Faraday cup's surface. The most widely used ways to suppress secondary electrons are to make long and small in diameter Faraday cups that minimize the number of escaping secondary charges; use high voltage suppression near the cup entrance that is above the mean secondary electron energy and finally to use a permanent magnet that will force the electrons to spiral around the magnetic field lines and return to the surface.

1.3 Transverse beam profile monitors

The particle beam density distribution along one of the 3 Cartesian space coordinates is called a 'beam profile'. Beam profile determination and monitoring is critical during routine accelerator operation, commissioning and accelerator tuning for experimental user groups. For the first, knowledge of the beam profile is crucial to ensure good performance of the accelerator and safe operation. For the latter, it is absolutely necessary for proper interpretation of the experimental data. In accelerator physics, it is common to separate transverse and longitudinal directions. The longitudinal direction expands along the beams trajectory, measurements of the longitudinal beam profile is outside the scope of this thesis. Transverse

beam profiles can be measured using a number of different methods both, invasive and non-invasive. In the rest of this section, the most common ways to measure transverse beam profiles will be presented. They range from scintillating screens that significantly attenuate the particle beam, Secondary Emission Monitors (SEMs) that operate in an almost non-invasive way and Residual Gas Monitors (RGMs) which can be a fully parasitical method. RGM includes Ionisation Profile Monitors (IPMs) and Beam Induced Fluorescence (BIF) monitors.

1.3.1 Scintillating screens

Scintillating screens are the most direct, simple and cost effective way for a transverse beam profile monitor [3].

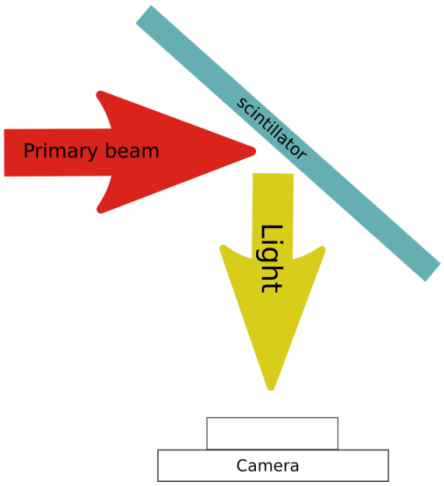

Figure 3: Principle of scintillator based beam profile monitor

In its simplest configuration, as shown in Figure 3, a scintillator screen based profile monitor consists of a scintillating screen that intercepts the primary particle beam at an angle of 45°. Usually, the screen can be moved in and out of the beamline by means of a pneumatic or stepper motor based feedthrough. Scintillation light emitted from the screen is recorded by a camera that sits usually outside the vacuum chamber and behind a viewport. These devices are installed nearly at every accelerator for beam profile evaluation at different locations but they are limited to relatively low beam intensities. Scintillators can be used to measure beams with low currents and if combined with MCPs or photomultipliers, they can be used for single particle detection. When a charged particle impacts the scintillator it loses energy which is transformed (not fully) to scintillation light. Various materials exhibit different properties, the most desired of them are:

- High light yield.
- High dynamic range and linearity, the light output should be linearly proportional to the number of charged particles impinging on the scintillator.
- No light absorption, the scintillator material should be transparent for the scintillation light wavelength for applications where the beam profile is observed from the rear side of the scintillating screen.
- Mechanical stability and rigidity.
- Fast decay time, the scintillation light should decay as fast as possible to allow good time resolution.
- Radiation hardness.

1.3.2 Secondary Emission Monitor (SEM)

In the case of a Faraday cup, the generation of secondary electrons is a problem to deal with. The SEM grid takes advantage of that effect. As can be seen in Figure 4, the SEM grid consists of a series of parallel and perpendicular wires with individual electronic readout. This is an electronic equivalent of a scintillating screen with the benefits of being least invasive and having a higher dynamic range. When the particle beam passes through the SEM grid and impacts the wires, secondary electrons are emitted and collected from the wires. Every channel of the SEM that corresponds to one wire has an individual amplifier and a current-to-voltage converter [8].

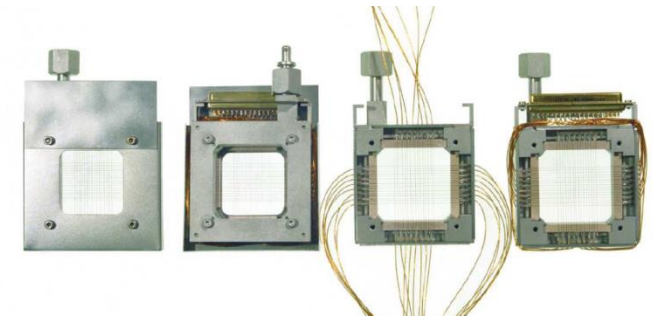

Figure 4: SEM grids, image taken from [3].

The spacing and diameter of the wires defines the beam attenuation and thus can be tailored depending on particle beam to be measured. Usually, a multiplexer is used to connect all these outputs to an ADC for voltage measurements. SEM readout can be very fast, limited only by the performance of the readout circuit.

A different configuration of a SEM monitor calls for three or more parallel metallic plates of a size larger than the particle beam, thickness of a few micrometres and spacing of a few

millimetres. The main beam passes through the plates; secondary electrons are generated from the surfaces of the foils and collected by appropriate voltages between them [9].

Instead of using an array of wires where the resolution is limited on the spacing which in turn is limited by the acceptable beam attenuation, a single scanning wire can be used [10]. In this case, the resolution can be very high and it depends only on the scan speed and the wire diameter which can be some micrometres. A photograph of a wire scanner is shown in Figure 5. The single wire in this beam profile monitor is moved across the particle beam by an external motor. The position of the wire is calculated from feedback by the motor rotation. The readout can be (i) from the wire itself by direct current measurements, (ii) from a scintillator/photomultiplier outside of the vacuum for higher energy particle beams or (iii) any other type of beam loss monitor that is available [10]. For the determination of the beam profile, the readout signal is plotted against the position of the actuator during the scanning of the beam.

One of the disadvantages of the wire scanner is that it cannot measure pulsed beams because of the time needed to complete a full scan. Another concern is that even for a DC beam the wire will sample the beam profile at different locations at different times [9]. The main limitation of this method similar to the scintillating screens is that it cannot be applied to very high-density beams.

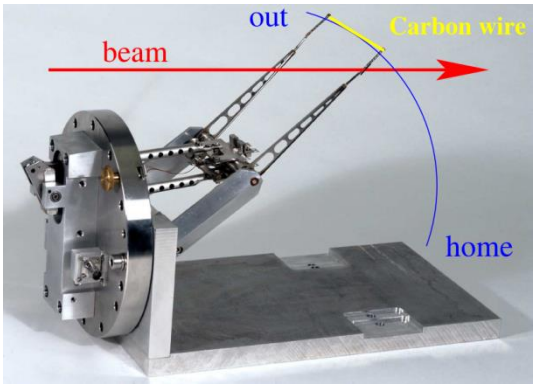

Figure 5: Wire scanner, the image was taken from [3].

1.3.3 Residual gas monitors

Possible candidates for minimally-invasive beam profile measurements are usually residual gas ionisation profile monitors (IPM's) [8]-[11] and beam induced fluorescence monitors (BIF) [10], [12]-[14]. The former operate by using an external electric field to collect the ions or electrons produced by the interaction of the main beam with the residual gas in the vacuum chamber. The latter uses fluorescence light emitted after the excitation of the residual

gas by the beam. For IPMs used to measure the beam profile of low current beams, residual gas ion detection is preferred over electron detection. The momentum transfer to the residual gas ions generated by ionisation from the primary beam is much smaller for accelerated ions when compared to electrons due to the large mass difference leading to smaller velocity spread and smaller image distortion. The image broadening by the transverse thermal spread could be minimised by applying a higher collecting voltage to reduce the collection time or reducing the distance the ions have to travel until they reach the detector. To obtain both beam profiles, it is necessary to have two IPMs rotated by 90^0 with respect to each other [15]. Nevertheless, in a very low-pressure environment, such a device is limited in both acquisition speed and resolution due to the very low-level signals produced by the low number density residual gas. For Beam Induced Fluorescence (BIF) monitors, since photons are emitted at all angles and are detected by the camera in a solid angle of about 10^{-4} steradians, the signal is lower than that of an IPM equipped with an MCP by about 5 to 6 orders of magnitude resulting in high integration time per measurement.

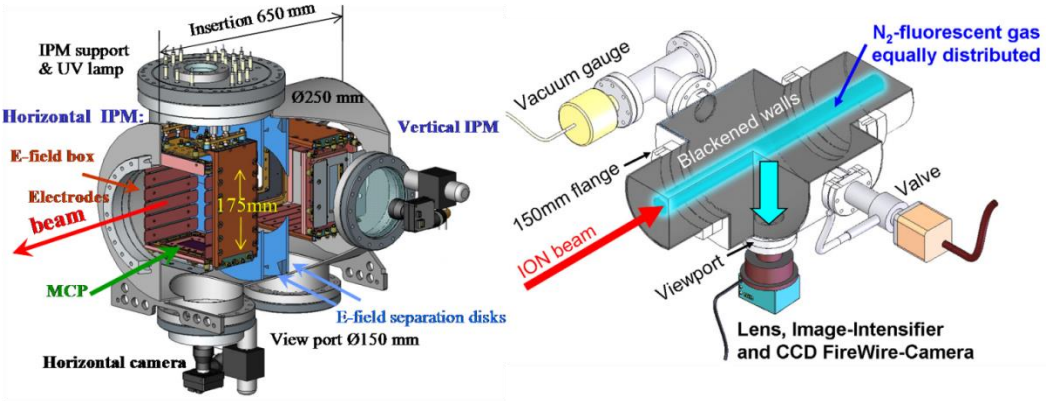

Figure 6: Left: IPM installation at the GSI storage ring with two monitors at right angles for horizontal and vertical beam profile measurement, Right: scheme of a beam induced fluorescence monitor for horizontal profile determination. Both images are taken from [15].

Applications of these beam monitoring methods are found in many accelerator facilities. The SIS18 heavy ion synchrotron at GSI accelerates beams of various species up to Uranium. Typically for the warm dense matter (WDM) experiments a beam of $^{238}U^{37+}$ ions with an energy of 300-400 MeV /u is used. Up to $4x10^9$ ions are delivered in bunches of 70 – 300 ns. The ionisation profile monitor acquires 100 profiles/s and consists of 2 identical devices oriented at 90° to each other for the acquisition of horizontal and vertical beam profiles [11].

The residual gas fluorescence monitor at the Relativistic Heavy Ion Collider (RHIC) is employed to measure the profiles of fully stripped gold, copper and uranium beams at 100, 99.9 and 96.4 GeV/nucleon. The passage of the beam excites the residual gas present in the

vacuum duct which consists mainly of hydrogen. During the de-excitation, it emits fluorescence light which is captured by a camera. The operating pressure is around 10^{-9} mbar but the measurement time is 60 s [13].

As a final example, at the Spallation Neutron Source (SNS) accumulator ring, Oak Ridge National Laboratory, the design of a new ionisation beam profile monitor has recently been implemented. It will be used to measure proton beam profiles in the 248 m accumulator ring after the 1 GeV linear accelerator. The monitor will operate at a pressure of around 10^{-9} mbar but the geometry of the detector (slit size of 4 mm) will require to scan it across the beam and leading to larger measurement time [14].

A feasible solution around the limitations of Residual Gas Monitors (RGM); namely longer acquisition time, low signal intensity and image broadening is a cold (<20 K) supersonic gas jet shaped into a thin curtain which allows for 2-dimensional beam profile imaging [18] in the same way an interceptive screen would do. Such a monitor could be seen as an enhanced IPM where additional gas injection improves the reaction rate and thus the acquisition time and resolution.

1.4 Transverse beam emittance monitors

1.4.1 Emittance definitions

Emittance is a property of a particle beam used in accelerator physics to characterise beam quality. It represents the area of the phase space occupied by the particle distribution which is generally an ellipse. Emittance is preferred over the beam physical dimensions for beam characterisation because according to Liouville's theorem, the area (or volume) of a particle distribution in the phase space remains invariant under conservative forces [19].

In an ideal machine, the longitudinal motion along the beam axis is decoupled from transverse motion. The result of this is that transverse 4-D phase space can be studied separately. With the assumption of ideal machines, transverse phase space can decompose into two orthogonal dimensions and thus into two 2-D transverse sub-phase spaces. The phase space area conservation is valid for each of the decomposed phase spaces. For the 2-D phase spaces the coordinates are represented as x (or y) in units of length for the position and x' (or y') in units of radians for the angular divergence.

In accelerators with very precisely known beamline optics the lattice functions (Twiss parameters α, β, γ) in combination with beam profile measurements are used to calculate beam emittance. The Twiss parameters relate emittance to beam parameters as shown in equation

(1) where the brackets denote average. Beam motion then can be described in the transverse phase space by the emittance ellipse defined in equation (2). Figure 7 shows how the Twiss parameters and beam emittance relate in a phase space plot.

$$\begin{aligned} \left\langle x^2 \right\rangle &= \beta_x \cdot \varepsilon_x \\ \left\langle x'^2 \right\rangle &= \gamma_x \cdot \varepsilon_x \\ \alpha_x{}^2 &= \beta_x \cdot \gamma_x - 1 \end{aligned} \qquad (1)$$

$$\gamma_x x^2 + 2a_x xx' + \beta_x x'^2 = \varepsilon_x \qquad (2)$$

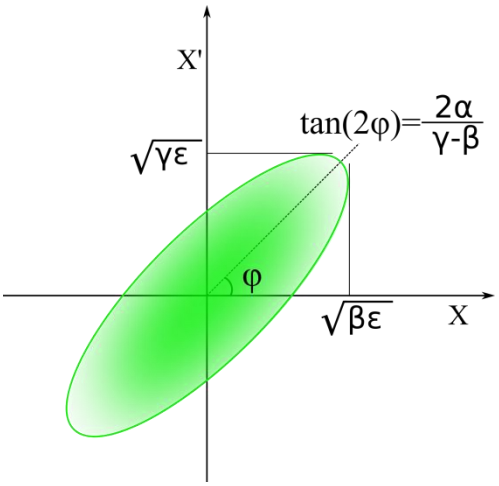

Figure 7: Emittance ellipse and Twiss parameters

1.4.2 Statistical emittance

In applications such as beam produced by Electron Cyclotron Resonance (ECR) ion sources with irregular beam size, it is preferred to determine the emittance statistically based on the particle distribution in the phase space. The statistical emittance, introduced by Chasman [20] and later refined by Lapostolle [21] is calculated using the equations (3) and (4) [19].

The brackets denote the weighted average over all particles and are the beam's second order moments. The parameter I is proportional to the intensity of the beam. Following equations (3) and (4) one can calculate ε_x or ε_y.

$$\varepsilon_x = \sqrt{\langle x^2 \rangle \cdot \langle x'^2 \rangle - \langle x \cdot x' \rangle^2} \qquad (3)$$

$$\langle x^2 \rangle = \frac{\sum_{all} (x - \bar{x})^2 \cdot I(x)}{\sum_{all} I(x)},$$

$$\bar{x} = \frac{\sum_{all} x \cdot I(x)}{\sum_{all} I(x)} \qquad \langle x'^2 \rangle = \frac{\sum_{all} (x' - \bar{x}')^2 \cdot I(x)}{\sum_{all} I(x)}, \qquad (4)$$

$$\bar{x}' = \frac{\sum_{all} x' \cdot I(x)}{\sum_{all} I(x)} \qquad \langle xx' \rangle = \frac{\sum_{all} (x - \bar{x}) \cdot (x' - \bar{x}') I(x)}{\sum_{all} I(x)}$$

1.4.3 4-D emittance

The following analysis is based on A.Wolski's beam dynamics book [22] and works done by L. Groening et al [23]–[26]. A 4-dimensional symmetric beam matrix C contains 16 elements. The diagonal blocks (green) describe the projections on the 2-D horizontal and vertical phase space ε_x and ε_y respectively while the off-diagonal blocks (purple) the interplane coupling. Using a pepperpot based emittance monitor all the elements of C matrix can be acquired in a single measurement.

$$C = \begin{bmatrix} \langle xx \rangle & \langle xx' \rangle & \langle xy \rangle & \langle xy' \rangle \\ \langle x'x \rangle & \langle x'x' \rangle & \langle x'y \rangle & \langle x'y' \rangle \\ \langle yx \rangle & \langle yx' \rangle & \langle yy \rangle & \langle yy' \rangle \\ \langle y'x \rangle & \langle y'x' \rangle & \langle y'y \rangle & \langle y'y' \rangle \end{bmatrix}, \varepsilon_{4D}^2 = \det C \qquad (2)$$

The projected 2-dimensional beam emittances can be calculated individually from the determinant of the diagonal components of matrix C.

$$C_x = \begin{bmatrix} \langle xx \rangle & \langle xx' \rangle \\ \langle x'x \rangle & \langle x'x' \rangle \end{bmatrix}, \varepsilon_x^2 = \det C_x \quad C_y = \begin{bmatrix} \langle yy \rangle & \langle yy' \rangle \\ \langle y'y \rangle & \langle y'y' \rangle \end{bmatrix}, \varepsilon_y^2 = \det C_y \qquad (3)$$

For beams with no interplane coupling between the 2 transverse planes (X and Y) the off-diagonal terms of matrix C are zero and the 4D beam matrix is:

$$C = \begin{bmatrix} \langle xx \rangle & \langle xx' \rangle & 0 & 0 \\ \langle x'x \rangle & \langle x'x' \rangle & 0 & 0 \\ 0 & 0 & \langle yy \rangle & \langle yy' \rangle \\ 0 & 0 & \langle y'y \rangle & \langle y'y' \rangle \end{bmatrix}, \det C = (\varepsilon_x \bullet \varepsilon_y)^2 \qquad (4)$$

The Eigen-emittances or intrinsic emittances are calculated as the eigenvalues of $C \bullet J$ where J is defined as:

$$J = \begin{bmatrix} 0 & 1 & 0 & 0 \\ -1 & 0 & 0 & 0 \\ 0 & 0 & 0 & 1 \\ 0 & 0 & -1 & 0 \end{bmatrix} \quad (5)$$

Eigen-emittances are invariant under symplectic transformations and they are equal to ε_x and ε_y in the case of no interplane coupling.

1.4.4 Emittance measurement methods

The knowledge of the transverse emittance is important for a number of reasons. Firstly is needed to evaluate the beam quality of new particle sources such as electron guns and ion sources. It is very useful during the commissioning of an accelerator when the beam energy is slowly increased while monitoring the beam evolution. In existing and already operating machine emittance measurements can be used to optimise the performance and increase the beam quality. Furthermore, emittance estimation and experimental measurements are required to match the beam to the beamline geometrical acceptance. Finally, emittance measurements are required to provide the requested beam quality for particle beam experiments where the requirements for beamspot size and divergence can be very tight.

The most widely used methods for the determination of the transverse emittance are the slit – grid method, the pepperpot method and the quadrupole scan method. The most relevant to this thesis, the pepperpot method is further analysed in the following section.

Pepperpot method

The main disadvantage of the slit – grid method is that it is time-consuming as it has to be scanned across the beam in small steps and acquire data at each step. For pulsed machines, only 1 step can be performed during a single pulse. By having an array of holes instead of a slit the emittance measurements can be done in a single shot for both transverse planes. In addition, for ion sources that may have fluctuations from pulse to pulse but also in continuous operation, this method is more suitable as it can capture the beam emittance instantly [3].

A pepperpot based emittance consists of a thin metal foil with an array of holes on it. Often, a thicker plate is positioned in front of the pepperpot with a similar array of holes but with a larger diameter as a beam attenuator. The foil intercepts the particle beam and splits it to small

beamlets that are projected on the following scintillating screen. Similarly to the slit – grid method, the position is defined by the hole's location on the pepperpot and the momentum is calculated from the projected beamlet on the screen. The main benefit of the pepperpot method is the ability for single shot measurement of both transverse planes simultaneously.

The operating principle of a pepperpot based beam profile monitor is shown in **Error! eference source not found.**.

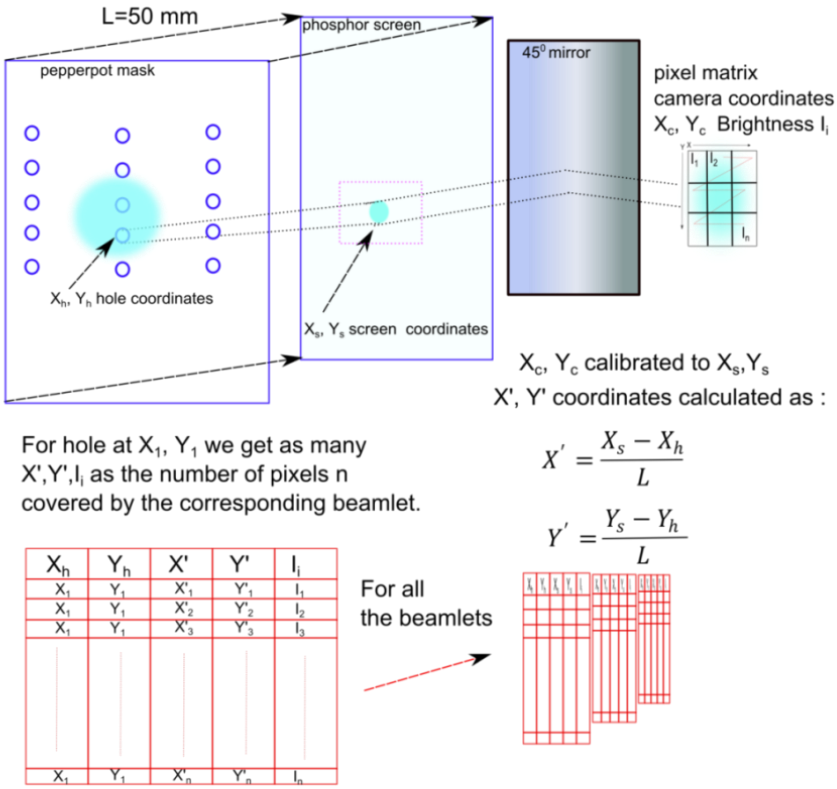

Figure 8 Pepperpot operating principle. Particle beam (blue spot) impinges in the pepperpot mask splits to small beamlets. Beamlets impact on the phosphor screen and produce visible light that is reflected on the camera via a tilted mirror. The array of pepperpot holes has spatial coordinates of X_h Y_h. The beamspot coordinates on the phosphor screen are X_s, Y_s . The coordinates on the reflected image on the camera change to X_c, Y_c .The coordinates on the camera sensor are translated to spatial coordinated using calibration images. Beam divergence X' and Y' is calculated for every beamlet and the data of the pepperpot hole location, divergence and pixel intensity are collected in an array. Several arrays are then created for all the beamspots.

The particle beam impinges on the pepperpot mask which is an array of equally spaced small holes. The hole's diameter is chosen so it is very small compared to the distance between the mask and the following scintillating screen and thus can safely be considered as a point source.

The pepperpot mask splits the beam into small beamlets that drift for a length L until they reach the transparent scintillating screen. Upon impact, visible light is produced and transported outside the vacuum chamber after reflecting on a 45° tilted mirror. Using the known locations of the holes, the distance L and the measured positions of the beamspots on the scintillating screen the beam emittance can be calculated from equations (3) and (4).

Other commonly used configurations of this basic design include:

- A tilted, non-transparent scintillating screen instead of a transparent screen and mirror.
    - The drawback of this configuration is that it requires image correction in the post-processing for the distortion caused by the tilted plane of the scintillating screen.
- A transparent screen and a vacuum viewport right behind it.
    - Much simpler but special arrangements have to be made in the beamline.
- Use an MCP instead of scintillating screen to increase the sensitivity for low current and low energy beams.
    - The increased cost of the MCP compared to scintillating screens and added complexity but unavoidable if the extra sensitivity is needed.
    - More reliable operations because scintillating screens tend to degrade quickly when used with heavy ions [27]–[30].

2. Pepperpot based emittance monitor

This chapter describes the development of an emittance monitor for low energy beams produced by an Electron Cyclotron Resonance (ECR) ion source. The first section discusses the motivation behind the emittance meter development.

The chapter then proceeds by presenting the ion source and the Low Energy Beam Transfer (LEBT) line where the emittance meter is installed and operated. Background on the operating principle of ECR ion sources is given followed by design details of RIKEN's 18 GHz superconducting (SC) ECR ion source, the relevant modifications required to improve beam quality and beam transport studies.

The chapter then delves into the development of the emittance monitor and presents all the design details. An important part of this device is the operating algorithm which starting from raw images acquired by the camera calculates the beam emittance in real time with a maximum frame rate of up to 5 fps.

The last section presents experimental results acquired from proton and heavier ion beams. The first part discusses the performance of scintillating screens under irradiation with various beams and how the screen performance affects the measured emittance. Finally, emittance measurements and correlations with various ion source operating parameters are shown and discussed.

2.1 Motivation

RIKEN's Radioactive Beams Facility (RIBF) utilises an 18 GHz ECR ion source [31] to produce highly charged ion beams. Firstly, for use in the Azimuthally Varying Field (AVF) cyclotron for stand-alone experiments, and also for the subsequent Riken Ring Cyclotron (RRC) and the Superconducting Ring Cyclotron (SRC) if higher beam energies are required.

User experience has shown that the transport efficiency from the ion source to the AVF is much lower when compared to the use of RIKEN's Linear ACcelerator (RILAC) as an injector. Moreover, it has been confirmed experimentally by using a scintillating screen at the entrance of the LEBT, that the beam size is larger than the LEBT aperture resulting in unwanted collimation and beam losses. Moreover, preliminary beam dynamics studies suggested that the transport efficiency from the ECR ion source to the LEBT is about 16 % and the beam emittance blows up in the area between the ion source and LEBT due to the intense fringe of the ECR solenoid.

The demand for higher beam intensities and more efficient beam transport triggered more extensive simulations and experimental studies into LEBT efficiency and optimisation, as well as R&D into the emittance measurement itself.

Work done in the context of this thesis focused mainly on two areas

- Development and operation of pepperpot based emittance meter. The emittance meter development covered also extensive studies on the performance of scintillating materials in order to find the most suitable for low energy ion beams.
- Experimental studies into LEBT, including ECR magnetic field measurement, optimisation of the ion extraction geometry and the design of an apparatus for direction beam current measurements.

2.2 ECR ion source and LEBT study

This section starts by describing the operating principle of ECR ion sources. It then moves forward to describe RIKEN's ECR ion source and LEBT. Following this description, experimental results of the ECR magnetic field measurements are shown and ion tracking simulations are discussed. Finally, the section closes presenting modifications of the ion source extraction geometry and a novel design for a beam current measurement apparatus.

2.2.1 Operating principle of an ECR ion source

The main building blocks and requirements of an ECR ion source include the following.

A vacuum vessel with low background pressure that allows the production of multiply charged ions by minimising recombination and charge exchange. In previous decades a two-stage vacuum system was implemented for ECR ion sources with a higher pressure area and a lower pressure area for the beam extraction. Nowadays a single stage high vacuum chamber is the standard [32].

A well designed magnetic field structure confines both ions and electrons in a magnetic bottle structure. The field is provided by superimposing an axial field generated by solenoids and a radial field produced by a sextupole (or another multi-pole) magnet. An atom injection system is injecting gases from a gas reservoir or condensables from a high-temperature oven. The confined electrons gain kinetic energy from an RF field (electron heating) and ionise the gas atoms through the process of impact ionisation. Lost energy during ionisation is replaced by the RF field and this cycle repeats multiple times leading to the production of multiple charged ions.

An extraction area that allows for beam extraction has usually the form of a conical biased electrode with a small aperture. By applying a high voltage to the electrode or grounding the electrode and applying a high voltage to the ion source chamber ion beams are extracted. The confining magnetic field has a small asymmetry on the extraction side to ease ion extraction.

The most critical processes in an ECR ion source are the magnetic field confinement and the electron heating. Confinement ensures that the electrons and ions are contained in a defined volume and leads to the production of stable plasma. Electron heating is required to sustain the plasma and produce high charge states by multiple ionisations.

2.2.2 ECR magnetic field

ECR ion sources feature a sophisticated magnetic field structure that can confine the plasma. It is a combination of an axially confining field and a radially confining field. The axial confinement is achieved by using two or three or more axial coils around the plasma chamber as indicated in Figure 9a. Figure 9b shows the three solenoids used to produce the axial field and the confining field. The current in the middle coil is opposed to the other two coils to create the dip in the overall magnetic field strength. The radial confinement is done usually by a sextupole magnet as shown in Figure 9c. The B_{med} in Figure 9a is also known as the minimum-B field.

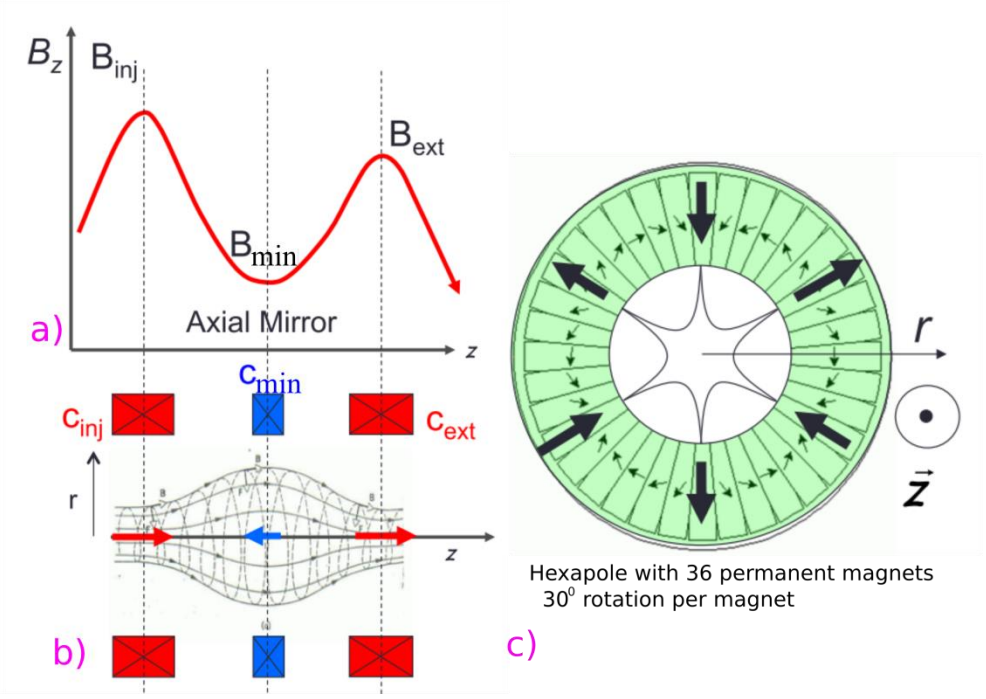

Figure 9: a) Axially confining magnetic field in an ECR ion source (not RIKEN ECR) produced by a set of 3 coils, b) Hexapole magnet used to produce the axially confining field [33]

The exact values of B_{inj} ,B_{min} ,B_{ext} and the radial field B_{rad} are suggested by the so-called ECRIS Standard Model l[34] which has been used for the past decade in ion source design. The main rules of this model can be summarised as:

1. $B_{rad} \geq 2B_{ECR.}$
2. $B_{inj} \approx 3\ B_{ECR.}$
3. $0.35 < B_{min} / B_{rad} < 0.45.$
4. $B_{ext} \approx B_{rad}.$

2.2.3 ECR electron heating

The free electrons in the plasma chamber are trapped in the magnetic field and move in spiral trajectories along the magnetic field lines. Their rotation frequency is called cyclotron frequency and is given by:

$$\omega = \frac{eB}{m}$$

Where *B* is the magnetic field, *e* the electron charge and *m* the electron mass. When injecting microwaves with frequency ω_{RF} the electrons are accelerated or decelerated depending on the phase of their cyclotron motion and the local RF field. This phenomenon takes place at the so called resonance surface or ECR zone which is defined by the condition

$$\omega_{RF} = \omega = \frac{eB}{m}$$

For a 18 GHz microwave frequency, the corresponding magnetic field strength on the resonance surface is 0.64 T. Figure 10 depicts the ECR electron heating process. Electrons trapped in the magnetic mirror cross the resonant surface several times and depending on the phase difference between their motion and the RF field they gain or lose energy. Overall, there is a net energy gain called stochastic ECR heating [35] that allows the electrons to reach energies up to several keV's and successively ionise the gas producing multiply charged ions. This repeats continuously as the electrons are reflected back and forth in the confining field. Electrons lose energy during ionisation and gain energy during the passage through the ECR zone. If more than one microwave frequency is used then several resonant surfaces can form leading to a higher density of hot electrons and improved production of high charged states [34].

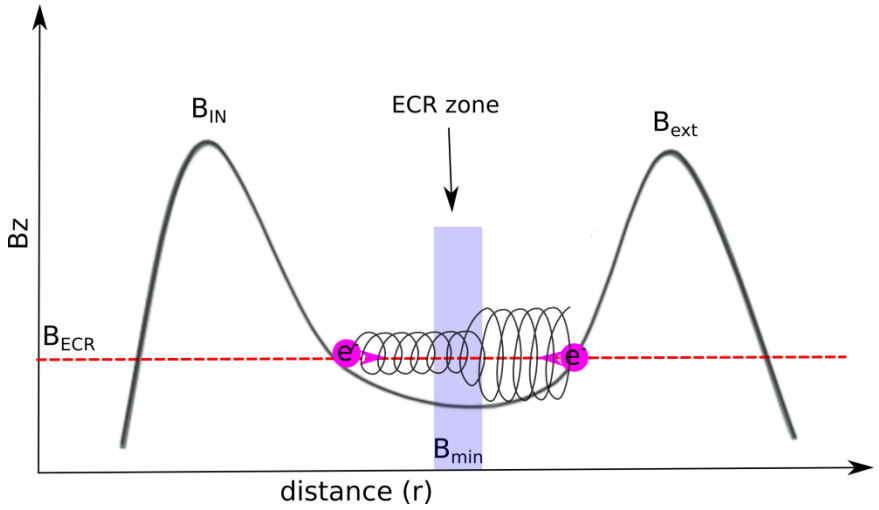

Figure 10: Electron motion in an ECR ion source. When passing through the ECR zone electrons gain energy from the RF field. This process repeats as the electrons are reflected back and forth in the confining magnetic field.

The magnetic field confinement is not symmetric in an ECR ion source; the field strength is lower on the extraction side easing the extraction of beams.

At the extraction side of the plasma chamber, there is a biased electrode to attract the positively charged ions. When plasma comes in contact with the extraction electrode, a sheath of sub-millimeter thickness is formed. The emitting surface is then the boundary between the sheath and the ion beam, so-called plasma meniscus [36]. The meniscus and thus the quality of the ion beam strongly depends on the geometry of the extraction electrode, extraction voltage, presence of electric and magnetic fields and plasma density. Optimisation of beam extraction is a very complex process and does not have a single solution; it rather depends on the operating conditions and the required beam species.

2.2.4 RIKEN 18 GHz SC-ECR and beam transport

Development on RIKEN's 18 GHz SC-ECR ion source started back in 1998 [37]. Currently the ECR ion source provides light and heavy ion beams of mainly gaseous elements to the Azimuthally Varying Field (AVF) cyclotron [38] which is used for Radioactive Isotope (RI) production, low energy nuclear physics studies and also as an injector for the RIKEN Radioactive Isotope Beam Factory (RIBF) [39], [40].

The specifications of the 18-GHz SC-ECRIS are summarised in Table 3 and a schematic of the ion source and the beam transport line are shown in Figure 11. The length and diameter of the plasma chamber are 378 mm and 70 mm, respectively. The plasma chamber is encapsulated by a sextupole permanent magnet of which the magnetic field is 1.1 T at the surface. A set of four superconducting solenoids is used to achieve the minimum-B condition.

A movable biased disc with a diameter of 30 mm is installed, to which a negative voltage of a few hundred volts with respect to the plasma chamber can be applied to increase the multi-charged ions flux. The effect of the biased disc and the material of the interior of the plasma chamber have been studied previously and optimised [41], [42]. A 750 W TWTA RF amplifier [43] connected to an 18 GHz reference source is installed to generate the 18 GHz microwaves that induce the ECR heating.

Table 3: Design specifications of the 18 GHz SC-ECR ion source.

Superconducting material	Nb-Ti	Analysing magnet	
Bore	220 mm	Pole gap	80 mm
Radius of plasma chamber	70 mm	Radius of curvature ρ	500 mm
Length of plasma chamber	378 mm	Bending angle	90°
Length of sextupole magnet	380 mm	B_{max}	0.15 T
B_{inj} (z= - 200 mm)	3.0 T	Edge angle	29.6°
$B_{min\|}$ (z= 0 mm	0.6 T		
B_{ext} (z= 200 mm)	2.0 T		
B_{rad}	1.0 T		
Microwave frequency	18 GHz		
Microwave power (max)	700 W		
Typical extraction voltage	10 kV		

The ions are extracted and accelerated towards a grounded extraction electrode by applying a high voltage of typically 10 kV to the plasma chamber. The extracted ion beam is focused by passing through an Einzel lens installed just behind the extraction electrode. It is then passed through the analysing magnet of the LEBT where the required ions are selected based on their charge-to-mass ratio. A typical ion spectrum is shown in Figure 12.

The gas supply of the ion source is done by two precision valves that allow for a single gas or mixture of gases to be used. There is also a high-temperature oven available for solid materials. The rest of the LEBT consists of a diagnostics chamber, two steering magnets, and a solenoid. The steering magnets are used to make small adjustments to the beam trajectory and the solenoid at the end to focus the ion beam. The diagnostics chamber contains a wire scanner based beam profile monitor; a set of horizontal and vertical slits for beam collimation and a Faraday cup [44]. The Faraday cup serves as an absolute current measurement device and is very frequently used to tune the analysing magnet in order to obtain the highest beam current for a given charge state . At the end of the LEBT, there is a dipole magnet that bends the beam by 90° and directs it to the AVF cyclotron located one floor below.

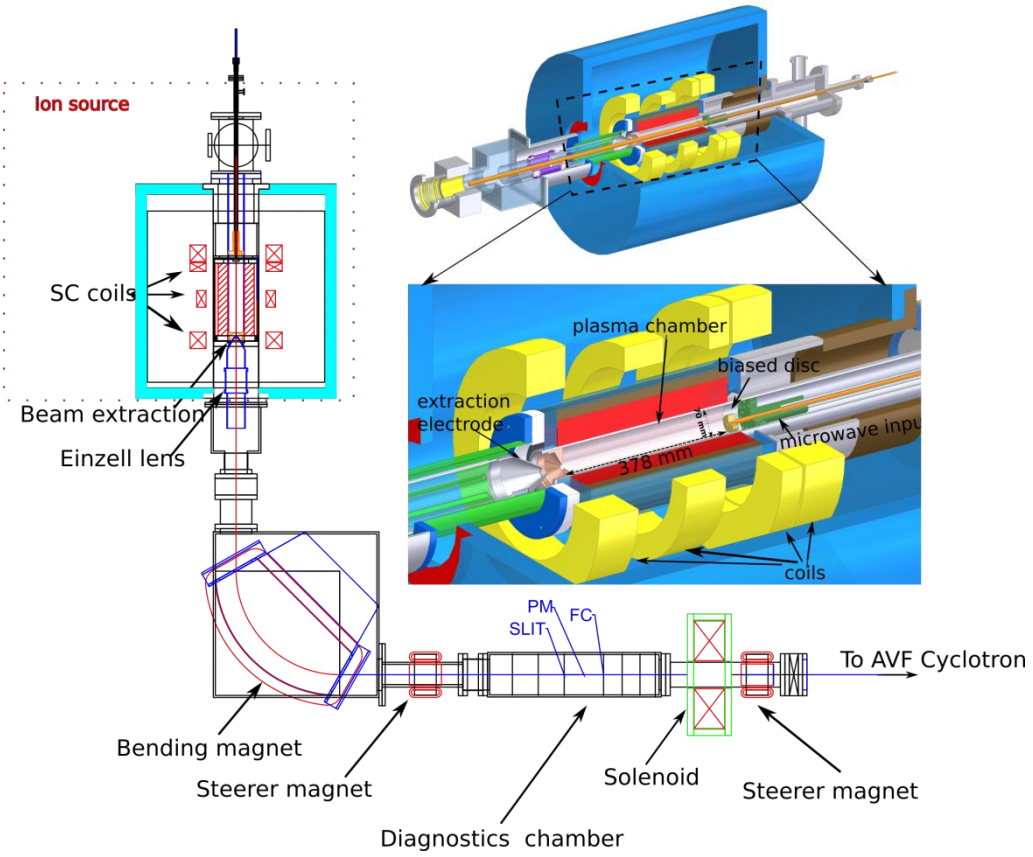

Figure 11: ECR ion source details and LEBT. The 2-d drawings have been created based on printed mechanical drawings by T. Nagatomo and the author. The 3-d drawings have been created by the author.

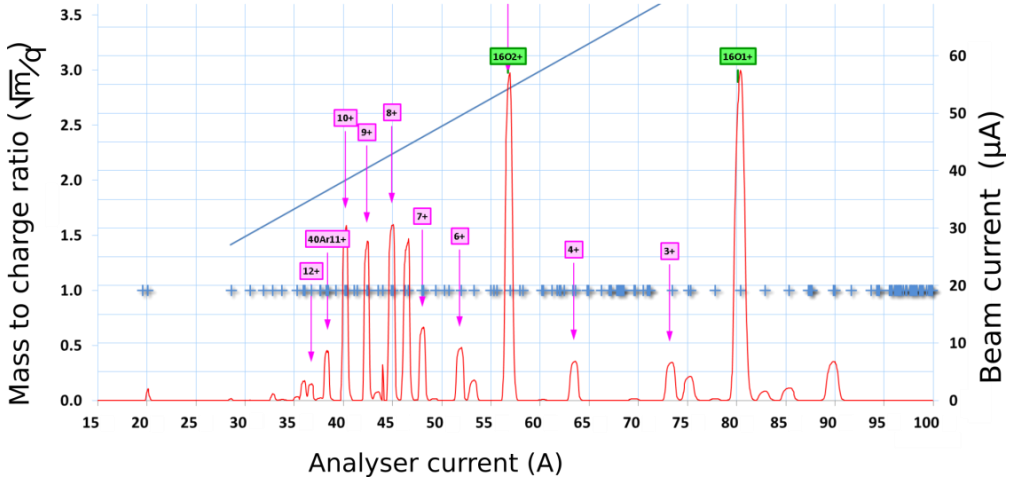

Figure 12: Spectrum of the ion source with Argon gas. Analysing magnet current is scanned up to 100 A and the beam current is measured by the Faraday cup at the diagnostics chamber.

2.2.5 Magnetic Field Measurement

The confining magnetic field of the ECR ion source is a critical parameter for its operation. Mainly it confines the electrons and ions but it has secondary effects on the beam quality as has been observed during beam emittance measurements. In the context of this thesis a measurement of the magnetic field of the ECR ion source was done.

The measurement of the magnetic field was carried out in order to examine if:

1. The design value corresponds to the measured value
2. The ion source design follows the ECR standard model

The measurement was done using a Hall-effect sensor and an aluminium structure to allow insertion in the ion source and controllable movement. The sensor was the LPT-141 with the DTM-151 unit supplied from Group3 [45]. It features adjustable ranges from 0.3 up to 3 Tesla scales with an accuracy of ±0.01% maximum error. The details of the setup used for the magnetic field measurements can be found in the appendix A.

With the plasma chamber open the probe can be inserted and measure both the axial and radial magnetic fields. The orientation of the probe needs to change for these 2 measurements because its surface must be perpendicular to the magnetic field lines. The axial magnetic field was measured at first only for the sextupole magnet with the superconducting solenoids being switched off and then with the solenoids energised. Results are shown in Figure 13.

A small irregularity of the sextupole magnetic field was found but it is a very small contribution of about 150 – 200 Gauss at the maximum when compared with the magnetic field induced by the solenoids (about 1 %) and it cannot affect the overall magnetic field. Figure 13 shows the measured magnetic field in the ion source. With reference to the blue curve, the right-hand side is the injection and left-hand side is the extraction. The peak magnetic field is smaller on the extraction side allowing beams to be extracted. The dip in the magnetic field strength in the centre enhances the trapping efficiency and the production of high charge states.

The radial magnetic field was measured by changing the orientation of the Hall Effect sensor and rotating it inside the plasma chamber. The sextupole magnet consists of 24 permanent magnets arranged in an annular shape as shown in Figure 14b. The magnetisation of every segment rotates by 60° and overall it produces the known sextupole magnetic field. Figure 14a shows the measured magnetic fields from 2 segments with opposite magnetisation (red and blue curves) while moving the sensor across the plasma chamber. The measurements

stop abruptly on the right-hand side of the plot because the geometry didn't allow for good support of the sensor. Figure 14b shows the radial field as measured at the centre of the plasma chamber while rotating the sensor.

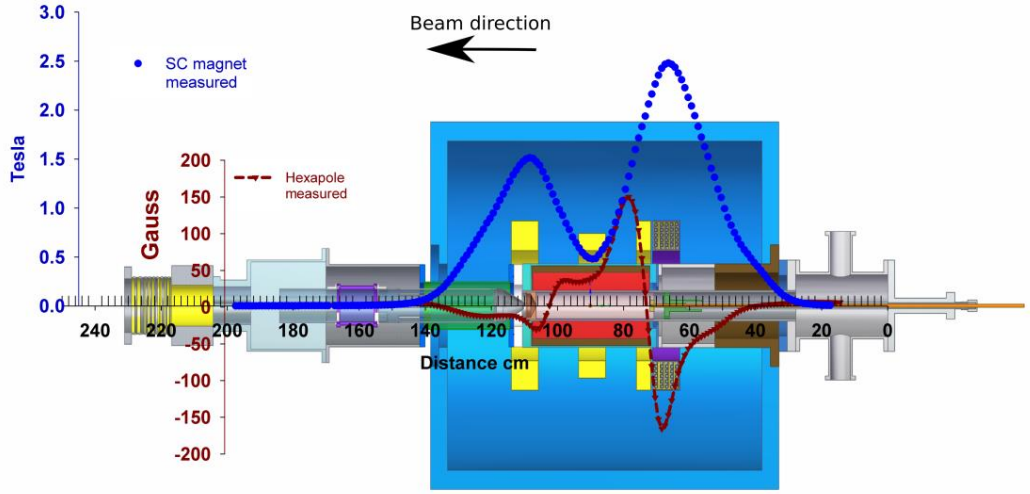

Figure 13: Measurements of the magnetic field in the ECR ion source. Blue curve and blue axis show the combined axial magnetic field from the solenoids and the permanent sextupole magnet. Brown curve and axis show the axial magnetic field from the sextupole magnet only.

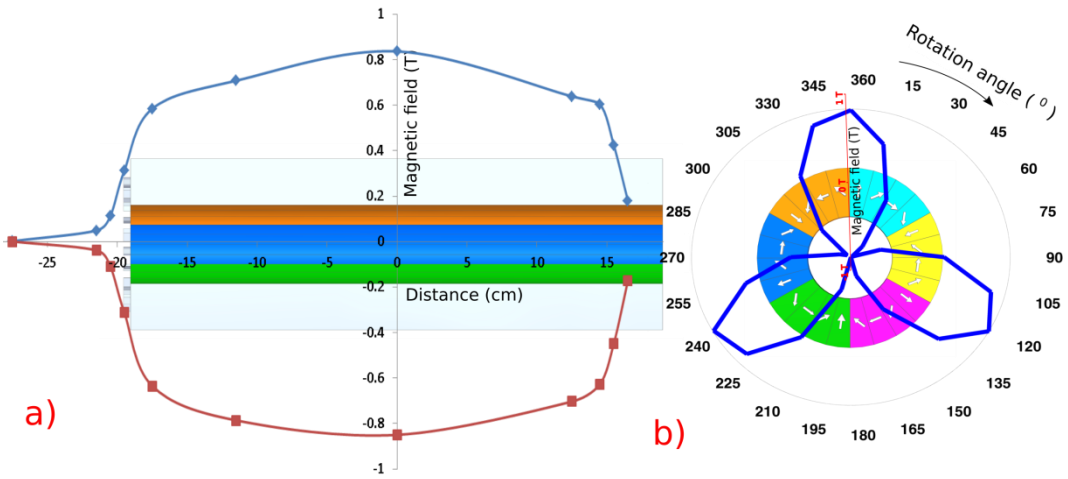

Figure 14: Measurement of the radial magnetic field from the permanent sextupole magnet.

Table 4 summarises the measured magnetic field values and compares against the design values. The B_{min} has a value of 0.13 T lower than the design value and its location is used as a reference for the position of B_{ext} and B_{inj}. The measured B_{ext} occurs 190 mm from B_{min} instead of 200 mm having a value of 1.50 T which is 0.5 T lower than the design value. The measured B_{inj} occurs 220 mm from B_{min} instead of 200 mm. Its value is 2.47 T and thus about 0.5 T

lower than the design value of 3 T. The measured radial field B_{rad} has a range of values from 0.6 T to 0.85 T in the plateau region instead of the 1 T according to the design value.

The measurement error due to the hall probe is less than ±0.01% and insignificant in these measurements. The main error comes from the positioning of the probe. For the case of the radial field, the probe could not reach exactly on the surface of the ECR chamber due to a thin (1 mm) aluminium sleeve inserted in the ion source and also due to the thickness of the probes aluminium mount (1 mm). Both of these errors account for an underestimation of the measured radial field of no more than 0.1 T.

For the case of the axial field, the error is due to the rough probe positioning again and the inability to guarantee a very good alignment along the entire measurement length. Nevertheless, after various measurements at a different location, it was estimated that this error doesn't account for more than 0.1 T of the measured field along the centre line.

Table 4: Comparison between ECR magnetic field design values and measured values.

Design values		Measured values	
B_{inj} (z= -200 mm)	3.0 T	B_{inj} (z= -220 mm)	2.47 ±0.1T
B_{min} (z= 0 mm	0.6 T	B_{min} (z= 0 mm	0.47 ±0.1T
B_{ext} (z= 200 mm)	2.0 T	B_{ext} (z= 190 mm)	1.50 ±0.1T
B_{rad}	1.0 T	B_{rad}	0.6 -0.85 ±0.1 T plateau value

When comparing the magnetic field measurements with the ECR standard model it can be seen that the standard model guidelines have not been followed precisely. Table 5 summarises the measured magnetic field values and present a comparison between the ECR ion source against the ECR standard model.

Table 5: Comparison of RIKEN's 18 GHz SC ECR with the ECR standard model.

Rule #	ECR standard model	RIKEN's18 GHz SC ECR
1	$B_{rad} \geq 2B_{ECR.}$	$B_{rad} = 1.3\ B_{ECR.}$
2	$B_{inj} \approx 3\ B_{ECR.}$	$B_{inj} \approx 3\ B_{ECR.}$
3	$0.35 < B_{min} / B_{rad} < 0.45.$	$B_{min} / B_{rad} = 0.55$
4	$B_{ext} \approx B_{rad}.$	$B_{ext} \approx 1.8\ B_{rad}.$

Only the second rule of the standard model is followed here. Nevertheless, the standard model is an empirical model based on experimental data from various ion sources and simulation studies. It does not exclude other magnetic field values but it states a set of optimal parameters. For RIKEN's 18 GHz ion source some of the parameters are bound by design. The sextupole magnet which defines the radial field cannot change and the B_{ECR} is restricted by the currently used RF source so the ion source cannot be made to comply with the first rule. The B_{inj}, B_{min} and B_{ext} depend only on the current fed to the independent solenoids and thus can be altered so the requirements by rules 3 and 4 can be met leaving only rule 1 not to comply with the standard model.

After the magnetic field measurement the aluminium sleeve, biased disc and end plug were replaced. Figure 15 show the etching marks on them caused by contact with the hot plasma. They correspond to the three lobes of the magnetic fields from Figure 14b.

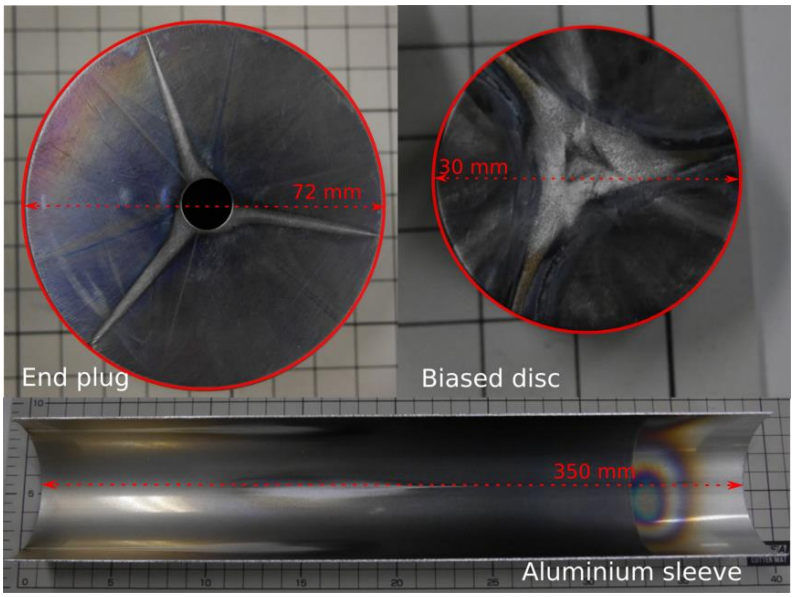

Figure 15: Etching marks from hot plasma on the end plug, biased disc and aluminium sleeve inside the ECR ion source.

Similar etching marks have been observed on other ECR ion sources. The marks, especially on the biased disc and the end plug, can be used as input or to benchmark results of ion extraction simulations for ECR ion sources [46]–[50].

2.2.6 Ion Extraction

The ion extraction is another critical aspect of the ECR ion source operation. The quality of the extracted beams depends on a number of parameters: extraction electrode size, shape, and location; plasma chamber end plug shape; extraction voltage; and Einzel lens voltage.

Without implementing extended design changes, the only parameters that can be easily manipulated are the Einzel lens voltage, extraction voltage and the extraction electrode longitudinal position within a range of 40 mm.

A simulation of the ion extraction and transport in the LEBT was done by T. Nagatomo in Geant4 [51] using 3D magnetic field maps calculated with the TOSCA package of Opera3D [52]. The first part of the simulation was to calculate the particle motion in the ion source under the influence of the magnetic fields. The particles (protons) starting position was a uniform 25 mm x 25 mm surface at the minimum point of the magnetic field with a uniform emission in 2p towards the forward direction. Particle initial energy was 1 eV. The particle distribution at the end of the plasma chamber is shown in Figure 16b. Figure 16a shows the plasma etching marks at the same location as have been previously observed. In Figure 16c the particle distribution is overlaid on the photograph of the plasma etching on the end plug. The etching marks match very well with the particle distribution verifying that the simulation model approximated to a high degree the particle motion in the ion source.

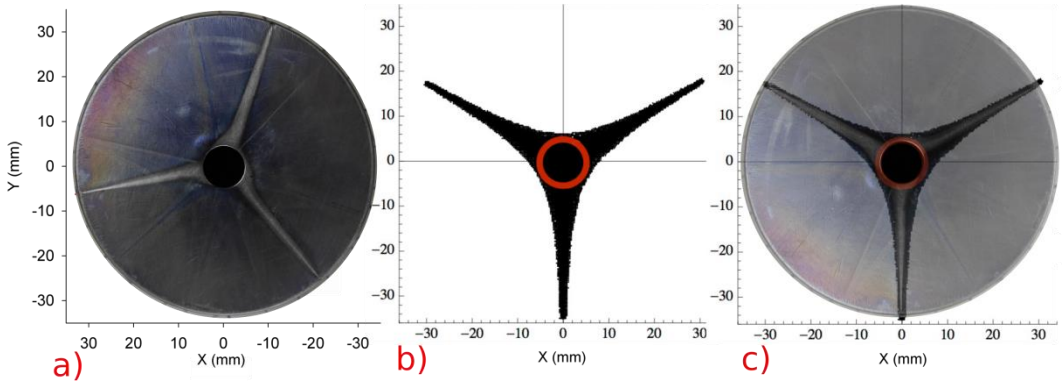

Figure 16: a) plasma etching mark at the end plug of the plasma chamber, b) results from ion motion simulation in the ion source using Geant4 and TOSCA done by T. Nagatomo. The red circle represents the extraction aperture, c) overlay of plot b on the picture a.

The second part of the simulation included beam extraction with an extraction voltage of 6.52 kV and particle tracking until the last chamber before the analysing magnet. Particle tracking and emittance evolution are shown in Figure 17.

Particle extraction takes place under an intense magnetic field (1.2 T at the tip of the extraction electrode). The emittance starts increasing as the particles leave the solenoid fringe field and eventually quadruples at around 800 mm from the extraction. As the beam enters the last chamber the particle number starts reducing due to collimation losses from the chamber's walls.

These results could not be experimentally tested in a precise way because of the geometry of the LEBT that does not allow for installation of an imaging device. For a single measurement only, a transparent scintillating screen was manually inserted in front of the LEBT aperture and was observed from around 1 m away through a viewport just before the bending magnet. The screen size was slightly smaller than the LEBT aperture but it was fully illuminated by the light produced by the proton beam – screen interaction confirming that the beam size is larger than the LEBT aperture.

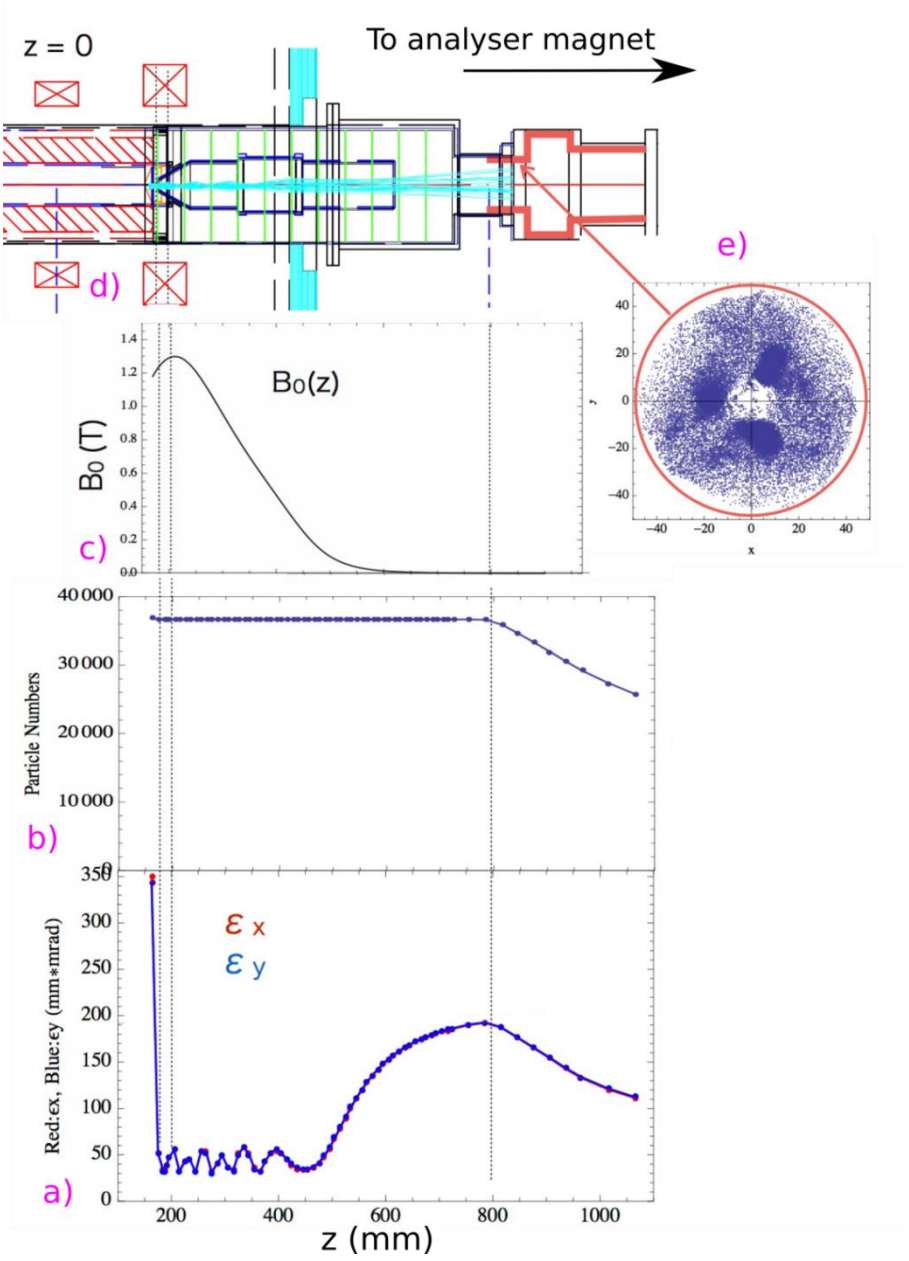

Figure 17: Particle extraction simulation by T. Nagatomo. a) emittance evolution, b) particle number evolution, c)magnetic field strength, d)geometry of the extraction, e) particle distribution at the entrance of the last vacuum section before the analysing magnet, plot scales are in mm [53].

The existing Einzel lens at the extraction side had a very small effect on focusing the beam. It was assumed that the Einzel lens operation was impeded by the intense magnetic field at the extraction region and thus had to be modified. In order to optimise the current production, the extraction electrode has been redesigned in order to allow the Einzel lens to be positioned further away in an area with almost zero magnetic fields. At the new location, the Einzel lens is fully operational and changes in the bias voltage are reflected on beam current and beam emittance.

As shown in Figure 18, originally the Einzel lens was at a distance of 150 mm from the tip of the extraction electrode. After the modification, the Einzel lens sat at 430 mm from the extraction completely outside of the fringe field. In addition, the extension cylinder featured oval cut-outs that improved the evacuation of the volume inside the cylinder.

After the extraction modification, the beam current almost doubled as measured with an oxygen beam. Similar extreme improvements in beam intensity have been reported by V.Toivanen [54]after using a scheme employing a double Einzel lens at the extraction of the JYFL 14 GHz ECR ion source increasing the beam current by 90%.

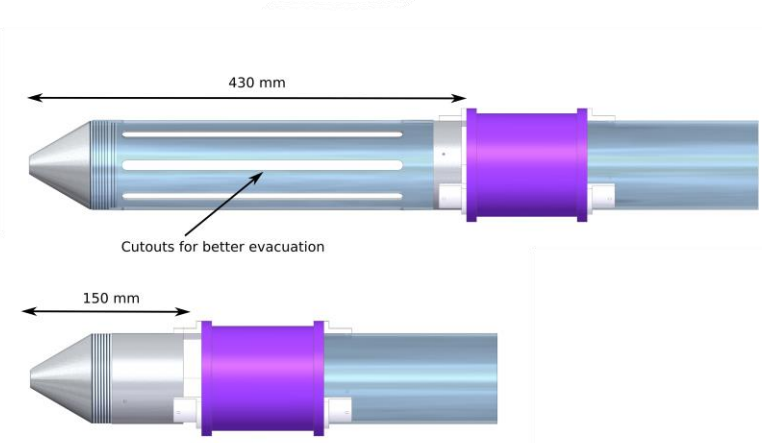

Figure 18: Extraction electrode and Einzel lens (purple).

2.3 Pepperpot based emittance meter

This section starts by describing the development process of the emittance monitor designed for RIKEN's ECR ion source and discussing all the design details. Following the hardware description, the algorithm for the control of the device and the emittance calculation is analysed in detail. The section then discusses the theory behind scintillating screens that are used as the imaging mediums for this application. Finally, the process for image calibration, resolution and error estimation is presented at the last part of this section.

2.3.1 Development process

The development of the pepperpot based emittance meter began based on an already existing device made by Y. Kotaka [55] from the Center for Nuclear Science (CNS) of the University of Tokyo .It served as a basis to develop software, identify possible design issues and define the requirements for the next instrument generation. This device, shown in Figure 19, was originally made to measure the emittance of RIKEN's HYPER ECR ion source. Four design iterations with minor or major changes arose during this work and they are briefly discussed in the following. A detailed design analysis will only be presented for the 4th and final prototype of the emittance monitor in the section 2.3.2 Hardware Design Details.

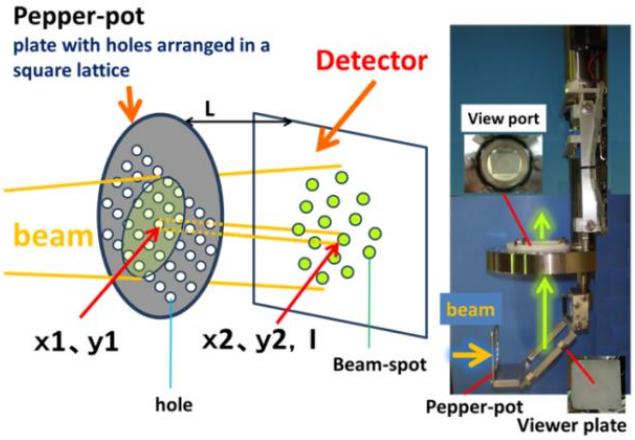

Figure 19: Emittance monitor of the HYPER ECR ion source [55].

It was quickly observed that the first device could be greatly improved on structural stability, resolution and ease of calculations. The pepperpot screen has large 0.3 mm diameter holes spaced at 3 mm intervals. It is mounted on a metal plate held in place with tension springs composing a folding mechanism to ease insertion in the chamber because of spatial restrictions. The large hole pitch lead to reduced resolution and the spring support in poor stiffness. Furthermore, the emittance meter was positioned at an angle in the beamline so in the data processing this had to be corrected in addition to the 45° of the scintillating screen.

The second design iteration is shown in Figure 20 and greatly improved the stability and rigidity of the system by using a solid structure with 10 mm diameter aluminium rods. The major difference in comparison to the previous design was the use of a transparent scintillating screen and a 45° tilted mirror to transport the light out of the vacuum chamber.

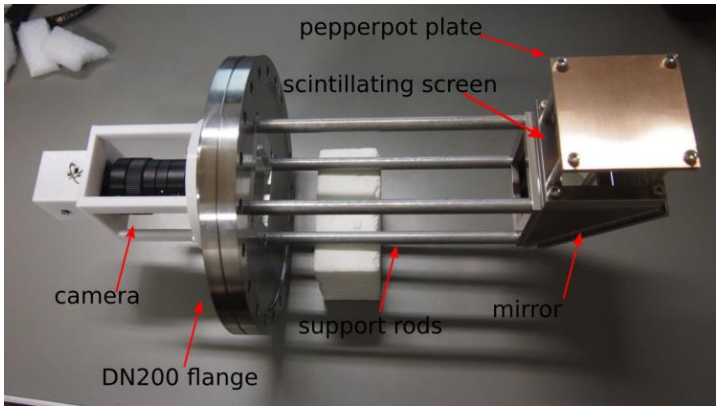

Figure 20: Emittance meter 2nd prototype.

The pepperpot mask used was a thin (0.2 mm) copper foil measuring 70 mm x 70 mm. It contained an array of 0.2 mm diameter holes with a pitch of 2 mm and sat 50 mm from the scintillator. Behind the scintillator, a tilted mirror reflected the light towards a camera through a transparent viewport on a DN200 flange.

The 3rd iteration shown in Figure 21 introduced an aluminium camera mount that replaced the previous one which was 3D printed from ABS plastic. The new mount included a custom water cooling solution for the camera that significantly reduced the thermal noise background.

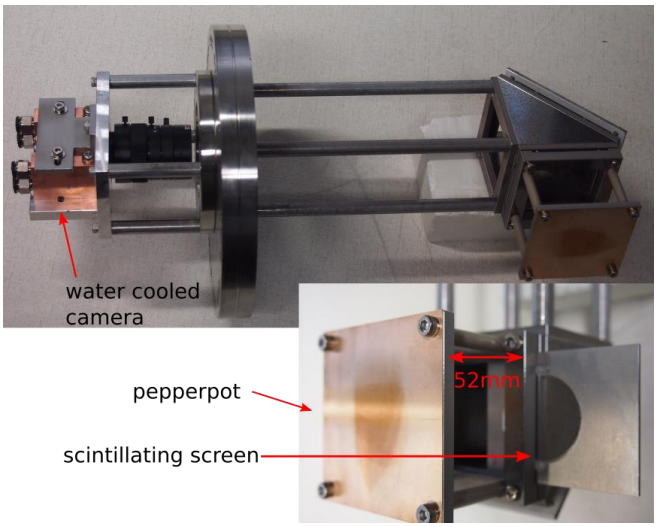

Figure 21: Emittance monitor, 3rd prototype.

For the previous three design iterations, the emittance monitor was located in the diagnostics chamber of the LEBT and did not include an insertion mechanism. For the 4th and final design iteration, a custom chamber was made and placed at the end of the LEBT replacing a vacuum duct of equal length. The improvements of the 4th version included the addition of a linear motion feedthrough for device insertion, a vacuum compatible stepper motor for

independent movement of the pepperpot mask only and the optional use of an MCP for higher sensitivity.

2.3.2 Hardware Design Details

Design overview

The new diagnostics chamber accommodating the emittance meter is built around a standard DN200 6-way cross with a length of 328 mm. The side holding the emittance meter is modified to allow a distance of 210.5 mm from the face of the flange to the centre of the chamber. The reason for this modification is to enable the previous prototypes without the retraction mechanism to be used interchangeably in the new chamber and the old diagnostics chamber should this be required. The 4th version of the emittance meter and the new chamber are shown in Figure 22. All the components of the emittance monitor are mounted on a DN200 flange and can be removed from the chamber in one piece.

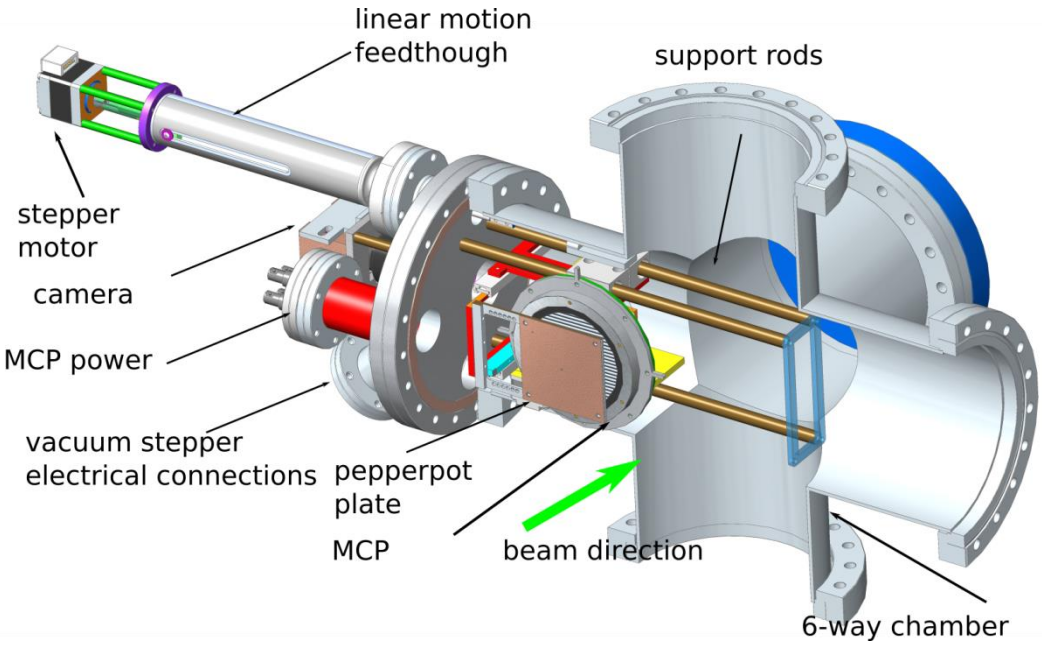

Figure 22: Emittance meter 4th prototype

Pepperpot sub-assembly

The pepperpot sub-assembly shown in Figure 23 is the moving part of the system. The sub-assembly is mounted on an 114 mmx75 mm aluminium plate. On the bottom side of the plate, there is the ultra-high vacuum compatible stepper motor (D35.1, Arun microelectronics [56] and one of the three bushing housings. The motor specifications allow use in vacuum up to 1x10$^{-1^{\circ}}$ mbar and bakeout up to 200° C.

The motor's shaft passes through the base plate and connects to a gear rack system by KOHARA gears for the separate movement of the pepperpot plate. The rack [57] is the SRG0_5-100 model with module 0.3 and length of 100 mm. The gear [58] is the SSG0.5-30A with module 0.5, 30 teeth and outside diameter of 16 mm. The bushing housings are custom made based on MISUMI MHCTS10 body. The oil free, 10 mm inner diameter bushings are provided by DAIDO metal, series DDK05 [59]. The inner surface is coated with PTFE for low friction and vacuum compatibility.

On the top side of the sub-assembly, there are two more identical bushing housings for the other two support rods. The entire system is compact and moves smoothly along the support rods. The last component of the top side is a support (red in Figure 23) for the top slider rail. The top and bottom rails (Figure 23 b) allow the pepperpot plate to move along the beam direction and vary the pepperpot to scintillating screen distance. The top and bottom sliders are provided by MISUMI (model SROMST15-90 rail, SROMS15 slider [60]). The original rails are made of aluminium and left unaltered. The original nylon sliders fit poorly and were not vacuum compatible. Custom sliders for tighter fitting and vacuum compatibility were made with nickel coated steel.

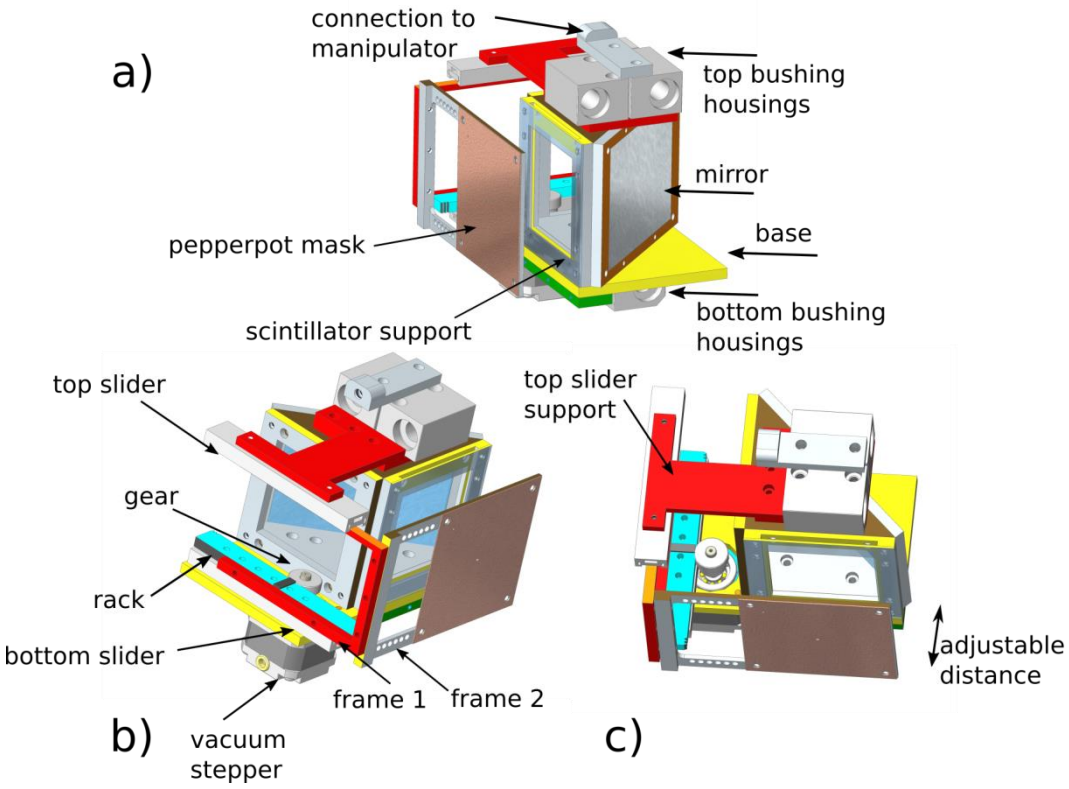

Figure 23: Different views of the pepperpot sub-assembly.

The pepperpot plate has the same size as in the prototypes 2 and 3. It is made from 0.2 mm thick copper foil, 70 mm x 70 mm in size with a 25 x 25 array of 0.2 mm in diameter holes with 2 mm pitch. The default pepperpot to screen distance is 52 mm as in the previous prototypes. The pepperpot is fixed on frame2 with 10 mm long ceramic spacers for electrical isolation allowing for beam current measurements directly from the pepperpot. Absolute current measurements are not possible due to the lack of secondary electron suppression but it is a useful feature to examine beam stability.

Behind the pepperpot mask on the main structure, there is a support for scintillating screens. The scintillating screens used here measure 65 mm x 54 mm x 2 mm with a usable surface of 50 mm x 50 mm. Materials used are transparent crystals of CsI(Tl) , KBR, SiO_2 and AlO_3. Screens can be exchanged without removing the emittance meter from the chamber. The top DN200 flange can be removed and the crystals are inserted in position. Following the scintillator, a 45° tilted mirror made of an aluminium coating on glass reflects the light towards the camera for image capturing.

The front side of the scintillator support in combination with a smaller support on the bottom side of the sub-assembly can hold an aluminium ring for an optional MCP detector. The MCP choice came later in the design process and after experiments with heavy ion beams where it was seen that the degradation of the scintillators was substantial. The use of MCP required several changes on the design and also contributed towards the development of a system with a movable pepperpot. The entire system could not physically fit in the chamber with the pepperpot being at the default distance from the scintillating screen.

2.3.3 Motion and manipulation

There are 2 linear manipulation systems on the emittance monitor.

1. Linear manipulator for insertion in the beam line.
2. In vacuum stepper motor for pepperpot – scintillator distance adjustment.

Linear Manipulator

The linear motion feedthrough is provided by MDC vacuum. It is the model 660010, which features 100 mm stroke length. It is mounted on a DN35 flange [61]. Originally this model was equipped with only manual control but it was updated to a custom setup with a stepper motor. The stepper motor is the PKP225D06A-L[62] from Oriental Motors. It is a two-phase small frame motor with 1.8° per step and a maximum current of 0.85 A per phase.

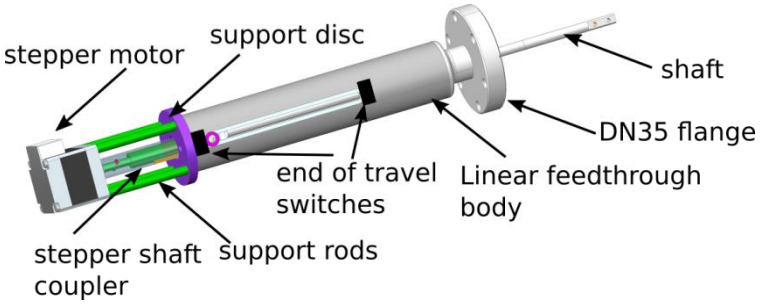

Figure 24: Linear motion feedthrough

The alignment of the pepperpot with the beamline centre was carried out with a laser and using existing alignment fiducials. The custom hardware and software control is based on a microcontroller board, the DRV DRV8834 stepper motor driver integrated circuit and Labview.

Movable pepperpot

For the pepperpot manipulation the DN35.1 model, vacuum compatible stepper motor and a standalone controller (SMD 210) were employed [56], [63]. The motor controller is interfaced with the data acquisition computer via a serial port connection. For remote control, a Labview algorithm has been developed based on the SMD 210 firmware commands provided by the manufacturer.

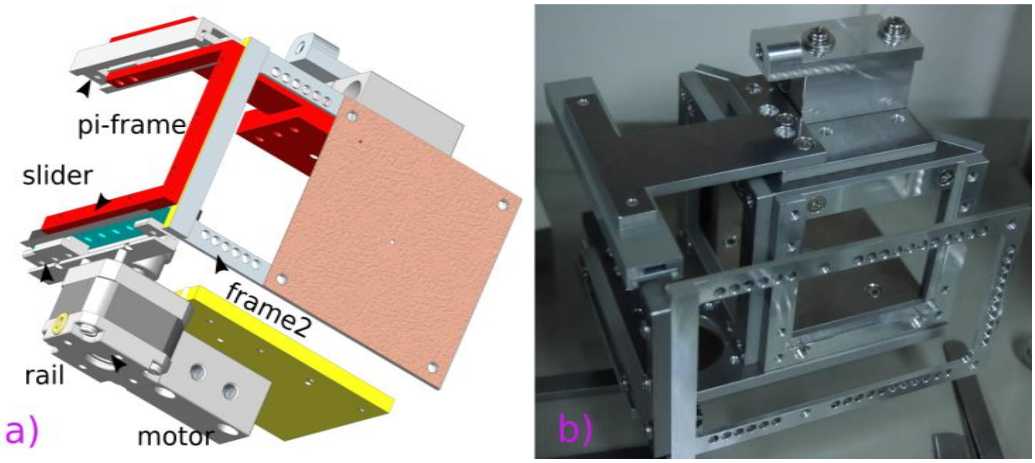

Figure 25: Movable pepperpot setup a) CAD schematic, b) real device.

The motor controller stores in a non-volatile memory the position of the motor so it is not erased after shut down. For the emittance calculation, the exact distance from the pepperpot to the scintillating screen is required. The calibration process to obtain the distances consisted of moving the motor in fixed increments and measuring the pepperpot to screen distance.

From the calibration measurements shown in Figure 26, the step to mm conversion factor which is also the movement resolution was obtained by a linear fit and was found to be 0.24 ±0.02 mm/step. For the optional MCP, the MCP to scintillating screen distance was taken into account in the distance calculation. Figure 26 shows the measured and calculated data for the step to mm conversion for the use of MCP or scintillating screen. The calculated data are produced by the gear and motor specifications. The pepperpot travel for 1 full rotation of the stepper motor is 47.25 mm given by the gear's pitch (15 mm) so the distance travelled in one step is 0.236 ±0.068 mm for the 200 steps per rotation of the motor which is in agreement with the value calculated from the measurements of Figure 26.

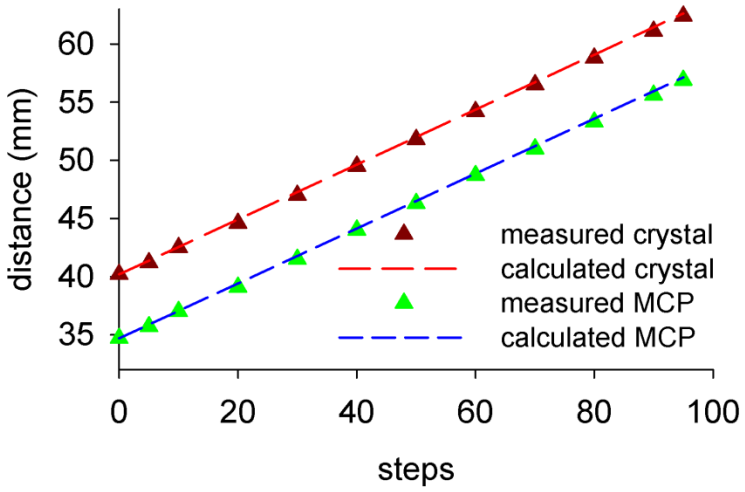

Figure 26: Stepper motor calibration.

2.3.4 Camera setup

The camera used here is the BFLY-PGE-13E4M-CS model from Point Gray [64]. It contains the 1/1.8'' e2v EV76C560 CMOS sensor with a pixel size of 5.4 μm. This camera belongs to a new series of cameras called scientific CMOS combining high image quality equivalent of CCDs and lower cost because of the CMOS technology. The sensor resolution is 1280x 1024 at 60 fps. It also offers higher frame rates at reduced resolution. The output images are monochrome (black and white) with selectable 8 or 16-bit colour depth. The exposure time is adjustable up to 999 ms. The camera comes in a miniature package of 29x29x30 mm. Connection with a computer is available using a 10/100/1000 Mbit/s Ethernet port which also powers the camera using Power over Ethernet (PoE). The camera is compatible with universal GigE drivers that support a wide range of Ethernet-based imaging devices providing a common framework for software development. A Computar 12-36 mm varifocal

lens [65] is attached to the camera providing a field of view slightly larger than the pepperpot usable area (50 x 50 mm).

The camera assembly is mounted behind the viewport of the support flange and located on a custom made support shown in Figure 27. It is fixed to the flange by 4 rods bringing the front side of the lens 2-3 mm away from the viewport.

During operation, long exposure times are usually required, of the order of a few hundreds of ms. For high exposure time, the image noise is dominated by the sensor's thermal noise leading to poor image quality when the light intensity produced by the scintillator is very low. In these conditions, it is very difficult to discriminate the beam induced signal from the noise. Background subtraction and image averaging can improve the signal to noise ratio but only up to a certain limit.

To rectify the noise issue a custom cooling system has been devised. As shown in Figure 27, the camera mount holds two copper blocks which allow water to be circulated through them. The blocks are connected to a chiller for water temperature control. The camera was disassembled and a thin (0.2 mm) copper foil was inserted right behind the sensor's main board. Thermal contact was ensured by a high-quality thermal paste and additional electrical isolation by a silicon insulating spray.

This modification greatly improved the signal to noise ratio as it drastically reduced the thermal noise. Figure 28 shows a plot where the background noise is measured by isolating the camera from any light sources. Pixel mean intensity was averaged in four different areas on the image. The plot represents the mean and the maximum of grayscale intensities in the regions of interest.

For the measurement shown in Figure 28, the sensor was initially cooled and while the measurement was ongoing the cooling was stopped allowing the sensor to heat up to its normal operating temperature. For water temperature of approximately 6° C, the camera temperature was about 10° C as measured by the on-board sensor. A small background noise inhomogeneity was observed with the lower part of the image being noisier than the rest of it. This was caused by temperature inhomogeneity due to the location of the sensor's power lines.

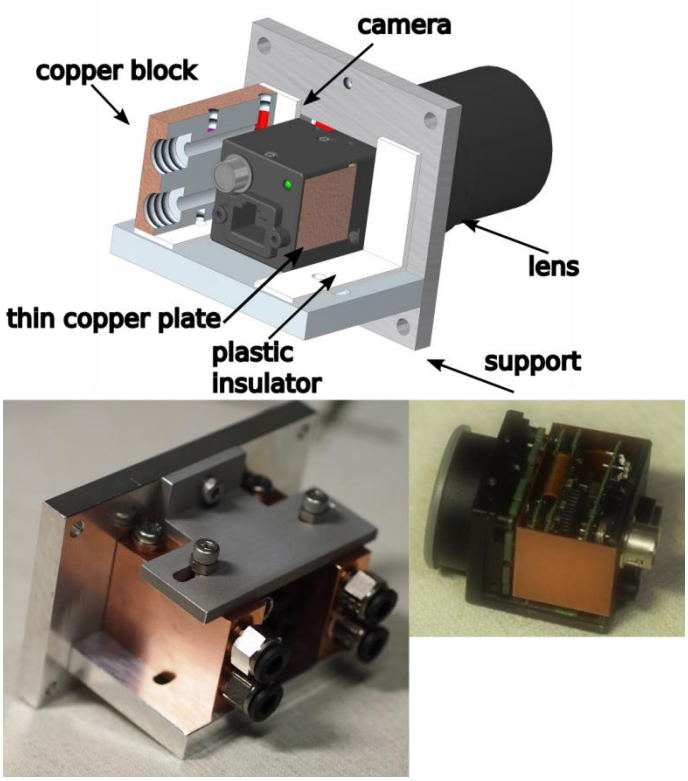

Figure 27: Camera setup and cooling method.

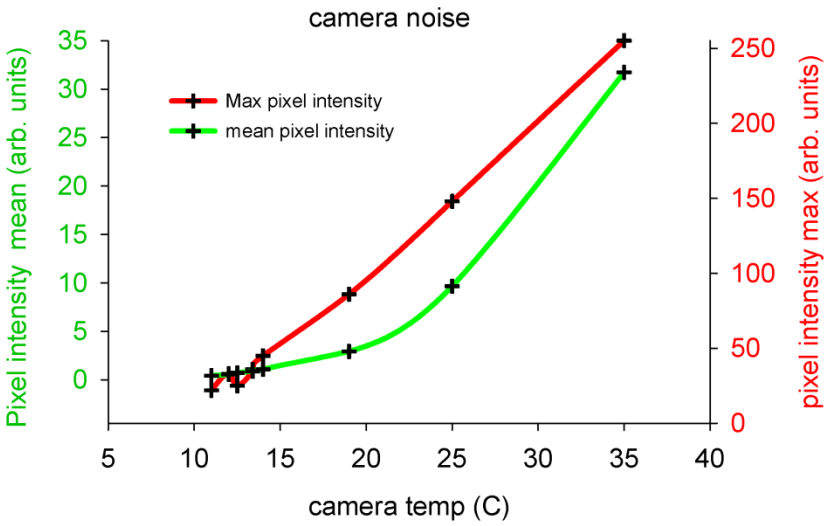

Figure 28: Camera noise dependence on temperature.

2.3.5 Electronics and controls

A single Labview programme controls the emittance meter sub-modules for the various components. The main structure is:

- Camera control, image acquisition and processing
- Emittance calculation
- Beam chopper control
- Motion control
- Current measurements
- EPICS interface for various beamline elements (magnets, RF power, inlet gas pressure)

From the above functionality, current measurement and motion control are handled by external hardware while the rest is controlled programmatically via the main algorithm.

External microcontroller based hardware

The external hardware is responsible for current measurements directly from the pepperpot plate and control of the pepperpot insertion in the beamline. It is composed of a number of discrete devices which are:

- Microcontroller board based on ATMega 328p low power microcontroller from Atmel [66]
- Ethernet interface board based on the Wiznet W5100 Ethernet chip [67]
- ADC board based on the ADS1015 12 bit ADC chip by Texas Instruments [68]
- Stepper controller board based on the DRV8834 chip by Texas Instruments [69]
  These boards are placed on a passive base board with interconnections and power distribution from a 1.5A 5V power supply.

Microcontroller firmware

The firmware on the microcontroller runs an Ethernet server and communicates with the computer exchanging TCP protocol based messages. The block diagram of the firmware is shown in Figure 29.

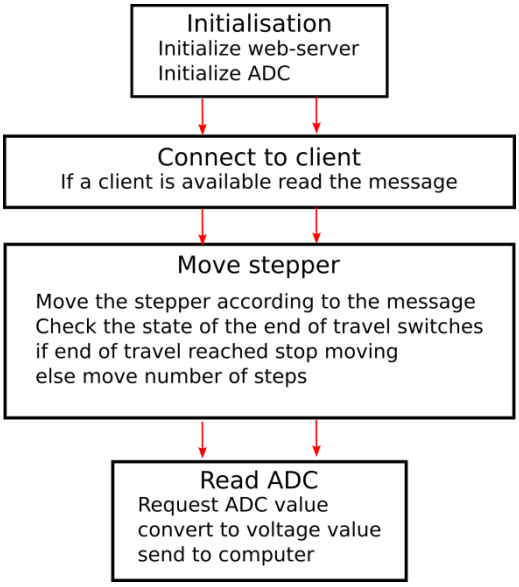

Figure 29: Firmware block diagram.

At first, a server is created and initialized to an allocated IP address followed by the ADC initialization. Several registers are initialized for the motor controller and the ADC operation. The server seeks for available clients and if one is found (only 1 client available here) it establishes a link and starts reading messages. The messages originate from a Labview module running on the computer, consisting of the number of steps and direction for the stepper motor to move. The firmware then starts sending step commands to the controller and checks if the end of travel is reached. End of travel signals are triggered by two switches appropriately positioned on the body of the linear motion feedthrough. The movement continues until the motor reaches the required number of steps or the end of travel. At this point, it sends back a confirmation message to the computer.

The second function of the firmware is to read the ADC and send the values back to the computer. The ADC measures the voltage drop across a resistor connected between its inputs and the pepperpot plate. If there is no step command the ADC is read out continuously with a frequency of about 100Hz. The microcontroller and all the related components are assembled and placed in a plastic enclosure as shown in Figure 30. BNC type connections are available for current measurements (2 currently used and 2 spares) while the stepper connections are terminal block type. The control unit is modular so in the case of failure the faulty component can be replaced without affecting the functionality of the others. The circuit design was done in National Instruments Multisim and the board layout in Ultiboard. The fabrication of this unit took place on the site except for the purchased boards.

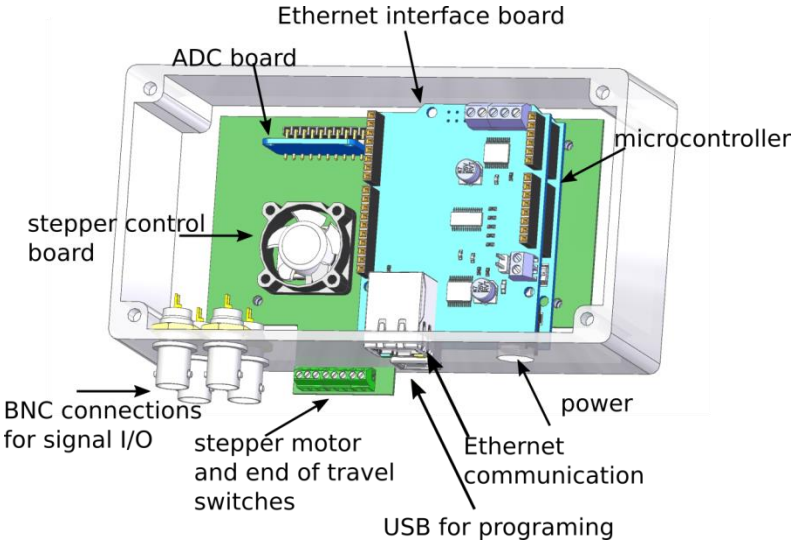

Figure 30: Control unit assembly.

Computer related software

The LabVIEW module running on the computer is a standalone routine and also exchanges information with the main control routine. It is structured in two parallel loops:

A. Device insertion and beam current measurements
B. Pepperpot motion.

The Loop A sends the number of steps and the direction of the insertion after user's input. In parallel, it displays the beam current as measured by the ADC. The Loop B communicates with the vacuum stepper motor via the Serial interface and moves the pepperpot plate to the required position. The in-vacuum motion system does not have the end of travel switches but software limits are set in the algorithm after measurements of the actual motion limits.

EPICS link

The overall ion source and the LEBT control system is based on EPICS [70] and links all the beamline parameters to a local network. Several operating parameters of the beam line, for instance, bending magnet current, solenoid magnet current, RF power etc. are occasionally needed during emittance measurements. For this purpose an external library that allows interfacing Labview and EPICS and establishes 2-way communication was used. The CA Lab library [71] was developed at BESSY Berlin and used there since 2009 for beamline control.

2.3.6 Emittance monitor software

The main control software of the emittance monitor runs on a Windows 7 computer with Labview 2014 64 bit and National Instruments Vision installed. Vision offers several image processing pre-compiled libraries which can execute operations quickly and efficiently in terms of computational resources. Several other 3rd party libraries were needed especially for convenient array manipulations. Labview is an excellent option for real-time applications and direct interface with hardware. For the particular case of Ethernet cameras, the universal GigE drivers give access to the most commonly used camera functions. Functionality that is not accessible this way can be added by direct register manipulation using low-level programming. There are two instances of the main algorithm, one that is used for real time emittance measurements and the other for offline data processing.

The algorithm can be loosely broken into 7 parts:

A. Image acquisition and camera settings
B. Filtering and processing
C. Extract pepperpot holes locations
D. Calculate x,x',y,y',I and beam emittance, x,y is the position, x',y' the divergence and I the grayscale intensity
E. Plotting
F. Control of peripheral devices (pepperpot motion, current measurements, beam chopper)

A – F takes place sequentially; G is controlled directly by the user and runs in parallel with the other processes.

A. Image acquisition and camera settings

The camera settings (gain and exposure time) are adjusted by the user from the GUI. The colour depth is usually 8-bit but it can be set to 16-bit as well. The exposure time is about 900 ms for the SiO_2 scintillator and a few 10s of ms for CSI. Gain is kept relatively high to about 80%-90% of the maximum. The acquisition frame rate is adjusted by a delay setting but the maximum achievable here is 4-5f ps. Images can be saved by with beam type, current and optionally other information embedded in the filename.

B. Filtering and processing

Basic filtering methods are used and include a median filter and background subtraction. The background image can be refreshed by a button in the GUI. There is an option to apply a

rotation to the image in case the pepperpot is tilted. For noise reduction, a threshold can be set and all the pixels with a value lower than the threshold are removed. The threshold is rarely used as a great portion of the thermal camera noise has been removed by cooling.

C. Beamspot identification

Identification of the beamspots is usually done by generating a grid and overlaying on the image with the beamspots [72]. The grid is centred to the centre of the pepperpot having as reference the blocked hole at the pepperpot centre. Every cell of the grid then covers the sensitive area around a unique beamspot. This approach works well in cases of small beamspots with good separation among them. For the device discussed in this thesis, the grid approach did not work because often the beamspots did not allow to contain them in the grid cell of the cell would cut through a beamspot causing errors in the emittance calculation.

The approach taken here was to detect every beamspot individually using image processing methods. Following the image filtering step, the acquired image is duplicated resulting in 2 identical copies, copy A and copy B. Copy A is converted to a binary image based on a user selected threshold so the beamspots can be clearly visible. A dilation operation inflates the size of the beamspots. Eventually, all the pixels on copy A have zero value except the ones representing the inflated beamspots which have a value of one. Following, copy A is used as a mask on copy B so all the area between beamspots is removed. The operation that takes place is multiplication so the pixels on copy B that are multiplied by zero become zero and those multiplied by one maintain their value.

The direct benefit of this method is that no cut threshold needs to be applied to the image and it is less sensitive than the grid method to irregular beamspot sizes and beamspot distribution in the image and How high the cut level should be and how it affects the emittance measurement should be calculated carefully [73]. It also reduces the amount of data to be processed making the algorithm faster. The above-mentioned processes are shown in Figure 31 step by step. The last step here is to find the pepperpot's centre. In order to use the centre of the pepperpot as a reference, the corresponding to the centre hole has been blocked. The algorithm then searches for a dark area near the centre of the image and fits a circle there returning its centre.

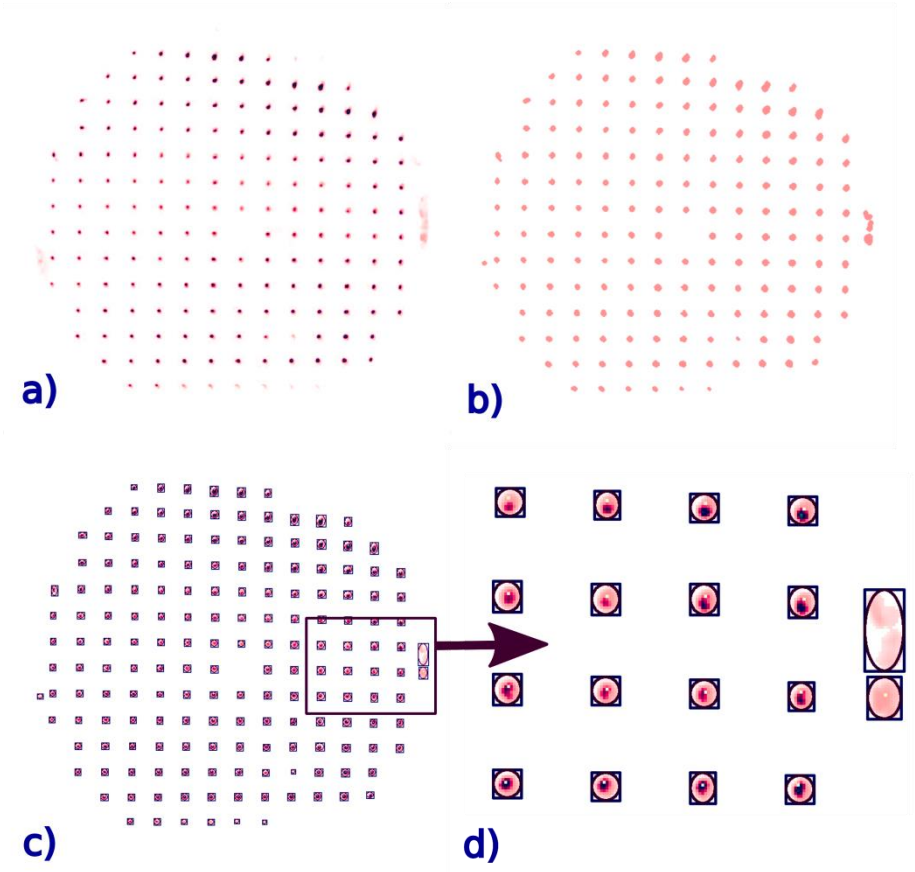

Figure 31: Steps of the operations on the image a) original image, b) binary image used as a mask, c) detected beamspots, d) magnified view of the selected area of c.

D. Extract pepperpot hole locations

The bounding boxes in Figure 31c are used to extract the pepperpot holes locations. Only the pixels inside the bounding box participate in the calculation and they are related to one specific pepperpot hole per bounding box. The locations of the holes are known but they must be correlated with the bright spots on the image. For this purpose, a function has been created that takes the centre of the bounding boxes in Figure 31c and fits them to a 2x2 mm grid representing the pepperpot pitch. By doing so a pepperpot hole can be directly related to one beamspot as it appears on the image. A verification step consists of plotting the positions of the hole as shown in Figure 32 and examine if they are spread across the 2x2 mm grid.

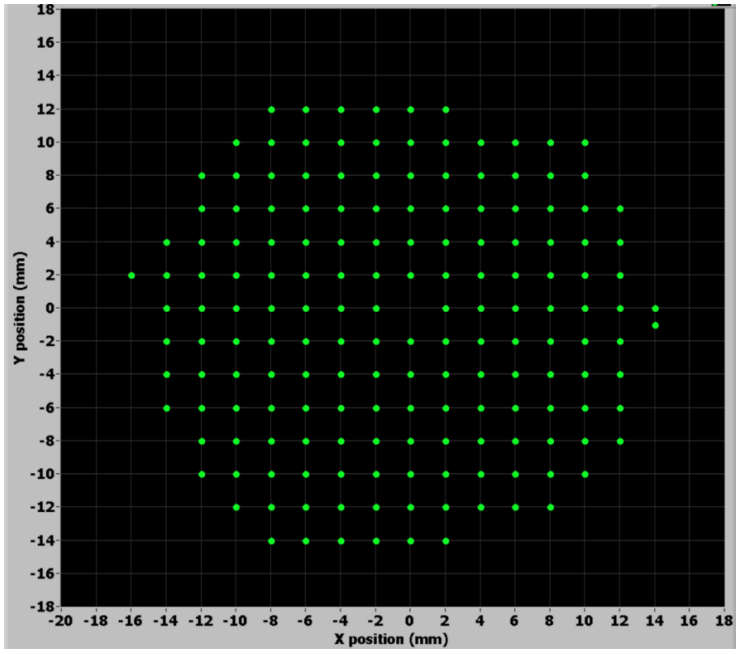

Figure 32: Positions of the pepperpot holes.

E. Calculation of x,x',y,y',I and beam emittance .

The data used in this step are pepperpot hole location, beamspot bounding box and image array. The algorithm moves sequentially from one hole to the next, takes the corresponding bounding box and for every pixel in there the divergence x' and y' are calculated according to equation (4). Beam emittance is calculated from (3).

F. Plotting

Two plots of the pairs of the phase space components , (x, x'), (y, y'), shown in Figure 33 are generated and updated in real time with every new image acquisition.

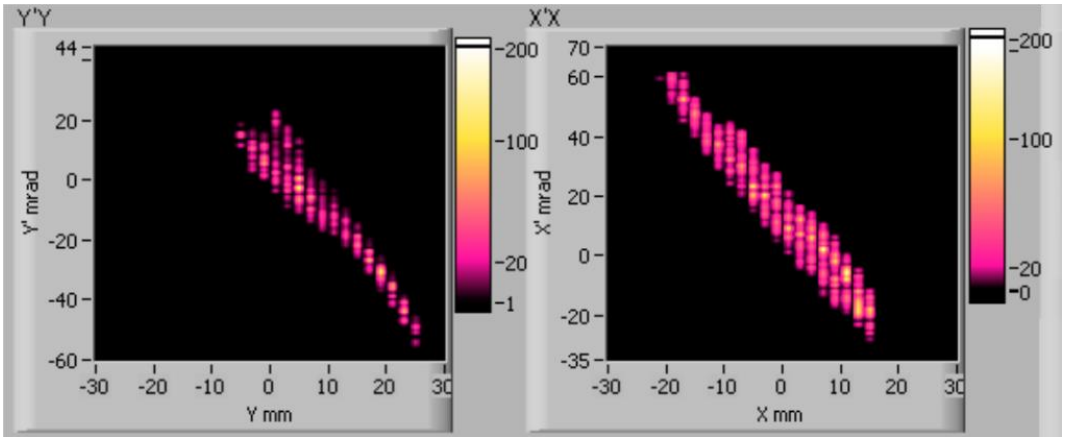

Figure 33: Sample emittance plots of the phase space components (y,y´), (x´, x), (y´, x´), (x´, y), (y, x) and (y´, x).

G. Control of peripheral devices

A number of other tasks take place in parallel with emittance calculations. A beam chopper is synchronised with the camera so it deflects the beam away from the pepperpot in the intervals between image acquisitions. This helps to preserve the scintillator and increase its lifetime. The control of the pepperpot motion and device insertion is done from a separate window which also displays direct current measurements from the pepperpot. Other devices of the beamline can be controlled by the link to EPICS.

To summarise this section, the key points of the approach used in this algorithm are the real time operation, no need to define a threshold in the image for noise reduction and the relative immunity on beamspot size and shape in the beamspot detection.

2.3.7 Scintillating screens

Scintillating screens rely mainly on the process of fluorescence, but other processes are also involved in the light production (phosphorescence, delayed fluorescence). The theory of scintillators is well studied and can be found in several reviews,[75] manufacturers datasheets and white papers [76]–[78]. Scintillating materials are broadly categorised as organic and inorganic. In organic scintillators, the fluorescence arises from transitions in energy levels of a single atom and can thus be observed from given molecular species independent of their physical state. Anthracene, which is used as a light yield reference for organic scintillators, is observed to fluoresce either as a solid, vapour or part of a compound substance. Plastic scintillators are made from organic scintillators dissolved in a solvent and then polymerised.

Inorganic scintillators, on the other hand, require a crystal lattice as a basis for the scintillation processes. In this case, the scintillation mechanism depends on the energy states dictated by the crystal lattice. In the crystal, electrons have discrete available energy bands that can be occupied. The lower (valence) band is occupied by electrons bound in the lattice while the conduction band is populated by free and more energetic electrons. Between these two bands, there is a forbidden band that electrons cannot occupy. For the transition from the valence band to the conduction band, they have to acquire enough energy.

To increase the light production in crystal scintillators, impurities known as activators are often introduced in the lattice forming intermediate energy bands. As a result, there are new intermediate energy states in the previously forbidden band, which the electrons are allowed to occupy and de-excite back from them to the valence band followed by photon emission. These de-excitation sites are called luminescence centres.

Recently, transparent ceramic (AlO_3 family) [79], [80] and glass scintillators [81], [82] have been developed. The ceramic ones are made by sintering nanocrystals on a polycrystalline solid so they can be made to size without having to grow large crystals.

Scintillators suffer from radiation-induced damage which deteriorates the material and reduces the light output. A very good description of radiation damage on crystal scintillators has been done by Zhu [83], [84] . The most common damage in crystal scintillators is the formation of colour centres and lattice displacements due to ion beam bombardment. Colour centres may or may not reduce the light yield depending on the radiation type. Lattice displacements, on the other hand, reduce light yield as they cause light absorption inside the crystal by the damaged regions.

When under irradiation, two competing processes happen in the crystal, which are scintillation and displacement damage defects. Scintillation depends on energy absorption causing electrons to occupy different energy states. Displacement damage creation depends on the beam species. Heavy ions are more likely to cause crystal defects[85] due to the higher mass.

There is a large number of studies on scintillating materials performance and radiation induced degradation but mostly focused on intermediate or high energy beams. A very good selection of such studies was presented at the scintillating screen workshop at GSI in 2011 showing applications with various types of particle beams ranging from electrons up to heavy ions. Buck et al reported on the use of plastic scintillators for a bunched 40 MeV electron beam showing excellent linearity over four orders of magnitude of light yield but with significant discrepancies on a material-depended resolution [86]. Lumpkin from Fermilab presented a study of YAG: Ce powder coated and crystal screens that confirmed a dependence of the resolution on the screen thickness and also the saturation of the light yield for charge densities over 10fC/μm [87].

Studies were done at GSI using a variety of scintillating screens including Al_2O_3, CSI: Tl, Chromox, P43, YAG: Ce, Herasil and others irradiated by a 269 MeV/u uranium beam. They confirmed the variation in the light yield and beam profile estimation among the screens. Some of the screens greatly overestimated the beam profile which is attributed to reflection from the rear side of the screen and absorption and re-emission within the bulk material [88]Another GSI lead study with lower energy ions beams of up to 11.4 MeV/u showed similar trends in light yield variation and beam profile estimation depending on the screen material. In addition, this study presented dependence of the light yield on the scintillator temperature [89].

Perdikakis from the Michigan State University [90] reports on using scintillating screens with a low current (1 nA) 48 keV helium beam. The material of choice was CaF_2 crystal stating that the light yield degradation is approximated by a two-component mechanism (slow and fast) similar to the finding of the work presented in this thesis.

Jan Maeder from GSI [91] presented a method of spray-coating scintillating materials of substrates similar to the use of KBR and CSI presented in this thesis.Finally, Strohmeier from LBNL [92] presented a study on the performance of scintillators for a low energy and low-intensity oxygen and argon beams comparable with the beams used in the current study. He stated the challenges posed by the material degradation under irradiation and the need for a new way to overcome these challenges.

The above studies have in common the material degradation and the material dependence uncertainty in beam profile estimation. The degradation differs greatly for various beam species and different screens but up to now, there is no way to overcome it.

A summary of the scintillating materials used here is shown in Table 6. All the materials in the table are commercially available. In addition to them, some other scintillators were used made by a different manufacturing process. KBR crystal powder was dissolved in purified water, which was then was sprayed onto glass and metal substrates which were placed on a heating element to evaporate the water. A similar process was followed with a CSI sample scintillator being dissolved in purified water, which was then spray-painted on a glass substrate. This process is not well controlled and the layer thickness and quality are inconsistent from sample to sample. However, it demonstrates the different light yield and radiation induced degradation between a material in the crystal form and a coating layer on a glass substrate.

Table 6: Characteristics of scintillating materials.

Scintillators characteristics				
Scintillator	Light yield (photons/keV) indicative values	Decay time (ns)	Refractive index	Emission wavelength(nm)
CsI(Tl)	54	1000	2	550
SiO2	--	--	1.46	--
CaF2	59	940	1.47	435
KBR	--	--	1.56	--
BC400	10	200	1.58	423
AlO3	16	300	1.94	385

2.3.8 Multi Channel Plate (MCP) detector

After the measurements using various scintillators it became apparent that image degradation was an important issue. For this, an MCP was used to provide high sensitivity along with reliable and stable operation. In the MCP, the heavy ions do not come in contact directly with the scintillating material and thus the degradation can be avoided .The model chosen here is the AF2226-A081E from Hamamatsu [93].

The MCP operates as a signal multiplier. Charged particles (ions here) enter the channels of the MCP and upon impact on the walls electrons are released. The electrons are accelerated between the front and rear surface of the MCP by a high voltage producing a cascade of electrons. After exiting the MCP, electrons still accelerate and impinge on a phosphor screen producing visible light. This way the heavy ions do not come in contact with the phosphor screen and thus the degradation is limited

The channels composing the MCP have a diameter of 25 μm and are tilted at an angle of usually around $10^{\circ} – 20^{\circ}$. The tilt enhances the electron production by forcing multiple impacts on the walls. According to the specifications data sheet, the minimum guaranteed gain is 10^4 which means that for every ion entering the channels 10^4 electrons will be produced. The gain, of course, is adjustable and based on the accelerating voltage. A brief list of the specifications can be found in Table 7. The maximum allowed high voltage is 1 kV between the front and rear surface of the MCP and 5 kV between the substrate and the MCP input of the phosphor screen. The bias configuration of the MCP is flexible and depends on the beam species. For positively charged ions the preferred configuration is to apply a negative voltage or ground to the input of the MCP, a positive voltage to the output, so it attracts the electrons and a higher positive voltage to the phosphor screen.

The resolution is quoted as 50 μm by the manufacturer. Even if the channel size is 25 μm the tilt angle must be considered and also the fact that the electrons exit the channels in a cone which leads to reduced resolution compared to the nominal channel size. In the case of two MCPs stacked together in a chevron configuration for higher gain up to 10^7, the resolution reduces to 80 – 100 μm.

Table 7: MCP characteristics.

MCP assembly characteristics	
Model	AF2226-A081E, Hamamatsu Photonics
Outer diameter	123 mm
Effective diameter	77 mm
Channel diameter	25 μm
Phosphor type	P46, 510 nm emission
# of MCPs	1
Gain	10^4 min
Resolution	50 μm

2.3.9 Image calibration and resolution

A. Image calibration

For the calibration of the device, a metal plate with a circular hole of 35 mm in diameter was used. The same plate was used in the early stages of the development to hold sample scintillators in place. The plate sits at the same positions as the scintillators in the emittance meter. A diffused light source was placed at the other side of the plate and the camera was focused on the edge of the hole for the reference image to be taken.

From the known diameter of the hole and the measured size in pixels the pixel to mm conversion factor was determined as 54 μm/pixel.

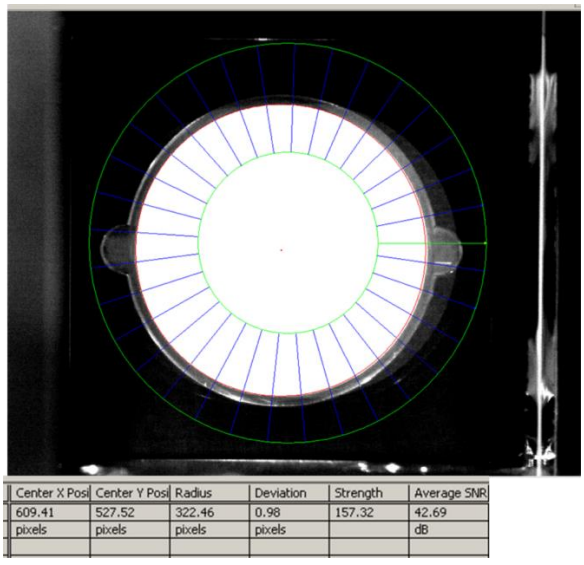

Figure 34: Picture of the image calibration process. A circle is fitted to the plate aperture and the centre and radius is shown in the table attached to the figure.

B. Pepperpot rotation

An LED-based light source with a diffuser illuminated the pepperpot from the rear side, the camera was focused on the pepperpot mask instead of the screen and a picture was taken as shown in Figure 35a. The image was then converted to binary and the circular bright spots representing the holes were detected (Figure 35b) and assigned an identification number according to their position. For vertical and horizontal rows and columns respectively the 2 most distant bright spots were connected from centre to centre in order to measure the rotation angle. Usually, this is less than 0.5 degree. In case this is larger due to assembly errors it can be corrected in the image processing algorithm.

C. Pepperpot pitch spacing

To evaluate the array pitch of 2 mm the spot to spot distances horizontally and vertically were measured for 221 hole pairs evenly distributed across the pepperpot area for each direction. The results are shown in Figure 36.a for horizontal and Figure 36.b for vertical. The units in the bin size are in pixels. From these measurements, the vertical and horizontal pitch can be calculated as $pitch_{vert}$=2.02±0.03 mm and $pitch_{hor}$=1.99±0.04 mm.

D. Magnification

Lastly, the magnification of the imaging system can be found by comparing a known dimension on an image (hole diameter in Figure 34) with its apparent size on the sensor. Here the hole diameter is 35 mm and measured by the camera as 645 pixels. The CMOS sensor pixel size is 5.4x5.4 μm^2. The product of these two quantities, hole size in pixels and pixel physical size in μm is 3.5 mm and thus 10 times smaller than the original hole diameter of 35 mm. From the above, the magnification is 1/10 or 0.1.

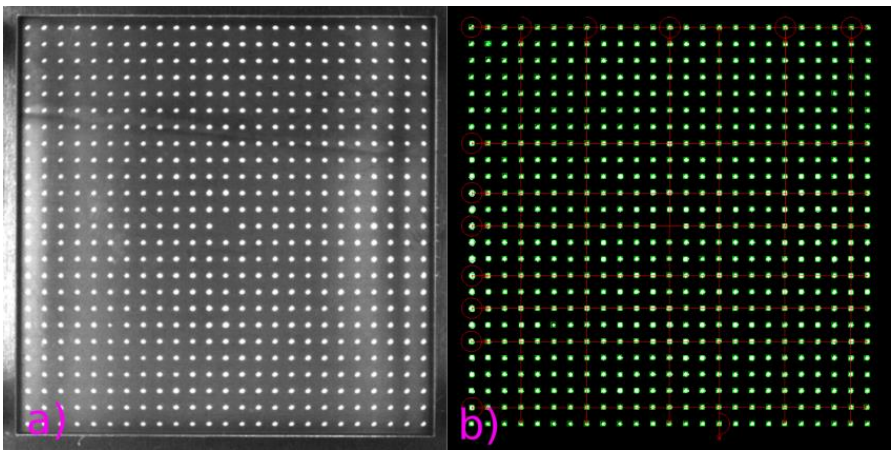

Figure 35: Original pepperpot array on the left. Processed image on the right with the pepperpot holes registered by the algorithm and reference lines (red) connecting the holes. The reference lines are used to measure the rotation of the pepperpot.

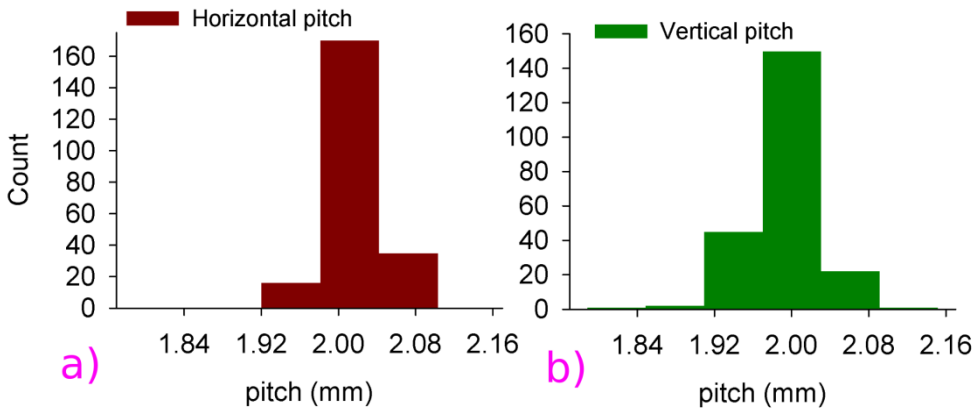

Figure 36: Vertical and horizontal pepperpot array pitch.

D. Pepperpot resolution

The position measurement resolution of the pepperpot device depends only on the pepperpot pitch. In this case, the pitch size is the equivalent of a pixel size if a camera is used to image the beam directly on a screen. If the standard deviation of the pitch is not known it can be defined by equation (6) considering the pitch as a uniform distribution with the length of 2 mm, In this case, the variance is given by the square of this length divided 12. The second term of equation (6) which comes from the camera resolution is much smaller and contributes less than 1% so it can safely be removed.

$$\sigma_x = \sigma_y = \sqrt{\frac{(hole\ \ pitch)^2}{12} + \frac{(resolution)^2}{12}} \qquad (6)$$

For the pepperpot discussed here with pitch of 2 mm the resolution according to equation (6) is

2.00±0.58 mm for both X and Y axis.

If the direct measurement of the pitch is used as mentioned previously, then the error can be minimised by about an order of magnitude. The resolution in this case is

$$2.02 \pm 0.03 \text{ mm} \ \text{ for X axis} \ , \ 1.99 \pm 0.04 \text{ mm for Y axis}$$

The angular resolution depends on the camera resolution and the pepperpot to screen distance and can be calculated as the inverse tangent (ATAN) of the ratio of camera pixel size over the screen to pepperpot distance. For small angles, it is simply the ratio of the above two quantities as shown in equation (7).

$$ang\ resolution = \frac{pixel\ size}{screen\ \ dist.} \qquad (7)$$

The standard deviation is then defined as in equation (8).

$$\sigma_{x'} = \sigma_{y'} = \sqrt{\frac{\left(\left[\frac{pixel\ size}{screen\ \ dist.}\right]\right)^2}{12}} \qquad (8)$$

Using the camera resolution as calculated by the image calibration and the screen to pepperpot distance of 50 mm the angular resolution is

$$1.04 \pm 0.30\, mrad$$

E. Error estimation

The errors in position and angular resolution have been discussed in the previous section. Another error contribution in emittance measurements comes from beam noise and the image noise (thermal noise). The image noise has been minimised after the camera cooling has been implemented and as shown in Figure 28 the average pixel intensity due to only thermal noise is almost zero.

The beam noise contribution depends mainly on the current fluctuations during the measurement and is expressed as the standard deviation of the pixel intensity *I*. Because of the relatively long exposure time, the large variation in beam current (up to 15%) is smoothed out and its effect on the light intensity variation is much smaller. Nevertheless, it also depends on the operating conditions of the ion source for different beam species and currents and it is difficult to narrow it down to one specific value. Measurements shown in the next chapter reveal that the standard deviation in pixels intensity is usually low (< 2 %) for stable ion beams but it is safer to assume a value of 5 % to cover even the worst case.

For beams with small emittances (<1 mm x mrad) as reported by Jolly for the Front End Test Stand (FETS) at Rutherford Appleton Laboratory (RAL) [94] and Hoffmann [95], [96] for the HITRAP system at GSI, the contribution of the above-mentioned errors in the emittance estimation is 4.8 % and 3.9 % respectively. For the emittance meter discussed here with better resolution in position and angle than the FETS emittance monitor and emittance values in the

order of a few tens of mm x mrad, the contribution of the error in emittance estimation accounts for less than 1 % and thus considered negligible. Table 8 summarises the pepperpot resolution and error terms from the various contributions.

Table 8: Summary of resolution and error terms.

Pepperpot resolution			
Parameter	Axis	measurement	σ
Position resolution	X axis	2.02 mm	±0.03 mm
	Y axis	1.99 mm	±0.04 mm
Angle resolution		1.04 mrad	±0.30 mrad
Beam noise		10% of max	0.1*I*
Image noise		~0	~0
Emittance		~20-40 mm x mrad	<<1

2.4 Experimental results

In this section, the experimental results with the pepperpot emittance monitor will be discussed. Before making any emittance measurements the ion source needs to be tuned. In the first part of the section, a basic ion source tuning is described including parameter scans that maximise the beam current. The measurements shown here are for a proton beam.

The next part of the section describes investigations into scintillating screens under irradiation with proton and heavier ion beams. Scintillating screens are a crucial component of the emittance monitor. Generally, requirements for scintillators are high light yield and low degradation. The first part of the investigation discusses the effect of the different screen materials on the beam profile size estimation using a proton beam. For this measurement, the emittance monitor is used without the pepperpot mask and basically operates as a transverse beam profile monitor. The second part discusses the performance of various materials under irradiation emphasising on the deterioration of the material. The visible effect of the deterioration is reduced light yield. Depending on the material the reduction can be quite large and quick rendering the scintillator unusable. Smaller deterioration can be tolerated as long as it is linear and slow or the light yield reaches a stable plateau. These measurements were carried out with the pepperpot mask on the emittance meter. Parameters monitored were the beam current measured directly with the pepperpot to verify current stability, light yield from selected beamspots on the image and area of beamspots.

The section ends showing emittance measurements with a proton beam which is the final project goal for developing this device. Various parameter scans are presented such as beam current, extraction voltage, ECR magnetic field, and their effects on beam emittance is discussed.

2.4.1 Ion source parameters scan and tuning

When the ion source is prepared to provide beams for experiments a tuning procedure is carried out. It is mostly based on operational experience and it is a rather time-consuming process taking away valuable time from the experiments. Such a process is very difficult to optimise and standardise as there are many operating parameters involved and several different beam species. The basic aim though is clear and it is to provide the maximum current. The rest of this section consists of a walk through some of the steps typically followed before a beam experiment. The main variables here are the Einzel lens voltage and its effect on beam current and size, gas pressure and RF power and its effects on beam current and finally the beam current stability during operation. The following process was carried out in order to provide a proton beam. The last part about the current stability refers to an oxygen beam because of the availability of data over a much longer period of operation.

Beam current and size dependence on Einzel lens voltage

In order to see the effect of the Einzel lens on the beam size the emittance meter was used here as a beam profile monitor by simply removing the pepperpot plate. A proton beam with an energy of 6.52 keV was used and the measurement location was approximately 5 m downstream the extraction. During this measurement, the integrated beam profile was irregular as shown in Figure 37 having two discrete peaks along the horizontal axis. In this case, it makes more sense to use the beam area expressed as the number of pixels occupied by the beam on the image instead of the actual beam profile. Here the beam area is expressed as the number of pixels with a value higher than a threshold of about 2% of the maximum.

Figure 38 shows the dependence of beam area and beam current on the Einzel lens potential. Both the beam area and current show a linear dependence on the Einzel lens bias voltage which varies from, 5.9 to 7.2 kV.

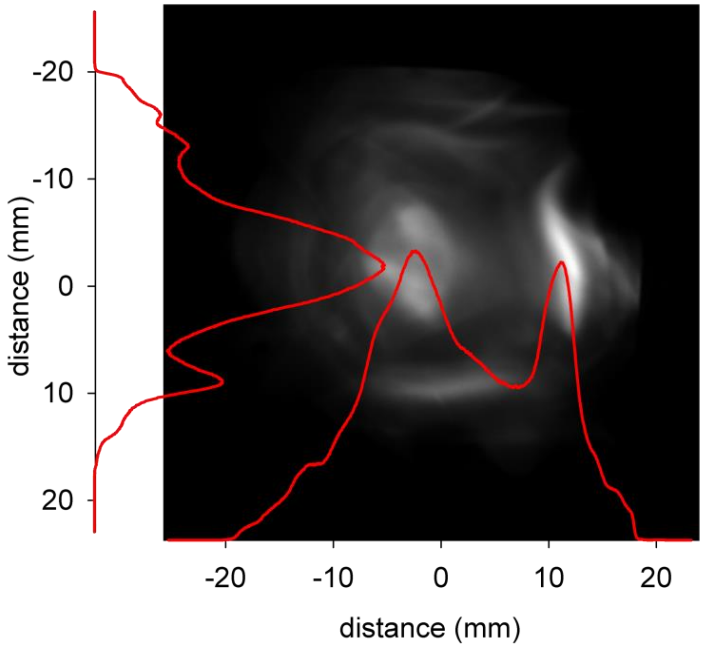

Figure 37: Proton beam with the vertical and horizontal beam profile overlaid on the image.

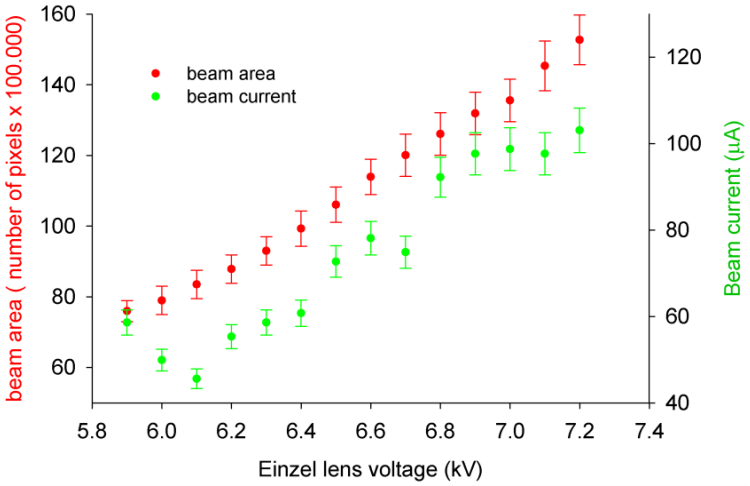

Figure 38: Beam area and beam current for a proton beam as a function of the Einzel lens voltage.

For a better interpretation of the results shown in Figure 38 but also for some of the following results the plasma formation near the extraction location must be considered. The trajectories of the ions extracted from an ECR ion source cannot be described only in terms of beam optics after the extraction. These trajectories are affected by several factors such as the strength of the solenoid magnetic field near the extraction, the shape of the plasma boundary layer and its interaction with the extraction electric field and the solenoid fringe field [97].

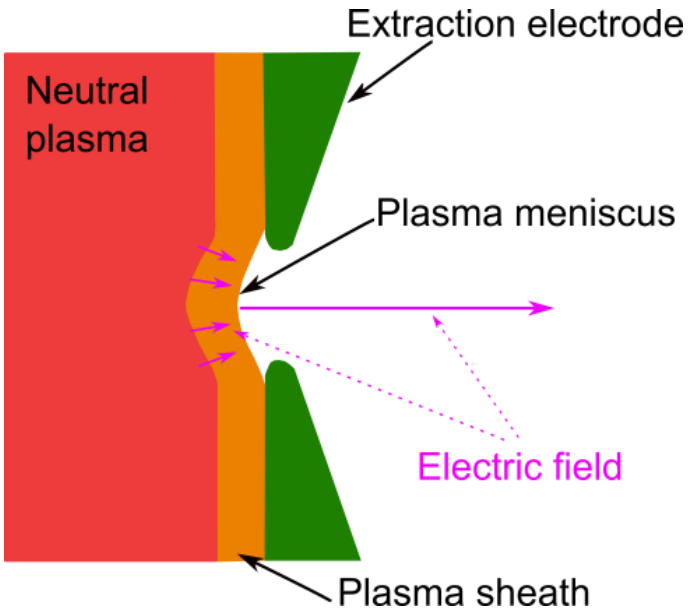

Figure 39: Extraction of an ECR ion source showing the plasma boundary layer (plasma sheath) forming in front of the extraction electrode and the plasma meniscus in front of the extraction aperture. Pictured redesigned based an illustration from [98].

The layer between the plasma and the extracted ion beam just behind the extraction aperture is called the plasma meniscus as shown in Figure 39. Its shape can vary from concave to convex depending on the plasma density and other parameters and it cannot be predicted [98]. The most favourable shape for ion extraction is a concave meniscus as shown in the above figure.

The results shown in Figure 38 can be interpreted by assuming a convex meniscus and a highly diverging ion beam entering the Einzel lens. Higher Einzel lens voltage leads to the better focusing of the ion beam, reduced beam losses and more efficient transfer through the lens and the following analyser magnet.

Beam current dependence on RF power and gas supply

The beam current depends on the ion source gas supply and the RF power for the ECR heating. The gas supplied to the ion source is chosen based on the desired ion species; here it is hydrogen gas for proton beam production. Because the gas flow is very low and impossible to measure and regulate with a commercial flow meter, a precision valve based on stepper motor is used. This method provided extremely precise control of the gas flow but there is no information of the actual gas flow.

At the time of this measurement the control of the RF amplifier was not working properly so the output power was set via a dial without having exact knowledge of the power but it approximately covers the entire range of the amplifier. Figure 40 shows the beam current

dependence on the RF power. The power was adjusted using the above-mentioned dials and the current was measured with a Faraday cup 2.5 m downstream the extraction. At every step of the RF power, the gas supply was slightly adjusted when needed to ensure stable plasma. The error bars represent the beam current range for fixed power and small variation of the gas supply required to achieve stable plasma.

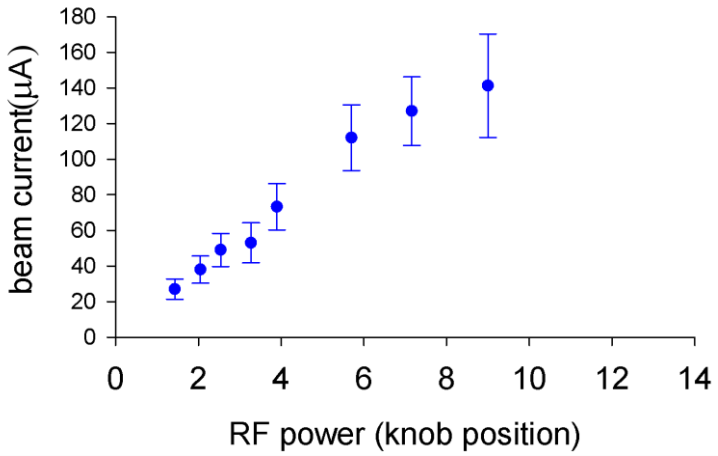

Figure 40: Particle beam current as a function of RF power. The error bars come from various settings of the gas supply for the same RF power.

Figure 40 presents the dependence of beam current on the gas supply. The gas supply itself is not known so the needle valve position in mm is used. As Figure 41 shows, similar values of beam current can be achieved either with low RF power and lower gas supply of higher RF power and higher gas supply. What is not shown in the plot but suggested by the points enclosed in the brown area is the stability. For higher RF power the beam current scales almost linearly with the gas supply but for lower RF power it is more unpredictable and difficult to reach stable ion source operation. The stability is usually examined experimentally during the ion source tuning and adequate RF power and gas supply values are chosen.

Generally, beam current increases with higher RF power or gas supply but these two parameters are not independent of each other. Higher gas flow increases the beam current due to more ionisation but higher plasma density requires higher RF power to keep increasing the ionisation rate[99]. For higher gas pressure than shown in Figure 41, the plasma becomes over-dense and the beam current reduces significantly.

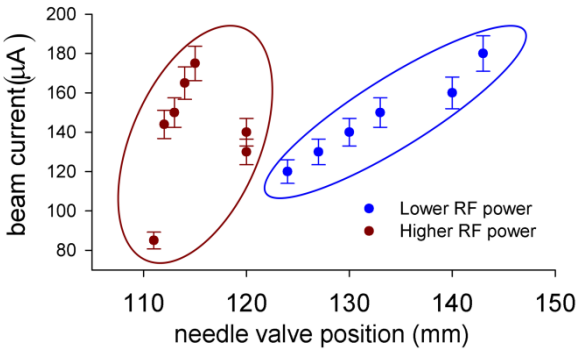

Figure 41: Dependence of beam current on gas supply for two RF power values.

Beam current stability

To examine the beam current stability, an Oxygen beam was used and beam current measurements were taken every 4 s using the faraday cup at the end of the LEBT for a period of about 10 h. Measurement results are shown in Figure 42. The reduction of beam current at around 180 minutes of operation has been repeatedly observed over long measurement periods. It is possible due to small temperature and humidity changes during the day even though the ion source is located in a temperature controlled room. The precise behaviour of the power amplifier with respect to environmental conditions is not very well known. The ion source stability is also examined by observing the beam current stability and also by monitoring the visible light from the plasma chamber with a camera during operation. The random variation in beam current due to plasma fluctuations is about 10% as shown here but it ranges from 5% to 15% according to many previous observations with various beams and operating parameters.

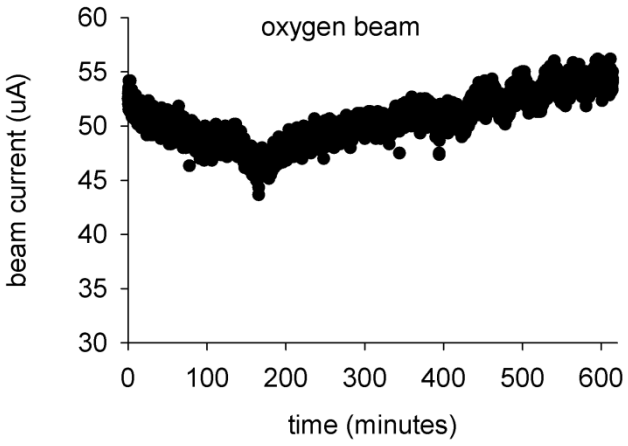

Figure 42: Current measurement with an Oxygen beam.

2.4.2 Scintillating screens evaluation

The available literature for scintillating screens used with low energy proton or heavy ion beams is limited so in the context of developing the emittance meter a measurement campaign to examine commercially available scintillating material was carried out. The main objectives of this study were to investigate the degradation of the materials and the beam size estimation. A summary of the materials used here is given in Table 6. Some of the screens were not used for the beam profile estimation measurements due to the small crystal size (smaller than the beam).

A preliminary study on the performance of scintillating screens was carried out in the summer of 2015 [100]. During that study, the scintillating screens were continuously exposed to a proton beam and thus degraded quickly with the only exception being the SiO_2. In contrast to all other materials, the light yield from SiO_2 was increasing with respect to irradiation time. Following that study, a beam chopper was added and synchronised with the image acquisition so the scintillators were exposed only for a short time leading to improved longevity.

A. *Beam size estimation*

For the beam size estimation, a proton beam of 6.52 keV was used. To investigate how the beam size changes with different beam currents the ion source was tuned and five different stable beam current settings were attained. The parameters and vacuum conditions of each setting are shown in Table 9. The RF power during the measurements was adjusted by an external dial and not by directly choosing the output power due to a small problem on the touch screen interface of the RF amplifier.

Table 9: Ion source parameters for beam size estimation using scintillating screens

#	RF power dial	Gas Needle valve	current (μA)	1st stage vacuum (10^{-4} mbar)	2nd stage vacuum (10^{-5} mbar)
1	12.2	135	∼142	2.30	1.30
2	12.2	125	∼122	1.7	1.2
3	7.16	124	∼120	1.6	102
4	3.85	123	∼61	1.7	1.2
5	2.54	120	∼48	1.7	1.2

The materials used for this test were: SiO_2, AlO_3 crystals, BC400 plastic scintillator and KBR coated on a glass substrate. CsI(Tl) was not used in this test due to the very small sample crystal size that was available. The emittance meter was used as a profile monitor by simply

removing the pepperpot mask and exposing the scintillator directly to the beam. The different screens were exchanged by venting only the small diagnostics chamber while isolating the rest of the beamline and the ion source.

For every setting, according to Table 9, several images were taken and averaged. The comparison on the beam size estimation among the available scintillating screens is shown in Figure 43 and Figure 44 for horizontal and vertical profiles respectively.

According to the measurements presented in these two figures the estimated beam size shows a dependence on the beam current and the different scintillating materials. The dependence on beam current is due to the physical beam size changing for different ion source operating conditions that are required to provide different beam currents. Such dependence has also been confirmed by others [89] For the same ion source settings, though, the difference in beam size estimation must be only due to the properties of the scintillating screen.

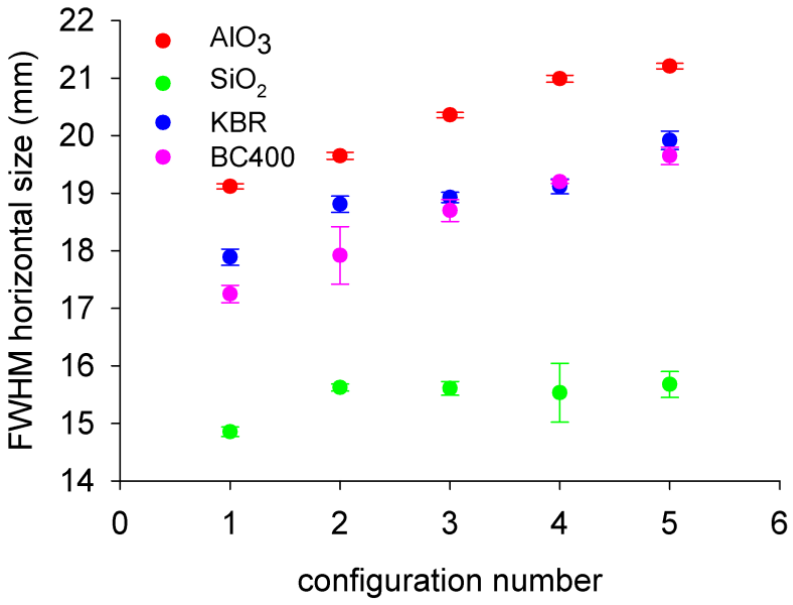

Figure 43: Horizontal beam size estimation for a variety of scintillating screens.

An additional uncertainty was introduced here because the experimental conditions were slightly different for every screen. During screen exchange, the experimental chamber was vented and the settings described in Table 9 were not exactly the same for every screen. Ideally, this experiment would be performed using a ladder where all the screens would be mounted and inserted in the beam line one after the other. If this effect is ignored then the measurements show a similar trend to measurement done at GSI investigating scintillating screens for higher energy heavy ion beams [101]. According to the GSI study, the maximum variation in profile

estimation was about 28%. For the measurements shown here, the maximum variation is 32% for the FWHM horizontal profile and 19% for the vertical. At the time the experiment was carried out, there were no means to precisely measure the real beam size and compare against the estimated size from the scintillators.

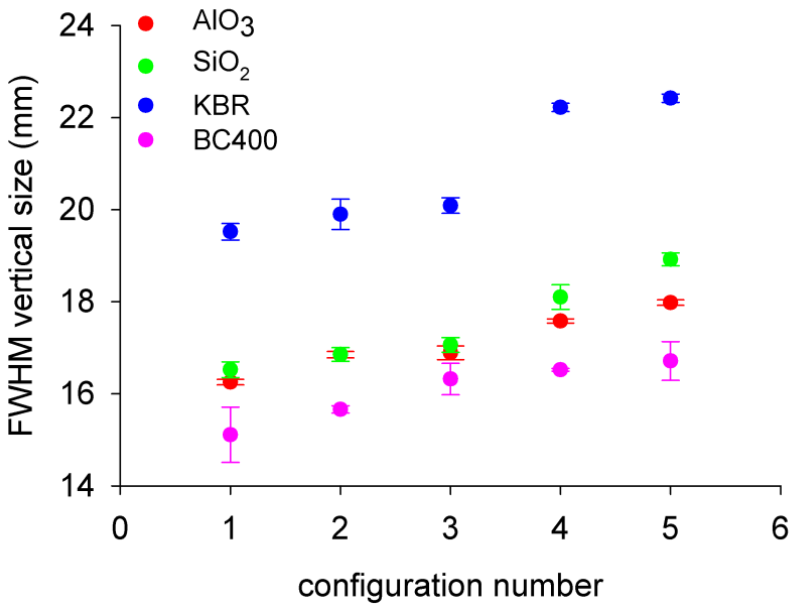

Figure 44: Vertical beam size estimation for a variety of scintillating screens.

The difference between the vertical and horizontal profile sizes is attributed to the better imaging of beam halo for some materials. Figure 45 shows the images of beam profiles acquired with the 4 different crystals and the integrated profiles along X and Y axis (horizontal and vertical profiles).SiO_2 and BC400 are lens sensitive and the imaged beam halo is minimal resulting in smaller estimated beam profiles. On the other hand, the AlO_3 clearly images the beam halo and the KBR shows a more pronounced vertical halo formation. The beam image on the AlO_3 appears more shifted to the top so the vertical halo formation was collimated.

Table 10 summarises the FWHM size measurements for the configuration #3 from Table 9. In Table 10 the differences in profile size are less pronounced. The horizontal profile FWHM size is almost constant for all material but the vertical profile follows the trend of Figure 43.

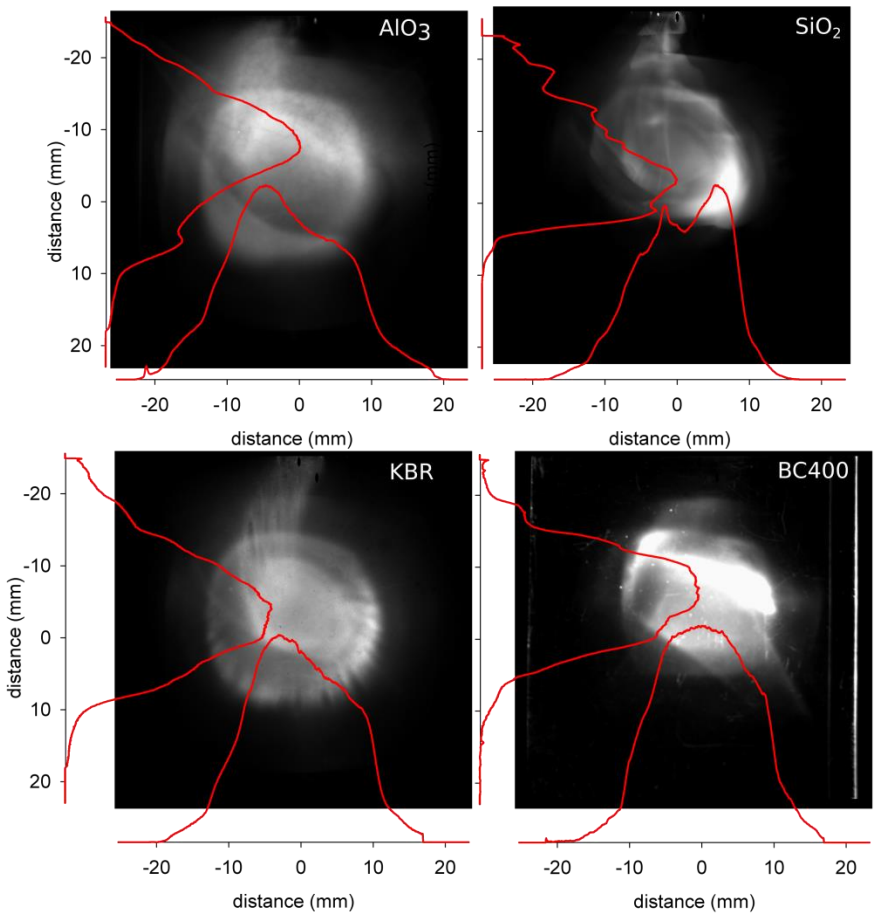

Figure 45: Profiles of a proton beam imaged by four different scintillators.

Table 10: FWHM vertical and horizontal profile size for a proton beam imaged with four scintillators.

Material	FWHM horizontal (mm)	FWHM vertical (mm)	Beam current (μA)
AlO_3	20.34±0.11	16.81±0.13	123
SiO_2	15.31±0.08	17.06±0.04	117
KBR glass	18.9±0.12	20.17±0.17	116
BC400	18.7±0.09	16.33±0.18	116
Max variation %	32%	19%	

B. *Scintillating screens performance – Proton beam*

To examine how the light yield from the scintillators change with time when under irradiation, the following experiment was carried out. The ion source was set up to provide a 6.52 keV proton beam with around 100 μA of current. The emittance monitor with the pepperpot mask fitted was used and four scintillating screens were tested, namely SiO_2, CaF_2, AlO_3 crystals, and KBR coated on a glass substrate. Every screen was exposed to the beam

and images were acquired at 2 s intervals with different exposure and camera gain settings for the different screens. At every image, four regions of interest were defined; each included one beamspot as shown in Figure 46 and remained the same throughout the test with all the screens. A gate valve adjacent to the measurement location allowed exchanging screens by venting only the small diagnostics chamber without disturbing the ion source. The light intensity was normalised with respect to camera gain and exposure time for comparison of light yield among screens. The parameters of interest for this experiment were the light yield and beamspot evolution with respect to irradiation time.

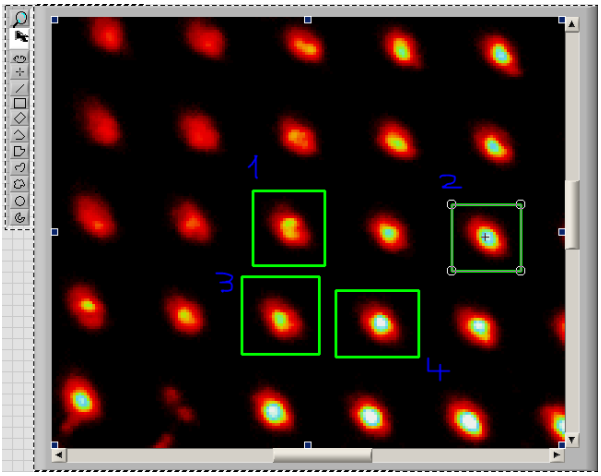

Figure 46: Selection of four beamspots for the measurement of light yield from various scintillating screens. The light intensity and beamspot size were monitored for the four Regions Of Interest (ROI).

B1. Light yield evolution

Measurement results are summarised in Figure 47. The evolution of light yield for CaF_2, AlO_3 crystals, and KBR coated glass is described by a double exponential decay curve fitted to the experimental data as in equation (9) which agrees with experimental data from other measurements [90].

$$y = ae^{-bx} + ce^{-dx} \qquad (9)$$

The SiO_2 exhibits a different behaviour and the light yield rises up to a maximum. This is described by a double exponential fitting according to in equation (10) and as shown by the dotted black curve in Figure 47. Such behaviour has not been found previously in the literature by the author.

$$y = a(1-e^{-bx}) + c(1-e^{-dx}) \qquad (10)$$

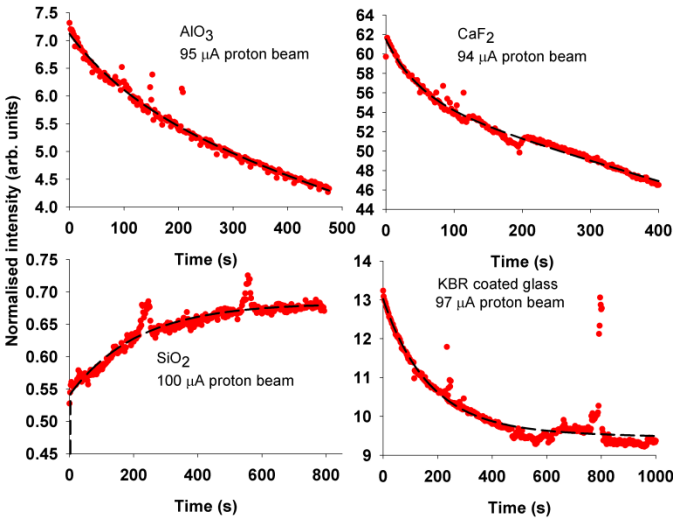

Figure 47: Evolution of scintillation light yield with respect to irradiation time for four scintillating screens. The mean value of pixels intensity is averaged from the four ROI's and normalised with camera gain and exposure time. The black dotted line represents the exponential decay or rise fitted to the data.

The parameters b and d from equations (9) and (10) with the time constants for all the screens are summarised in Table 11.

All the screens perform relatively well in terms of light yield with the proton beam. The SiO_2 crystal and KBR coated glass reach a stable light yield plateau but the CaF_2 and AlO_3 crystals continue dropping to almost undetectable levels (not shown here). Moreover, the SiO_2 exhibits a small variation in light yield and allows keeping a stable exposure time and camera gain for the entire range of proton beam current. The SiO_2 was also found to recover in a matter of a few hours after irradiation and the initial light yield was restored.

Table 11: Time constants for light yield evolution from scintillating screens

Material	b	d	τ1 (s)	τ2 (s)
AlO3	8.6-03	7.6E-04	115	1310
SiO2	2.92	4.7E-03	0.3	212
CaF2	2.1E-02	4.4E-04	48	2288
KBR glass	5.9E-03	1.2E-05	168	80645

The light yield from the screens depends also on the beam current in an almost linear fashion. The best linearity was shown by the SiO_2 crystal among the other screens. Figure 48 shows the light yield evolution of the SiO_2 crystal for irradiation under proton beam for two different beam currents. As expected the light production is higher for higher beam current while maintaining the characteristic SiO_2 behaviour.

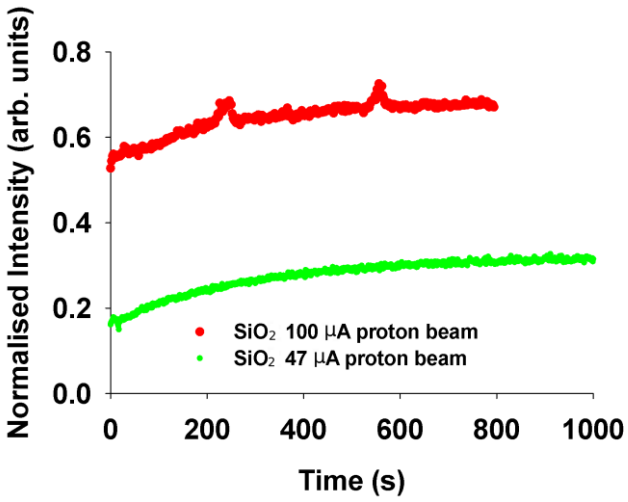

Figure 48: Light yield with respect to irradiation time for SiO_2 crystal and two beam current values. Higher beam current produces higher light intensity.

B2. Beamspot size

Regarding the size of the beamspots in all 4 ROI's, it is more stable that the light yield and does not show similar fast decay. The limiting factor here is the small plasma fluctuations of the ion source which cause the varying size of beamspots from picture to picture. Figure 49 shows the beamspot size in pixels (area in pixels) as measured with respect to irradiation time for SiO_2 crystal and KBR coated glass.

For the SiO_2 the beamspot size evolution follows the trend of the light yield evolution for larger beamspot areas. For smaller areas, it shows a more stable trend. In both cases shown in Figure 49, there are some dips and peaks mainly caused by plasma fluctuations. Table 12 shows the beamspot average size and standard deviation for all of the tested screens.

When compared to the full beam profile estimation the beamspot sizes shown above approaches the trend of the horizontal beam profile size dependence on the screen material. The CaF_2 screen that was not used for full beam profile estimation previously, overestimates the beamspot size in the ROI1 but not in the other three ROI's. This is probably due to some measurement issue only for ROI1.

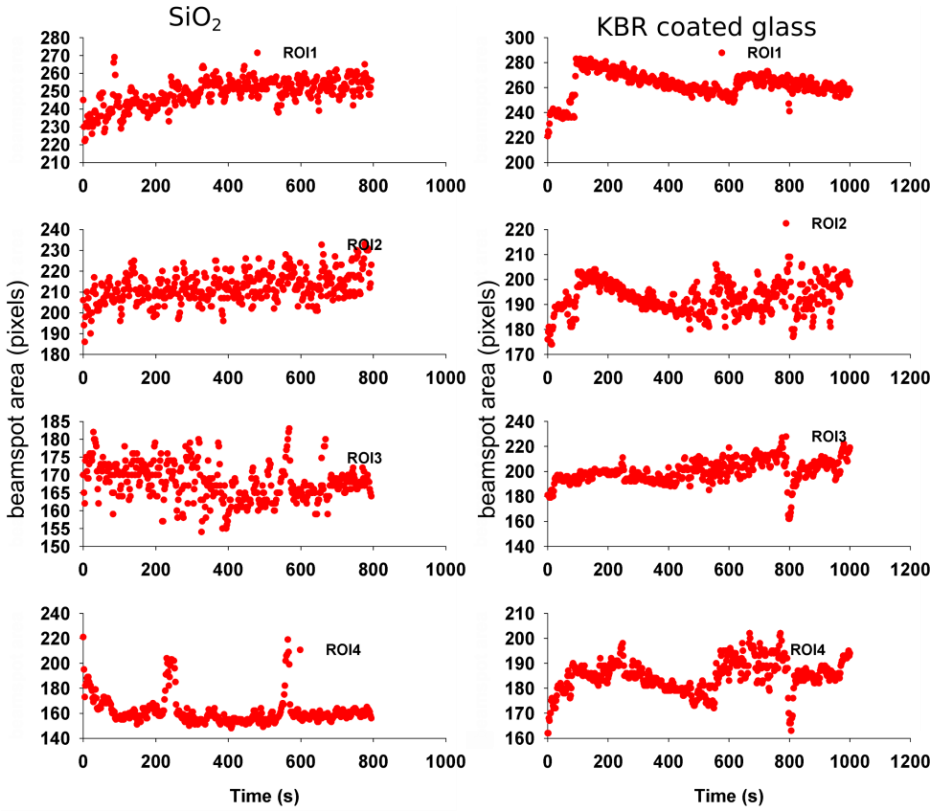

Figure 49: Beamspot area (number of pixels occupied by the beamspot) for SiO_2 crystal and KBR coated glass for the four ROI's. The beamspot area is calculated as the number of pixels belonging to a single beamspot. All data is thresholded at 5% of the maximum value to remove any noise contribution.

Table 12: Beamspot size for the four ROI's of all the screens.

materials	statistics	ROI1	ROI2	ROI3	ROI4
AlO_3	Average area	319.8	335.0	251.3	263.8
	σ	17.93	39.29	11.14	16.03
	σ % of average	5.6	11.7	4.4	6.1
SiO_2	Average area	248.8	212.1	167.9	161.8
	σ	7.83	7.32	5.18	11.53
	σ % of average	3.1	3.4	3.1	7.1
CaF_2	Average area	450.6	216.6	214.3	192.6
	σ	23.74	12.82	11.71	20.57
	σ % of average	5.3	5.9	5.5	10.7
KBR glass	Average area	262.2	192.8	200.0	184.9
	σ	10.3	6.4	9.0	6.4
	σ % of average	3.9	3.3	4.5	3.5

B3. Effect on emittance measurements

The fluctuations in the beamspot size and light intensity make emittance calculations very challenging. Figure 50 shows the light yield from SiO_2 crystal and the proton beam current for a period of about 2000 s. The emittance is affected by the screens varying light yield which is

in part attributed to the screen's change in light yield (long term variation) and also to the ion source instability (shot to shot variation).

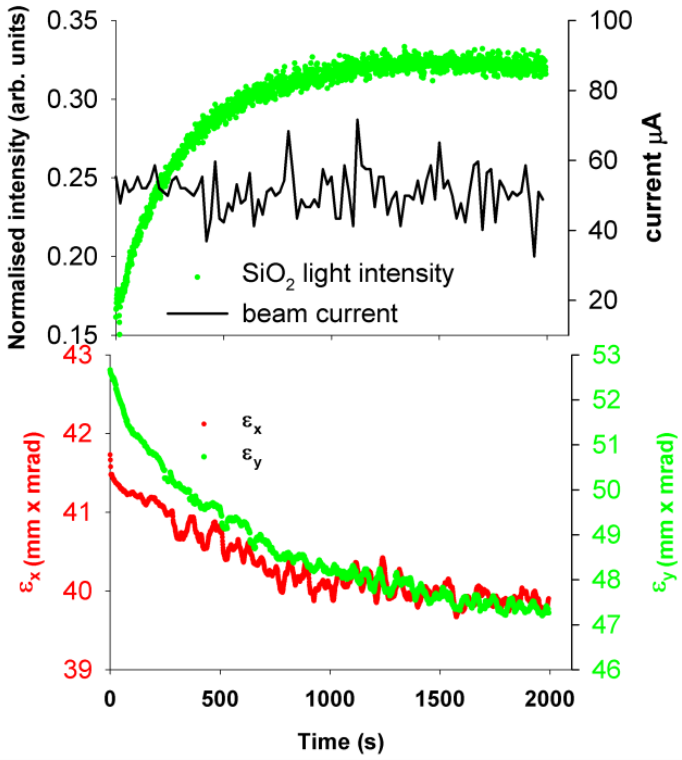

Figure 50: Top: light yield and beam current from SiO_2 crystal for irradiation with a nominal 51 uA proton beam. Bottom: emittance ε_x and ε_y for the same operating conditions.

For the measurement shown in Figure 50, beam emittance follows a decaying trend opposite of the growth trend of the light yield. The change in emittance is about 10% and 5 % for ε_x and ε_y respectively expressed as the percentage of the peak value with respect to the plateau. When in the plateau region, the standard deviation is about 2% for both ε_x and ε_y.

The change in emittanceobserved in data of Figure 49 is not well understood but in this specific case it was caused only by the behavior of the crystal and the beam was very stable. The beam current average of 51 uA throughout the measurement has a standard deviation of 7 uA which corresponds to about 14% of the average value. In the plateau region, the beam current fluctuation is the main error contribution in emittance measurement, outside of the plateau it is mostly the screen's behaviour (light yield decreasing or increasing and beamspot size variation).

B4. Irradiation with the full beam

The behaviour of the scintillators when irradiated by the full beam without the presence of the pepperpot plate are different when compared with the use of pepperpot. Figure 51 shows

the light yield evolution of a SiO_2 crystal irradiated with the full beam. In this case, the characteristic behaviour of the crystal as previously observed is different showing a slower decay and the light yield is much higher.

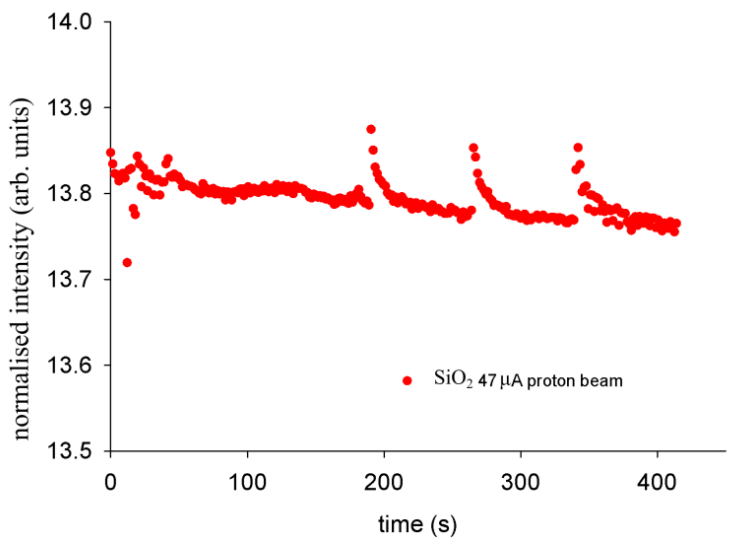

Figure 51: Light yield evolution of SiO_2 crystal with the full beam. The three peaks occurred when the beam chopper was activated for several minutes allowing the crystal to recover.

The case of KBR is also very interesting. As shown in Figure 52 the KBR coating on glass or metal exhibits about five times higher light yield when compared to the KBR crystal. Such a comparison has not been found in the literature previously.

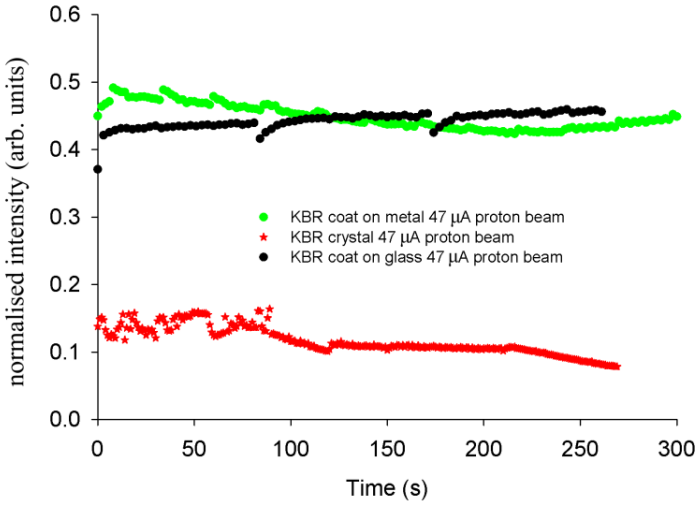

Figure 52: Light yield from KBR crystal and KBR coating on a glass substrate after irradiation with the full beam.

For all the above cases a beam chopper was employed so the crystals were exposed to the beam for a brief amount of time equal to the acquisition time with a period of 2 s. Figure 53 shows a comparison of the light yield from KBR coated glass for beam currents of 47 and 117 μA with the beam chopper activated and deactivated. For the lower beam currents and the chopper deactivated the light yield reduces quickly. When the chopper activates the light yield starts to rise and it grows significantly for higher beam currents. Note here that comparisons between Figure 52 and Figure 53 cannot be done. These two figures are from different measurements with different exposure times and different ROIs.

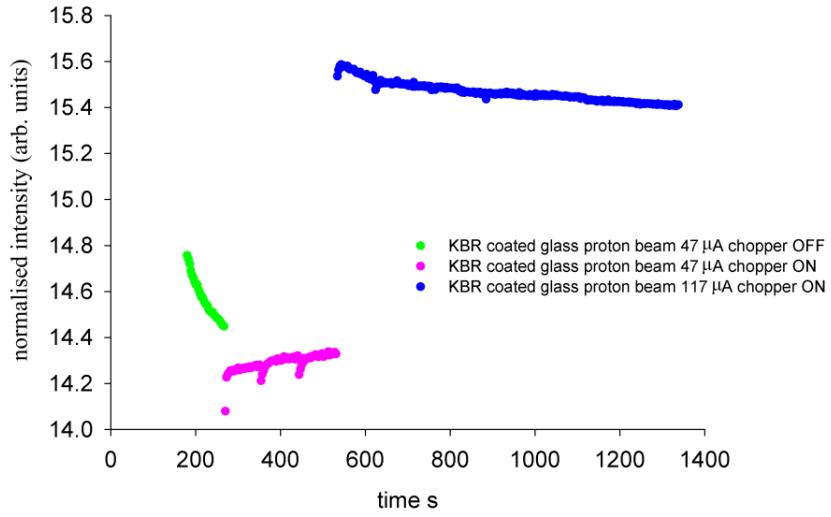

Figure 53: Light yield evolution of KBR coated glass with the full beam of 47 and 117 μA with the beam chopper ON and OFF.

C. *Scintillating screens performance – heavier ion beams*

For the case of heavier ion beams such as $^{16}O^{4+}$, $^{40}Ar^{9+}$, $^{40}Ar^{11+}$ and $^{86}Kr^{26+}$ with a 10 kV extraction voltage the performance of the scintillating screens is completely different. The crystals tested with the proton beam (CaF_2, AlO_3, SiO_2) show very quick degradation with the light yield being very low and decaying dramatically in the first few seconds of irradiation. The only exceptions are the KBR coated glass. Another material that performs relatively well with heavier ions is the CSI coated glass.

Figure 54 shows the evolution of scintillation light yield under irradiation with argon, oxygen and krypton beams for the CSI and KBR coated glass. The KBR coated glass screen performs the best under these circumstances in contrast with KBR crystal that degrades in a matter of a few seconds. A similar trend has been observed for the CSI screen which in the

crystal form degrades quickly but in the form of a spray-coat on glass demonstrates improved resistance to radiation degradation.

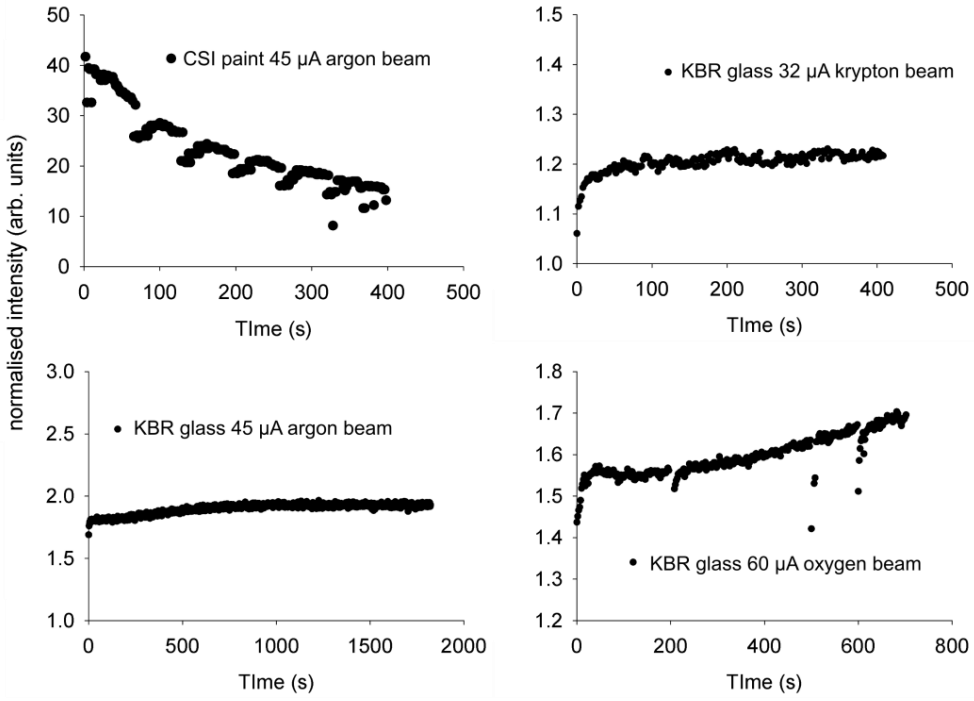

Figure 54: Light yield evolution for KBR coated glass and CSI coated glass under irradiation with ion beams.

C1. Energy loss mechanisms for heavy ions in the scintillators

Although the penetration depth for the heavier ions beams measured above is comparable to the proton beam from the previous experiment the quenching mechanism is different for the heavy ions. To investigate this phenomenon the SRIM (Stopping and Range of Ions in Matter) [102] simulation code was employed. The various scintillators were created in the material editor and the impinging particle type and energy was created. The selected beam types were 6.52 keV protons and 10 keV/u argon ions. For all the simulations 1000 particles were tracked.

Figure 55 shows the results from the simulation for penetration depth (a) and energy loss mechanism (b). The penetration depth for every material is comparable between protons and argon ions. The energy loss mechanism, on the other hand, is quite different. The protons lose more than 90% of their energy via ionisation but the heavy ions transfer more than 50% of their kinetic energy to crystal lattice oscillations. Similar results were obtained for oxygen ions. The mechanism behind the energy loss of the heavier ions cause lattice displacements and thus produces less light and degrades the material faster.

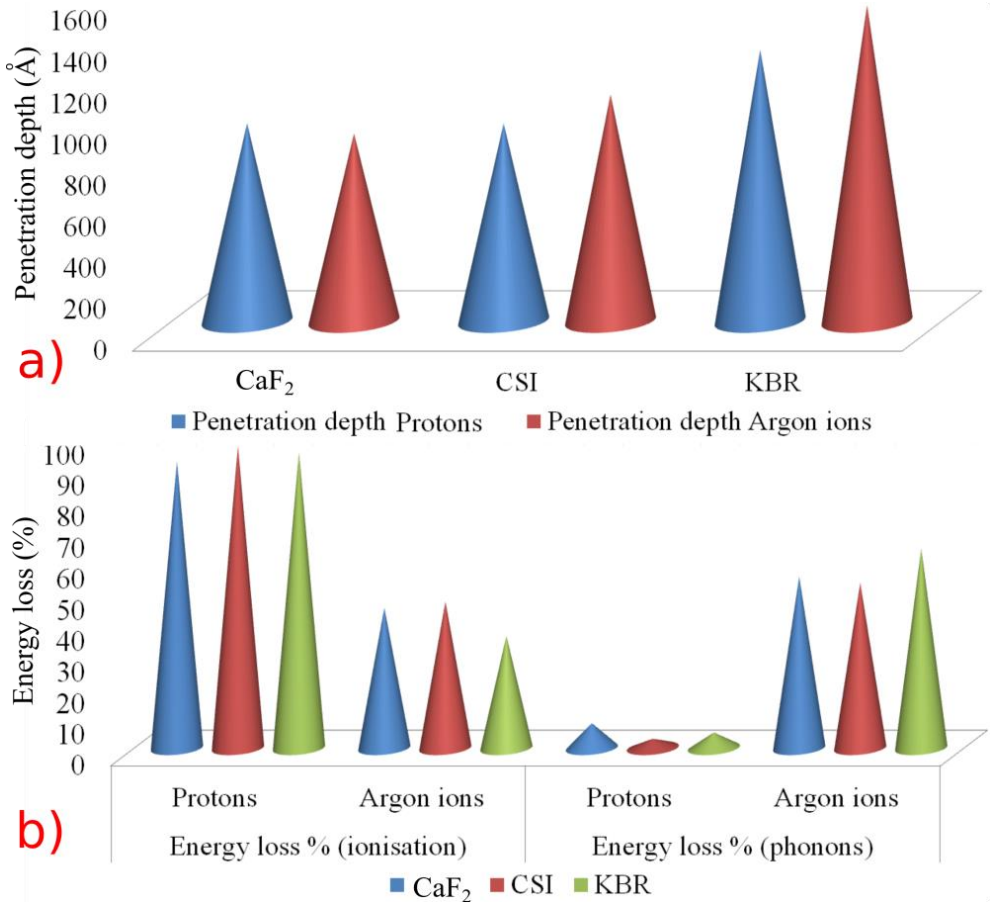

Figure 55: Results from SRIM simulation, a) penetration depth for protons and argon ions impinging on CaF_2, CSI and KBR crystals, b) energy loss for two quenching processes for the same beam species and crystals.

C2. Effect on emittance measurements

In order to examine how the emittance of the heavier ion beams is affected by the performance of the scintillating screen, a $^{40}Ar^{11+}$ beam of around 45 μA and a KBR coated glass were used. The pure crystals cannot provide any meaningful measurements with the heavier ions because of the very fast degradation. Figure 56 shows the evolution of the beamspot intensity and the beamspot area for an irradiation time of about 1000 s. Table 13 shows relevant statistics for the same beam and screen combination. When compared to the proton beam case mentioned earlier, the beam stability here is much better. The beamspot size and intensity remain almost constant throughout the irradiation period of around 1000 s.

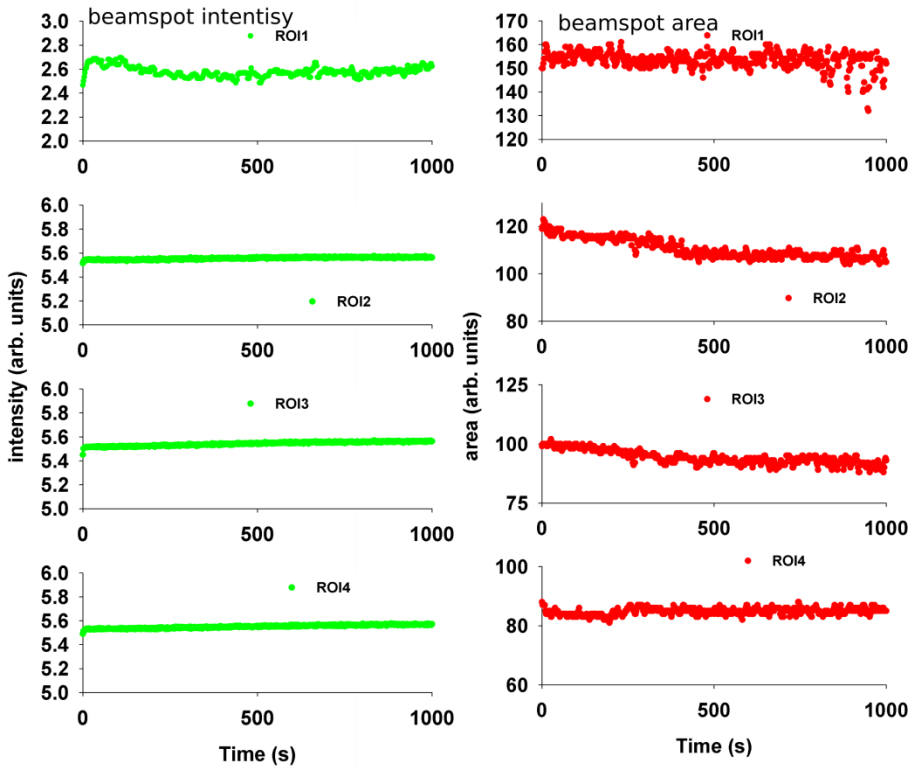

Figure 56: Evolution of light intensity and beamspot area for KBR coated glass under irradiation with a $^{40}Ar^{11+}$ beam.

Table 13: Statistics for the beamspot size and intensity for KBR coated glass under irradiation with a $^{40}Ar^{11+}$ beam.

Light intensity inside beamspots					
	ROI1	ROI2	ROI3	ROI4	Average ROI
average	2.62	5.56	5.55	5.56	4.82
σ	0.06	0.01	0.02	0.02	0.027
σ %	2.35	0.15	0.30	0.30	0.77
Beamspot size (area in pixels)					
average	146.85	108.40	92.65	84.39	
σ	9.75	4.11	2.99	1.28	
σ %	6.64	3.79	3.22	1.52	

Figure 57 shows emittance measurements with a $^{40}Ar^{11+}$ beam as previously described. The variation in both emittances is about 2% including some peaks caused mainly by the ions source instabilities. Table 14 summarises emittance values of this measurement.

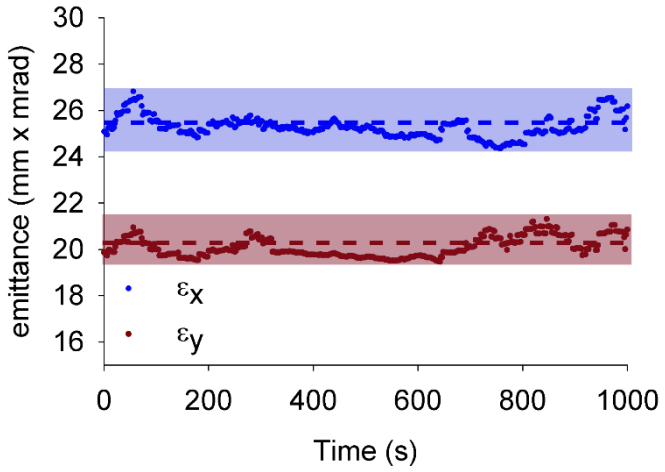

Figure 57: Emittance ε_x and ε_y for $^{40}Ar^{11+}$ beam using a KBR coated glass. The colour bands include all the measured values and range around ± 5 % from the average.

Table 14: Statistics for emittance ε_x and ε_y for $^{40}Ar^{11+}$ beam using a KBR coated glass.

	ε_x (mm x mrad)	ε_y (mm x mrad)
average	25.3	20.1
σ	0.5	0.4
σ%	1.9	2.2

2.4.3 MCP evaluation

Because of the limitations (light yield dependence on irradiation time and beam intensity) and measurement uncertainty of the scintillating screens an MCP was tested as an alternative detector. The MCP does not suffer from the beam induced degradation of the scintillating screens previously used. The scintillating screen at the back side of the MCP does not come in direct contact with the heavy ions but only with the electrons produced inside the MCP. Sample measurements with a $^{40}Ar^{9+}$ beam of around 32 μA are shown in Figure 58.

The light yield and the beamspot size are constant apart from ROI1 which shows a small reduction in both size and intensity. Overall and as it has been observed from several previous measurements there is a minimal reduction in light yield even with the MCP but it appears only in long measurement times which probably will never be needed in any emittance measurements. Table 15 shows relevant statistics about beamspot size and beamspot light intensity from the measurements of Figure 58.

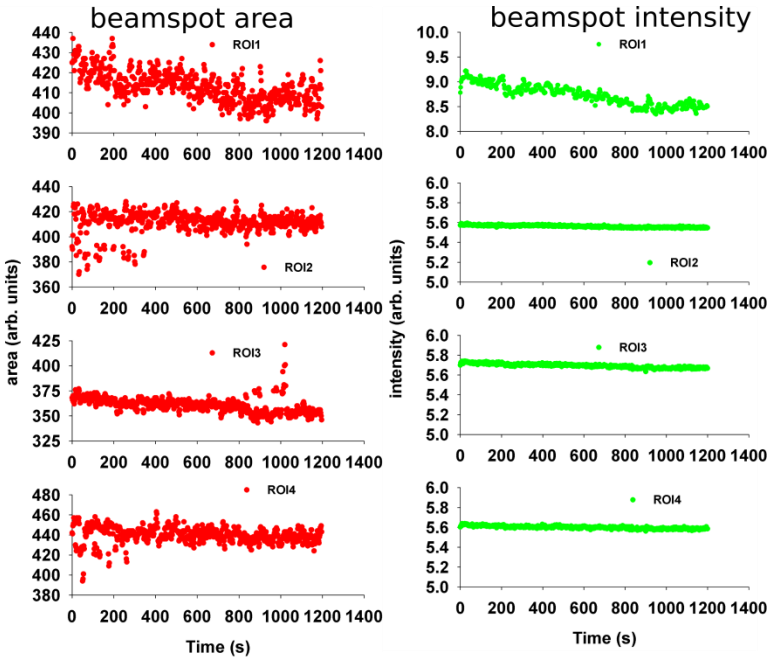

Figure 58: Beamspot size and evolution of light yield for four ROI's using MCP and $^{40}Ar^{9+}$ beam.

Table 15: Statistics for the beamspot size and intensity using an MCP and a $^{40}Ar^{9+}$ beam.

Light intensity inside beamspots					
	ROI1	ROI2	ROI3	ROI4	Average ROI
average	8.7	5.6	5.7	5.6	6.4
σ	0.21	0.01	0.02	0.01	0.06
σ %	2.4	0.2	0.3	0.3	1.0
Beamspot size (area in pixels)					
average	413.1	411.3	360.7	439.7	
σ	7.5	8.6	7.7	8.1	
σ %	1.8	2.1	2.1	1.8	

Figure 59 shows beam emittance evolution with respect to irradiation time. The emittances ε_x and ε_y are very stable which is attributed to the performance of the MCP but also to the beam stability during the measurement. The measurement uncertainty when using MCP as shown in Table 16 is the smallest observed during the investigation presented here.

When compared to the KBR coated glass the MCP performance is obviously superior but does not justify the extra cost. If the fabrication method of the KBR coated glass screens is improved and produces consistent screens then they can be the screen of choice for similar applications.

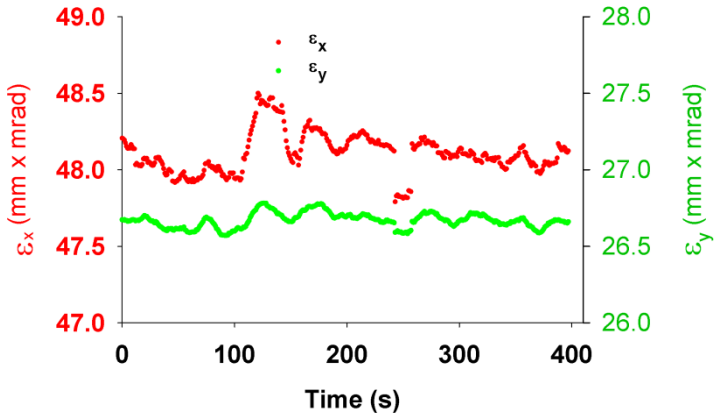

Figure 59: Emittance ε_x and ε_y for 32 uA $^{40}Ar^{9+}$ beam using an MCP detector.

Table 16: Statistics for the beamspot size and intensity for KBR coated glass under irradiation with a $^{40}Ar^{9+}$ beam.

	ε_x (mm x mrad)	ε_y (mm x mrad)
average	48.1	26. 7
σ	0.13	0.05
σ%	0.3	0.2

2.4.4 Emittance dependence on ion source parameters

The measurements shown here demonstrate the effect various operating parameters of the ion source have on the emittance of a proton beam. More specifically, the examined parameters are: beam current (adjusted by RF power and/or gas injection), acceleration gap, extraction voltage and ECR magnetic field. Throughout all the measurement mentioned here, the coupling parameter had a very low value corresponding to no interplane coupling so it is omitted from the graphs. For all the following measurements a 6.53 keV proton beam was used and the scintillating screen was SiO_2.

A. Emittance dependence on beam current

During the time of the following measurements, the faraday cup was not available so the beam current was measured directly on the pepperpot. This was achieved by isolating the pepperpot plate and connecting it directly to a precision resistor and measuring the voltage drop with a 10-bit ADC. The measured current, in this case, is not the absolute value and it is dominated by the secondary electron production on the pepperpot mask due to the lack of compensation. The absolute current for a proton beam ranges from about 35 uA to 200 uA. The current measured with the pepperpot can reach up to 800 uA when the RF amplifier is at its maximum power.

Figure 60 shows the emittance dependence on current for a proton beam extracted at 6.52 kV. ε_x rises almost linearly with respect to beam current while ε_y is almost stable Both emittances show irregular behaviour in the range of 130-290 μA. ε_x increases abruptly from around 30 mm x mrad to 40 mm x mrad and keeps rising after that. ε_y jumps to 40 mm x mrad and then returns to 30 mm x mrad where it remains for the entire range of the measurement.

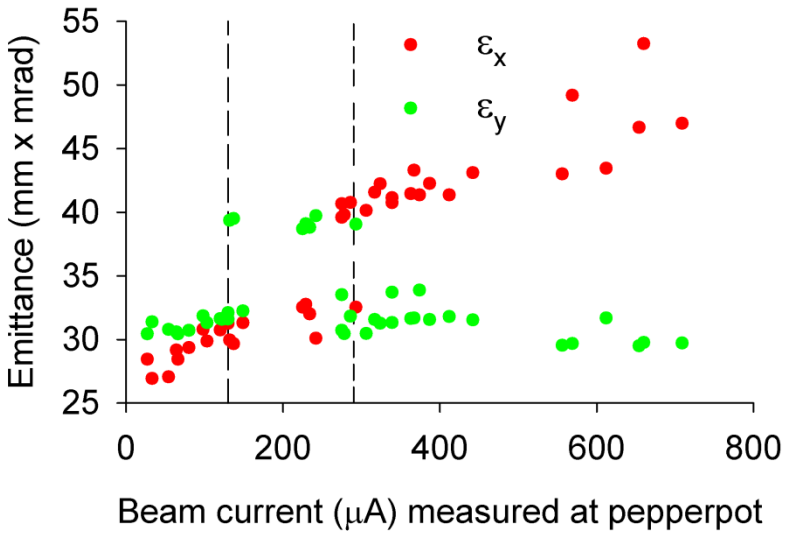

Figure 60: Emittance dependence on beam current. These are single shot measurements (no averaging) and the error is only the intrinsic error of the measuring which is too small to show with error bars.

As mentioned by Leitner[46] after measurements performed with the VENUS ECR ion source at LBNL, the emittance of a single charge state tends to remain almost constant with a variation of ±10% as long as the total extracted beam current (the sum of current over all species) remains constant For the measurement presented here, there was no method available to measure the total beam current for all species and validate that claim.

In an attempt to explain the irregularity in the emittance, the beamspots in the acquired images were examined more carefully by measuring the horizontal and vertical size of every individual beamspot and observe how the average values change for different beam currents. Figure 61 shows the average lengths over all the beamspots of the horizontal and vertical size. The horizontal size grows from about 8 pixels to 10.5 in the range of 130-290 μA of beam current and keeps. The vertical size grows by 0.5 pixels in the previously mentioned range and the returns to a stable size of around 9 pixels where it remains for the rest of the measurement. Over the entire measurement range, the horizontal beamspot size almost doubles in size while the vertical size grows up to 18%. These trends follow closely the trends of the horizontal and

vertical emittance and thus the observed emittance behaviour is not due to a possible error in the calculation but is caused by the beam itself.

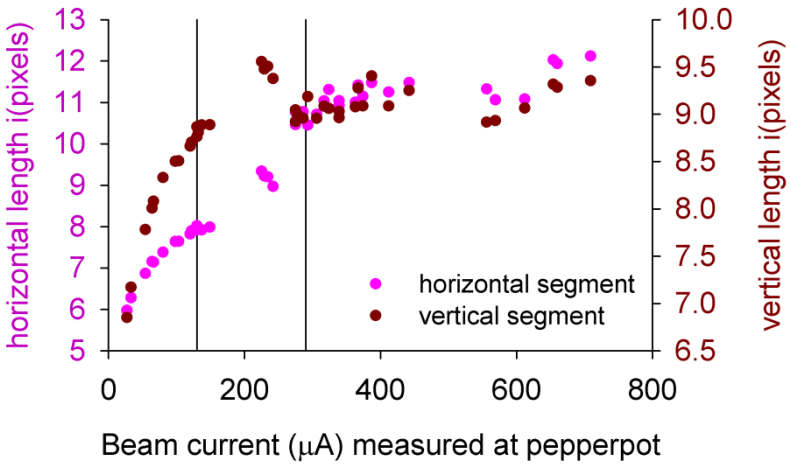

Figure 61: Dependence of the horizontal and vertical beamspot size on the beam current.

Figure 62 shows the dependence of the total area occupied by beamspots and the total intensity of all the beamspots in the image with respect to beam current. Both of these parameters vary linearly with the beam current which verifies the linearity of the scintillator.

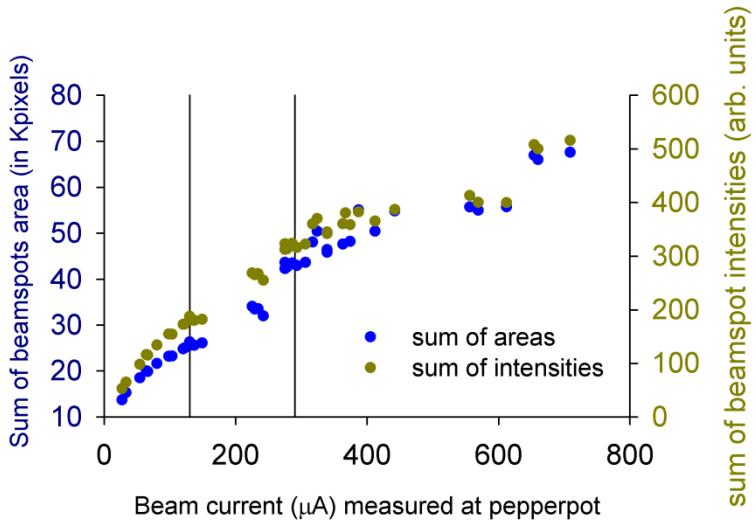

Figure 62: Dependence of the sum of beamspot intensity (total intensity) and the sum of beamspot area (total area occupied by the beamspots) on the beam current.

B. Emittance dependence on extraction voltage and acceleration gap

Positive ions are extracted from ECR ion sources by applying a high voltage to the device with respect to a grounded extraction (puller) electrode. The large electric field near the extraction confines the electrons and at the same time accelerates the positive ions to higher energies compared to their thermal energy [103]. The application of the high voltage causes the formation of a narrow plasma sheath or plasma meniscus in the extraction aperture as mentioned earlier in this chapter. A typical diameter of the plasma meniscus is about 1 cm but its thickness is only a few microns. The plasma sheath plays a critical role in beam extraction and thus beam transfer at the initial stages cannot be treated by using ion optics only [103]. It must be noted also that ion extraction and beam formation takes place under the influence of the intense magnetic field from the ECR solenoids leading to different focusing and transfer properties for different ion masses and charge states [104]. In the extraction region the magnetic fields from more than 1 T to zero which leads to considerable emittance increase. The magnetic field is the main contribution to ion beam emittance for most ECR ion sources, according to simulated ion extraction done by Leitner [104] the 'magnetic emittance' accounts for about 90% of the total uranium beam emittance.

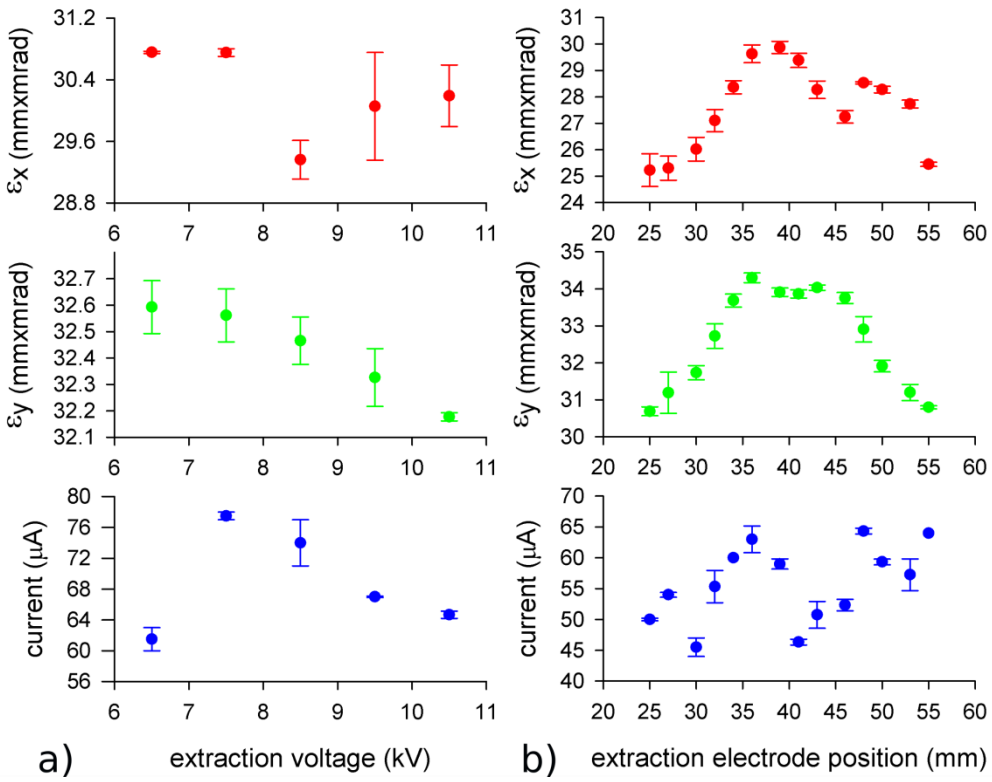

Figure 63: Emittance and beam current dependence on extraction electrode position and extraction voltage. These are averaged measurements. The error bars are one standard deviation.

The extraction voltage of the ion source affects mainly the beam current and less the beam emittance. The extraction electrode is grounded and the ion source chamber is biased at a high voltage adjustable from 6.5 to 10.5 kV. As shown in Figure 63 (a), the maximum beam current is obtained for about 7.5 kV of extraction voltage. The horizontal and vertical emittances vary by approximately 5% and 1% respectively for the entire extraction voltage range. The error bars shown in Figure 63 (a) are from averaging several measurements at every step.

The extraction electrode position has a range of motion of 30 mm starting at 25 mm from the extraction aperture and reaching up to 55 mm. For this measurement, the distance was scanned in steps of 2.5 mm while monitoring beam current and emittance. Figure 63 (b) shows the measurement results. As shown in Figure 63 (b) the beam current fluctuates but it generally has a rising trend with respect to increasing extraction electrode position. Beam emittances peak for an acceleration gap of 35 to 45 mm and attain lower values towards both ends of the ends of the extraction electrode range. Similar behaviour has been reported by Higurashi [105] from measurements taken at RIKEN's normal conducting 18 GHz ECR ion source with argon, krypton and xenon beams.

Further analysis of the results presented above would require a sophisticated ion source model and is beyond the scope of this thesis.

C. Emittance dependence on ECR magnetic field

The ECR magnetic field is created by superimposing a solenoidal field and sextupole field. The solenoidal field produced by four superconducting solenoids can be altered by changing their current. To examine how the magnetic field at the extraction side B_{ext} is affecting the emittance five settings for the solenoid currents were selected so the B_{ext} is changed while B_{inj} and B_{med} remain almost the same. The variation range of the B_{ext} is ±10% of the value that is normally used. Figure 64 shows the axial magnetic field for the five different settings named conf #1 to #5 according to Table 17.

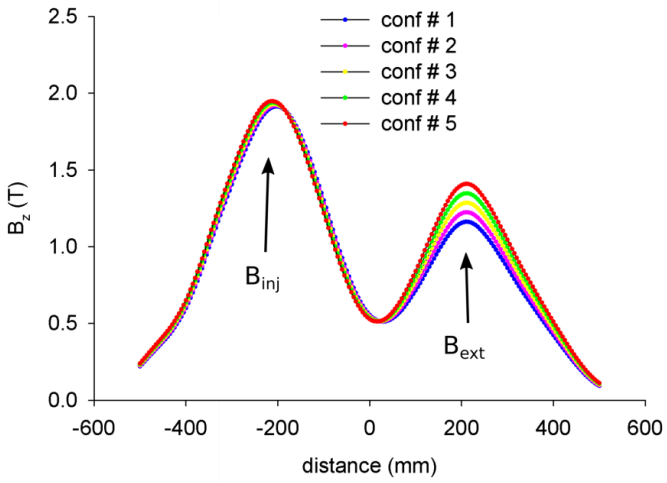

Figure 64: ECR magnetic field for five different configurations that change only the value of B_{ext}.

Table 17: Magnetic field peak values at extraction for the five different settings of the solenoid current.

Configuration #	B_{ext} (T)
1	1.16
2	1.22
3	1.29
4	1.35
5	1.41

Figure 65 shows the emittance and beam current evolution for the above-mentioned configurations. The currents of the four solenoids were adjusted according to every setting and several measurements were taken automatically using the LabVIEW gateway to EPICS. The horizontal axis indicates the number of measurements.

The beam current starts from about 60 μA for the lowest value of B_{ext} and rises to 120 μA for the highest value of B_{ext}. Beam emittances, on the other hand, follow more closely the stepwise increment of the B_{ext}. The vertical emittance shows a very small variation or around 2%similar to the previous measurements with the other operating parameters. The horizontal emittance changes up to ±10%and peaks for B_{ext}=1.29 T. The effect of B_{ext} on beam emittances is rather small as discussed previously. The magnetic field values explored in this measurement were rather conservative. With a careful calculation the B_{ext} range can be extended and allow for investigations on emittance is affected for more extreme values. B_{ext} plays a role in both plasma confinement and beam extraction. For the ion confinement and ECR heating, higher magnetic field values are required, ideally equal to the B_{inj}. For beam extraction, the magnetic field must be low to allow for ions to escape and ideally zero to reduce the ‘magnetic emittance’.

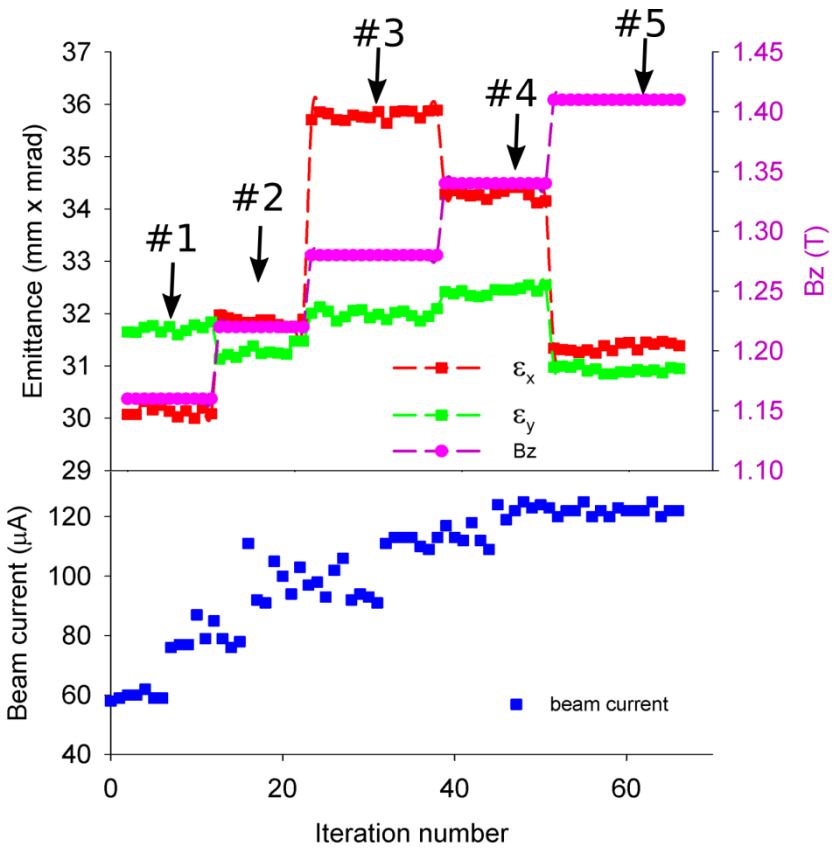

Figure 65: Emittance dependence on the ECR magnetic field. These are single shot measurements and thus the error bars are included in the points.

2.5 Chapter summary

This chapter presented work covering beam emittance diagnostics for an ECR ion source at RIKEN, Japan. The work was split into three main sections focusing on the ECR ion source and LEBT study, the development of the pepperpot based emittance monitor and experimental results obtained with protons and heavier ions.

The first part of the chapter presented the operating principles of ECR ion sources and the most important characteristic from the beam diagnostics point of view. The ion source of interest for this thesis, RIKEN's 18 GHz SC-ECR and its main components were described.

The measurement of the ion source magnetic field offered a way for a direct comparison against the design values. The results revealed that the currently used magnetic field from the solenoid magnets is smaller than the design values by 0.5 T for both the injection and extraction side but it can be adjusted by controlling the solenoid current. Adjusting the field

though has to be done also considering the compliance of the ion source to the ECR standard model.

Particle-tracking simulations revealed that there are substantial beam losses after the extraction region which may be a result of the intense magnetic field in the region that prevents the Einzel lens from properly focusing the beam. The extraction geometry and Einzel lens position have been modified leading to a) increased beam current and b) correct operation of the electrostatic lens. The ion tracking study and the effect of the improved positioning of the electrostatic lens are not yet conclusive and are the subject of future studies and further investigations.

In the second main section or the chapter, the design of the emittance monitor for RIKEN's ECR ion source was presented and analysed. They key features are the variable screen-pepperpot distance and the real-time algorithm that identifies the beamspots. The camera cooling implementation dramatically reduced the image noise and contributed in minimising the measurement error. The overall error in emittance measurement is extremely small due to the very good angular and spatial resolution and also due to the relatively large value of the measured beam emittance. If the device is used as a beam profile monitor by simply removing the pepperpot screen, the spatial resolution is 54 μm when the beam is imaged with scintillators and about 100 μm when imaged on an MCP. The angular resolution of the pepperpot device is 1.04±0.30 mrad.

The intrinsic error of the device for a single shot emittance measurement is less than 1%. In the case of averaging several measurements, the main factor contributing to the error are the fluctuations of the ion source which are more intense for proton beams and less evident for heavier ions.

The third main section presented experimental results using the pepperpot device. At the beginning, a parameter scan of the ion source was performed highlighting the dependence of beam current and beam size on various operating parameters. After the modification of the extraction geometry, the Einzel lens became fully operational and able to focus the beam and increase the current which is demonstrated by a linear increment in beam current with respect to the lens potential. The next part of the section discussed the performance of various scintillating screens under irradiation with protons and heavier ions. For the case of protons, several screens performed well but overall all of them exhibited a change in light yield with respect to irradiation time and beam intensity. The SiO_2 crystal showed increasing light yield with respect to irradiation time in contrast to all the other materials that were degraded and the

light yield was reduced. The beam size estimation using a proton beam varied up to 32% among the used screen. Similar results have been presented also by GSI. In the current study, there were no means to measure the beam profile independently so it is not known which of the screens estimates the beam profile the best.

For heavier ions, the only usable screens were KBR and CSI coatings on a glass substrate. These screens performed very well with heavy ion beams up to krypton showing very good stability and acceptable light yield. Their disadvantage is that at the time they were fabricated in house and the coating thickness could not be consistent. In comparison with all the screens, the MCP had the best performance with very stable light yield and minimum effect on the emittance measurements. Nevertheless, the KBR coated screens followed closely and given their very low cost they are a very strong candidate for such applications or even beam profile monitors. When several of these monitors are needed and the cost becomes an important factor than the KBR coating on glass (for viewing from the rear side) or on metal (for observation under 45°) could be the materials of choice.

The last part of the chapter presented emittance measurements using the pepperpot device and correlations among various operating parameters. In all the measurement the vertical emittance had very small variation while the horizontal emittance varied from around 30 to 50 mm x mrad. From all the operating parameters examined here, the beam current had the biggest effects on beam emittance while extraction voltage and acceleration gas caused very little change. The magnetic field at the extraction (B_{ext}) affected mostly the beam current which grew from 60 to 120 μA for increasing B_{ext} while the horizontal emittance varied by ±10%. The vertical emittance changed only by ±2% as for most of the other measurements.

For a better interpretation of the results presented here a sophisticated model of the ECR ion source is needed which will take into account all the geometry details and delve into the dynamic and interactions of plasma.

3. Gas jet based beam profile monitor

This chapter presents work done on non-invasive beam profile monitoring and more specifically on a supersonic gas jet based transverse beam profile monitor. The first two sections discuss the motivation of developing this device and the relevant background on least invasive beam monitoring techniques.

The chapter then advances in describing the operating principle and the first results obtained with the monitor at the Cockcroft Institute using a 5 keV electron beam. The hardware design and details of the ion detection system are presented and discussed in detail stressing out the importance of the differentially pumped section in order to achieve and maintain very low pressure in the gas jet-charged particle beam interaction chamber.

The chapter then proceeds to the analysis of the gas jet operation focusing on the production of the gas curtain and the required skimming to ensure a finely collimated and monochromatic jet.

Experimental results are discussed emphasising on the vacuum performance, the effect of the gas jet in the background pressure and also on the imaged beam profile. Diagnostics for the gas jet itself are presented highlighting the necessity for high resolution in the measurement of the gas jet density distribution and size.

Finally, the resolution of the system is estimated and all the factors contributing to measurement uncertainty are discussed.

3.1 Motivation

Non-interceptive beam profile monitors are highly desirable in almost all particle accelerators. Such techniques are especially valuable in applications where real-time monitoring of the beam properties is required while beam preservation and minimal influence on the vacuum are of the greatest importance. This applies to many kinds of accelerators such as high energy machines where the normal diagnostics cannot withstand the beam's power, medical machines where treatment time is valuable and cannot be allocated to diagnostics and also low energy, low-intensity accelerators where the beam's properties are difficult to measure. This rest of this thesis presents the design, operation and evaluation of a gas-jet based beam profile monitor which was developed and commissioned at the Cockcroft Institute and can operate in a very large background pressure range from 10^{-7} down to below 10^{-11} mbar.

3.2 Background

The use of gas jets in beam profile monitoring can be traced back more than 4 decades when metal vapour [106] and carbon vapour [107] were used. Recently, it was applied in the Heavy Ion Medical Accelerator (HIMAC) [108] in Chiba, Japan, where an oxygen gas jet was used. This monitor [109] is skimmed and shaped to a thin curtain by focusing magnets [110] to measure the 2D profile of carbon ion beams. Another application by the same author was at the Japan Proton Accelerator Research Complex (J-PARC) [111]. By using a nitrogen molecular jet they managed to measure the proton beam's bi-dimensional profile [112]. For both cases, the compression gauge or through gauge method was used to identify the 2-D density distributions of the jets, which showed the thinness and homogeneity of the jet density distribution [109], [113]. Another example is a previous proton polarimeter with polarised atomic hydrogen jet used as an independent beam profile monitor by Tsang et al. for RHIC at Brookhaven National Laboratory [114]. It uses the fluorescent light emitted by the excited hydrogen atoms which is a consequence of the interaction between the projectile proton beam and the hydrogen jet. Since this monitor is not purpose designed, the beam profile measurement is limited to the vertical plane of the accelerator.

Compared to residual gas monitoring IPM's or fluorescence monitors, the supersonic gas jet based beam profile monitor offers several advantages. First, the monitor is intrinsically very flexible, in that the interaction it relies upon, namely, ionisation or fluorescence is well understood and usable with most projectile species. Furthermore, operating parameters such as acquisition rate and beam perturbation can be easily scaled by varying the target gas density, and tailored for the particular application. Therefore, the gas jet based beam profile monitor can be used in most accelerators across large energy, current and vacuum ranges, and is not restricted in only low energy storage rings such as the USR which is the target environment of our supersonic gas jet monitor, where low-intensity antiproton beam with short lifetime travels in an ultra-high vacuum.

The monitor presented here was designed to operate in an ultra-high vacuum environment in the order of 10^{-11} mbar and probe proton and antiproton beams ranging from 20 to 300 keV [115][116]. These are the requirements for the profile monitor at the Ultra-low energy Storage Ring (USR) at the Facility for Low-energy Antiproton and Ion Research (FLAIR) in Darmstadt [117]. According to these specifications, low energy beams with ultra-low currents (1 nA or less), few particles ($< 10^7$) and beam size varying from 2 centimetres to a few millimetres will require the development of new diagnostic devices. The beam monitor is based on the reaction microscope design, developed by the Ullrich group at MPIK for high

precision atomic physics experiments [118]. In a reaction microscope, a neutral gas undergoes a supersonic expansion into the vacuum reaching Mach number 7 and an internal temperature of a few K. It is then skimmed and shaped into a pencil jet. Such a low temperature minimises the thermal motion of the gas so that after the interaction with a beam and imaged on a position sensitive detector the cold ion trajectories can be traced backwards to the exact point of interaction.

For beam monitoring purposes the principle of operation remains the same but the skimmer shape is altered to produce a thin gas sheet. According to the design considerations of this beam profile monitor and the case of USR, acquisition times compatible with millisecond imaging will be feasible [18]. Although designed initially for the strict specifications of the USR, the monitor is flexible and can also operate in different vacuum environments and different beams. The interaction with the beam relies on ionisation, a well-studied process with rich literature available for different gas species, primary beam types and energies. The reaction rate which determines the measured profile quality can then be controlled by the stagnation pressure or by using gas species with convenient cross sections, making the monitor easily adaptable to different applications.

The basic components of the supersonic gas jet beam profile monitor closely match the ones needed for a Reaction Microscope (ReMi): a momentum spectroscope for analysis of fragmentation molecular and atomic reactions, e.g. developed at the Max Planck institute for Nuclear Physics in Heidelberg [119]. Currently, the supersonic gas jet monitor shares the design of the components with the ReMi including the position sensitive detector for imaging of ions, the electric field based extraction system and the supersonic gas jet target. Previously, it has also been proposed to operate the ReMi as a transverse beam profile monitor at the point of interaction [120].

3.3 Operating principle

The monitor presented utilises a cold (<20 K) neutral supersonic (Mach number 7 or around 800 m/s) gas jet shaped into a thin curtain after passing through a series of collimators. The low temperature of the jet minimises the effect of the motion of the gas particles on the spatial resolution of the measurements. The high directionality of the jet, produced by the supersonic expansion, allows the efficient evacuation of the chamber and the preservation of the vacuum. On the other hand, the generation of such supersonic gas jet poses a number of challenges, in particular, linked to the manufacturing of very small apertures with thin walls and the tight alignment they require [109], [121], [122].

A supersonic gas jet based beam profile monitor is very flexible and can be modified to match the specifications of various machines. The monitor relies on impact ionisation which is very well studied for a variety of gas species, projectile types and energies. A few examples are presented in Table 18 [123]–[125]. The reaction rate, which is controlled by the gas density, can be tuned according to the beam's properties, i.e. its energy, intensity, pulse structure, etc.

The monitor is based on a neutral gas, shaped into a thin sheet. The jet is travelling perpendicularly to the particle beam propagation axis with its plane tilted at 45° with respect to the horizontal plane.

Table 18: Example values of ionisation cross sections.

Projectile	Energy (keV)	Target a.n.)	Cross section (Å^2)
Electron	5	Nitrogen(7)	0.181
Electron	10	Argon (18)	0.155
Proton	50	He (2)	0.743
Antiproton	100	Nitrogen (7)	2.86

At the point of interaction ionisation occurs and the produced ions are accelerated by an external electric field toward a microchannel plate detector (MCP). Every ion produces a cascade of electrons which are incident on a phosphor screen. The light emitted by the phosphor screen is then detected by a CCD camera. After interaction with the beam, the jet enters a turbo molecular pump which evacuates the non-ionised gas away from the chamber. A schematic of the gas jet monitor is presented in Figure 66.

This monitor allows for 2-dimensional transverse beam profile imaging. Due to the 45° of inclination of the gas jet plane, it acts as a mirror reflecting the beam's transverse profile onto the MCP. The vertical and horizontal profiles can then be computed by integrating the acquired profile along the X and Y axes. Furthermore, the monitor can be operated with residual gas only, which can be useful during the commissioning of the instrument.

In order to estimate the reaction rate one should take into account the estimated jet number density of 2.5×10^{16} particles/m^3 for stagnation pressure of 10 bars and the expected curtain thickness of 0.5 mm. For nitrogen gas whose ionisation cross-section by 5 keV electron impact is in the order of 1.2×10^{-21} m^2 [125], these values correspond to a probability of ionisation per particle of 1.25×10^{-8} which leads to reaction rates per mA of beam current in the order of 8×10^7 /s or a corresponding acquisition time of 20 μs.

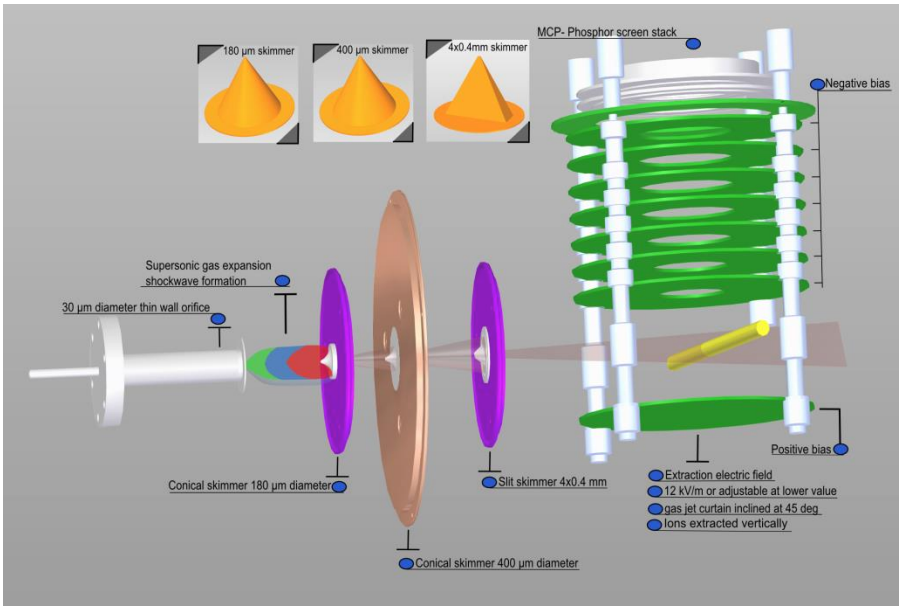

Figure 66: Schematic representation of gas jet setup. Starting from left the gas inserts the chamber though the nozzle, passes through the 3 skimmers and attains the curtain shape and finally crosses the charged particle beam inside the extraction field apparatus.

The experimental setup is composed of four main sections. In the direction that the jet travels, these are: the nozzle chamber where the jet is generated, a differential pumping section where the jet is further collimated and the background pressure reduces as shown in Figure 66, the interaction chamber which also contains the extraction field, and finally the dumping section which evacuates the jet [18].

In the nozzle chamber, a neutral gas is injected through an aperture of 30-micron diameter with initial pressure between 1-10 bars, see Figure 67. Immediately after the aperture and within a distance of less than 2 cm there is the first collimator with a diameter of 180 μm. More than 99.9% of the gas is evacuated from the nozzle chamber, which underlines the need for very intense pumping. In the absence of very efficient evacuation turbulences would occur in the gas flow around the nozzle, disrupting the supersonic flow.

The second circular collimator which sits on the green gasket in Figure 67 has a diameter of 400 μm and collimates the jet even further. After that stage, the number density of the jet is reduced to less than 10^{16} m^{-3} so the flow lies in the molecular regime. The third collimator has the shape of a rectangular slit of 4 mm by 0.4 mm and is located 30 cm away from the second aperture. It is rotated by 45° around the jet's propagation axis and it shapes the jet into a thin curtain tilted by the same angle. The jet finally enters the interaction chamber where it crosses the measured beam at the centre of the chamber. The produced ions are extracted by a 12 kV/m electric field towards the detector.

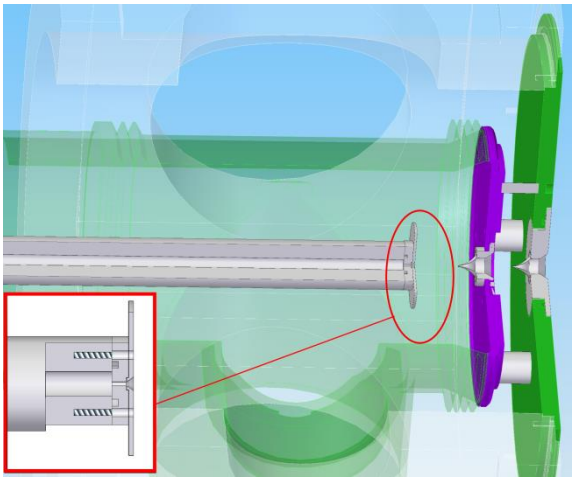

Figure 67: Illustration of the internal part of the nozzle chamber [120].

Finally, after the interaction, the jet is evacuated by a turbo molecular pump at the end of the vacuum pipe. The pump is inclined at 45° to the jet. This angle compensates for the turbo pump's tilted blades and guarantees efficient extraction of the jet as it can pass most easily through the pumps' blades in this configuration.

To be able to install such a monitor in a vacuum environment such as a storage ring where the pressure reaches down to 10^{-11} mbar, strong differential pumping is required. Six turbo molecular pumps (TMP) are used, one after every skimmer, one evacuating the interaction chamber and two for the dumping section. These six TMPs are connected to three pre-vacuum roughing pumps. One more roughing pump is installed to evacuate the hollow tube which holds the 30 μm orifice.

The ions generated at the interaction point are collected by means of an external electric field and directed to the MCP detector. One of the main considerations is to produce an electric field strong enough to minimise the ion's drift due to the initial velocity of the gas jet in the order of 800 m/s.

Simulations with OPERA3D [126] suggested that an electric field of 12 kV/m is high enough for the cold ions to travel in almost straight lines and values higher than that didn't offer any significant improvement in terms of monitor resolution. The extraction field is generated by a repeller plate, nine ring electrodes, the MCP assembly which includes two MCPs stacked in a chevron configuration, and a phosphor screen. The MCP's amplification is of the order of 10^6. The light is then recorded by a Ueye 1024x768 8-bit CCD camera that sits outside the vacuum chamber behind a viewport. A schematic is presented in Figure 68. A potential difference of 1800 V is distributed across nine electrodes via a voltage divider. The repeller plate is positively biased to create a homogeneous electric field. The electron beam

and jet are crossed in the large gap between the repelling plate and the first electrode. The length of the extraction system is 150 mm which increases the drift space for the ions but this was selected so that an optional reaction microscope could be realised in the same setup.

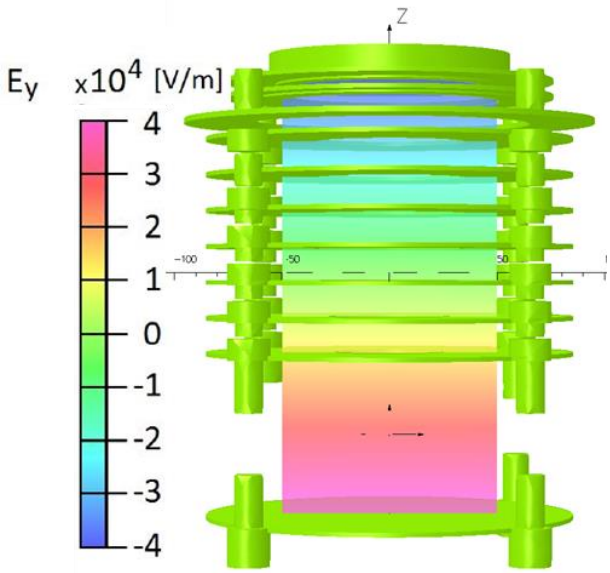

Figure 68: Extraction field scheme. From bottom to top, repelling plate and ring electrodes [120].

After the completion of alignment, first experimental results were obtained. The beam source was a 5 keV electron gun manufactured by PSP vacuum with adjustable focus, beam current and beam position.

In Figure 69 the first acquired beam profile is presented. The background pressure was around $4x10^{-8}$ mbar so that the signal of the residual gas ionisation is still visible. As it can be seen, the gas jet profile is more intense because of the high number density of the gas in the jet. It is also narrower due to the very small thermal motion of the gas jet particles in comparison to the residual gas.

In Table 19 the pressure at three different sections of the vacuum chamber is shown. Measurements were taken before firing the gas jet and also during operation. The nozzle chamber had to handle a heavy gas load so a significant rise in the pressure was expected. The experimental chamber and the dumping chamber are almost unaffected by the operation of the jet. Moreover, the pressure readings can be used for the fine alignment of the setup while in operation and also to select the optimal nozzle-skimmer distance and stagnation gas pressure.

The first experimental measurements have confirmed the results from simulations which were carried out during the design phase. The beam profile measured with the gas jet is much more intense and sharper than the residual gas profile. Keeping the pressure in the chamber

higher than 10^{-8} mbar allows for imaging the projectile beam profile with the rest gas and thus benchmarking results against a known technique.

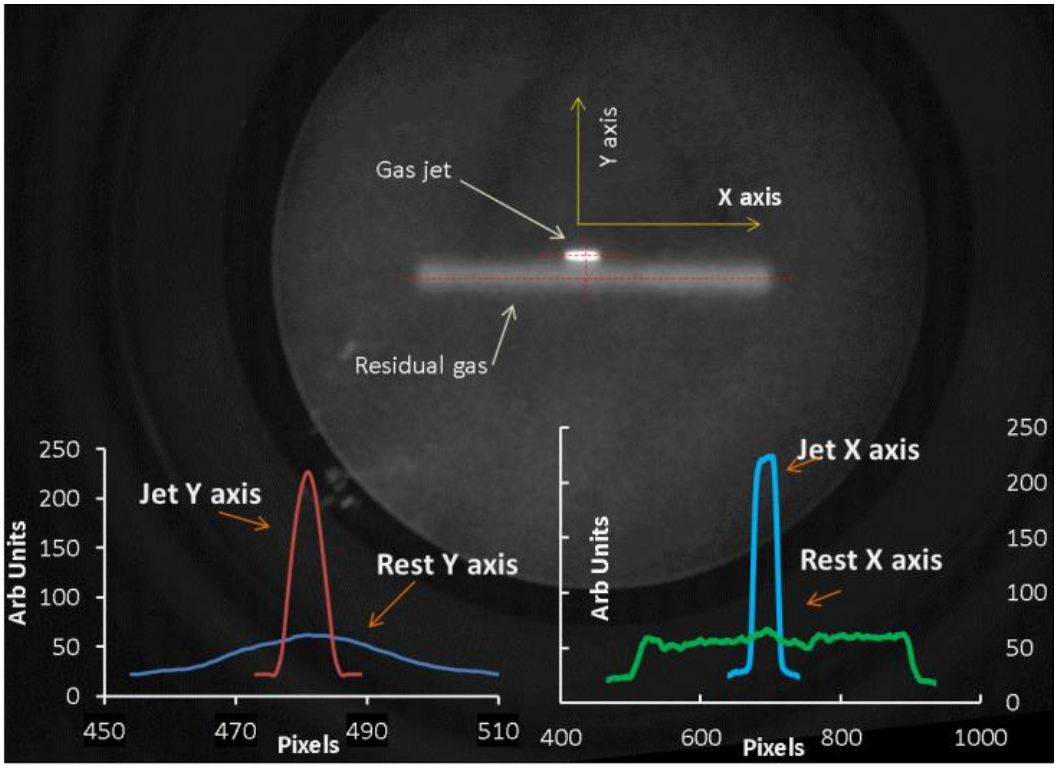

Figure 69: First beam profile obtained with the gas jet monitor [127].

Table 19: Pressure values in separate vacuum chambers.

Pressure (mbar)			
	Nozzle chamber	Experimental chamber	Dumping chamber
Without jet	3.23×10^{-8}	4.20×10^{-8}	2.18×10^{-9}
With jet	2.39×10^{-5}	5.00×10^{-8}	3.12×10^{-9}

3.4 Hardware design

The gas jet test stand is composed of five discrete sections according to Figure 70 and Figure 71. These are the gas generation (nozzle) chamber, the differential pumping section, the interaction chamber, a diagnostics chamber to probe the gas jet properties and finally a dumping section consisting of two chambers where the jet evacuates the system.

The nozzle chamber is where the jet is generated. The gas at room temperature, from a high pressure (1-10 bars) tank is fed to the nozzle chamber via an aluminium tube of 6 mm internal diameter with a 30 μm aperture at its end. The nozzle orifice is laser drilled in a

300 µm thick platinum plate of 4 mm diameter. The tube is connected to a three axes manipulator from VGScienta for fine alignment. It allows movement of 50 mm in the z direction and 12.5 mm in the transverse directions via three independent dials. At a distance of a few millimetres from the orifice, the first skimmer is located, separating the nozzle chamber from the outer jet chamber

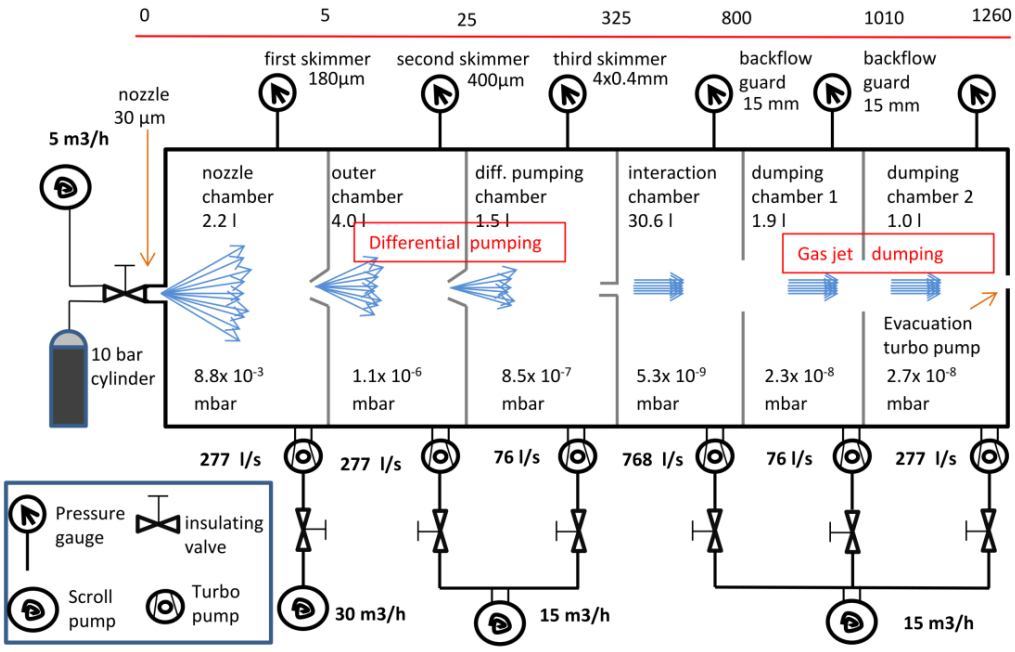

Figure 70: Gas jet setup layout, including vacuum pumping system.

The translating stage used to precisely align the orifice offers the flexibility of adjusting the orifice-skimmer distance from 1 to 50 mm. The 2 chambers are differentially pumped by turbomolecular pumps. The skimmer has a conical shape and the diameter of the aperture is 180 μm. Most of the gas is pumped out between the nozzle and the first skimmer resulting in less than 0.1% of the initially injected gas continuing to travel downstream. Following at a distance of 25 mm from the first skimmer the second conical skimmer with 400 μm diameter further skims the flow. The volume between the 2 skimmers (gas jet outer chamber) is separately pumped by a Turbo Molecular Pump (TMP). These 2 skimmers have been purchased from Beam Dynamics Inc. [30]. They are manufactured out of copper with a double wall thickness to withstand the large pressure differentials. These skimmers are commonly used in gas jet generation experiments. The conical skimmers are named model 7 where 7 is the nominal apex height, and have an orifice diameter of 0.180 ± 0.025 and 0.400 ± 0.025 mm, a height (tip to base) of respectively 6.6 and 6.2 mm and a base diameter of 12.7 mm. The angle at the tip is 25˚ internally and 30˚ externally, which becomes 75˚ at the base.

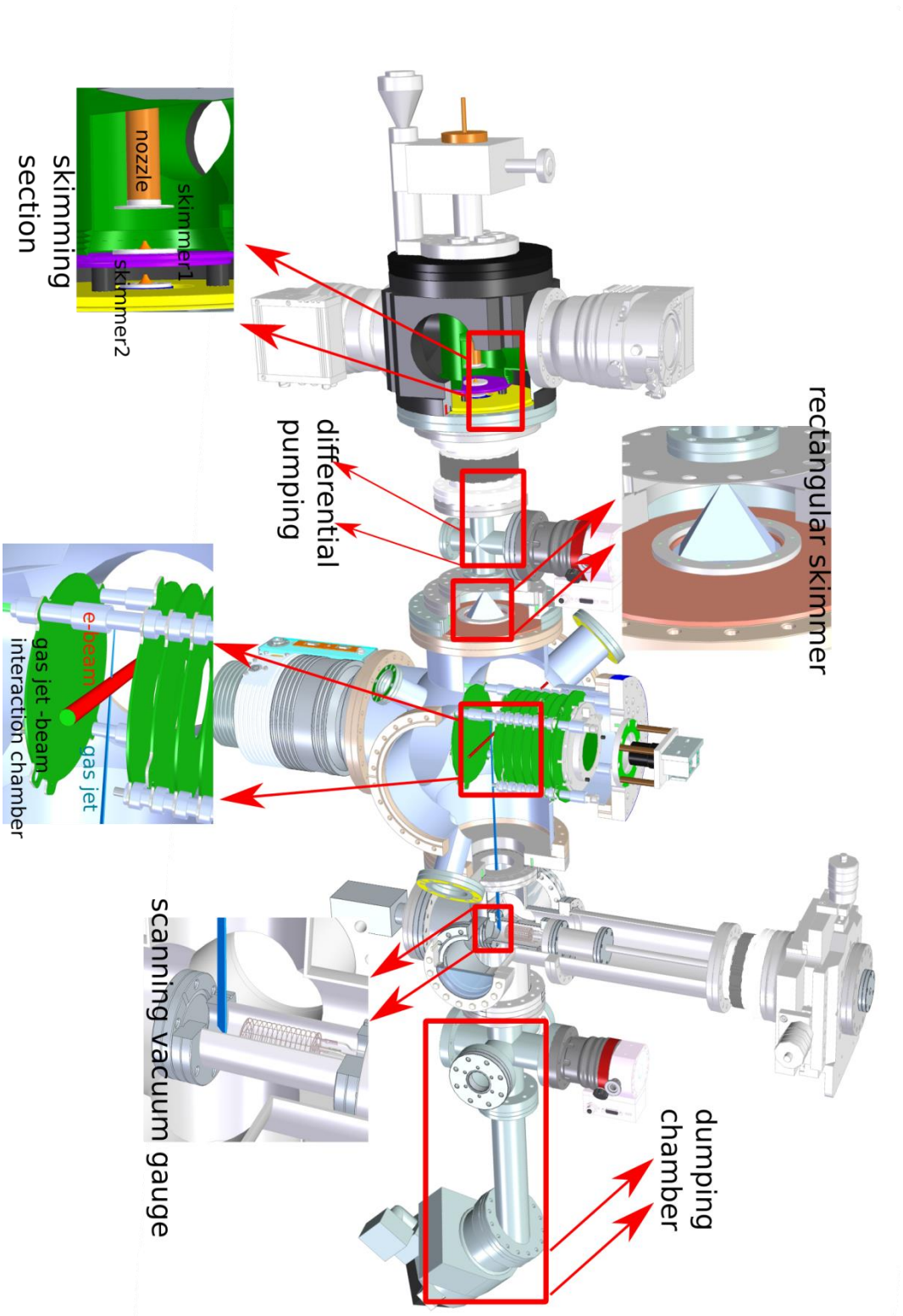

Figure 71: CAD schematic of the gas jet test stand with highlighted details of the various sections.

There are two sizes available for the last rectangular shaped collimators, 7.2×1.8 mm^2 and 4×0.4 mm^2 as shown in Figure 72, which are interchangeable and placed 365 mm downstream from the first skimmer. They are normally rotated by 45˚ so they can create the thin tilted gas curtain. They were manufactured by Direct Metal Laser Sintering (DMLS), a laser induced additive layering process usable on different metals including stainless steel. The skimmers have been constructed by additive layering by the CRDM UK Prototyping & Tooling [128] and subsequently mechanically polished by TJW Precision, UK [129]. This process guarantees the possibility of very thin walls (100 μm) at the tip of the skimmer, comparable with the circular skimmers wall thickness. The set of three skimmers separates the vacuum chamber in differentially pumped volumes necessary to reduce the gas load and maintain the high vacuum in the interaction area. After the final shaping, the jet enters the interaction chamber at the centre of which and at a distance of 600 mm from the nozzle it crosses the particle beam.

The dumping section is composed of 2 vacuum chambers evacuated by two turbopumps. They are separated with 40 mm diameter backflow guard rings to minimise gas scattering backwards into the interaction chamber. The vacuum pump at the end of the dump chamber is mounted at 45˚. This angle equals the angle of the pump's first blades and maximises the open area seen by the jet, thus increasing pumping efficiency and reducing backwards diffusion of the gas. Every chamber is equipped with a hot cathode gauge able to measure low pressures. The setup was designed to reach pressures as low as 10^{-11} mbar after bakeout.

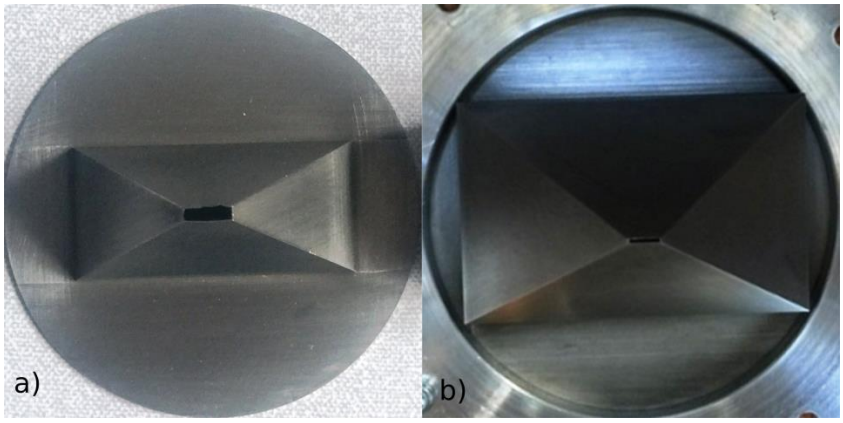

Figure 72: Picture of the third skimmers: (a) larger slit (7.2×1.8 mm^2); (b) smaller slit (4.0×0.4 mm^2).

To restrict the gas usage and control the gas flow as well as to conserve better vacuum conditions, an MHE3-MS1H-3/2G-1/8 solenoid pulsed valve by Festo [130] is used. It features a maximum switching frequency of 280 Hz with 2 ms switching time, an operating pressure of 0-8 bar and a standard nominal flow rate of 200 l/min. A TGP110 pulse generator

manufactured by Aim & Thurlby Thandar Instruments [131] is used to trigger the pulsed valve externally. It offers a variable frequency range from 0.1 Hz to 10 MHz and an individually adjustable pulsed width and pulse delay. Its maximum output amplitude is 10 V which is less than the requirement of the valve operating voltage of 24 V. A DC power supply IPS-3303 manufactured by ISO-Tech [132] and a solid state relay DMO063 manufactured by Crydom [133] are used to drive the valve. The electrical connection is shown is Figure 73. The relay receives the 5 V trigger from the pulse generator and generates a 24 V signal to trigger the pulsed valve. An oscilloscope is used to monitor the generated pulses.

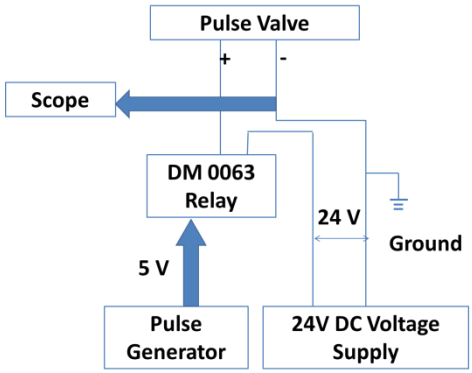

Figure 73: Illustration of the pulsed valve operation and control.

The optimisation of the setup in terms of skimmer dimensions, shapes, distances between them, pumping specifications and inlet gas pressure has been studied through extensive computer simulations by M. Putignano [134]–[136]. These studies have led to the final form of the optimal rectangular skimmer and the conical skimmers as these parts play a crucial role in the generation of a supersonic gas jet suitable for a beam profile monitor. The most important parameters for the quality of the gas curtain that were studied concern the geometry of the skimmer, namely the depth, the width and construction angles and also the nozzle-skimmer distance. Furthermore, the studies included the time evolution of the Mach number until the equilibrium state which requires a few milliseconds.

3.5 Detector and imaging

The detector assembly consists of a set of electrodes for the generation of the extraction field, an MCP paired with a phosphor screen and a camera that sits outside of the vacuum chamber. With reference to Figure 74, the extraction system is composed of one repeller plate, 9 ring electrodes (two of them to hold optional meshes) and the MCP detector assembly. The electrodes are supported by three metallic rods which are insulated by ceramic cylinders from the plates. The overall length of the system is 200 mm and the large gap between the repelling plate and the first electrode is 75 mm. The rest of the rings are spaced at intervals of 16.5 mm

and the distances between the last electrode, the two optional meshes and the bottom of the MCP are smaller.

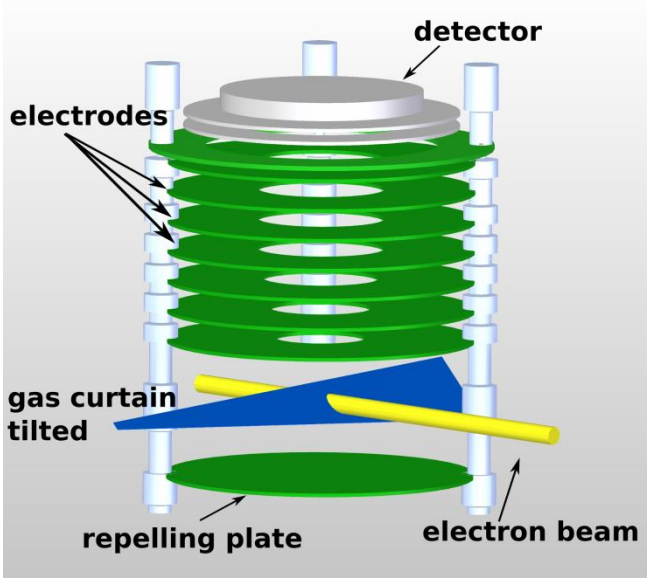

Figure 74: Extraction field scheme and particle beam-gas jet interaction visualisation.

For the voltage supply, two high voltage power supplies from Microlab Devices [137] were used. They have 2 channels each, one for negative and one for positive voltage and they can provide up to ± 6k V. For the extraction electrodes, one negative channel is used after passing through a voltage divider in order to apply the proper voltage to every ring. The voltage scales according to the geometric distance between the electrodes from -1800 V for the top to -400 V for the bottom for the generation of a homogeneous electric field. The positive channel of the same power supply is used to bias the repelling plate at 400 V. The MCP and phosphor screen are connected to the positive and negative channel of the other power supply biased at 3.5 kV and -2 kV respectively. Usually, the voltage gradient is around 11 kV/m but it can easily be adjusted to any value within the range of voltages that the power supplies can provide.

The main requirement for the extraction field is to pull the ions towards the MCP in a straight line and on the other hand not to deflect the particle beam so much that it falls outside of the gas curtain area or hits some other element in the experimental chamber. In a future application of the setup, compensating electrodes for the application of correction electric fields will be added.

The MCP detector is provided by Photonis [138]. It contains two plates stacked in a chevron configuration and a phosphor screen. The plates have a channel diameter of 10 µm and a pitch between channels of 12 µm, which dominate the spatial resolution of the MCP.

When including the effects of the non-constant amplification in the channel and electron smearing between plates, the actual resolution of this chevron type of MCP is reported to be around 80 μm by the manufacturer [138]. The MCP can be biased up to 2.4 kV but it is usually kept lower than 2 kV for safer operation and improved longevity.

The phosphor screen used in this work is a common green glowing P22 (ZnS: Cu,Al) [138]. It features a typical emission wavelength of 530 nm and a decay time of 70 μs. Such a long decay time may limit the acquisition speed of the monitor for pulsed beams. For the purposes of the current experimental setup where a continuous beam is used the decay time is not a concern. The camera is a Point Gray Grasshopper3 [139] 1920 × 1200 CMOS camera with USB interface.

For the purposes of the development of the current setup, an electron gun was used to provide the projectile beam. It is a model ELS 5000 manufactured by PSP Vacuum Technology [140]. It features a common design for electron guns and it provides a steerable electron beam with spot diameter < 1 mm at the best focus with energies and currents from 1 to 5 keV and 10 nA to 10 μA respectively. It is mounted in one of the openings of the interaction chamber vertically to the propagation axis of the molecular beam. The beam current is adjusted by changing the filament current. It is usually operated at nearly the maximum of the kinetic energy and at a beam current which gives a clear signal on the camera with the filament current being usually set between 2.0-2.6 A. The operating conditions of the electron gun have to be adjusted every time the electric field configuration changes. The reason for this is the lack of correction fields causing the beam to bend under the extraction field forces. Depending on the extraction field strength, the electron beam current and intensity are selected and then fine-tuned with respect to the image on the camera. Furthermore, the MCP and phosphor screen bias are adjusted in order to have a clear image of the beam profile. Note that when the filament current of the electron gun is over 2.3 A, it causes a small pressure rise.

3 .6 Analysis of gas jet operation

3.6.1 Free jet expansion

A neutral gas, nitrogen here, is allowed to expand freely into the vacuum through a series of skimmers. It is supplied from a high pressure (1-10 bars) tank (P_0) and enters the vacuum chamber (P_a) via an orifice which is commonly referred to as the nozzle. Because of the pressure difference, the gas accelerates towards the nozzle exit. For an ideal gas, if viscous effects and heat conduction are ignored, the expansion can be treated as isentropic and

adiabatic. The minimum condition to attain sonic speed (Mach number 1) at the nozzle exit is met if the pressure ratio P_o/P_a obeys the condition [141]:

$$\frac{P_o}{P_a} \geq \left(\frac{\gamma+1}{2}\right)^{\gamma/\gamma+1} \quad ,\gamma = C_P/C_V \tag{11}$$

In equation (11) C_P is the specific heat capacity of a gas at constant pressure, C_V the specific heat capacity at constant volume and γ is the isentropic expansion factor expressed as their ratio. If the inlet pressure P_0 increases beyond this point then the pressure at the nozzle exit becomes independent of the pressure ratio and is given by:

$$P = \left(P_o \cdot \frac{2}{\gamma+1}\right)^{\gamma/\gamma-1} \tag{12}$$

In this case, the gas pressure at the nozzle can exceed the background pressure P_a, the flow is said to be underexpanded [141] and a Mach disk as shown inFigure 76 is formed expanding past the nozzle. The Mach number of the flow is then given by equation (13) with the pressure in pascal and γ as explained above. Figure 75 shows the evolution of Mach number for varying stagnation pressure and varying background pressure.

$$M = \sqrt{\frac{2}{\gamma-1} \cdot \left(\frac{P_o}{P}\right)^{\gamma-1/\gamma} - 1} \tag{13}$$

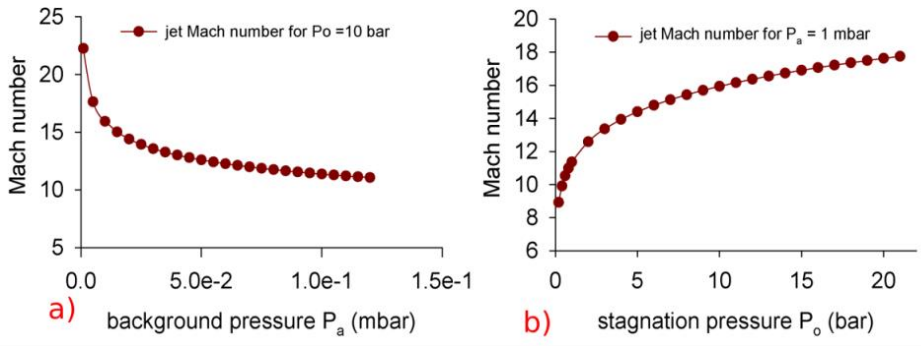

Figure 75: Mach number evolution with varying a) background pressure and b) stagnation pressure.

For the current gas jet application as it has been studied before [135], with orifice diameter D, the height, H_D and the width W_D of the Mach disk can be calculated as given by the empirical correlation by Ashkenas & Sherman [142] as:

$$H_D = 0.67D\sqrt{\frac{P_{inlet}}{P_{chamber}}} \quad (14)$$

$$W_D = 0.5H_D \quad (15)$$

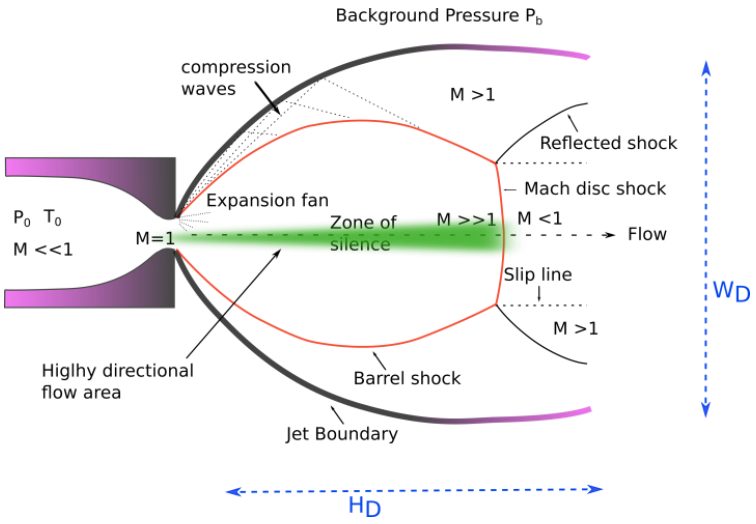

Figure 76: Structure of the supersonic gas expansion.

For an inlet pressure of 1 bar and chamber equilibrium pressure of 0.1 mbar, the H_D stretches to about 2 mm and the Mach disk width W_D is around 1 mm. For a more realistic scenario and using the measured pressure in the first vacuum chamber of about $1x10^{-2}$ mbar the Mach disc height is 6.4 mm for a stagnation pressure of 1 bar and 2.1 cm for 10 bars. The first skimmer has to be located in the innermost area of the shockwave formation, known as the 'zone of silence' and shown in green in Figure 75. The flow in this area is purely supersonic and not affected by the ambient pressure variations in the chamber, thus ideal for the production of a homogeneous gas jet.

3.6.2 Jet velocity and temperature

The velocity of the flow can be deduced from the assumption that the gas expansion can be treated as adiabatic and isentropic as previously mentioned. In this case, the enthalpy of the gas in the reservoir when the flow is stationary equals to the sum of enthalpy and kinetic energy of the flow after the expansion [141]. Using the enthalpy per unit mass *h* this relation can be expressed as in the equation (16).

$$h_0 = h + u^2/2 \quad (16)$$

Here, h_0 is the stagnation enthalpy and u the flow velocity. The stagnation enthalpy for the stationary gas in the cylinder can be expressed as shown in equation (17) with T_0 the stagnation temperature.

$$h_0 = C_P \cdot T_0 \qquad (17)$$

The conservation of enthalpy due to the adiabatic assumption (no heat transfer to the system) leads to the conversion of the thermal energy of the gas in the cylinder to kinetic energy during the expansion, therefore; the gas undergoes substantial cooling while the flow velocity increases.

The terminal velocity can be expressed as in equation with R being the gas constant in $JK^{-1}mol^{-1}$, W the molar mass in $kgmol^{-1}$, T_0 the stagnation temperature in K and γ the isentropic expansion factor.

$$U_\infty = \sqrt{\frac{2R}{W} \cdot \frac{\gamma}{\gamma - 1} \cdot T_0} \qquad (18)$$

The gas flow velocity can also relate to the Mach number by considering that the Mach number is expressed as the ratio of the flow velocity to the local speed of sound.

Past the nozzle the gas flow for the equivalent distance of a few nozzle diameters is in the continuous regime dominated by high collision frequency. As the flow expands and the collision frequency reduces the gas flow enters the molecular regimes characterised by large mean free path. In this regime, the molecules are in a nearly collision-free area and follow straight trajectories. A concept to understand the boundary layer between the two flows is the "quitting surface" or "sudden freeze" model introduced by Anderson and Fenn [143] and suggests an abrupt change between the two flow areas rather than a slow transition. Based on this model, the temperature of the gas molecules decouples after the "quitting surface" in two components, one parallel to the gas flow ($T_\perp$) and one perpendicular to the flow ($T_{/\!/}$) and can be treated the same way as the velocity components. Beyond the "quitting surface" the distribution of parallel velocities does not change and is described by a Maxwell-Boltzmann distribution. The perpendicular velocities, however, continue to decrease because of geometrical constraints. Following Figure 77, particles with a larger perpendicular velocity component are not able to remain on the centerline (or any other streamline along the expansion) whilst particles with smaller perpendicular velocity component are more likely to merge to the streamline. It is then purely a geometrical effect referred to as geometrical cooling [141] that the perpendicular temperature decreases along the propagation of the molecular beam.

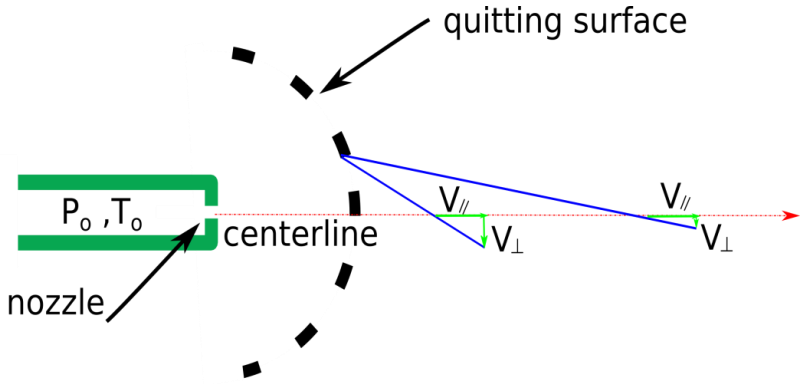

Figure 77: Schematic diagram of the parallel and perpendicular velocity components using the sudden freeze model [141].

The theoretical and experimental determination of the parallel component of the velocity (or temperature) can be accurately done but the same does not hold for the perpendicular component. Most often the term speed ratio is used to describe the ratio between the two speed components (parallel and perpendicular). Speed ratios more than 1000 [144] have been observed for pulsed helium beams .

3.6.3 Jet number density

The density of the gas jet is a very important factor as it is directly related to the ionisation cross section for interaction with the particle beam .The jet centerline density can be estimated by firstly calculating the density at the nozzle using equation (19) [141] with P_0 the stagnation pressure in pascal, k_b Boltzmann's constant and T_o the stagnation temperature in K.

$$n_0 = \frac{P_0}{k_b \cdot T_0} \qquad (19)$$

The centerline density for a 2-atomic ideal gas with heat capacity ratio (γ) equal to 7/5 at a distance x away from the nozzle (at least x>4D) is approximated by equation (20) [141].

$$n(x) = 0.092 \cdot n_o \cdot \left(\frac{D}{x}\right)^2 \qquad (20)$$

Here D is the nozzle diameter, n_0 the number density at the nozzle and x the distance from the nozzle along the centerline of the jet. Number densities for stagnation pressure of 2, 3 and 10 bars are shown in Figure 78.

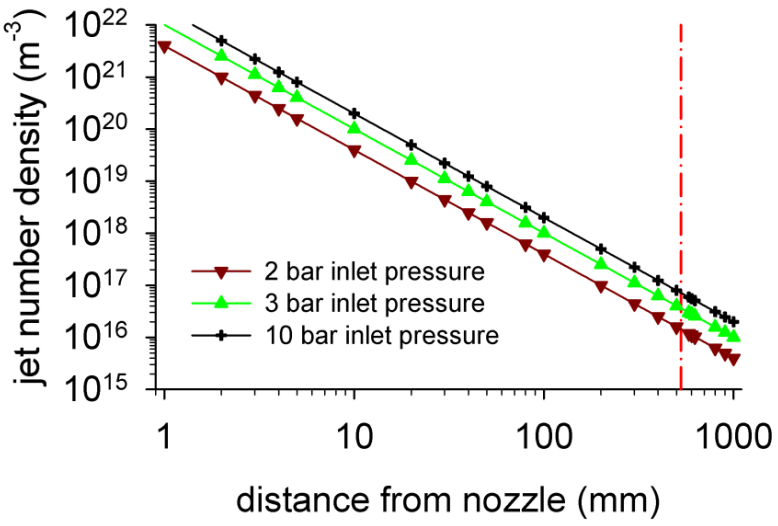

Figure 78: Gas jet centreline density for three different stagnation pressure values. The red vertical line shows the distance from the gas source to the centre of the interaction chamber.

3.6.4 Further skimming and interaction

As the gas jet keeps expanding in the vacuum it is further skimmed by passing through the second skimmer, separated by differentially pumped chambers. Next downstream is the third skimmer, a rectangular slit that shapes the jet into a thin gas curtain as it enters the interaction chamber.

In the interaction chamber, the jet is hit by the particle beam, producing ions which are in turn extracted by an applied electrostatic field and accelerated towards the MCP detector. The electron cascade leaving the MCP is converted into light in the phosphor screen, which is imaged by a camera. The majority of the gas jet, which has not interacted with the beam, is evacuated from the system by a turbopump mounted at the end of the dumping chamber.

This monitor allows two-dimensional transverse beam profile imaging. Due to the 45° of inclination of the gas jet plane, it acts as a mirror reflecting the beam's transverse profile onto the MCP. The vertical and horizontal profiles can then be computed by integrating the acquired profile along the X and Y axes, as shown in Figure 79. Furthermore, the monitor can be operated with residual gas only, which can be useful during the commissioning of the instrument.

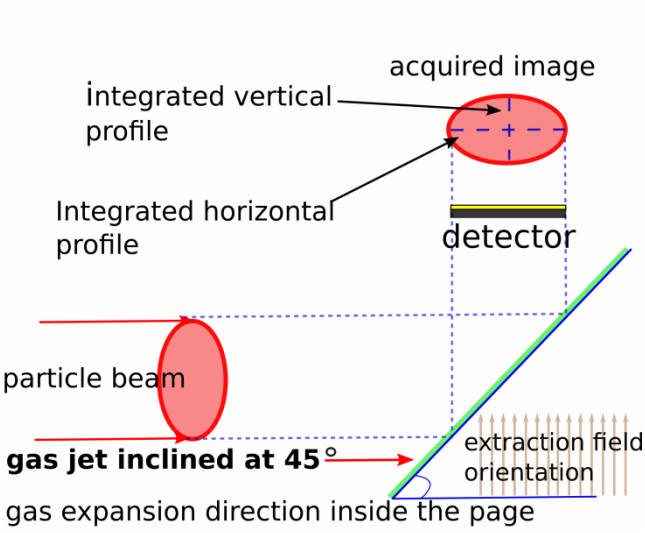

Figure 79: Principle of the two-dimensional imaging (Ions are extracted by the external electric field).

3.6.5 Gas curtain properties

As shown in Figure 80 (a) and (b) for a more clear description of the setup and the measurements, the Z axis is along the particle beam propagation, the X axis is along the gas jet propagation direction and the Y axis is pointing upwards and towards the direction of the detector. The top view which is the camera view of the system shows how the above-mentioned coordinates correspond to the measured beam profile coordinates. Ionisation takes place ideally at the centre of the interaction area but as the gas jet has an initial velocity the imaged profile will be shifted along the X axis. This will provide a separation from the residual gas induced signal. The particle beam horizontal and vertical profiles can be calculated by direct integration along the corresponding direction on the image acquired by the camera. With reference to Figure 80 (b), for a jet curtain of thickness W and tilted at an angle θ of 45˚ with respect to the particle beam propagation axis (Z axis in the figure) the effective width or the distance that the particle beam will travel in the jet d, is equal to:

$$\frac{W}{\sin\left(45^0\right)}$$

In this case, a particle of the beam passing through the point (x, y, z) as noted in the figure, can ionise the gas anywhere in a segment along the Z axis according to equation (21).

$$z \pm \frac{1}{2} \cdot \frac{W}{\sin\left(45^0\right)} \qquad (21)$$

This adds an uncertainty in the measurement of the vertical beam profile introducing an error in the measurement that depends on the thickness W. In principle it is possible to

minimize this error by increasing the angle but the chosen value of 45˚ offers the advantage of maintaining the aspect ratio of the imaged profile thus preventing any distortion that would require more complicated image processing. The above-mentioned error contributes less in the measurement when the beam diameter is significantly larger than the jet thickness. The same issue has been reported elsewhere [109] and in this work, special care was taken to create a thin gas curtain. The horizontal axis of the acquired profile is completely unaffected by the gas curtain thickness.

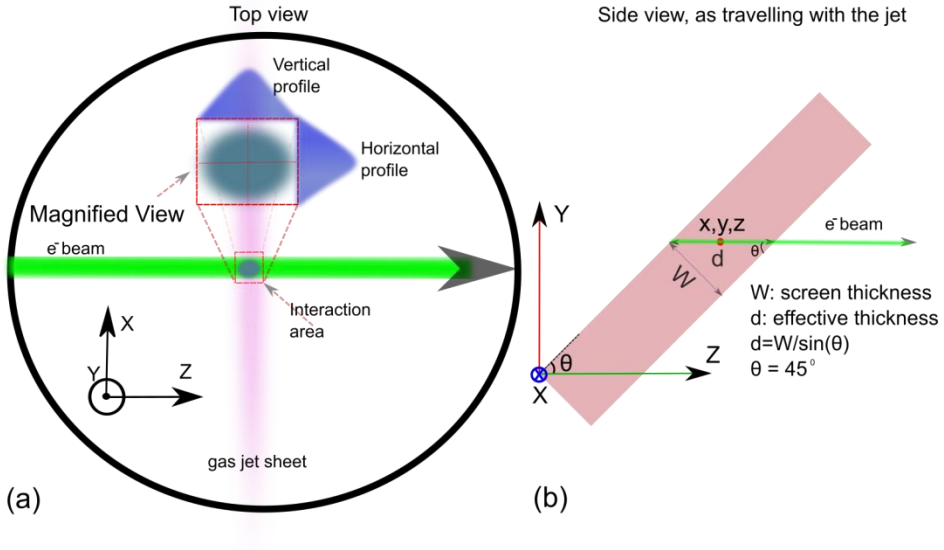

Figure 80: (a) scheme of the top view of the particle beam-gas jet interaction, (b) side view and gas screen details.

3.6.6 Acquisition time estimation

The acquisition time for our monitor depends on both the number of measurements required for a beam profile and the reaction rate. For the diagnostics purpose of a Gaussian beam, from the statistical point of view [37], if confidence intervals of 5% in beam position determination can be accepted, this will require about 1500 ionisation events be recorded which give a 96% precision on the determination of beam profile width [24]. The reaction rate R is given by:

$$R = P_{ion} \cdot \frac{I}{q_p}$$

Where P_{ion} is the probability of ionisation of a gas molecule by the projectile beam, I is the projectile flux in particles per second or projectile current and q_p is the projectile charge. The probability can be expressed as

$$P_{ion} = \sigma_{ion} \cdot \rho_{gas} \cdot d_{gas}$$

Where σ_{ion} is the ionisation cross section, ρ_{gas} is the gas target number density and d_{gas} is the gas curtain thickness. Cross sections for many gas species and projectile type and energies can be found in the literature. Here, ionisation reaction rates for antiproton and electron impact will be discussed. This is based on the available electron beam for the experimental setup and the antiproton beam of the USR.

For the case of the USR and antiprotons of 20 - 300 keV with a beam current of 1 nA and impact on nitrogen or helium, with a typical gas jet density of 2.5×10^{16} particles/m^3 and the gas jet thickness as 0.5 mm, we calculate the expected reaction rates as in Figure 81. The single ionisation cross sections for energies relevant to the USR beam for helium and nitrogen are available as measured with the ASACUSA slow antiproton beamline at CERN [38].

As shown in Figure 81, the reaction rate does not change much over the entire energy range of the USR. For helium, this value is smaller compared to nitrogen due to its higher ionisation energy. The acquisition time for a reasonable measurement of 1500 ionisation events will be about 1 s and 3 s for nitrogen and helium gas respectively.

Nevertheless, the device discussed here is inherently flexible to increase the reaction rates by simply increasing the gas pressure or using a larger nozzle. It has to be noted though that any changes should be carefully considered as they can affect the pumping efficiency in the first stages of the differential pumping. Generally, particle densities of 10^{17} to 10^{18} m^{-3} are achievable [23].

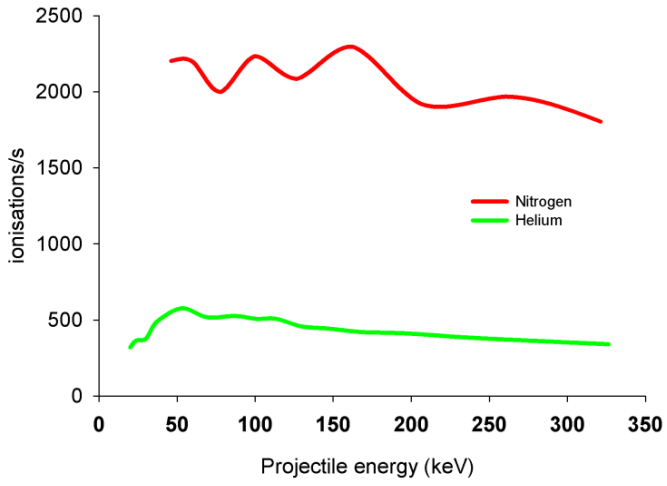

Figure 81: Calculated reaction rates for antiprotons [38]

Regarding the experimental stand at Cockcroft Institute, an electron beam with maximum 7 μA of beam current can be produced by the electron gun for 2.5 A of filament current with maximum energy 5 keV. The reaction rates are calculated using available data for electron impact ionisation on helium, nitrogen and argon [39], the estimated but scalable number density of the gas jet as 2.5×10^{16} particles/m^3 and the gas jet thickness as 0.5 mm which also depends on the rectangular skimmer dimensions.

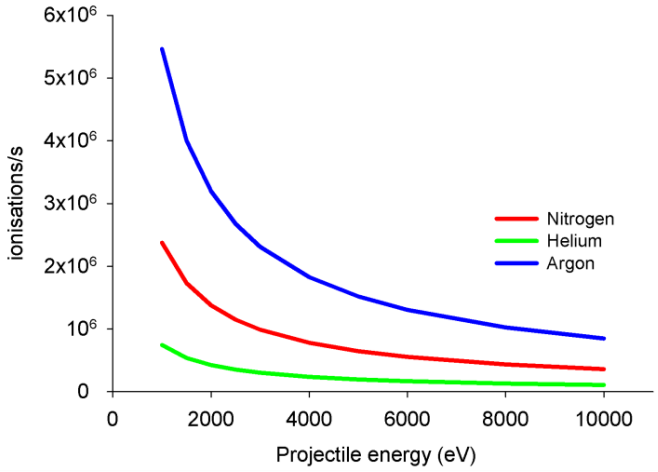

Figure 82: Calculated reaction rates for electrons [39] .

As shown in Figure 82, the reaction rate is much higher due to the higher beam current although the ionisation cross section does not change significantly. For a typical value of 1.5×10^6 ionisation events per second using nitrogen gas, an acquisition time about 1 millisecond can be estimated to obtain a meaningful measurement.

It has to be stated that although the larger cross-section of low energy particles works in favour of the monitor at the same time it limits the beam lifetime. Based on this, the thickness and density of the jet can be fitted to the specific application so the signal intensity is sufficient while the particle beam is not disturbed.

For the diagnostics of the USR beam, with residual gas pressure in the order 10^{-11} mbar corresponding to number densities at room temperature of about 10^{11} particles m^{-3}, the jet to residual gas density ratio would be about 10^5. The effect of a 0.5 mm gas jet screen would be equivalent to 50 m of residual gas which is comparable to the storage ring circumference of 42.6 m. Therefore, the beam lifetime is expected to be roughly halved for the specific operating conditions.

3.7 Vacuum gas dynamics

The first part of this section discusses the alignment of the system and effects of the moving stage the holds the orifice. When the system is evacuated the moving parts of the previously mentioned stage are slightly displaced due to the pressure difference and the alignment of the system is lost. Due to this effect, an optical method based on camera tracking has been developed so the alignment can be quickly restored.

Next, the section focuses on investigations in the gas dynamics of the supersonic gas jet. More specifically, the effect of the operation of the gas curtain on the background pressure is examined in all the chambers composing the experimental setup. At this stage of the development, the parameters that can be varied are the stagnation pressure and the nozzle to skimmer distance for different gases. All the measurements in this section were carried out with the gas jet operating in continuous mode.

The section then presents beam profile measurements using a 5 keV and three gas targets, namely helium, nitrogen and argon. Due to different ionisation cross sections and different effective pumping speeds, the various gas species affect the profile imaging and the vacuum performance.

The section ends discussing additional alignment considerations regarding the reduced gas jet intensity when compared to the expected one from gas dynamics calculations. The reduced intensity leads to lower ionisation yield and thus less light recorded by the camera when imaging the beam profile. Theoretically, the beam profile imaged by the gas jet should be a few orders of magnitude more intense than when images by the residual gas but the experimentally measured intensity differ only about four times.

For all the measurements presented in this section, the larger rectangular skimmer was used measuring 7.2 mm x 1.8 mm.

3.7.1 Alignment of the system

Because of the tight alignment tolerances dictated by the nozzle-skimmer precise positioning, and small acceptance angles, a method for precise alignment was required. At the first attempt to align the setup it was noticed that the translating stage which holds the aluminium cylinder with the first aperture at its tip was moving during pump down. This led to the assumption that others parts could also be prone to minor but non-negligible displacements due to pressure differentials. At the top right of Figure 83 is the evidence of deformations of the setup during pump down causing loss of alignment. This was recorded

using a laser mounted on a reference point next to the experimental setup pointing to a white paper placed on the side of the translating stage. A picture was taken with the setup exposed to atmospheric pressure and another after the chamber was evacuated. The laser spot on the paper moved by about 2 millimetres during this process. To prevent such phenomena affecting the operation of the gas jet setup, the alignment had to be monitored continuously during pump down and restored if necessary.

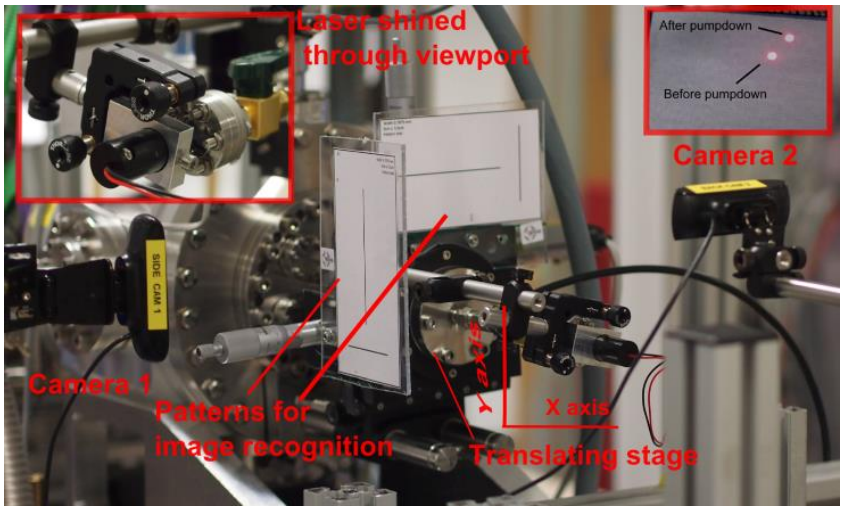

Figure 83: Alignment instrumentation. Top left, laser shined through a viewport and along the gas expansion axis. Top right, initial proofs of displacements during pump down.

The alignment instrumentation that has been developed [147] has solved all major problems and led to the first experimental results from the monitor. As shown in Figure 83, the translating stage is equipped with two printed patterns on white paper that allow for real-time monitoring from the two cameras (Logitech C902) of displacements on any axis. At the back of the stage a viewport has been placed and a 100 mW solid state laser was shined through and along the gas propagation path as shown in Figure 84. The laser beam is monitored at the other end of the setup through a mirror by a uEYE 1024x768 8 bit camera.

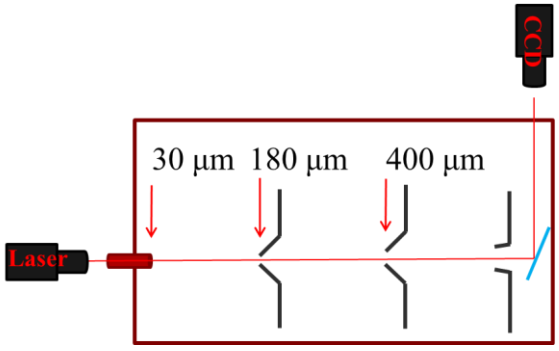

Figure 84: Laser setup for monitoring the alignment of the system. The laser shines through the nozzle and all the skimmers and recorded by a camera after being reflected by a retractable mirror located in the dumping chamber.

An additional refinement was a helium detector that was used as a leak tester connected with the output of the turbopump at the dump chamber. When a helium jet is fired the detector can measure the helium flow into the dump and thus finding the maximum leak rate has proven to be a good indicator for the overall alignment of the system. A more detailed description of the optical alignment instrumentation is presented in Appendix 2.

Before taking any measurements the alignment method was tested for resolution and repeatability. At first, the image processing method was used to align the setup. Moving the stage vertically by steps of 10 μm for 100 μm in total the displacement readings in pixels with sub-pixel accuracy from the 2 cameras were recorded.

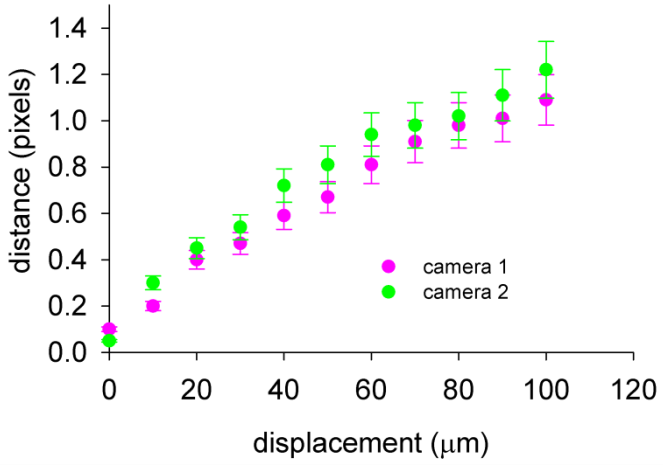

Figure 85: Measurements for algorithm resolution.

The results are presented in Figure 85 and the scale factor is calculated as 0.1 mm/pixel. The resolution of this method is highly affected by the light conditions and the location and resolution of the cameras. As it used primarily for the initial alignment and as an indicator for displacements in the order of a few hundred of microns such effects are considered negligible.

The repeatability of the method was tested by using the helium detector and firing a helium jet until the location of the orifice where the maximum leak rate of 3.76 x10^{-6} mbar l s^{-1} was identified. This location was recorded as the reference position and then the orifice was displaced to a random position where no gas jet induced signal was visible. Using the horizontal and vertical displacement dials of the translating stage the initial position was restored according to the readings provided by the LabVIEW code and the corresponding leak rate was logged.

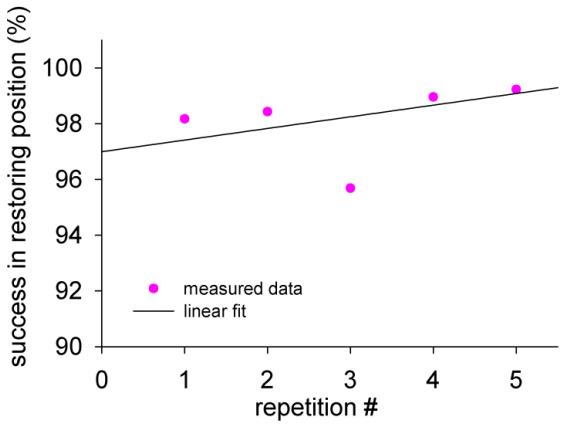

Figure 86: Repeatability of the alignment procedure.

This step was repeated 5 times and the results are shown in Figure 86. The readings from the leak detector were normalised and varied around the average of 0.98 ± 0.01 while the average error in restoring the initial position was 1.4 %

As a second verification of the alignment methods that were developed, the orifice was displaced horizontally and vertically with the dials by steps of 10 μm and at every step, the reading from the leak detector, a picture from the camera recording the laser spot and a beam profile were logged. All the measurements were normalised so they can be plotted on the same graph against the corresponding displacement. The results are shown in Figure 87 for X axis Y axis and as it can be seen all the methods are in good agreement. All the values have been normalised for plotting as they came from different sources and were expressed in different units. It is obvious now how crucial the good alignment is and how it affects the gas jet operation. Even 20 μm is enough to half the intensity recorded from the gas jet induced profile whereas it has been identified that displacements of hundreds of micrometres in a random direction occur as the pressure drops.

The measurements presented in Figure 87 show that the displacement range along the Y axis is about half of the range for the X axis due to the tilt angle of the nozzle holding stage. In principle both of these measurements were expected to be symmetric so it will be assumed that the correct range is the one measured from X axis, equal to roughly 200 μm.

Equations (14) and (15) used to calculate the Mach disk height (H_D) and width (W_D) result in W_D size in the order of a few mm. The directionality of the gas jet during the expansion is not very well known but the measurement suggests that from the few mm of the Mach disk width, only a fraction of 200 μm can travel all the way up to the interaction chamber. That small fraction (shown in Figure 76 with green) corresponds to gas particles moving along the right trajectories to avoid collimation by the series of skimmers.

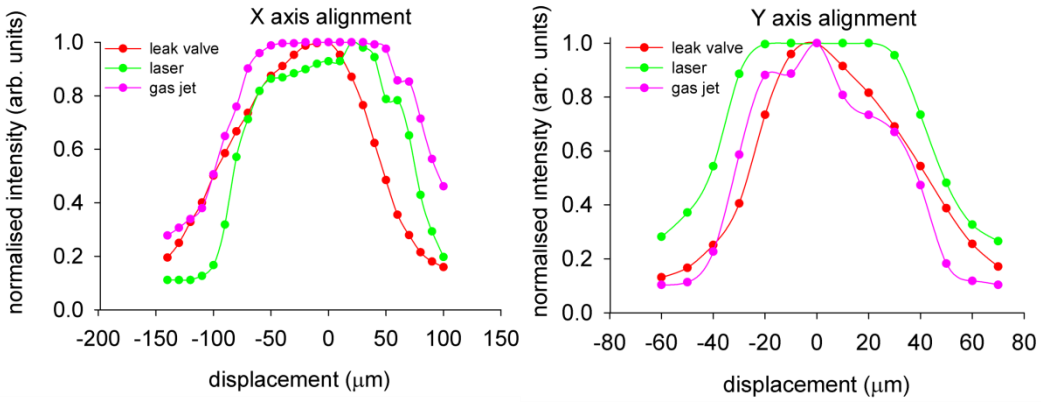

Figure 87: Normalised values from leak detector, laser beam and gas jet profile over the X (left) and Y (right) axis displacement.

3.7.2 Background pressure dependence on gas jet operation

The dependence of the pressure at three locations in the setup namely the gas generation chamber, experimental chamber and dumping chamber on the inlet pressure was studied. The dial that controls the longitudinal displacement of the orifice and thus the orifice to skimmer distance was at the position 59 mm. The absolute orifice to skimmer distance is not precisely defined and it was not possible to measure it directly due to the setup's geometry but it is restricted to around a 2 mm. The initial pressure before firing the nitrogen jet was as follows:

- Outer jet chamber 3.25 x 10^{-8} mbar
- Experimental chamber 4.20 x 10^{-8} mbar
- Dump chamber 2.18 x 10^{-9} mbar

A high-pressure cylinder was used as a gas source. The gases used were nitrogen, argon and helium. The gas inlet pressure was varied from 1 to 11 bars by steps of 1 bar and the pressure from the gauges located at the outer jet, experimental, and dump chamber was logged. At every step, a beam profile picture was also acquired. The results of the measurements are shown in Figure 88, Figure 89 and Figure 90 for nitrogen, helium and argon, respectively.

Some small fluctuations are expected as a result of the change in the pressure differential which in turn causes minor displacements in parts of the setup. At every step of the pressure, a few seconds were allowed to pass before logging the readings from the sensors to prevent any transient phenomena affecting the measurements. There is a linear increment of the recorded pressure from all the sensors that follow the increment of the inlet pressure with the only exception being helium.

For the nitrogen case, the pressure in the outer gas chamber which has to handle large gas loads shows the biggest increment ranging from 2.37 x 10^{-6} to 1.75x 10^{-5} mbar. The

experimental chamber, as the most critical area where the background pressure has to remain unaffected by the operation of the jet, changes from 4.7 x 10^{-8} mbar for 1 bar inlet pressure to the maximum of 5.4 x 10^{-8} mbar for the maximum inlet pressure of 11 bars. This corresponds to a pressure rise of 12 % to 29 % with respect to pressure without gas injection

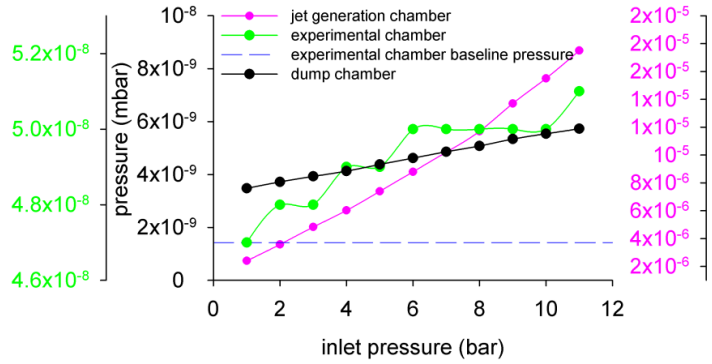

Figure 88: Pressure profiles from measurements at 3 chambers with respect to gas inlet pressure. Nitrogen gas was used. Dashed line indicates equilibrium pressure at the experimental chamber before firing the jet.

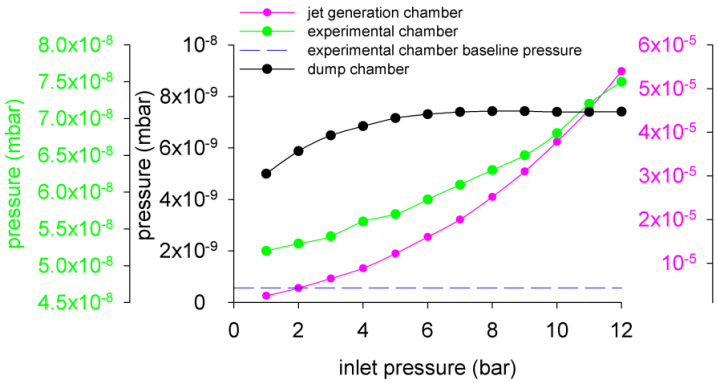

Figure 89: Pressure profiles from measurements at 3 chambers with respect to gas inlet pressure. Helium gas was used. Dashed line indicates equilibrium pressure at the experimental chamber before firing the jet.

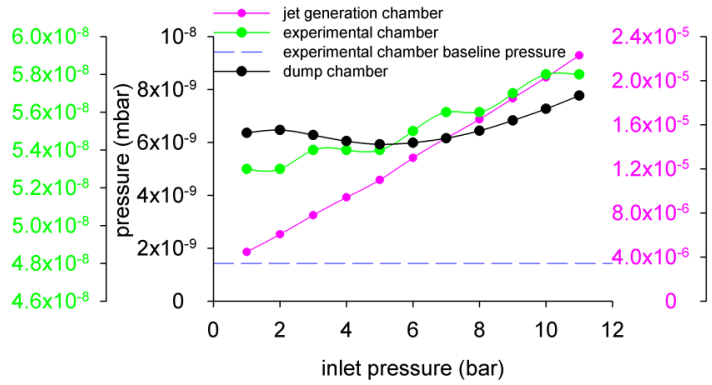

Figure 90: Pressure profiles from measurements at 3 chambers with respect to gas inlet pressure. Argon gas was used. Dashed line indicates equilibrium pressure at the experimental chamber before firing the jet.

. In Figure 91 the percentage of pressure increment with respect to the equilibrium pressure (pressure before firing the gas jet) at the interaction chamber is shown for the three gases used. Table 20 summarises the pressure changes at the experimental chamber for the three gases.

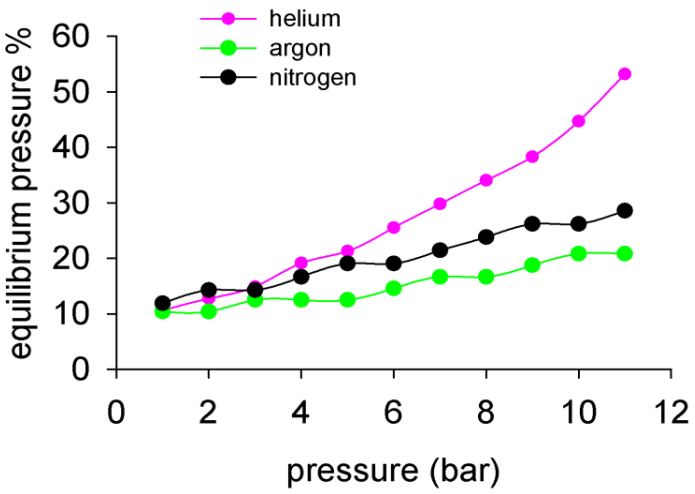

Figure 91: Change in pressure at the experimental chamber with respect to the equilibrium pressure without the gas jet. Result for nitrogen, helium and argon gas.

Table 20: Changes in pressure at the interaction chamber from minimum to maximum during gas jet operation and differences from the equilibrium pressure (before the get is fired) for nitrogen, helium and argon gas.

Gas	Min to max pressure with the gas jet (10^{-8} mbar)	Equilibrium pressure to maximum pressure (10^{-8} mbar)
Helium	1.65	2.8
Nitrogen	0.7	1.2
Argon	0.5	1

According to the TMP theoretical pumping speeds shown in Figure 92, helium is the most difficult gas to remove and thus the pressure increment is higher. The difference in pumping speeds for nitrogen and argon is much smaller and not reflected in the measurements. It must be noted that the hot filament vacuum gauges have inherently large measurement error in the order of 20% for the pressure range discussed here. This systematic error is expected to be present in every measurement and thus is not shown in the graphs. Despite the large error, some trends in the pressure evolution are clearly observed.

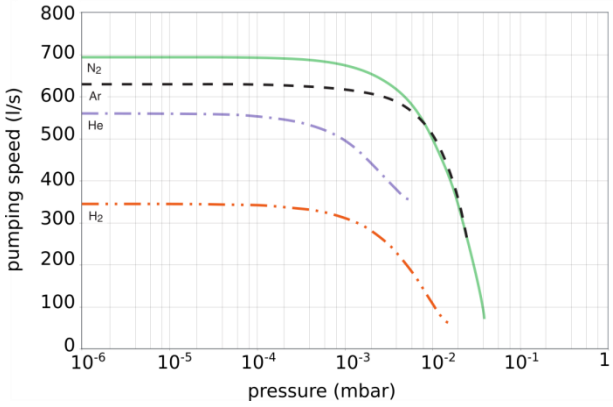

Figure 92: Theoretical pumping speed for different gases for the SL700 turbomolecular pump [148].

The use of helium in the application of the gas jet monitor in a particle accelerator is not a suitable option being so difficult to evacuate. The exact gas species can be selected only after an overall examination of the system taking into account ionisation cross section, the effect of the gas on other systems (e.g. getters) and the effective pumping speed.

3.7.3 Effect of gas curtain properties on beam profile imaging

For the following set of measurements, a 5 keV electron beam was used produced by an electron gun with an adjustable filament current (2.5 A here) focus and beam deflection from PSP vacuum. Figure 93 shows an example of the acquired particle beam profile for nitrogen. The smaller bright spot corresponds to the beam profile imaged by the gas jet and the long track corresponds to the profile imaged by the residual gas. The beam profile obtained with the gas jet appears brighter due to the higher density of the jet comparing with the residual gas. It is also much smaller because of the small velocity spread of the ultra-cold gas jet. The 2-D profile measurements apply only for the gas jet imaged profile as the residual gas imaging can offer only 1-D profile measurements. For lower background pressure it disappears leaving only the gas jet induced signal. All the acquired beam profiles were analysed offline with a dedicated Labview program. The pictures were initially stripped from the 3 colour layers resulting in grayscale images and filtered with a smoothing local average filter. Filtering is required because the beam profile occupies a width of only a few pixels and the grayscale differences from pixel to pixel can be intense resulting in a noisy profile. Furthermore, the image was rotated by about 2° to account for the camera's imperfect alignment and then a series of measurements took place. For these measurements, the system was not calibrated so the length units are expressed in pixels.

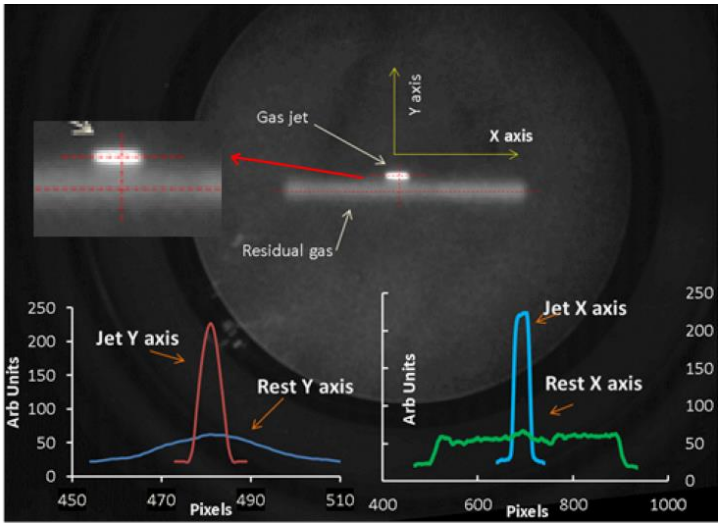

Figure 93: Example of acquired image and beam profile measurements.

The average grayscale intensity in the selected region of interest that surrounds the beam profile imaged with the gas jet is plotted against the inlet pressure in Figure 94 for two different nozzle – skimmer distances. The nozzle-skimmer distance is not very precisely known, what is known in the reading of the linear manipulator moving the nozzle towards the 1st skimmer. The actual nozzle – skimmer distance is estimated at about 2 mm for position 1 and less than 1 mm for position 2. Position 2 is the smallest attainable nozzle-skimmer distance. The intensity follows the same rising trend as the pressure readings, corresponding to the increased inlet pressure for position 1. It appears though that it saturates as it approaches the 10 bar value. The same observation has been done by Hashimoto et al for the nitrogen gas jet at J-PARC [113]. This suggests that the system reaches a maximum point for its performance with a certain set of operating conditions. For position 2 the saturation arrives much earlier revealing that there is an optimum nozzle –skimmer distance.

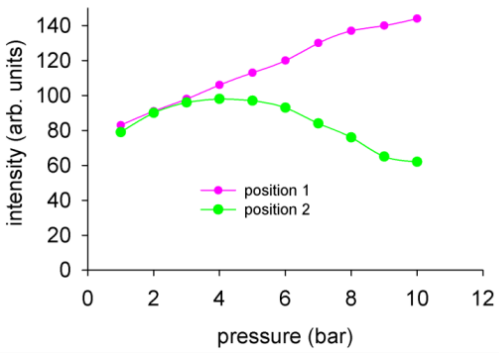

Figure 94: Average intensity of the beam profile imaged by the gas jet as recorded with the CCD camera for 2 positions of the nozzle. Position 1 is at 59 mm and position 2 at 61 mm.

Of more interest for beam diagnostics is the behaviour of the system when imaging a particle beam for a range of inlet pressures and the optimisation of the system so it can be more efficient in terms of pumping requirements. The greyscale intensity distribution of the profile relates directly to the gas density distribution and the most desired property is its good homogeneity.

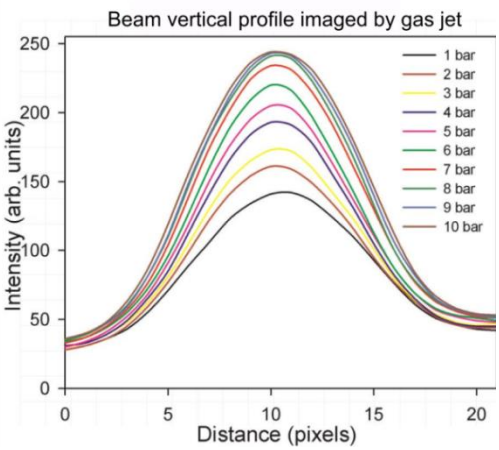

Figure 95: Beam profile imaged with the gas jet vertical (short) profile for pressures from 1 -10 bars.

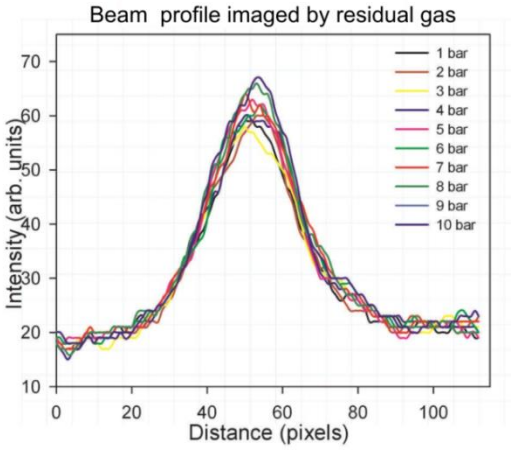

Figure 96: Beam profile imaged with the residual gas vertical (short) profile for pressures from 1 -10 bars

As it can be seen Figure 95 where the beam profile imaged by the gas jet is depicted, the profile distribution corresponds to a theoretically Gaussian beam and the intensity of the profile varies accordingly to the gas inlet pressure. The right side of the plot appears slightly elevated and the reason for this is the close distance between the gas jet profile and the residual gas profile. For a direct comparison, Figure 96 shows the residual gas profile distribution which is less affected by the gas inlet pressure. This is not a surprise as the monitor is designed to be non-disruptive to the vacuum system. This result is also suggested from the small pressure increment in the experimental chamber mentioned earlier.

One more noticeable fact is that while the pressure in the experimental chamber rises by 15 % (4.7×10^{-8} mbar to 5.4×10^{-8} mbar) for inlet pressure ranging from 1 to 10 bars, the maximum grayscale level from the residual gas acquired profile plot follows the same rise by 14 % (from 57 to 65 arbitrary units). The same is not happening though for the gas jet imaged profile as the grayscale intensity grows from around 138 to 244 or 77 % because of the gas jet higher number density compared to the residual gas.

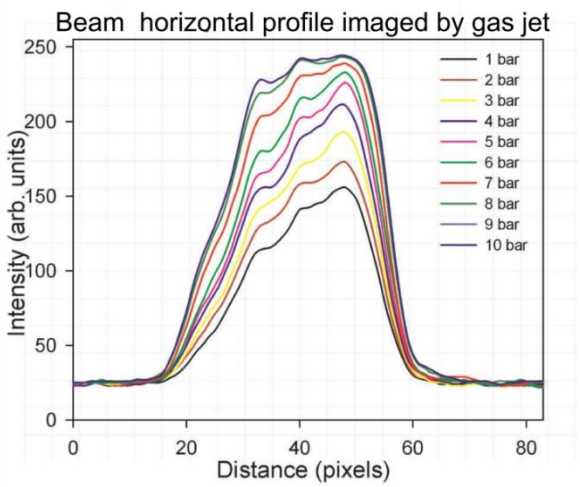

Figure 97: Beam profile imaged with the gas jet horizontal (long) profile for pressures from 1 -10 bars.

The long (horizontal) beam profile is shown in Figure 97. It does not have the expected shape but the lower left side of the profile and the bump that is present in all the pressures suggest that the alignment was not perfect. The expected shape here would not be a gaussian curve as the jet curtain size exceeds the diameter of the beam. On the contrary, it would have a flat top distribution with the sides to be similar to the short profile sides. As mentioned before, the setup is very sensitive because of the tight mechanical tolerances and small displacements can introduce errors which are very hard to identify during operation. In this case, the orifice was slightly off centred on the horizontal plane or the rectangular skimmer was not perfectly positioned causing the misshaped profile.

Figure 98 shows the electron beam profile imaged by the gas jet for a range 1-10 bar gas inlet pressures using argon, helium and nitrogen.

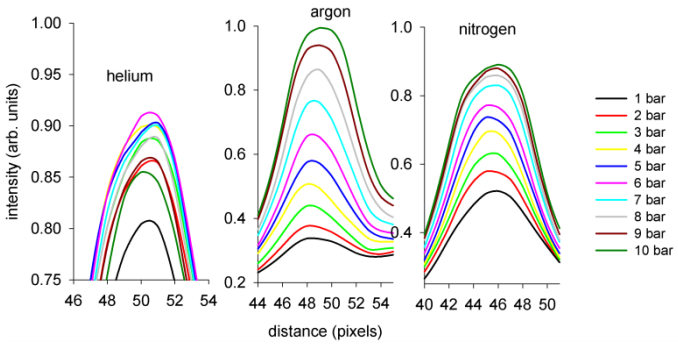

Figure 98: Beam profiles imaged by the gas jet for helium, argon and nitrogen for a range of 1-10 bar of inlet pressure.

The highest profile intensity was obtained with argon due to its higher ionisation reaction rate (see Figure 82). For argon and nitrogen higher inlet pressures lead to higher intensities in

the beam profile measurement. Helium does not follow the above trend with the highest profile intensity obtained for 6 bar inlet pressure. With helium, the highest intensity in the residual gas imaged beam profile was obtained as shown in Figure 99. Overall, nitrogen and argon resulted in the best imaged beam profiles with clear separation in the profile intensity with respect to gas inlet pressure. Background gas pressure and thus beam profile imaged by the residual gas kept at a lower level. The reduced pumping efficiency for helium renders it the least preferred gas for beam profile measurements.

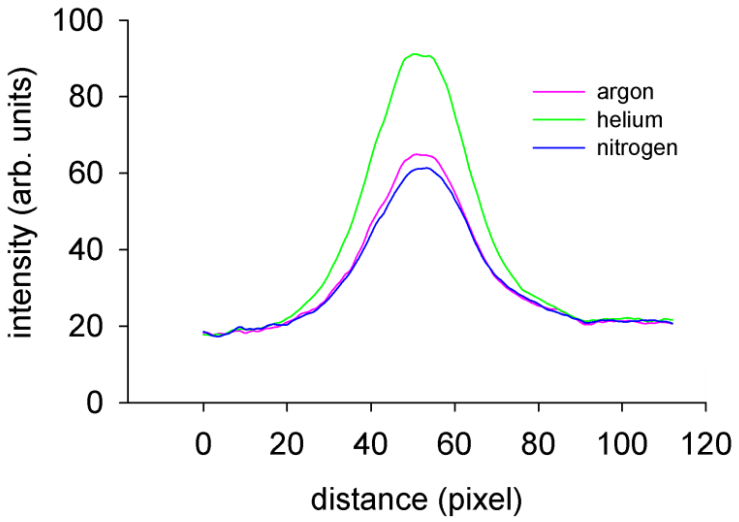

Figure 99: Intensity of the electron beam profile imaged by the residual gas for argon, nitrogen and helium.

Argon was used to estimate how nozzle–skimmer distance affects the beam profile intensity and also how the inlet pressure affects the beam profile size.

Figure 100 shows additional measurements on the intensity variation with respect to nozzle-skimmer distance variation. Clearly, as the distance increases the measured intensities drop for both 5 and 10 bar inlet pressure. For higher inlet pressure the obtained intensity starts at a higher value for the same nozzle-skimmer distance. A small perturbation appears for the case of 10 bar inlet pressure and for 1-2 mm nozzle-skimmer distance which might have occurred due to the not perfect alignment of the setup during motion. This perturbation can also be partially accounted to intensity saturation for the specific inlet pressure where if the nozzle – skimmer distance is already very small, further small variations do not affect the gas flow. After the 3 mm position, the intensity follows the expected drop.

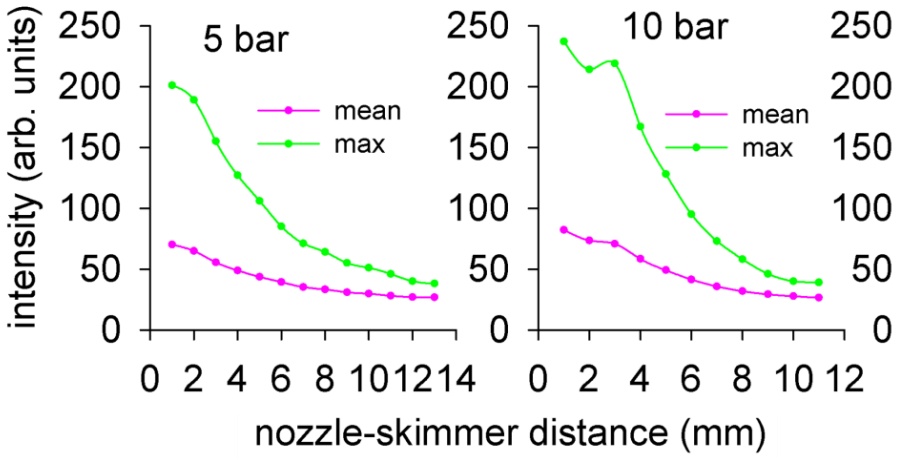

Figure 100: Variation of beam profile intensity as measured with the gas jet with respect to nozzle – skimmer distance for inlet pressure 5 and 10 bars.

Figure 101 shows the variation in profile intensity while varying the nozzle-skimmer distance from 1 – 11 mm. Here for argon, the profile intensity for different nozzle-skimmer distances is clearly seen to increase as the distance decreases.

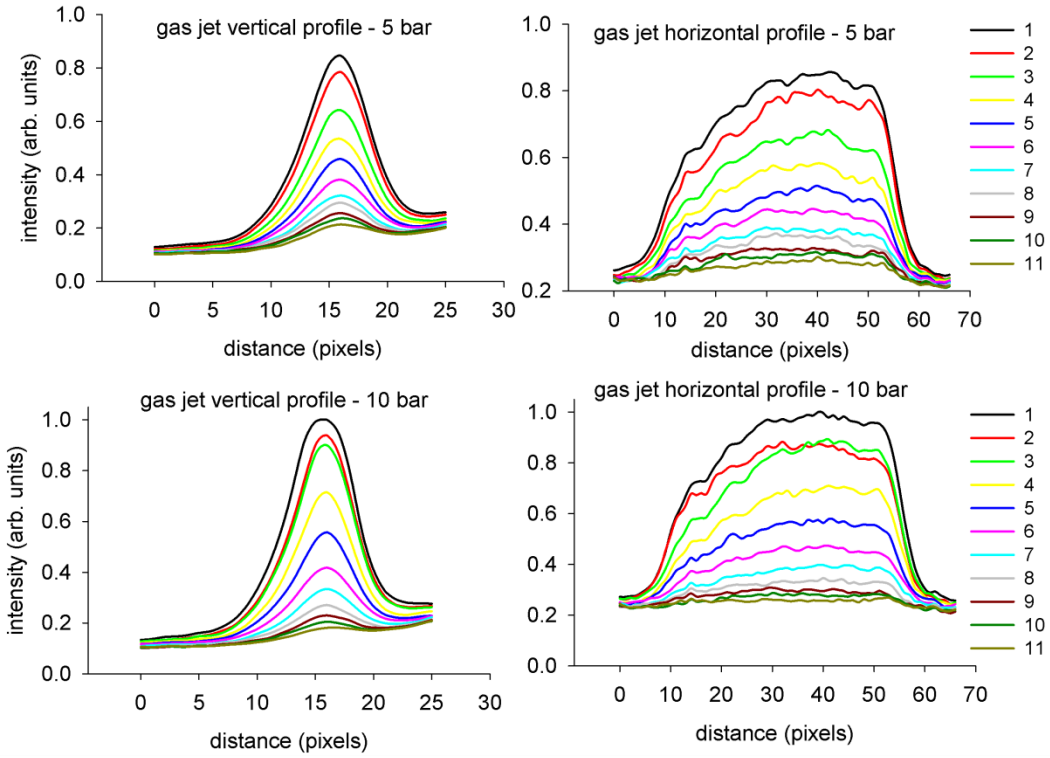

Figure 101: Beam profile intensity for argon 5 and 10 bar inlet pressure as a function of varying nozzle-skimmer distance.

To estimate how the beam profile size changes while varying the gas inlet pressure argon was chosen. Figure 102 shows the integrated beam profile imaged with the gas jet (higher peak) and residual gas (lower peak) for 1-10 bar inlet pressure.

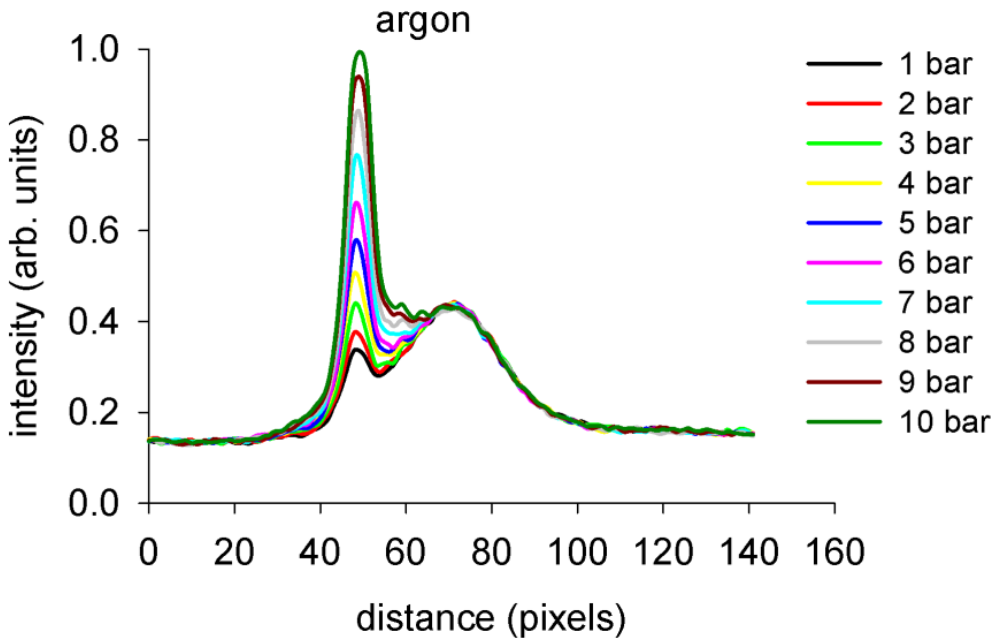

Figure 102: Integrated beam profile using argon.

A Gaussian function was fitted to the experimental data with the least squares method in Matlab. The function in the form of equation (22) is a double Gaussian plus a constant that describes to a very good extend the measured data. The parameters a_1, b_1, c_1 and a_2, b_2, c_2 corresponds to the fitting parameters for the curve describing the gas jet and residual gas imaged beam profile. The constant d is for the non-zero minimum of the experimental data.

$$y = a_1 e^{-\left(\frac{x-b_1}{c_1}\right)^2} + a_2 e^{-\left(\frac{x-b_2}{c_2}\right)^2} + d \qquad (22)$$

From the fitting parameters, the Full-Width Half-Maximum (FWHM) size of the beam profile for both residual gas and gas jet was extracted as FWHM=2.35 σ. Both sizes and the R^2 parameter are plotted against the gas inlet pressure as shown in Figure 103. The profile imaged by the residual gas tends to shrink for higher pressure. Higher pressure increases the profile intensity and the tails of the distribution appear more pronounced resulted to more reliable fitting. The gas jet imaged profile shows a small variation but is within 1 pixel which is the resolution of the measurement taking into account only the contribution from the camera.

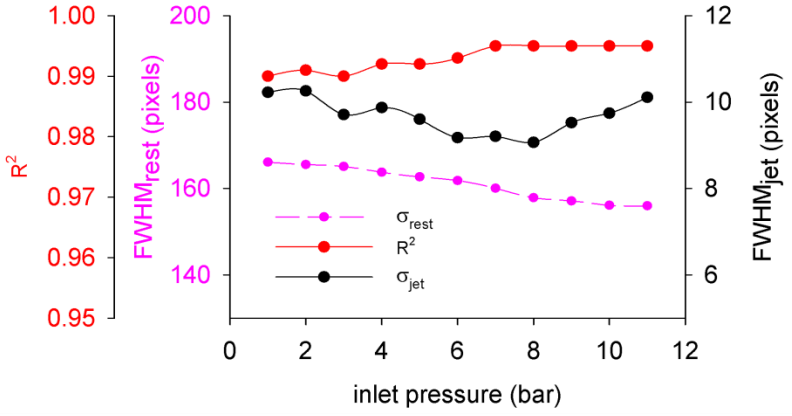

Figure 103 : Beam profile FWHM size imaged with the residual gas and gas jet for varying gas inlet pressure.

3.7.4 Performance considerations

Using one of the images acquired using argon, as shown in Figure 104, the difference in recorded intensity between the signal from the residual gas and the inlet pressure of 10 bars. As mentioned earlier, the probability of ionisation which is directly related to the signal intensity recorded on the phosphor screen depends on the ionisation cross section (σ), the gas number density (n, background gas or gas jet) and the path length in the target gas (d). This is expressed as in the following formula.

$$P_{ion} = \sigma_{ion} \cdot n_{gas} \cdot d_{gas}$$

The plot in Figure 104 shows the projection along a single line of pixels (single line profile) from the image sensor so the distance travelled by the electron beam does not make any difference for gas jet or residual gas. The probability of ionisation is assumed to be the same for both gas jet and residual gas as during the operation of the gas jet the main component of the residual gas in the vacuum chamber is expected to be the target gas, argon in this case. The only different parameter then between the gas jet and residual gas is the number density.

The density for the gas jet is estimated from equation (20) around 7×10^{15} particles/m^3 for stagnation pressure of 1 bars and 7×10^{16} particles/m^3 for the pressure of 10 bars. The number density of the background gas at a pressure of 4.2×10^{-8} mbar is around 1×10^{15} particles/m^3. These values are in good agreement with gas dynamics simulations performed by M. Putignano which are described in detail in his PhD thesis [120].

From the above considerations, it is expected that the difference in signal intensity should be more than one order of magnitude for inlet pressure of 10 bars but this could not be

experimentally verified. In the rest of this section, possible causes of this discrepancy are going to be examined.

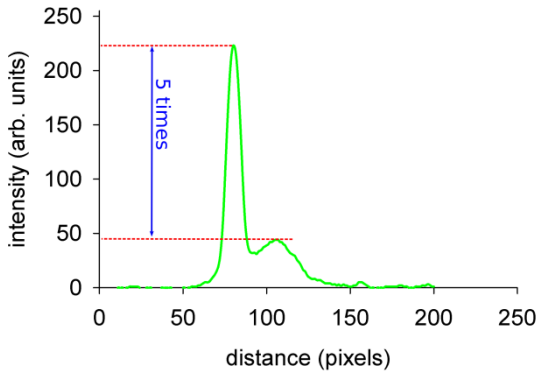

Figure 104: Beam profile imaged using nitrogen gas at 10 bar inlet pressure indicating the difference in signal intensity between the residual gas and the supersonic gas jet.

A. Departure from the ideal conditions.

In the theoretical estimation of the expected density for the gas jet, the underlying assumption relies on the ideal gas model approximation and this might not be valid. Moreover, the effects of the skimmers on the gas flow and the interactions with the chamber walls are completely ignored. In a non-ideal case, the skimmers impede the flow and scattered gas molecules from the skimmers and the walls might interfere with the flow and reduce the gas jet density.

B. Elevated background pressure

The background pressure in the interaction chamber is measured with a hot filament gauge located at one of the chamber's ports. The gauge is measuring the pressure locally but cannot provide any information on the pressure gradient inside the interaction chamber when the gas jet is operating. Even though the supersonic gas jet is composed or particles moving in their majority towards the forward direction, a few stray particles could create a "cloud" of higher pressure around the centre of the chamber. In this case, the beam profile imaged by the residual gas can appear more intense. This argument can be supported by Figure 104 where the beam profile imaged by the gas jet and also the residual gas is shown. According to the theoretical calculation for background pressure of 4.2×10^{-8} mbar and gas inlet pressure of 10 bars, the difference in signal intensity should be more than one order of magnitude in favour of the gas jet imaged beam profile. As seen in Figure 104though, the intensity of the gas jet imaged beam profile is only about 5 times higher than the one imaged by the residual gas.

C. Alignment errors

The alignment process of the setup has revealed that the three-axis moving platform deforms under evacuation and the orifice is displaced. The alignment can be corrected but only by translational movement. Any angular motion cannot be compensated by the moving stage. In order to measure angular displacement, an optical method was devised similar to the alignment monitoring method. A printed pattern consisting of an array of dots was mounted on one of the sides of the translating stage and was recorded by a camera placed on a reference point.

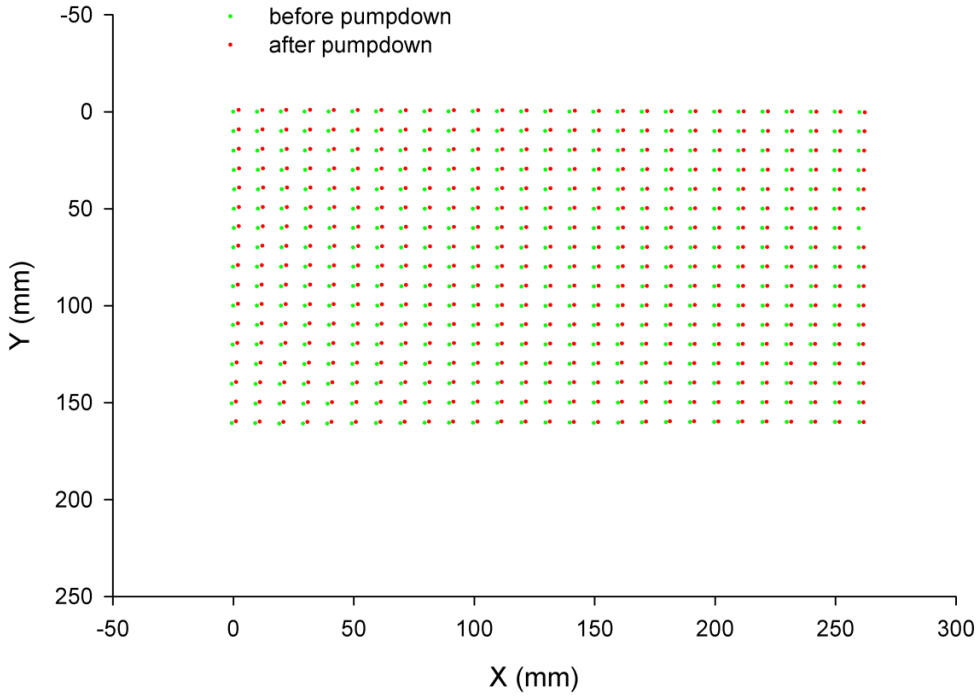

Figure 105: Dot grip position before (green) and after (red) pump-down of the gas jet setup.

Figure 105 shows the positions of the dots as imaged by the camera with green and red for before and after pump-down respectively. From the above figure, the rotation was estimated as 0.115° around the vertical axis of the stage. This means that the rotation angle affects only the vertical positioning of the orifice with respect to the rest of the setup and agrees with the findings shown in Figure 87.

Although the error in the measurement of this very small angle can be large, the value of 0.1150 will be used to further examine the effect of this angle in the gas jet density. Taking this value as a reference and for a range of nozzle to skimmer distance from 1-10 mm the vertical displacement of the gas jet centreline on the skimmer plane was calculated as shown in Figure 106. The displacement here is shown for the estimated angle of 0.115° and for a

larger angle of 0.52°. According to user experience with the gas jet setup, in order to restore the alignment after evacuation, the vertical displacement required is more than both of the cases shown here and thus the rotation angle might have been underestimated.

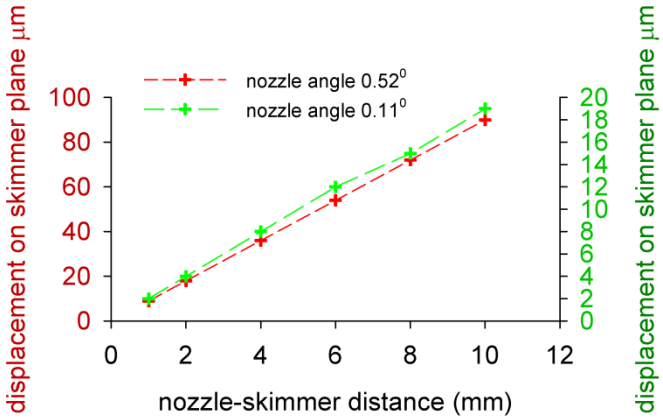

Figure 106: Calculation of vertical displacement of gas jet centreline on the skimmer place for two rotation angles.

The rotation of the system and the tilt induced to the orifice holder leads in having the centre line of the gas jet tilted along the vertical axis. This results in minimised gas transition through the series of skimmers due to a) not achieving to transmit the gas jet centreline which is the highest density portion of the jet and b) further geometrical collimation by the skimmers as areas of the gas jet off the centre line are characterised by larger angular divergence.

The flow properties of the gas jet off the centre line can be approximated by the analytical expression of equation (23) with an accuracy of ± 3% as shown by Ashkenas and Sherman [149] and further explained by H. Pauly [141]. In equation (23) *n* is the density, *x* the distance along the expansion centreline, *y* the distance off the centerline axis and φ a constant which for the case of nitrogen equals to 1.662

$$n(x,y) = n(x,0)\frac{x^2}{x^2+y^2}\cos^2\left(\frac{\pi}{2\phi}\arctan\left[\frac{y}{x}\right]\right) \qquad (23)$$

Figure 107 shows the ratio of the centre line intensity over the off-centreline intensity as a function of the distance from the centre line of three different distances from the orifice. Near the nozzle, the off-centreline intensity shows an intense reduction as a function of the distance from the expansion centreline. For larger distances from the nozzle the intensity it is less affected.

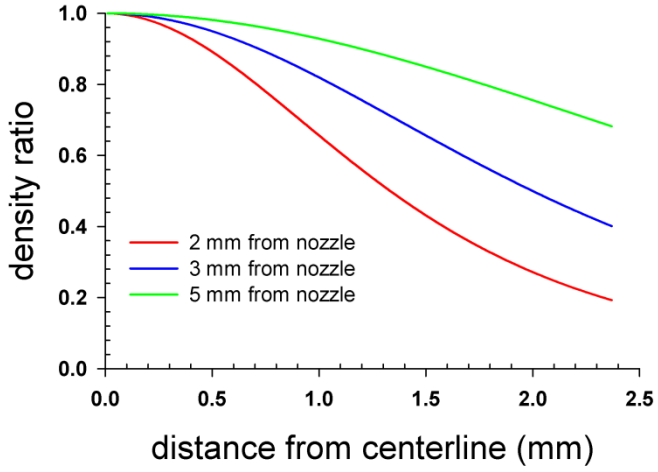

Figure 107: Ratio of the centre line over the off-centreline intensities of the gas jet as a function of the distance from the expansion centreline calculated at three different distances from the nozzle.

Despite all the efforts to maximise the gas jet induced signal and bring it closer to the theoretical predictions this has not yet been achieved. After personal communication with other laboratories working with molecular beams around the world, their obtained gas jet densities closely follow the theoretical values predicted by equation (20). From the above mentioned possible cases for the reduced intensity, case A has not been mentioned in the literature. Usually, the ideal gas model can be used to approximate to a very good agreement the measured values. Case B and C are the most prominent explanations for the reduced intensity

In order to directly measure the jet number density an accumulation detector has been designed and implemented. This detector was placed in an adjacent vacuum chamber downstream the interaction chamber and it is analysed in the next section.

3.8 Gas jet diagnostics

A. Device description

To probe the gas jet density distribution the solution of a vacuum gauge enclosed in a small accumulation chamber with a slit or pinhole aperture for the gas to enter was chosen [150]. A similar apparatus has been developed and used by Y. Hashimoto at JPARC [113]. The gauge, a Granville-Phillips Series 274 Nude, is mounted on a VACGEN Miniax XYZ 3-D translating stage [151]. The stage is moved by three steppers motors allowing motion with a resolution of 5 μm. The gauge is powered by a VG IG26 gauge controller but the collector current from the gauge is fed to an external pico-ampere meter and the voltage is observed by

an oscilloscope. A schematic of the scanning gauge is shown in Figure 108. The entire assembly is mounted on a free flange at the first dumping section 578 mm downstream the rectangular skimmer. Assuming a purely geometric expansion of the gas jet and the proved validity of the theoretical formula for the jet number density, the gas jet size and density can be calculated at the centre of the interaction chamber. Alternatively, the scanning gauge can be temporarily placed in the interaction chamber.

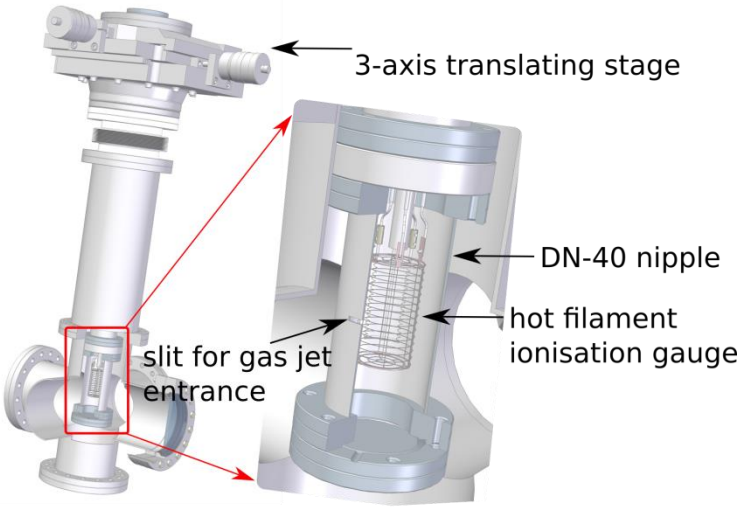

Figure 108: Scanning vacuum gauge detector for gas jet diagnostics. The main chamber including the 3-axis translating stage and the detector details are shown.

B. Detector calibration

A separate setup consisting of a small vacuum chamber and an 80 l/h TMP backed up by a 5 m^3r/h scroll pump was assembled in order to calibrate the vacuum gauge and translate the current readings to meaningful pressure measurements. The gauge was powered from the controller and the current was measured directly from the filament while the pressure in the chamber was controlled by a precision leak valve. Another reference vacuum gauge was attached to the chamber to record reference pressure values. According to the measured data shown in Figure 109 and a linear fit (red line), the conversion factor from the measured current pressure is:

$$y = 6.42 \times 10^{-5}\, x + 4.22 \times 10^{-6}$$

The lowest attainable pressure of 9.14×10^{-6} mbar in the small test chamber was not low enough to allow calibration of the gauge for the expected pressure in the gas jet setup chamber with pressure in the order of 1×10^{-9} mbar. For the full calibration of the detector, the pumping system will have to be upgraded or another leak valve must be added to the final installation chamber.

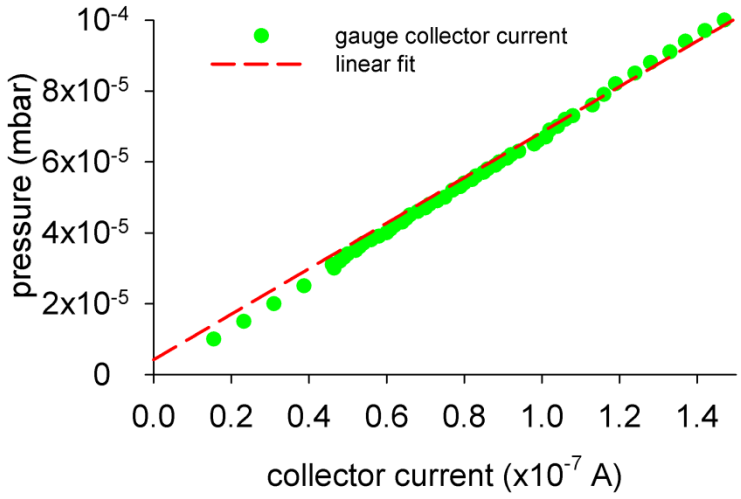

Figure 109: Calibration measurements for the scanning vacuum gauge.

C. Gas jet profile measurement

In order to measure the gas jet density, the gauge scans the area inside the vacuum chamber near the expected location of the gas jet. At every step the gas jet fires and the gauge output is read in synchronisation. The enclosure around the gauge allows for gas accumulation producing a more intense signal. The vacuum gauge was also tested in a semi-open configuration with its enclosure having the shape of half-cylinder but no measurable signal was produced. One of the serious issues of this detector is the heat generated by the filament which leads to increased pressure in the accumulation chamber giving false readings. To prevent this, the gauge is operated in carefully selected time intervals allowing time to pass between the measurements for cool-down.

During operation, the gauge is turned on and it takes about 20 s to outgas. There is a short time window of around 10 s between the initial outgassing and before the temperature rises due to the heat caused by the filament. Within this window, the pulsed valve opens for 1 s injecting gas into the chamber and the vacuum sensor is interrogated. A typical measurement and gate time for the gauge operation is shown in Figure 110. The red pulse shows the valve gate time and the other two curves show the signal measured by the gauge. The blue curve represents the signal when the jet is aligned with the accumulation chamber's slit entrance and the purple one when the gauge is out of the gas jet path rising only due to the background pressure. To estimate the jet number density (or equivalent pressure), the linear portion of the blue curve is selected and fitted with a linear function whose gradient represent the change in number density inside the accumulation tube. The pressure in Figure 110 is quoted in arbitrary units as it has not been translated to pressure units.

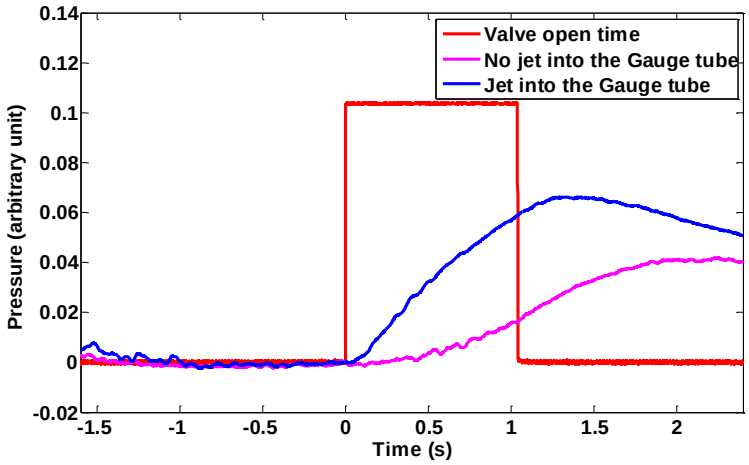

Figure 110: Snapshot of the gate time and gas jet density measured with the scanning vacuum gauge [150].

The measurement cycle then repeats until all the scanned area is covered and all the measurement points are assembled in a 2-D array as shown in Figure 111. A 2-D density distribution of the gas jet curtain profile is shown in Figure 111 by scanning an area of 12.5 x 20 mm^2. The detector in this measurement was equipped with a 10 x 0.5 mm^2 (width x height) rectangular slit which is much larger than the gas jet longitudinal size. Due to the large slit width, the horizontal axis of the gas jet profile appears much larger than it really is. As the gauge scans the area along the width of the slit the recorded number density remains constant and any change is only seen when the gas jet is intercepted by the edges of the slit. The vertical profile of the gas jet is unaffected because the slit height is much smaller than the jet height [150].

In order to estimate the gas jet profile despite the large slit a fine scan with smaller step size around the edge of the slit is required. The 2-D image is the converted to an array whose rows are differentiated element by element according to the following formula:

$$y_{i,j} = k_{i,j+1} - k_{i,j}$$

In the above formula, *i* is the index for the rows, *j* the index for columns, *k* is the array element and *y* is the newly calculated element. Figure 112 shows on the left the result of a scan with 0.125 mm step size and on the right the result from the differentiation. The size of the jet is 5.44 x 1.55 mm in full width and it is tilted by 42.9°. The nominal angle should be 45° but it can be only adjusted roughly by hand during mounting.

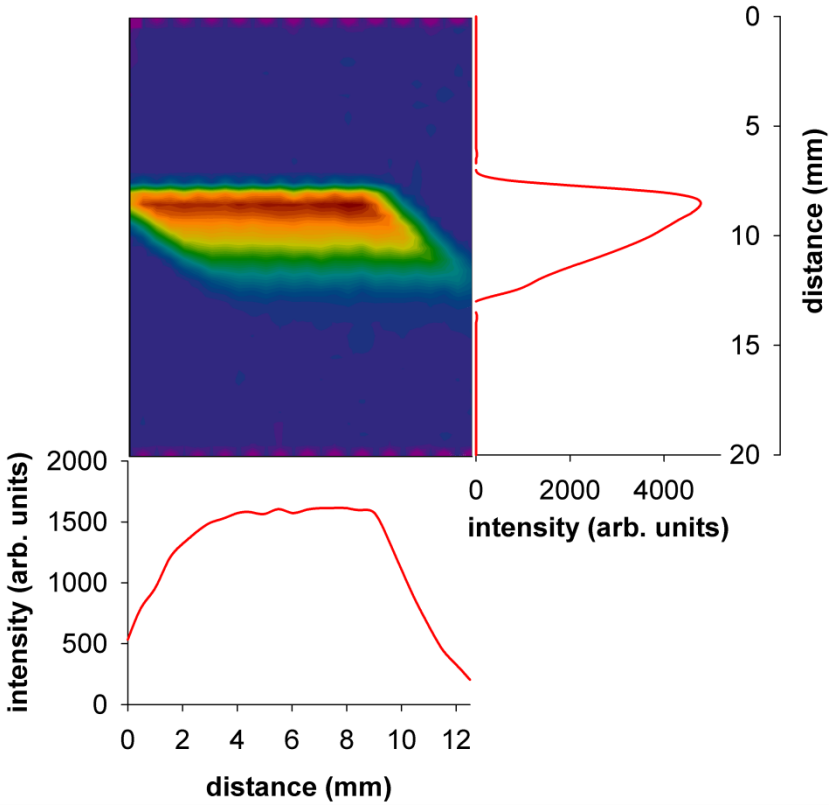

Figure 111: Gas jet transverse density distribution measured at 3 longitudinal positions along the jet propagation axis[150].

The gas jet in this measurement shown here originates from a 4 x 0.4 mm^2 rectangular skimmer its size at the measurement location was expected to be linearly scaled to the skimmer size. The measurement revealed the jet aspect ratio is not constant, with the length increasing 1.36 times (from 4 mm to 5.44 mm) and the width by 3.4 times (from 0.4 mm to 1.36 mm). Based on this aspect ratio, the gas jet size at the centre of the interaction region is estimated to 4.66 mm x 0.90 mm.

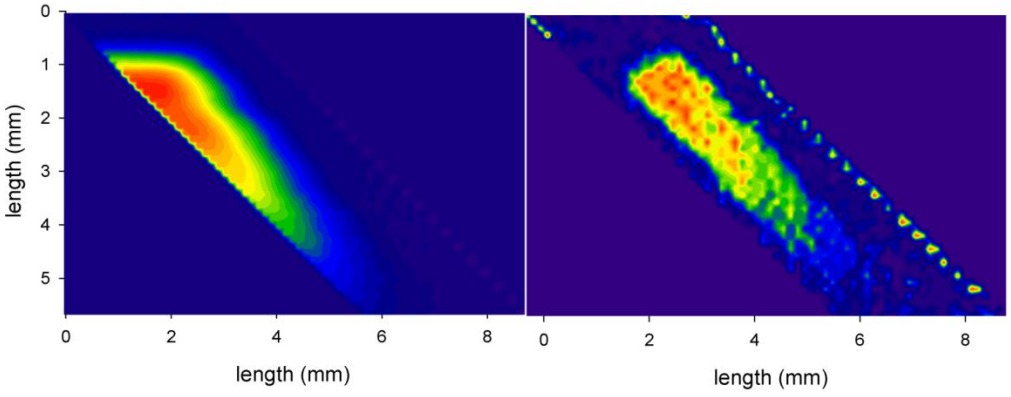

Figure 112: Edge fine scan (left) and the estimated gas jet density distribution after differentiation (right) [150].

D. Detector performance considerations

Regarding both gas jet size and density measurements with the accumulation tube, the main limiting factor is the detector sensitivity. As seen from Figure 110 the gas jet induced signal is not much higher than the background and the large slit size impedes the precise measurement of the gas jet dimensions. Using a pinhole aperture on 0.5 or 1 mm in diameter resulted in no detectable signal. Furthermore, the detector suffers from frequent vacuum leaks as the gauge is placed between two DN-40 flanges but only of them has a knife edge allowing using a copper gasket.

The limiting factor on the sensitivity is the increased internal temperature due to the hot filament and the poor pumping due to the small aperture. A solution around these limitations is to use a penning gauge instead. The penning gauge can form a similar accumulation chamber and can additionally be cooled with liquid nitrogen so the background signal is minimised. The only disadvantage of the penning gauge is the larger size because of the surrounding magnet and thus the whole scanning mechanism is currently redesigned. In order to simplify the setup and reduce oscillations due to the large mass of the moving parts, the new detector will be fixed in the chamber and the small pinhole aperture will be scanned in front of it. A similar instrument has been developed at Bergen University and has been tested with extremely small molecular beams focused with a Fresnel zone plate [152].

3.9 System resolution and beam profile measurements

This section deals mainly with the resolution of the monitor, operation in pulsed more and beam profile measurements using two different rectangular skimmer sizes. The rectangular skimmer is the last shaping element in the gas jet path and the available options include two different sizes producing a thin and a thick gas curtain. Furthermore, the camera was calibrated and the profile size was calculated in physical units (mm) instead of pixels. The planning of the experiments presented in this section and analysis of the results was done in collaboration with Dr Hao Zhang of the Quasar group. Dr Zhang carried out the measurements using the gas jet monitor test stand at the Cockcroft Institute.

3.9.1 Monitor resolution

There are 6 main components that define the final resolution of the monitor which are camera resolution, MCP resolution, image broadening due to the gas jet curtain thickness; the thermal velocity spread induced image broadening, distortion caused by the space charge of the projectile beam and nonlinear external field.

A. Camera and MCP

Out of these, the camera resolution σ_{CCD} is the one that can be easily changed by having a high-resolution camera and a suitable lens for the geometry of the detector. Currently, the camera resolution is estimated at 100 μm. The MCP resolution is defined by the channel pitch and it is difficult and costly to change. Usually, the MCP is selected at the beginning of the detector design, and as discussed previously, the contribution from the MCP is $\sigma_{MCP} = 80\ \mu$m.

B. Gas jet thickness

The next element that affects the system resolution is the gas jet screen thickness. The jet acts as a thick screen and ionisation can occur anywhere in the common volume of the particle beam and gas jet intersection. For a screen with effective thickness *d* as shown in Figure 80, the point spread function (PSF) is stretched by a factor of *d* which limits the resolution in the axis perpendicular to the jet's travelling direction or the vertical beam profile in Figure 80. The resolution along the other axis is not affected.

Using the gas jet size measurement from the previous section and its estimated size at the centre of the interaction chamber of 4.66 mm by 0.92 mm produced by the 4 x 0.4 mm^2 skimmer the measurement uncertainty due to the gas curtain thickness can be calculated from the following formula:

$$\sigma_{jet} = \frac{w_{jet}}{2\sqrt{3}\cos(\vartheta)}$$

The parameter W_{jet} equals to 0.92 mm and θ is the curtain tilt angle. Normally the tilt angle is 45° but for the measurements shown here with the smaller skimmer the tilt angle was 32°. The uncertainty is then 0.36 mm for the 45° angle and 0.31 mm for the 32°. Smaller angles reduce the uncertainty but they do not maintain the aspect ratio of the measured beam profile.

Assuming the same aspect ratio for the gas curtain produced by the larger skimmer, the size at the centre of the interaction chamber is estimated at 8.38 mm x 4.04 mm and the measurement uncertainty due to the jet thickness for the tilt angle of 45° is 1.60 mm.

C. Thermal spread and extraction field non-linearity

To determine the image broadening by the thermal velocity spread and distortion due to the external electric field, the ion collection process was simulated using the PIC code WARP [41]. Initially, a round Gaussian N_2^+ distribution was created at the interaction point with 10^6 particles representing the ionised nitrogen by the electron beam. The N_2^+ ion was assumed to

have the same velocity spread as the N_2 gas jet whose temperature was 10 K. The voltage settings for the repeller plate, top metallic ring electrode and MCP were 200 V, -1500 V and -2200 V which were similar to the normal experimental setting. An initial N_2^+ rms beam size (corresponding to the electron beam profile) was assumed to be 0.50 mm. Figure 113 shows the simulated potential of the external electric field. The equipotential lines near the MCP are dense and curved which indicates a large electric field in the z-direction and also a radial component. Figure 114 shows how the beam profile size changes during the drift process. From Figure 113, the radial component of the external field between the repeller plate and the first metal plate is insignificant. In this case, the thermal spread will dominate the drift process. As indicated in Figure 114 in the area between z = 0.0 m and 0.04 m, the slope of the beam size growth is large due to thermal spread. After entering the metal rings region from z = 0.04 m to 0.12 m, the focusing field is moderate and compensates for the effect of thermal velocity spread. Therefore, the growth of the beam profile size slows down and later it decreases slightly. In the area between the last metal ring and the MCP, because of the rapid growth of the electric potential, the radial component of the field is large enough to focus the beam counteracting and overpowering the thermal spread and space charge force. As a result, the beam size shrinks. The final size of the beam is decreased to 0.46 mm which is a combined effect from the thermal spread and the focusing from the external electric field.

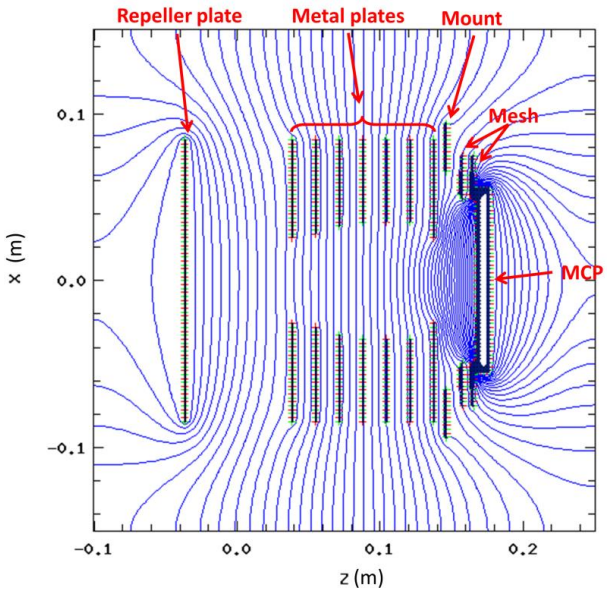

Figure 113: Electrostatic potential in z-x plane [154].

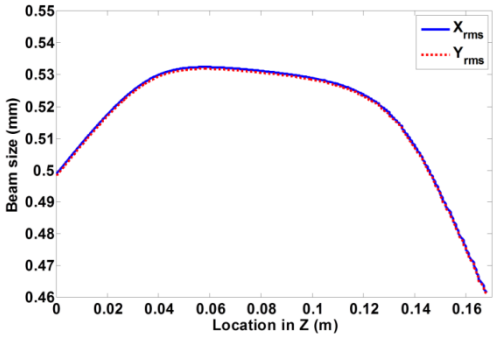

Figure 114: The change of the ion beam size when propagating to the MCP under an external electric field [154].

To further investigate this, the initial rms N_2^+ ion distribution size (ionised by the electron beam) was scanned from 0.2 mm to 1.7 mm while keeping the total number of simulated particles the same. The result of the expected ion distribution size after it reaches the MCP is shown in Figure 115. Since the external field is radially symmetric, the external focusing field will magnify or de-magnify the real beam profile size. In this sense, the formula from equation (24) can be fitted to the experimental data to describe both the focusing (or defocusing) due to the electric field and the thermal spread effect.

$$\sigma_{measured} = \sqrt{M^2 \cdot \sigma_{real}{}^2 + \sigma_{thermal}{}^2} \qquad (24)$$

M represents the magnification factor of the external field applied on the real beam profile size; σ_{thermal} is the contribution from the thermal spread. The fitted curve to this formula also shown in Figure 115 gives a magnification factor $M = 0.87$ and $\sigma_{\text{thermal}} = 0.17$ mm. The R^2 value is 1, which indicates the model is in good agreement with the simulation data. Notice that the magnification factor of M is based on the particular external field settings while the thermal spread depends on the drift time which eventually depends again on the external field setting as it directly affects the ion drift time.

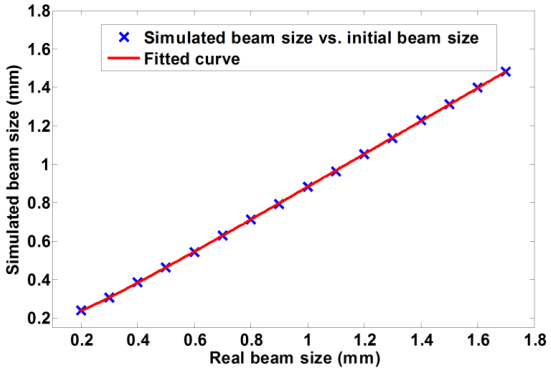

Figure 115: Image broadening by the thermal spread and radial component of the external field with varying initial beam profile size (real beam size). The curve is fitted according to equation (24) with $R^2 = 1$ [154].

D. Space charge

The last, but not the least factor affecting the resolution is the space charge induced image distortion σ_{sc} For our test stand, the current of the projectile electron beam is as low as several microamperes, so the induced space charge field is rather low compared with the external field and thus the distortion effect can be ignored. However, for other applications of this monitor, especially if it is used to detect the profile of a higher current beam, the space charge would be a key factor to consider for the resolution.

Equation (25) concludes all the contributing factors to the monitor resolution which are also summarised in Table 21 .

$$\sigma_{measured} = \sqrt{M^2 \cdot (\sigma_{real}{}^2 + \sigma_{jet}{}^2) + \sigma_{thermal}{}^2 + \sigma_{sc}{}^2 + \sigma_{MCP}{}^2 + \sigma_{CCD}{}^2} \qquad (25)$$

Table 21: Summary of the image broadening terms.

Error term	Value
σ_{jet} (small skimmer 32°)	0.31 mm
σ_{jet} (small skimmer 45°)	0.36 mm
σ_{jet} (large skimmer 45°)	0.91 mm
$\sigma_{thermal}$	0.17 mm
σ_{sc}	0
σ_{MCP}	0.08 mm
σ_{CCD}	0.1 mm
$\boldsymbol{M}$	0.87
σ_{jet} only applies to the Y axis	

3.9.2 Gas jet operation in pulsed mode

The gas-jet can operate in a pulsed mode to reduce the gas load on the vacuum system, minimise gas consumption and synchronise with the beam arrival to increase the signal to noise ratio. Figure 116 shows typical pressure curves for the different chambers of the setup in the pulsed mode operation; the blue curve represents the valve operation. In this measurement, helium gas was used with an inlet pressure of 6 bars and the valve was activated by pulses of 0.8 s period and 50% duty cycle. To measure the pressure at the differential and dumping chambers, two Bayard-Alpert type ion-gauges powered by an ion gauge controller (IONIVAC IM 540) were used. The signals from the ion-gauges (were collected and converted to a voltage by two pico-ampere meters and then recorded by the oscilloscope. As shown in purple and red in Figure 116, when the pulsed valve is open, the pressures rises both in the differential and dump chamber. After the pulsed valve closes, the pressures drops slowly approaching the initial level. Note that the pressure data has been smoothed using a moving average filter of the neighbouring 20 points, which gives a time resolution of 8 ms. Three

different experiments were carried out in order to assess the performance of the gas jet in pulsed mode and examine the effect of the non-continuous operation on the background pressure.

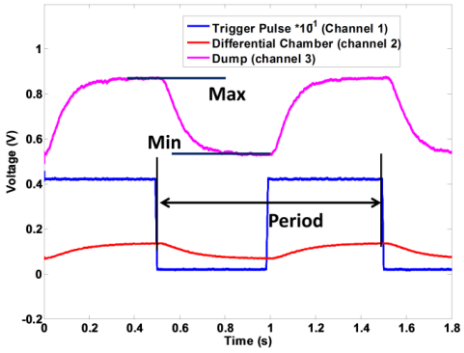

Figure 116: Time structure of the pulse valve and pressure response in the two chambers. The conversion factor between the displayed voltage (V) and the pressure in the chamber are 4.33×10-10 mbar / V for the differential chamber and 1.00 ×10-9 mbar / V for the dumping chamber. Figure provided by Hao Zhang.

The parameters of the first experiment in the pulsed mode were:

- inlet pressure 2 bar
- pulse duty cycle 50%
- pulse period from 0.1 to 2 s

Figure 117 suggests that with high-frequency pulses (short period), the pressures in both chambers reach to a state that the minimum and maximum value approach each other. With a longer period, the maximum and minimum pressures are discriminated more clearly while the system has the required time to return to higher vacuum by removing the injected gas. The transition period between the maximum and minimum pressure is about 0.8 - 0.9 s.

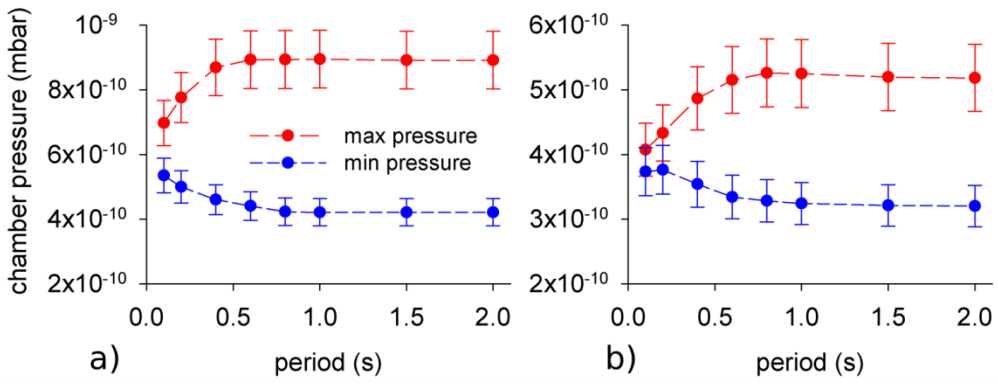

Figure 117: Plot of pressure at (a) differential chamber and (b) dump chamber versus pulse valve period. The duty cycle of the pulse valve is 50%, the pressure at pulse valve is 2 bar and helium is used.

The parameters of the second experiment were:

- inlet pressure 2 bar
- pulse duty cycle from 10% to 100%
- pulse period 1 s

The maximum and minimum pressures in both chambers are shown in Figure 118. For small duty cycles, the valve ON time is shorter than the OFF time, so the chamber has enough time to pump out the gas and restore the initial pressure as indicated by the minimum pressure that stays constant. Meanwhile, as the duty cycle increases, more gas is loaded into the chambers and the maximum pressure continues to grow within a single period. There is transition duty cycle where the vacuum cannot return to the initial condition which is about 40% - 60% corresponding to 0.4 - 0.6 s. Based on these results the differential and dump chambers will reach to the highest possible background pressure for 2 bar inlet pressure when the valve is enabled for about half a second and it also requires the same time to return to the initial pressure where the initial pressure is considered the pressure before the gas jet operates.

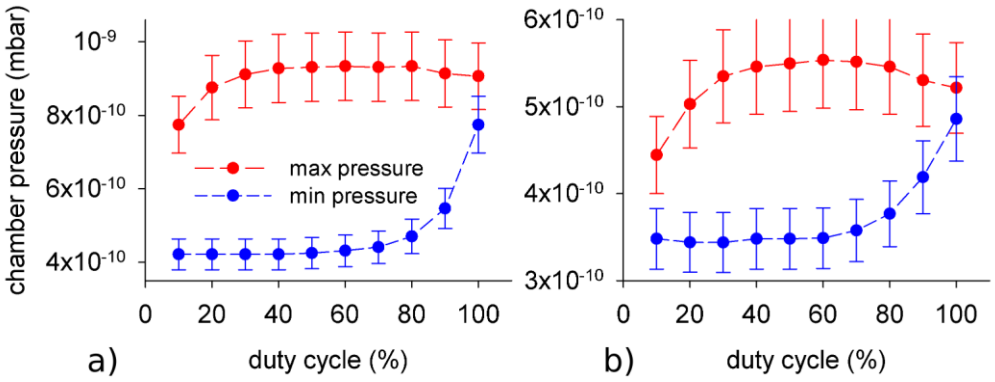

Figure 118: Plot of pressure at (a) differential chamber and (b) dump chamber versus the pulse valve duty cycle; the period of the pulse valve is 1 s, the pressure at pulse valve is 2 bar and helium is used.

The parameters of the third experiment were:

- variable inlet pressure
- 50% duty cycle
- pulse period 1 s

As shown in Figure 119, the maximum pressure in both chambers is linearly proportional to the inlet pressure. Meanwhile, the valve OFF time is enough for the pressure to return to

the initial level, which means that the minimum value for each case in both chambers remains approximately constant.

These results show a characteristic time of about half a second for the pressure to be restored to the initial value after each cycle of the gas-jet. The maximum pressures inside both the differential and dump chambers scale quite linearly with the inlet gas pressure. They also suggest that by synchronising the camera with the pulsed and setting a proper shutter time, the signal ratio between the supersonic gas jet and the residual gas can be at least doubled.

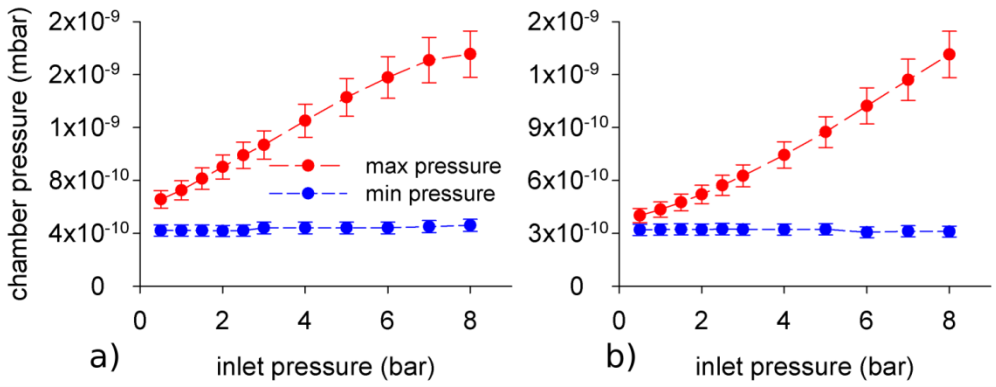

Figure 119: Plot of pressure at (a) differential chamber and (b) dump chamber versus inlet pressure; 1s period, 50% duty cycle, variable helium pressure.

3.9.3 Electron beam profile measurements

During the measurements which are presented in this section, the stagnation pressure was at 5 bars , filament current and the electron gun voltage was set at around 2.40 - 2.60 A and 3.5 - 4.0 kV respectively. Two different skimmer size were used, a large one of 7.2 x 1.8 $mm^2$and a smaller of 4 x 0.4 mm^2. Comparing the previous measurements presented in section 3.4, for the measurements shown here the camera system was calibrated and the system resolution can be estimated after having analysed all the contributing factors. For the current setup, the electron beam in the interaction chamber will travel only 400 mm until it reaches the flange on the other side of the chamber. Reflected electrons or secondaries from this will travel back to the interaction area, interact with the residual gas and create a flat background noise. For this reason, we usually decide to keep the filament current at the moderate value mentioned above in order to obtain a better signal to noise ratio. For a longer beam pipe in an actual beam line where there will be few object to stop or reflect the electron beam in the vicinity of the interaction area, and the noise from this will be negligible. Another parameter that is taken into account and is valid only for the experimental test stand is that the projectile electron beam from the gun is deflected by the external field. The deflection angle

depends on the electron energy and the electric field between the repeller plate and the bottom ring electrode. In order to let the electron beam collide with the gas-jet, we need to change the dipole setting of the gun, the voltage of the metallic plate and the bottom ring electrode as well as the electron energy. By tweaking these four parameters, we can also reduce some of the reflected electrons into the metallic electrodes region and thus reduce the background noise. The voltage applied to the MCP can be allowed to stay at a higher value unless the image is saturated. The camera was mounted at around 11 cm away from the top viewport.

A. Large skimmer (7.2 × 1.8 mm^2)

The image shown in Figure 120 (a) was acquired when the larger third skimmer (7.2 × 1.8 mm^2) was installed. The voltage setting for the repeller plate, top metallic ring electrode, MCP and phosphor screen were 200 V, -1500 V, -2200 V, 3000 V. The electric field gradient was about 7.5 kV/m between the repeller plate and the bottom ring electrode as calculated from the simulation. The electron gun settings were 2.40 A for filament current and 3.75 keV for electron energy. Nitrogen gas was used in this experiment. The residual gas induced signal (elongated line across x-axis) is also visible in the figure due to the high surrounding pressure about 10^{-8} mbar. The separation between the gas jet induced signal and the residual gas induced signal is a result of the high initial velocity of the gas jet as expected.

For the calibration of the image, the known dimension of the phosphor screen on top of the MCP of 75.0 mm was used. This length translates to 900 pixels in the image and gives the calibration factor as 12.0 pixels/mm. In case the camera is moved or repositioned at a different location, the calibration needs to be performed again. A region of interest (ROI) was chosen as indicated in Figure 120 (a) with the dotted black line for the data analysis. Figure 120 (b) shows the X-projection of the ROI and the fitted curve is the sum of two Gaussian functions plus a constant. The constant is required to account for the background. Similarly, Figure 120 (c) shows the Y-projection of the ROI highlighted by the black dotted line but here only one Gaussian function is fitted plus a constant. The fitting from the projected profiles result to a spot size of $\sigma_{x\_jet} = 0.37 \pm 0.01$ mm, $\sigma_{y\_jet} = 1.21 \pm 0.09$ mm for the gas jet image and $\sigma_{x\_res} = 1.05 \pm 0.05$ mm for the residual gas image. The error quoted here is the statistical error of the fit with a 95% confidence bound.

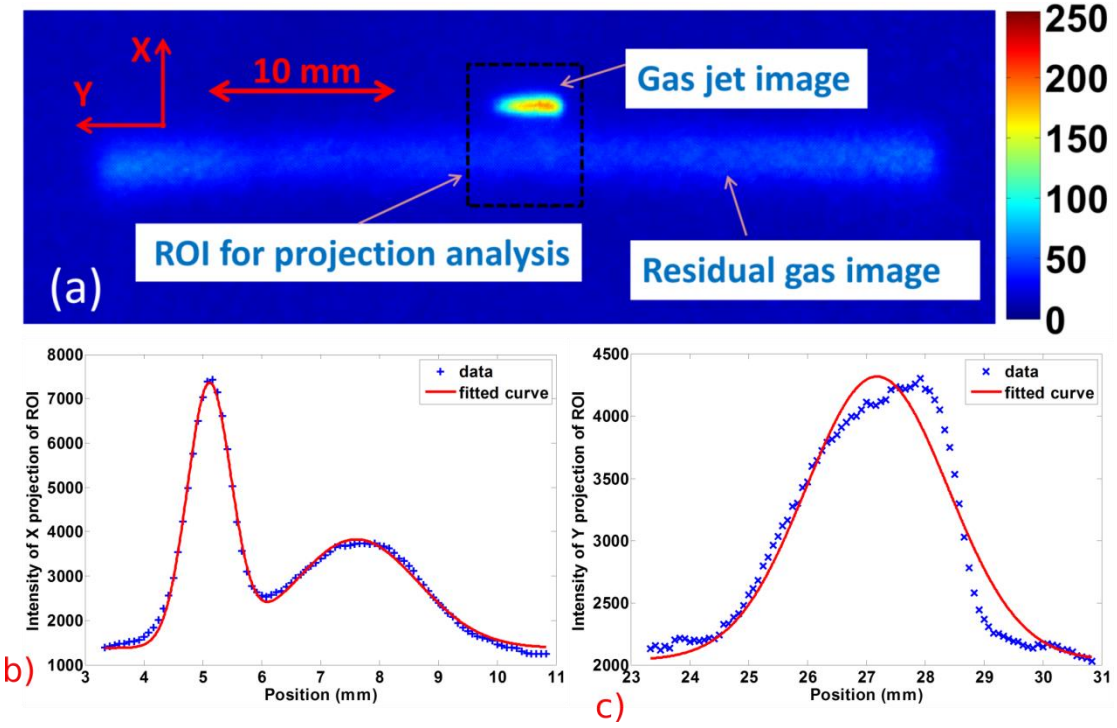

Figure 120: (a) Images of electron beam measured from both gas jet (larger size third skimmer) and residual gas; Projected profiles (b) in x-direction and (c) in y-direction (Electron beam energy is 3.75 keV, external collecting E-field is 7.5 kV/m, the gas pulse duration time is 1s and the exposure time of the camera is 70 ms). Figure provided by Hao Zhang.

Re-arranging equation(24) to directly calculate the real size beam profile size for the X axis and also including the MCP and camera error will result in:

$$\sigma_{x\_real} = \sqrt{\frac{\sigma^2_{measured} - \sigma^2_{thermal} - \sigma^2_{MCP} - \sigma^2_{CCD}}{M^2}} \qquad (26)$$

The real size in X axis is $\sigma_{x\_real} = 0.38$ mm.

The measurement resolution in X axis will be improved with a new camera and a lens with a field of view matched for the application. The position and mounting of the camera are of high importance also as they can introduce measurement errors.

In Y axis, an additional error is contributed to the thickness of the jet. As discussed earlier, this was estimated as $\sigma_{jet} = 1.63$ mm. Equation (25) is re-arranged as previously done for the X axis beam profile size resulting in:

$$\sigma_{y\_real} = \sqrt{\frac{\sigma^2_{measured} - \sigma^2_{thermal} - \sigma^2_{MCP} - \sigma^2_{CCD} - M^2\sigma^2_{jet}}{M^2}} \qquad (27)$$

If the calculated value of σ_{jet} from Table 21is used in the above formula then the quantity in the square root becomes negative. This indicates that the assumption of the same geometric scaling for the jet produced by the small and large skimmer is not valid. The jet produced by the large skimmer must be expanding less on the short dimension (width).

B. Small skimmer (4 × 0.4 mm$^{2)}$

By using the smaller 3rd skimmer (4 × 0.4 mm^2) the resolution in Y axis is expected to improve by producing a thinner gas curtain. The skimmer orientation angle was set to be 32˚. After the change of the third skimmer, to the smaller one, the electron beam was slightly re-tuned and thus it cannot be directly compared to the previous measurement. In order to compensate for the reduced brightness which is a result of the thinner gas curtain leading to smaller ion production, the electron gun was set at 2.6 A filament current and 3.5 keV electron beam energy. The voltage settings for the repeller plate, top metallic ring plate, MCP and phosphor screen were 300 V, -1300 V,- 2100 V and 3000 V respectively. The corresponding electrostatic gradient between the repeller plate and the bottom ring electrode was about 8.0 kV/m. The resulting image is shown in Figure 121 (a). Compared to Figure 120, the increased filament current is not enough to compensate for the intensity reduction due to the smaller skimmer. It increases the intensity of the residual gas image and the background noise. In a real beamline application with much lower vacuum pressure and no interference from scattered or reflected electrons, this noise will be greatly reduced. It has to be noted here that a good synchronisation with the pulsed valve and a sensitive camera can also improve the image quality because the intensity of the gas jet induced signal rises much faster than the one of the ionised residual gas.

For this measurement and the new camera position, the phosphor screen on top of the MCP was 825 pixels in diameter. This gives a calibration factor 11.0 pixels / mm. Again an ROI was used as indicated in Figure 121 (a) with the black dashed line to analyse the measured profiles. Figure 121 (b) and (c) shows the X-projection and Y-projection of the ROI region, and the curves are fitted the same way as for the larger skimmer case. The fitting results to a beam size σ_{x_jet} = 0.54 ± 0.02 mm, σ_{y_jet} = 0.56 ± 0.03 mm for the gas jet image and σ_{x_res} = 1.34 ± 0.02 mm for the residual gas image. Similarly, from equation (26), the beam size in X axis is σ_{x_real} = 0.57 mm.

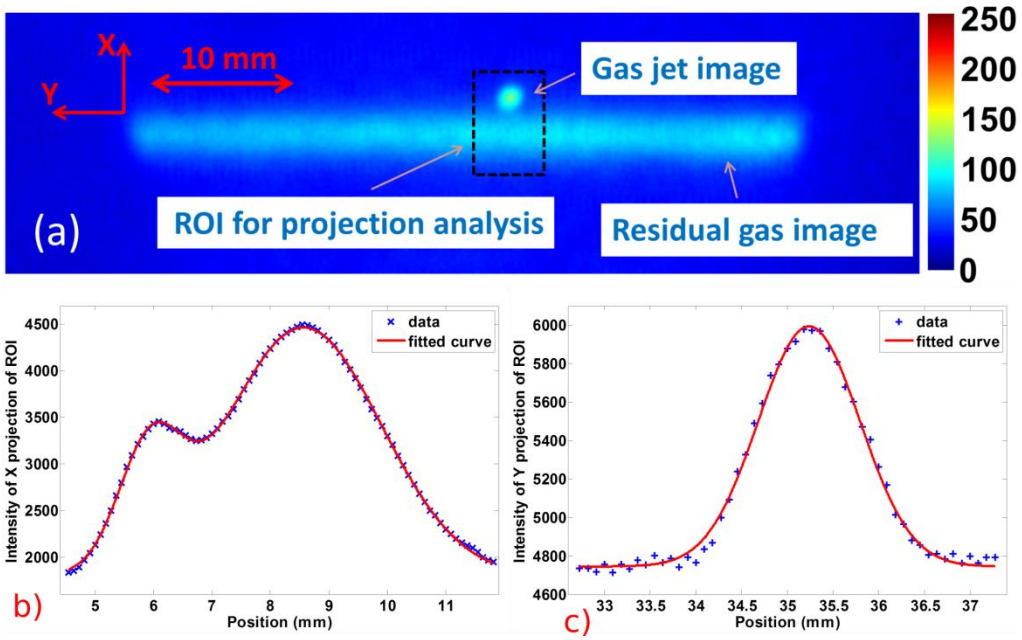

Figure 121: Images of the electron beam profile from both gas jet and residual gas; Projected profiles (b) in x-direction and (c) in y-direction (Electron beam energy is 3.5 keV, external collecting E-field is 8.0 kV/m, the gas pulse duration time is 1s and the exposure time of the camera is 120 ms in the mid of the pulse) [154].

For the Y-axis, taking into account the jet thickness which is 0.31 mm and the thermal spread contribution of 0.17 mm, according to equation (27) the beam size will be σ_{y_real} = 0.51 mm. It is clear that the difference between the $\sigma_{y,\,real}$ and the σ_{y_jet} is very small but cannot be directly compared against the large skimmer. Generally, smaller 3rd skimmer size affects less the measurement resolution in y-axis due to the smaller gas jet thickness. However, the reduction of the jet thickness decreases the reaction rate and then a longer integration time might be required. For every application, the skimmer size must be carefully chosen based on both the acquisition time and the overall resolution requirements. The results of the beam profile estimation for both large and small skimmer are summarised in Table 22.

Table 22: Summary of the beam profile measurements for both large and small skimmer.

Term	Value
Large skimmer (7.2 × 1.8 mm2)	
σ_{x_real}	0.38 mm
σ_{y_real}	Not found
Small skimmer (4 × 0.4 mm2)	
σ_{x_real}	0.57 mm
σ_{y_real}	0.51 mm

3.9.4 Resolution and profile estimation considerations

As summarised in Table 22 the measurement of the electron beam profile using the small skimmer resulted in an almost round beam while for the large skimmer the final resolution along the Y-axis was not possible to calculate. It is also noticeable that there is a significant discrepancy between σ_{x_real} measured with the large and small skimmer. The main sources of error are the camera setup and the accumulation detector.

A. Camera setup error

The currently used camera setup can be dramatically improved and become more suitable for the application. The apparent contribution to the system resolution is the σ_{CCD}=0.1 mm which accounts for much less than the gas jet thickness. Another important factor is that it also affects the σ_{jet} and $\sigma_{measured}$ estimations adding another 0.1 mm for each. On a more practical approach, the image of the beam profile covers only a few pixels on the camera sensor and thus it is hard to decide where exactly the measured beam profile starts and ends. To solve this issue a new camera and lens are planned to be purchased and mounted on the MCP flange. A high-resolution camera equipped with a lens with high enough magnification will allow spreading the beam profile image across a large number of pixels (at least one order of magnitude higher) minimising the readout error and the overall contribution in σ_{jet} and $\sigma_{measured}$.

In addition to the camera, a more proper calibration method using a grid or an array of dots will assist in more precise pixel to millimetre conversion and also in eliminating any imaging errors of the lens.

B. Accumulation detector error

The main source or error and discrepancies currently is the scanning ionisation detector. A number of issues with this device include poor repeatability of the measurements, low sensitivity, slow operation, small pressure variation in the main chamber due to the heat of the filament and others. This detector was initially conceived and assembled with the aim to provide qualitative results and provide a first approximation of the gas jet curtain size and density. Although it's successful operation has been confirmed by Yoshinori Hashimoto at J-PARC, that specific setup is based on a much higher intensity gas jet which requires more than three times the pumping speed of the Cockcroft Institute setup. For the case of the gas jet setup developed at the Cockcroft Institute, the accumulation detector needs to be upgraded.

The next design of the accumulation detector is based on a penning gauge as mentioned earlier which will provide much higher sensitivity and thus reduce the measurement errors in mainly the gas jet number density estimation and also the jet size estimation

C. Lack of alternative methods to verify the electron beam profile size

In the current configuration of the system, there is no available precise method to measure the electron beam profile at the centre of the interaction chamber and directly compare against the gas jet beam profile image. There is a small phosphor screen that can be extended to reach the centre of the chamber and imaged by another external camera but this option cannot offer high-resolution measurements without upgrading the camera and the lens. After these are upgraded and a careful calibration is performed, a very precise method to benchmark the gas jet monitor performance will be available.

3.10 Chapter summary

This chapter presented work done at the Cockcroft Institute covering non-invasive beam profile measurements based on a supersonic gas jet. The challenges were to operate the monitor in the gas jet mode (instead of only residual gas mode), solve the alignment challenges and characterise it in terms of vacuum performance and measurement resolution.

In order to achieve these goals the experimental setup was upgraded with alignment instrumentation and a method to monitor the alignment during pump down was developed. The loss of alignment after the evacuation of the chamber was one of the main factors that did not allow earlier success in operating the gas jet monitor. After accumulating enough operational experience the alignment was obtained very quickly.

With the alignment issue solved, the first experimental beam profile measurements were obtained using both the residual gas and the gas jet for direct comparison. The beam profile imaged by the gas jet is characterised by higher intensity and improved resolution comparing the residual gas due to the very little thermal motion and high intensity of the gas jet curtain

Further investigation in the vacuum gas dynamics allowed characterising the setup in terms of vacuum performance and verifying that the background pressure in the experimental chamber varies very little while the gas jet is in operation verifying the very good directionality of the gas curtain and its suitability for high vacuum environments.

It was found that operating parameters such as inlet pressure and nozzle-skimmer distance and gas species have a direct effect on the beam profile measurement intensity and background pressure. Higher than 9-10 bar inlet pressure of nitrogen seems to saturate the system and the same stands for nozzle-skimmer distance less than 2 millimetres. The gas species affect less the measured signal intensity and more the background pressure, for example, helium is difficult to evacuate and also to ionise leading to reduced signal intensity and elevated

background pressure. Nitrogen and argon can be removed from the system more easily by the turbomolecular pumps.

A performance issue relevant to vacuum dynamics is the reduced gas jet number density compared to the theoretical estimation and values obtained by other experiments. The most probable reasons for the intensity loss are the elevated background pressure around the gas jet and some remaining alignment issues. These issues become important after considering the very small apertures the gas jet propagates through and the even smaller acceptance angles.

An accumulation detector based on a hot filament ionisation gauge enclosed in s small accumulation chamber with a slit for the gas jet entrance was developed. The purpose was to mount this detector on a moving stage and scan the gas jet probing its density and measuring its size. The detector development resulted in very encouraging results but soon its limitations were impeding further progress. Main limiting factors are the low sensitivity and the slow scanning speed. It takes several hours to perform a complete scan of the gas jet curtain. A second iteration of the accumulation detector is currently undergoing including a cold cathode gauge which could be potentially cooled with liquid nitrogen to further minimise the background signal. Instead of scanning the whole detector, in the new version, it will be stationary and a small metal plate with a pinhole aperture will be scanned.

The last objective was to calibrate the imaging system for measuring an electron beam profile and also estimate the resolution. All the factors contributing to the monitor resolution were analysed and taken into account in the profile size estimation. The most dominant error sources are the poor camera resolution which has multiple affects the overall resolution and the gas jet thickness. The camera will soon be updated with a high-resolution sensor and a zoom lens. The gas jet thickness is a direct consequence of the rectangular skimmer size. The two available rectangular skimmer sizes were tested producing a thin and a thick gas jet curtain. The gas jet thickness affects the resolution only on the Y-axis profile. This results from the uncertainty on where exactly the ionisation events take place along the path length of the charged particles through the gas jet curtain The thin curtain estimated the beam profile including all the error sources as 57 mm in the X-axis and 51 mm in rms on the Y-axis (almost round beam). The thick skimmer estimated only the X-axis profile including all the error sources as 0.35 mm in rms while with Y-axis profile was only estimated by the direct measurement without including errors as 1.21 mm in rms.

Factors contributing to poor measurement resolution include the camera system as mentioned earlier which can be updated, the gas jet thickness which can be controlled and gas jet direct measurement from the accumulation detector which is under redesign and upgrade.

4. Conclusions and outlook

4.1 Thesis summary

The primary objective of the work carried out in the scope of this PhD thesis was to develop transverse beam diagnostics for electron and ion beams. The first part of this thesis was a review on diagnostics methods for beam profile, beam emittance and beam current measurements.

In Chapter 2 the application of a real-time pepperpot based emittance monitor was investigated for application at RIKEN's 18 GHz ECR ion source along with required modifications to increase the beam current. By redesigning the extraction geometry of the ion source and changing the position of the existing Einzel lens the oxygen beam current almost doubled. For the development of the emittance monitor, extensive experimental studies on various scintillators were carried out resulting in selecting SiO_2 as suitable only for proton beams and KBR (potassium bromide) coating on glass for heavier beams up to krypton. The common problem with scintillating screens experienced by multiple users is the quick degradation when under irradiation which is more intense when using low energy heavy ion beams. An MCP was also tested and its superior performance was confirmed against all the screens except the KBR coating which performed equally well. At the end of the chapter, emittance measurements were presented and the correlation between beam emittance and other operating parameters such as beam current, extraction voltage, acceleration gap and ECR magnetic field. The main influencing parameter on the beam emittance was found to be the beam current which tends to increase the emittance mainly in the horizontal plane. This happens possibly due to beam collimation at the vertical plane which does not allow the beam size to further increase.

Chapter 3 presented work done on non-invasive beam profile measurements based on a supersonic gas jet at the Cockcroft institute. The main challenges consisted of solving the alignment issues and operate the gas jet monitor. After careful initial alignment and development of an online alignment monitoring method, the gas jet setup was successfully commissioned and the first results were obtained. Further experiments included investigations into vacuum gas dynamics and the effect of the gas jet parameters on the beam profile imaging. Some considerations regarding the lower than expected signal intensity were discussed and solutions were investigated. An accumulation detector was developed to directly probe the gas jet and characterise it in terms of number density and size but resulted on only rough estimation of the size and no estimation yet of the number density. A new prototype detector is currently

designed to improve upon the first prototype. Finally, electron beam profile measurements were presented using an electron beam at the Cockcroft Institute test stand. These measurements helped to estimate the monitor resolution and identify areas for future improvements.

4.2 Outlook

4.2.1 Emittance monitor outlook

The emittance meter developed for RIKEN is planned to be used for further beam studies, benchmark against simulations and overall to better understand beam production from the ECR ion source. Currently, the 18 GHz ECR ion source provides beams to experiments but also doubles as a test stand for the next 28 GHz ECR ion source which will be completed in 2018.

The monitor is undergoing another iteration which will improve the accuracy by upgrading the moving mechanism. The upgraded monitor will feature larger pepperpot to screen image which will allow resolving better overlapping beamspots from tightly focused beams and investigate deeper the effect of the solenoid magnet in beam emittance

The emittance meter development led also to collaboration with the accelerator group of Sumitomo Heavy Industries (SHI) in Japan for developing a prototype to measure high current proton beams. Another collaboration has been developed with the Institute of Modern Physics in China aiming to test scintillating screens and develop an emittance monitor based on RIKEN's device for heavy ion beams.

4.2.2 Gas jet monitor outlook

The gas jet monitor test stand at the Cockcroft Institute is undergoing improvements at the moment mainly focused on increasing the gas jet intensity by using a higher pressure pulsed valve and developing a new accumulation detector. The recent result from the gas jet operation attracted interest from CERN for the diagnostics of the hollow electron lens system that is under development as part of the high luminosity upgrade of the LHC [155]. In this setup, a 1.1 A and 7 TeV proton beam will propagate through a hollow electron beam of 5 A and 10 keV enclosed by a 4 T magnetic field. In these conditions, ion extraction is impossible so the solution of beam induced fluorescence is investigated. Towards this purpose, the Cockcroft Institute in collaborations with GSI and CERN has taken the challenge to build another gas jet monitor optimised for this specific environment. The existing gas jet test stand had been

modified with the addition of a black chamber to minimise the scattered light and an intensified CCD camera which can detect single photons

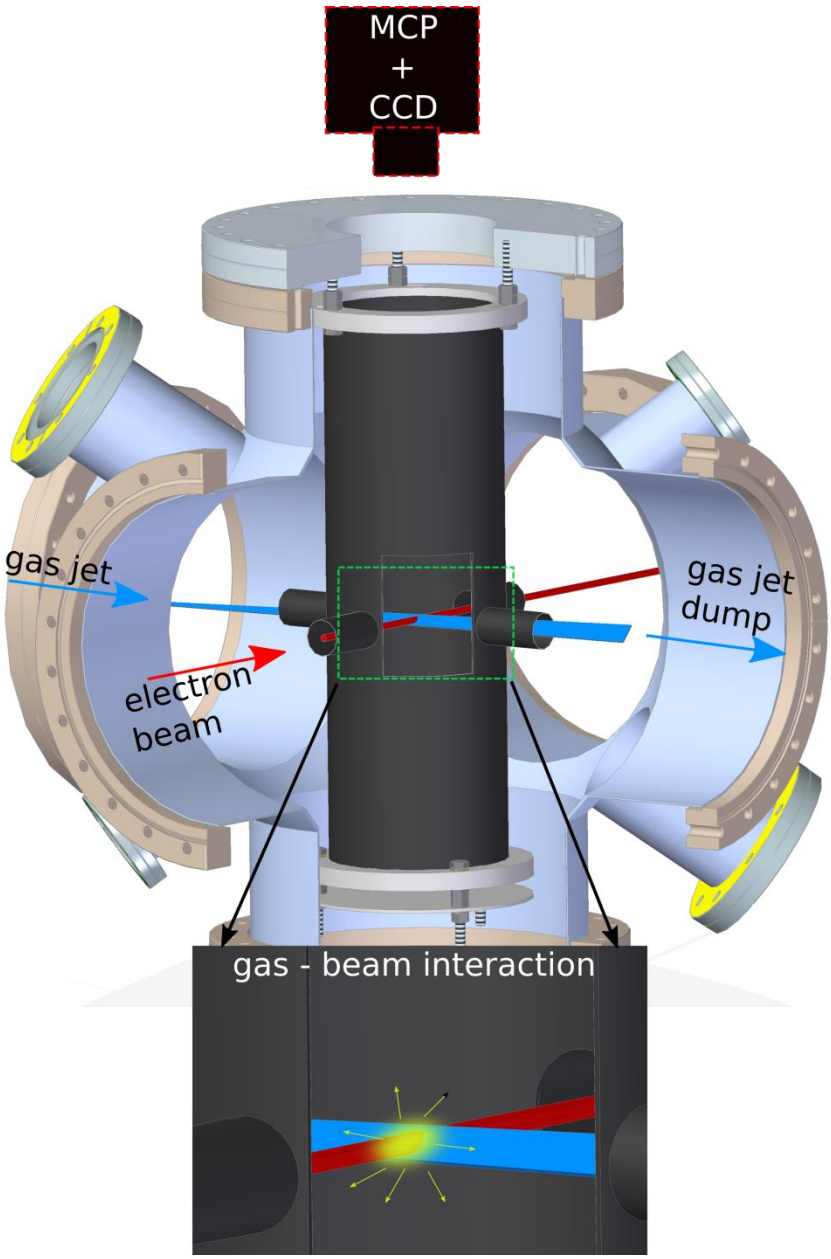

Figure 122: Schematic of the experimental setup to investigate the BIF mode at the Cockcroft Institute. A blackened chamber has been inserted into the gas jet experimental chamber with apertures for the gas jet and electron beam passage.

The first and very encouraging experimental results have already been obtained and the design of the next prototype has been already agreed between all the partners.

Appendices

A. Magnetic Field Measurement Apparatus

The ECR magnetic field measurement is based on a Hall-effect sensor that is inserted into the plasma chamber of the ion source and scanned longitudinally or rotated to measure the axial and radial magnetic field respectively.

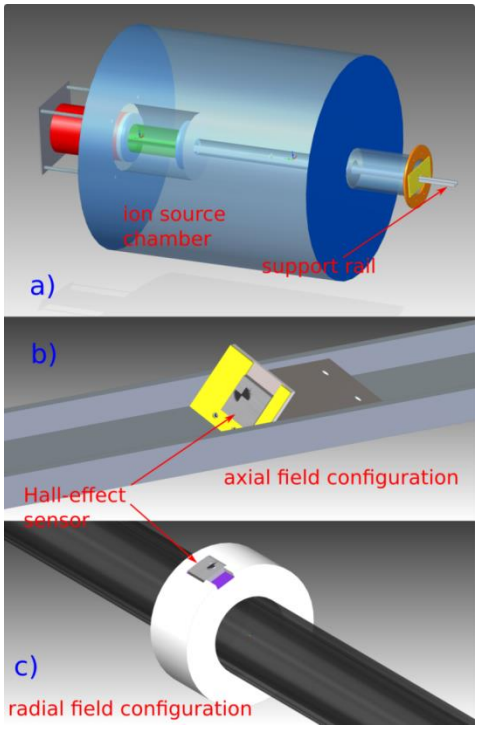

Figure 123: a) ion source chamber with the support rail for the Hall-effect sensor, b) configuration for the axial field measurement where the probe is scanned longitudinally, c) configuration for the radial field measurement where the probe is rotated.

For the axial magnetic field measurement, the probe was mounted on an aluminium cart as shown in Figure 123 b sliding along aluminium U-shape profile in the ion source. Magnetic field measurements were registered every 1 cm.

For the radial field, the probe was attached to the surface of an acrylic hollow cylinder with a diameter 0.5 cm smaller than the diameter of the ion source chamber. A plastic tube was then inserted into the hollow cylinder and the whole assembly was placed in the ion source chamber. Measurements here were logged while rotating the sensor.

B. Gas Jet Alignment instrumentation

The alignment of the nozzle – skimmer system is a very delicate task given the very small nozzle's diameter and the very tight tolerances. The most crucial part is the nozzle- 1st skimmer alignment as they have the smallest dimensions in the system. The initial manual alignment requires a laser beam to be shined through the nozzle and all the skimmers.

The misalignment of the setup has been a problem for a long period of time. Even if initial alignment was correct it has been observed that it was not maintained during the operation. This led to the assumption that elements might move during pump down.

For the continuous monitoring and any corrections required, 2 High Definition (HD) cameras are used .The signal is then fed to an edge detection algorithm in NI Labview software. Similar techniques are used in machine vision applications and robotics [156]

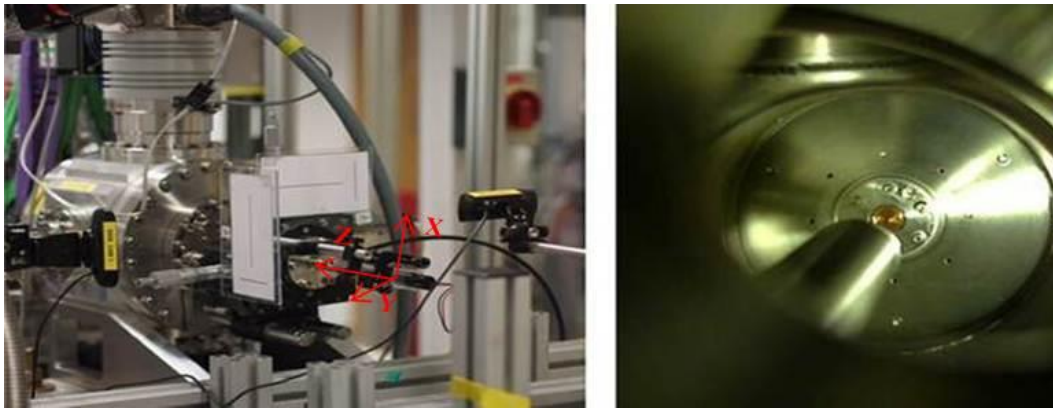

Figure 124: Left: translating stage with 2 cameras for X and Y plane, right: image from the interior of the first vacuum chamber, nozzle's tube and first skimmer can be seen [122].

Observations

It has been observed that when the pressure in the vacuum chamber drops, the alignment is lost. Measurements of pressure profiles in the different parts of the setup indicated that there might be problems related to parts of the setup moving during pump down. For this purpose, a dedicated movement detection system had to be installed to provide qualitative and quantitative information about the observed displacements.

The main source of the above-mentioned displacements is probably mechanical tolerances of the translating stage that support the gas inlet tube see Figure 124 left. They appear when the pressure in the chamber is lower than the atmospheric pressure. When the translating stages moves along the Z axis, in order to change the distance between the nozzle and the 1st skimmer,

small displacements occur along the X and Y axis. The source is again the mechanical tolerances of the stage.

Methodology

In the current application, the most important considerations are the accuracy requirements due to the small nozzle - skimmers dimensions. It is also very important to identify good measurement spots, have detection in different directions simultaneously, acquire and analyse information quickly.

The movement detection system consists of 2 HD Logitech C902. They are top of the line web cameras operating at 2592 x 1944 resolution and 8-bit colour depth. They are equipped with a high-quality lens with 20 steps manual or auto focus. The cameras come with a USB 2 connection that makes their control an easy task. For the edge detection algorithm, a pattern with high contrast gradient is required. After experimentations with various combinations of shapes, a pattern consisting or 2 perpendicular black lines of known dimensions printed on a white paper was selected.

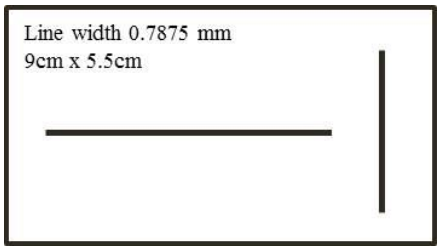

Figure 125: Pattern consisting of two black lines [122].

Two of those patterns were placed on the two faces of the translation stage for displacements on X and Y plane, respectively see Figure 125. The cameras were fixed opposite of the patterns at a distance of 20 cm see Figure 124 left.

National Instruments (NI) Labview was chosen as it offers drivers for a great range of cameras, friendly environment and it can be integrated into the overall gas jet control system. The proposed solution consists of an image processing algorithm based on pattern recognition and edge detection. In Figure 126 the software's flowchart is depicted.

The inherent parallelism of data flow programming makes the National Instruments Labview graphical development environment ideal for parallel execution. Taking this into account, the algorithm runs in two parallel loops for both cameras in real time Initially the Region of Interest around each line has to be selected manually and also the edge detection parameters have to be set.

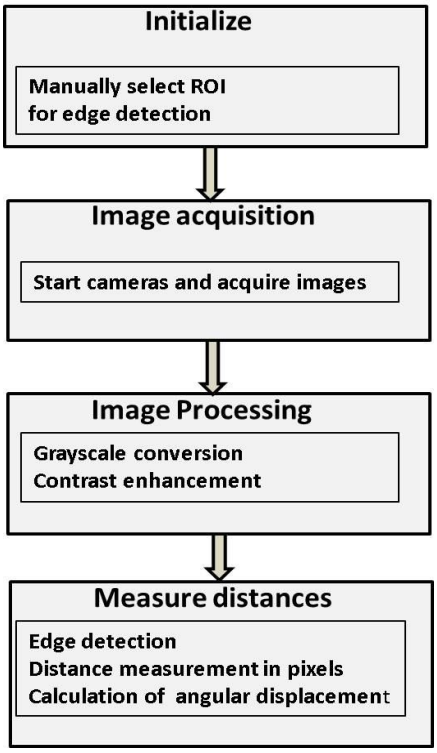

Figure 126: Labview algorithm flowchart [122].

Algorithm description

After the images are acquired a single colour plane is extracted and a smoothing low-pass filter is applied. The edge detection algorithm scans the Region of Interest (ROI) vertically and horizontally along a group of 9 path lines until it detects the set of 2 lines as shown in Figure 127. The distance from the edge of the ROI until the first point on the detected line is measured by Labview. The most important are the central points which will give the average linear displacement from the edge of the ROI and the 2 corner ones which are used to calculate the angular displacement.

The end user interface consists of a table with the vertical and horizontal displacements for X and Y plane from each camera. The angular displacements are in the order of 1° and they are considered negligible.

The algorithm takes the initial position when alignment is achieved as reference. After any displacement occurs the new position is subtracted from the reference position giving the difference in pixels. All distances remain in pixels as there is no interest for the actual displacement but only for recovering the initial position. When this difference is zero it means that the initial position is restored. As the algorithm runs in real-time, the user can recover the reference position with the translator's dials to minimise the difference.

For the proof of operation of the algorithm, a high power laser was shined through the aligned nozzle – skimmer system and imaged by a camera from the other side. The algorithm recorded this position as the reference position and with the laser turned off a random displacement on X and Y plane was introduced. Using the dials and consulting the readings the initial position was restored. When the laser turned on, the bright spot appeared again on the camera at the end of the pipeline.

Initial alignment

For the apparatus to operate properly a very precise alignment is required. The same 2 cameras are also used in this step but they are placed in different locations. The alignment starts with the last skimmer which is the closest to the interaction area and has to be tilted at 45°. All skimmers are mounted on disks which are fixed with screws on specific locations in the vacuum chamber minimising any motion. The second and first conical skimmers with diameters of 400 and 180μm, respectively, are also manually fixed in position. The following step is to shine a laser through all skimmers and detect the light at the other side with a camera. In a further step, the intensity is then maximised while moving slightly the skimmers with fine manipulation of the disks. After a few iterations very good alignment can be achieved. It was found that the most critical part of this procedure it to align the nozzle.

The nozzle is mounted on a hollow aluminium cylinder of 2 mm internal diameter and 30 cm length. In a separate setup, with the nozzle's tube removed from the main setup, a laser is shined through it and light is detected using a web camera right after the nozzle. By observing the image which has to match the pattern of diffraction through a circular aperture, the shape and the condition of the aperture can be examined. If the aperture is blocked or it is not perfectly circular the diffraction pattern is affected as in Fig.5 upper row. Because of the small diameter of the aperture, the light that reaches the other side is minimal so the camera needs to operate in high saturation and high gain mode.

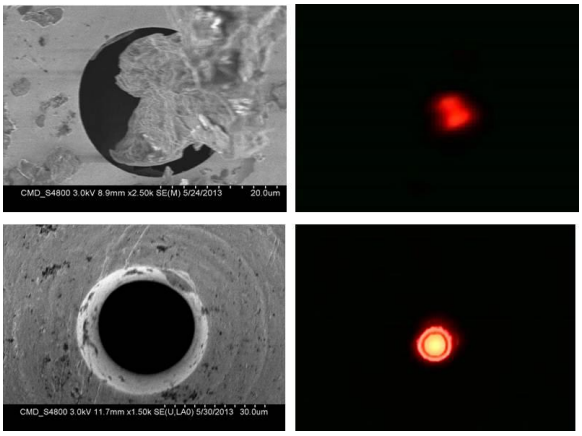

Figure 127: upper row: orifice blocked, lower row: orifice is proper [122].

With the aperture tube mounted on the setup and the laser in operation, two cameras are required for the final alignment. The first camera observes the interior of the first vacuum chamber, see Figure 124 right .The second one is placed after the dumping session imaging the light that reaches the end.

Using the first camera and the translating stage that holds the aperture's tube, the light is directed on the first conical skimmer. Looking at the video stream from the second camera while trying to find the maximum intensity and after very fine manipulation of the translation stage, the aperture is aligned with the skimmers.

The gas jet setup was modified to allow a laser to be shined along the gas expansion path while the chamber is evacuated see. This can verify that the movement detection algorithm is tracking any displacement as there is a camera permanently positioned after the dump session imaging the laser beam. It is composed of a T-connector that leads to the gas tank from the one side and to a glass viewport via a safety valve from the other side see Figure 128.

Figure 128: Gas jet modification to allow including an alignment laser [122]

C. Ion beam current measurement apparatus

At the time this work was undertaken there was no diagnostics to allow for measuring the ion beam current directly after the ion source. Geometry constraints did not allow for insertable devices such as scintillating screens and Faraday cups. A device that will allow for a beam current measurement has been designed and semi-assembled waiting to be used after the next ion source maintenance. It is based on a movable segmented metallic plate with rings of different diameters. This will allow measuring beam current and correlate with varying Einzel lens voltages and other operating parameters. A schematic of the current meter is shown in Figure 129.

The ring segments are machined on a high-temperature circuit board material commercially available as HITT plate fabricated by DENKA. This material is similar to common FR4 circuit boards but it features a thick aluminium back-plate that allows withstanding higher beam power without needing external cooling. The second benefit of using the HITT material is again related to the aluminium backplane. The ring segments are made by milling the front surface of the board but in this case, the milling depth reaches up to the aluminium layer. The front copper layer and the rear aluminium layer are electrically isolated with a non-conductive material. The front surface is then used for current measurements and the rear can be biased to a suitable voltage to assist in compensation of the secondary electron emission. The device can be inserted in the Einzel lens and the movable plate allows scanning a distance of around 15 cm and measure beam current. Every metallic ring is isolated from the others and has an individual readout. The signals can be driven outside of the vacuum chamber by a multi-pin instrumentation feedthrough and directly fed to an array of current meters or current to voltage converters.

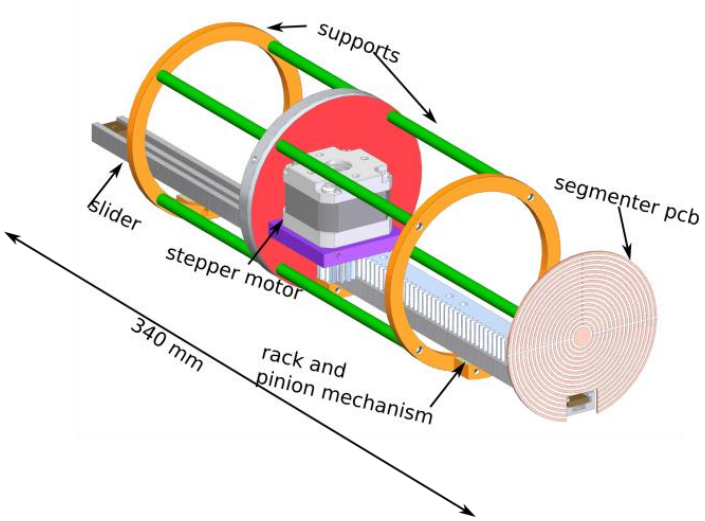

Figure 129: Proposed instrument to measure directly beam current after the extraction

The proposed device will be able to measure beam current and beam size assuming round beams. The resolution in beam size measurement in restricted by the pitch of the concentric rings related to the manufacturing limits. The beam current can be approximated by summing the signal on all the electrodes. The beam size can be estimated by counting how many electrodes read beam current induced signals and by the known spacing between them.

References

[1] H. Koziol, “Beam diagnostics for accelerators,” *CAS - Cern Accel. Sch. Basic Course Gen. Accel. Phys.*, pp. 1–44, 2005.

[2] U. Raich and C. A. B. Bdi, “Beam Diagnostics,” *Cern Accel. Sch.*, 2005.

[3] P. Forck, “Lecture Notes on Beam Instrumentation and Diagnostics,” *Jt. Univ. Accel. Sch.*, pp. 0–152, 2011.

[4] P. Forck, “Measurement of Beam Current,” in *JUAS*, 2016.

[5] U. Ratzinger, “Commissioning of the new GSI high current linac and HIF related RF linac aspects,” *Nucl. Instruments Methods Phys. Res. Sect. A Accel. Spectrometers, Detect. Assoc. Equip.*, vol. 464, no. 1–3, pp. 636–645, May 2001.

[6] E. Bravin, E. D. Cantero, A. G. Sosa, C. G. Ch, and C. P. Welsch, “Optimization of a Short Faraday Cup for Low-Energy Ions using Numerical Simulations,” in *IBIC*, 2014, no. September.

[7] J. Harasimowicz and C. Welsch, “Faraday Cup for Low-energy, Low-intensity Beam Measurements at the USR,” in *Proceedings of BIW10, Santa Fe, New Mexico, US*, 2010, pp. 4–6.

[8] D. Belver *et al.*, “DESIGN AND MEASUREMENTS OF A TEST STAND FOR THE SEM-GRID SYSTEM OF THE ESS-BILBAO,” in *IPAC*, 2012, pp. 867–869.

[9] P. Strehl, *Beam Instrumentation and Diagnostics*. Berlin/Heidelberg: Springer-Verlag, 2006.

[10] S. Burger, C. Carli, M. Ludwig, K. Priestnall, and U. Raich, “THE PS BOOSTER FAST WIRE SCANNER,” in *DIPAC 2003*, 2003.

[11] T. Giacomini, P. Forck, D. Liakin, J. Dietrich, and G. Villiers, “Ionization profile monitors - IPM @ GSI,” in *DIPAC*, 2011, pp. 419–421.

[12] J. Mießner, M. Sachwitz, M. Markert, R. Sternberger, K. Tiedtke, and a. Hofmann, “An Ionization Profile Monitor for the determination of the FLASH photon beam parameter,” *Nucl. Instruments Methods Phys. Res. Sect. A Accel. Spectrometers, Detect. Assoc. Equip.*, vol. 635, no. 1, pp. S104–S107, Apr. 2011.

[13] T. Tsang, D. Gassner, and M. Minty, “Residual gas fluorescence monitor for relativistic heavy ions at RHIC,” *Phys. Rev. Spec. Top. - Accel. Beams*, vol. 16, no. 10, p. 102802, Oct. 2013.

[14] D. a. Bartkoski, C. Deibele, and Y. Polsky, “Design of an ionization profile monitor for the SNS accumulator ring,” *Nucl. Instruments Methods Phys. Res. Sect. A Accel. Spectrometers, Detect. Assoc. Equip.*, vol. 767, pp. 379–384, 2014.

[15] P. Forck, “Minimal Invasive Beam Profile Monitors for High Intense Hadron Beams,” in *IPAC 2010 Contributions to the Proceedings*, 2010, pp. 1261–1265.

[16] F. Becker and C. Andre, “Beam Induced Fluorescence (BIF) Monitor for Intense Heavy Ion Beams,” *BIW2008, Lake …*, pp. 236–240, 2008.

[17] F. Becker *et al.*, “Beam Induced Fluorescence - Profile Monitoring for Targets and Transport,” *Proc. HB2012, Beijing, China*, pp. 586–590, 2012.

[18] M. Putignano, K.-U. Kühnel, C.-D. Schröter, and C. P. Welsch, “A fast, low perturbation ionization beam profile monitor based on a gas-jet curtain for the ultra low energy storage ring,” *Hyperfine Interact.*, vol. 194, no. 1–3, pp. 189–193, Aug. 2009.

[19] A. Wolski, “Linear beam Dynamics for Accelerators,” 2012. [Online]. Available: https://www.cockcroft.ac.uk/archives/course/linear-beam-dynamics-for-accelerators.

[20] C. Agritellis, R. Chasman, and T. J. M. Sluyters, “Design of the Low-Energy Beam Transport System of the Brookhaven 200-MeV Injector Linac,” *IEEE Trans. Nucl. Sci.*, vol. 16, no. 3, pp. 221–226, Jun. 1969.

[21] P. Lapostolle, “Quelques Proprietes Essentielles Des Effets De La Charge D’Espace Dans Des Faisceaux Continus.” 1970.

[22] A. A. Wolski, *Beam Dynamics in High Energy Particle Accelerators*. ICP, 2014.

[23] L. Groening, “Concept for controlled transverse emittance transfer within a linac ion beam,” *Phys. Rev. Spec. Top. - Accel. Beams*, vol. 14, pp. 1–9, 2011.

[24] L. Groening *et al.*, “Experimental Proof of Adjustable Single-Knob Ion Beam Emittance Partitioning,” pp. 1–5, 2014.

[25] L. Groening, C. Xiao, M. Maier, O. K. Kester, and M. Chung, “Emittance Transfer in Linacs,” in *HB2014*, 2014.

[26] C. Xiao, O. K. Kester, L. Groening, H. Leibrock, M. Maier, and P. Rottländer, “Single-knob beam line for transverse emittance partitioning,” *Phys. Rev. Spec. Top. - Accel. Beams*, vol. 16, pp. 1–9, 2013.

[27] Y. Koba, H. Iwamoto, K. Kiyohara, and T. Nagasaki, “Scintillation Efficiency of Inorganic Scintillators for Intermediate-Energy Charged Particles,” *Prog. Nucl. Sci. Technol.*, vol. 1, pp. 218–221, 2011.

[28] A. Lieberwirth, W. Ensinger, P. Forck, and S. Lederer, “Response from inorganic scintillation screens induced by high energetic ions,” *Nucl. Instruments Methods Phys. Res. Sect. B Beam Interact. with Mater. Atoms*, vol. 365, no. 5, pp. 533–539, Dec. 2015.

[29] M. Vogel, D. F. A. Winters, H. Ernst, H. Zimmermann, and O. Kester, “Scintillation light produced by low-energy beams of highly-charged ions,” *Nucl. Instruments Methods Phys. Res. Sect. B Beam Interact. with Mater. Atoms*, vol. 263, no. 2, pp. 518–522, Oct. 2007.

[30] E. Gutlich, P. Forck, W. Ensinger, and B. Walasek-Hohne, “Scintillation Screen Investigations for High-Current Ion Beams,” *IEEE Trans. Nucl. Sci.*, vol. 57, no. 3, pp. 1414–1419, Jun. 2010.

[31] T. Nakagawa, “Production of intense beams of highly charged heavy ions from RIKEN 18 GHz ECRIS and liquid He free SC-ECRIS,” in *AIP Conference Proceedings*, 2001, vol. 600, no. 2001, pp. 232–234.

[32] A. A. Efremov, A. I. Ivanenko, V. B. Kutner, J. Pivarc, and K. D. Tumanov, “Vacuum system for the Dubna ECR-ion source DECRIS-14,” *Vacuum*, vol. 44, no. 10, pp. 983–986, 1993.

[33] T. Thuillier, “CERN ACCELERATOR SCHOOL 2012 : ELECTRON CYCLOTRON RESONANCE ION SOURCES - I,” 2012.

[34] L. Celona, “Microwave Coupling to ECR and Alternative Heating Methods,” Nov. 2014.

[35] T. Stix, *Waves in Plasmas*. 1992.

[36] I. Brown, *The Physics and Technology of Ion Sources*. 2004.

[37] T. Kurita, T. Nakagawa, T. Kawaguchi, and S.-M. Lee, “Design of electron cyclotron resonance ion source using liquid-helium-free superconducting solenoid coils,” *Rev. Sci. Instrum.*, vol. 71, no. 2, p. 909, 2000.

[38] S. Kohara *et al.*, “Flattop acceleration system in the RIKEN AVF cyclotron,” *Nucl. Instruments Methods Phys. Res. Sect. A Accel. Spectrometers, Detect. Assoc. Equip.*, vol. 526, no. 3, pp. 230–238, Jul. 2004.

[39] Y. Yano, “The RIKEN RI Beam Factory Project: A status report,” *Nucl. Instruments Methods Phys. Res. Sect. B Beam Interact. with Mater. Atoms*, vol. 261, no. 1–2, pp. 1009–1013, Aug. 2007.

[40] H. Sakurai, “RI Beam Factory Project at RIKEN,” *Nucl. Phys. A*, vol. 805, no. 1–4, pp. 526–532, 2008.

[41] T. Nakagawa and Y. Yano, “Recent performance of Japanese electron cyclotron resonance ion sources (invited),” *Rev. Sci. Instrum.*, vol. 71, no. 2, p. 637, 2000.

[42] T. Nakagawa, Y. Higurashi, M. Kidera, T. Aihara, M. Kase, and Y. Yano, “Production of multi-charged ions in the RIKEN 18 GHz ECRIS,” *Nucl. Instruments Methods Phys. Res. Sect. B Beam Interact. with Mater. Atoms*, vol. 226, no. 3, pp. 392–400, Nov. 2004.

[43] Comtech, “TWTA RF amplifier.” [Online]. Available: http://xicomtech.com/products-twta-touchscreen.

[44] E. Bravin, E. D. Cantero, A. G. Sosa, C. G. Ch, and C. P. Welsch, “Optimization of a Short Faraday Cup for Low-Energy Ions using Numerical Simulations,” no. September, 2014.

[45] Group3, “LPT-141 Hall probe,” 2005. [Online]. Available: http://www.group3technology.com/lpt-series.

[46] D. Leitner, D. Winklehner, and M. Strohmeier, “Ion beam properties for ECR ion source injector systems,” *J. Instrum.*, vol. 6, no. 7, pp. P07010–P07010, 2011.

[47] D. Winklehner and D. Leitner, “ECRIS extraction and LEBT simulations with the PIC code WARP,” p. 1.

[48] D. Winklehner, D. Todd, D. Grote, D. Leitner, J. Benitez, and M. Strohmeier, “Plasma-To-Target Warp Simulations of Uranium Beams Extracted From Venus Compared To Emittance Measurements and Beam Images *,” pp. 81–83.

[49] D. Winklehner, “Ion Beam Extraction From Electron Cyclotron Resonance Ion,” Michigan state University, 2013.

[50] D. Winklehner, D. Todd, J. Benitez, M. Strohmeier, D. Grote, and D. Leitner, “Comparison of Extraction and Beam Transport Simulations with Emittance Measurements from the ECR Ion Source VENUS,” *J. Instrum.*, vol. 5, no. 12, pp. P12001–P12001, 2010.

[51] “Geant4.” [Online]. Available: https://geant4.web.cern.ch/geant4/.

[52] COBHAM, “Opera simulation software.” [Online]. Available: http://operafea.com/.

[53] T. Nagatomo, “RIBF intarnal report,” Wako, 2014.

[54] V. Toivanen, T. Kalvas, H. Koivisto, J. Komppula, and O. Tarvainen, “Double einzel lens extraction for the JYFL 14 GHz ECR ion source designed with IBSimu,” *J. Instrum.*, vol. 8, no. 5, pp. P05003–P05003, May 2013.

[55] Y. Kotaka *et al.*, “DEVELOPMENT OF LOW-ENERGY HEAVY-ION BEAMS BY THE RIKEN AVF CYCLOTRON AND HYPER ECR ION SOURCE OF CNS,” in *HIAT*, 2015, pp. 58–61.

[56] Arun microelectronics, “Ultra High Vacuum Stepper Motors,” 2014.

[57] KOHARA, “Hardened Ground Racks catalogue,” 2014.

[58] KOHARA, “Ground Spur Gears catalogue,” 2014.

[59] Daido metal, “Metal bearings catalogue,” 2014.

[60] MISUMI, “Sliders and Rails catalogue,” 2014.

[61] MDC Vacuum, “Linear motion catalogue,” 2013.

[62] Oriental Motors, “PKP225D06A-L , Stepper Motor ·,” 2014.

[63] Arun microelectronics, “SMD210 Stepper Motor Drive,” 2014.

[64] PointGray, “Point Gray BFL-PGE- 3E4M-CS datasheet.”

[65] Computar, “12mm - 36mm F2.8 for 2/3 type Cameras, Megapixel Vari-focal C-Mount.”

[66] Atmel, “ATMEL 8-BIT MICROCONTROLLER,” 2015.

[67] Wiznet, “W5100 Datasheet,” 2010.

[68] Texas Instruments, “ADS1015-Q1 Low-Power 12-Bit Analog-to-Digital Converter With Internal Reference,” 2016.

[69] Texas Instruments, “DRV8834 Dual-Bridge Stepper or DC Motor Driver,” 2015.

[70] EPICS, “Experimental Physics and Industrial Control System.” [Online]. Available: http://www.aps.anl.gov/epics/.

[71] CA Lab, “EPICS library for Labview.” [Online]. Available: http://www-csr.bessy.de/control/SoftDist/CA_Lab/index.html.

[72] M. Strohmeier, J. Y. Benitez, D. Leitner, C. M. Lyneis, D. S. Todd, and M. Bantel, “Development of a pepper-pot device to determine the emittance of an ion beam generated by electron cyclotron resonance ion sources,” *Rev. Sci. Instrum.*, vol. 81, no. 2, p. 02B710, 2010.

[73] H. R. Kremers, J. P. M. Beijers, and S. Brandenburg, “A pepper-pot emittance meter for low-energy heavy-ion beams,” *Rev. Sci. Instrum.*, vol. 84, no. 2, p. 25117, 2013.

[74] S. Saminathan, J. P. M. Beijers, H. R. Kremers, V. Mironov, J. Mulder, and S. Brandenburg, “Optimization of a charge-state analyzer for electron cyclotron resonance ion source beams,” *Rev. Sci. Instrum.*, vol. 83, no. 7, p. 73305, 2012.

[75] G. Knoll, *Radiiation detection and measurement*. Wiley, 2011.

[76] Saint-Gobain, “Crystals Physical Properties of Common Inorganic Scintillators,” 2009.

[77] Saint-Gobain, “Efficiency Calculations for Selected Scintillators.”

[78] Saint-Gobain, “CsI (Tl), CsI (Na) Cesium Iodide Scintillation Material,” 2012.

[79] A. Lempicki, M. H. Randles, D. Wisniewski, M. Balcerzyk, C. Brecher, and A. J. Wojtowicz, “LuAlO/sub 3/:Ce and other aluminate scintillators,” in *Proceedings of 1994 IEEE Nuclear Science Symposium - NSS’94*, 1995, vol. 1, pp. 307–311.

[80] J. A. Mares, M. Nikl, J. Chval, I. Dafinei, P. Lecoq, and J. Kvapil, “Fluorescence and scintillation properties of LuAlO3:Ce crystal,” *Chem. Phys. Lett.*, vol. 241, no. 4, pp. 311–316, Jul. 1995.

[81] R. J. Ginther and J. H. Schulmian, “Glass Scintillators,” *IRE Trans. Nucl. Sci.*, vol. 5, no. 3, pp. 92–95, Dec. 1958.

[82] J. Amare *et al.*, “Study of scintillation in natural and synthetic quartz and methacrylate,” *Opt. Mater. (Amst).*, vol. 36, no. 8, pp. 1408–1417, Jan. 2014.

[83] R. Zhu, “Radiation damage in scintillating crystals,” *Nucl. Instruments Methods Phys. Res. Sect. A Accel. Spectrometers, Detect. Assoc. Equip.*, vol. 413, no. 2–3, pp. 297–

311, Aug. 1998.

[84] R. Zhu, “Radiation Damage Effects,” Pasadena, 2012.

[85] L. Y. Lin *et al.*, “Investigation of ion induced damage in KBr, YAG:Ce, CaF 2 :Eu and CsI:Tl irradiated by various-energy protons,” *J. Instrum.*, vol. 10, no. 3, pp. P03024–P03024, Mar. 2015.

[86] A. Buck *et al.*, “Scintillating Screens for laser-accelerated relativistic electron bunch diagnostics,” in *Scintillating Screen Workshop GSI*, 2011.

[87] A. H. Lumpkin, F. National, and U. S. A. Il, “FEASIBILITY OF OTR IMAGING OF NON-RELATIVISTIC IONS AT GSI,” in *Scintillating Screen Workshop GSI*, 2011.

[88] R. Krishnakumar, C. Andre, F. Becker, P. Forck, and R. Haseitl, “Investigation of Scintillation Screens for High Energetic Heavy Ion Beams at GSI Plan of talk Motivation,” in *Scintillating Screen Workshop GSI*, 2011.

[89] E. Gütlich, P. Forck, W. Ensinger, and B. Walasek-höhne, “Scintillating screens for ion beams,” in *Scintillating Screen Workshop GSI*, 2011.

[90] G. Perdikakis, “Scintillator Screens at ReA3,” in *Scintillating Screen Workshop GSI*, 2011, no. February, pp. 14–16.

[91] J. Maeder, “Usage of viewing screens at the ECR ion source at GSI ECR – Ion Source,” in *Scintillating Screen Workshop GSI*.

[92] M. Strohmeier, “SCINTILLATOR BASED LOW ENERGY BEAM DIAGNOSTICS AT THE LBNL 88-INCH CYCLOTRON,” in *Scintillating Screen Workshop GSI*, 2011.

[93] H. Photonics, “MCP (Microchannel plate) and MCP Assembly,” *Hamamatsu Cat.*, pp. 1–20, 2016.

[94] S. Jolly *et al.*, “Data acquisition and error analysis for pepperpot emittance measurements,” *Dipac*, pp. 7–9, 2009.

[95] T. Hoffmann, “Emittance measurements of high current heavy ion beams using a single shot pepperpot system,” in *AIP Conference Proceedings*, 2000, vol. 546, pp. 432–439.

[96] P. Forck, F. Heymach, T. Hoffmann, A. Peters, and P. Strehl, “Measurement of the six Dimensional Phase Space at the New GSI High Current Linac,” *Linac2000*, pp. 166–168, 2000.

[97] O. Tarvainen, “Studies of Electron Cyclotron Resonance Ion Source,” JYVÄSKYLÄ, 2005.

[98] T. Thuillier, “ION BEAM EXTRACTION AND LEBT,” in *JUAS school*, 2015.

[99] S. Kumar and A. Mandal, “TRANSVERSE EMITTANCE MEASUREMENT FOR LOW ENERGY ION BEAMS USING QUADRUPOLE SCAN METHOD,” in *IPAC*, 2015, pp. 6–8.

[100] T. Nagatomo, V. Tzoganis, M. Kase, O. Kamigaito, and T. Nakagawa, “Development of a pepper-pot emittance meter for diagnostics of low-energy multiply charged heavy ion beams extracted from an ECR ion source,” *Rev. Sci. Instrum.*, vol. 87, no. 2, p. 02B920, Feb. 2016.

[101] P. Forck *et al.*, “Scintillation Screen Investigations for High Energy Heavy Ion Beams At GSI,” in *DIPAC2011*, 2011, no. 6, pp. 170–172.

[102] J. F. Ziegler, M. D. Ziegler, and J. P. Biersack, “SRIM – The stopping and range of ions in matter (2010),” *Nucl. Instruments Methods Phys. Res. Sect. B Beam Interact. with Mater. Atoms*, vol. 268, no. 11–12, pp. 1818–1823, Jun. 2010.

[103] B. P. Cluggish, S. A. Galkin, and J. S. Kim, “Modeling Ion extraction from an ECR Ion source,” in *2007 IEEE Particle Accelerator Conference (PAC)*, 2007, pp. 1826–1828.

[104] M. A. Leitner, D. C. Wutte, and C. M. Lyneis, “Design of the extraction system of the superconducting ECR ion source venus,” in *PACS2001. Proceedings of the 2001 Particle Accelerator Conference (Cat. No.01CH37268)*, 2001, vol. 1, pp. 67–69.

[105] Y. Higurashi *et al.*, “Status of Riken Ecr Ion Sources for Intense Heavy Ion,” in *2nd Annual Meeting of Particle Accelerator Society of Japan*, 2005, pp. 18–20.

[106] B. Vosicki and K. Zankel, “the Sodium Curtain Beam Profile Monitor of the Isr,” *IEEE Trans. Nucl. Sci.*, vol. 22, no. 3, pp. 1475–1478, 1975.

[107] R. Galiana, D. Manglunki, and C. Mazeline, “A carbon jet beam profile monitor for LEAR,” *IEEE Part. Accel. Conf. San Fr.*, pp. 1198–1200, 1991.

[108] E. Takada, “Carbon Ion Radiotherapy at NIRS-HIMAC,” *Nucl. Phys. A*, vol. 834, no. 1–4, p. 730c–735c, 2010.

[109] Y. Hashimoto *et al.*, “Oxygen gas-sheet beam profile monitor for the synchrotron and storage ring,” *Nucl. Instruments Methods Phys. Res. Sect. A Accel. Spectrometers, Detect. Assoc. Equip.*, vol. 527, no. 3, pp. 289–300, Jul. 2004.

[110] T. Fujisawa, Y. Hashimoto, T. Morimoto, and Y. Fujita, “Multi-pole magnets to focus an O2 sheet beam for a non-destructive beam-profile monitor,” *Nucl. Instruments Methods Phys. Res. Sect. A Accel. Spectrometers, Detect. Assoc. Equip.*, vol. 506, no. 1–2, pp. 50–59, Jun. 2003.

[111] S. Sawada, “J-PARC Facility,” *Nucl. Phys. A*, vol. 834, no. 1–4, p. 701c–706c, 2010.

[112] Y. Hashimoto *et al.*, “Development of a Beam Profile Monitor using a Nitrogen-Molecular Jet for the J-PARC MR,” *Ibic 2012*, pp. 848–851, 2012.

[113] Y. Hashimoto *et al.*, “Development of a Beam Profile Monitor using a Nitrogen-Molecular Jet for the J-PARC MR,” in *IBIC 2013*, 2013, pp. 848–851.

[114] T. Tsang *et al.*, “Optical beam profile monitor and residual gas fluorescence at the relativistic heavy ion collider polarized hydrogen jet.,” *Rev. Sci. Instrum.*, vol. 79, no. 10, p. 105103, Oct. 2008.

[115] J. Harasimowicz, “Beam Diagnostics for the USR,” in *PAC*, 2009, pp. 4048–4050.

[116] M. Putignano, D. Borrows, and C. P. Welsch, “Experimental characterization of a flexible ionization monitor for transverse profile measurement in the USR,” in *BIW*, 2012, pp. 198–200.

[117] C. P. Welsch *et al.*, “Ultra-low energy storage ring at FLAIR,” *Hyperfine Interact.*, vol. 213, no. 1–3, pp. 205–215, Nov. 2011.

[118] J. Ullrich, R. Moshammer, a Dorn, R. D rner, L. P. H. Schmidt, and H. Schmidt-B cking, “Recoil-ion and electron momentum spectroscopy: reaction-microscopes,” *Reports Prog. Phys.*, vol. 66, no. 9, pp. 1463–1545, 2003.

[119] J. Ullrich, R. Moshammer, A. Dorn, R. Dorner, L. P. H. Schmidt, and H. Schmidt-Bocking, “Recoil-ion and electron momentum spectroscopy: reaction-microscopes,” *Reports Prog. Phys.*, vol. 66, pp. 1463–1545, 2003.

[120] M. Putignano, “Supersonic Gas-Jet Based Beam Profile Monitor (PhD thesis),” Liverpool University, 2012.

[121] Y. Hashimoto *et al.*, “Development of a nondestructive beam profile monitor using a sheeted nitrogen-molecular beam,” in *Proceedings of IPAC’10, Kyoto, Ja*, 2010, p.

987,989.

[122] V. Tzoganis and C. P. Welsch, “Alignment of a nozzle skimmer system for a non-invasive gas jet based beam profile monitor.”

[123] M. E. Rudd, R. D. DuBois, L. H. Toburen, C. A. Ratcliffe, and T. V Goffe, “Cross sections for ionization of gases by 5-4000-keV protons and for electron capture by 5-150-keV protons,” *Phys. Rev. A*, vol. 28, no. 6, pp. 3244–3257, Dec. 1983.

[124] M. U. Bug *et al.*, “Ionization cross section data of nitrogen, methane, and propane for light ions and electrons and their suitability for use in track structure simulations,” *Phys. Rev. E*, vol. 88, no. 4, p. 43308, Oct. 2013.

[125] P. L. Bartlett and A. T. Stelbovics, “Electron-impact ionization cross sections for elements Z=1 to Z=54,” *At. Data Nucl. Data Tables*, vol. 86, no. 2, pp. 235–265, 2004.

[126] Opera electromagnetics finite element software, “Opera electromagnetics finite element software.” [Online]. Available: http://operafea.com/.

[127] V. Tzoganis and C. P. Welsch, “A non-invasive beam profile monitor for charged particle beams,” *Appl. Phys. Lett.*, vol. 104, no. 20, p. 204104, May 2014.

[128] CRDM, “3D systems prototyping.” [Online]. Available: http://crdm.co.uk/.

[129] TJW, “Precision engineering.” [Online]. Available: http://www.tjwire.co.uk/.

[130] Festo, “Solenoid pulse valve.” [Online]. Available: https://www.festo.com/cms/en-gb_gb/14380.htm.

[131] Aim & Thurlby Thandar Instruments, “TGP110 pulse generator.” [Online]. Available: http://www.tti-test.com/products-tti/text-pages/gen-tgp110.htm.

[132] ISO-Tech, “DC power supply IPS-3303.” [Online]. Available: http://www.iso-techonline.com/product/.

[133] Crydom, “Solid state relay DMO063.” [Online]. Available: http://www.crydom.com/en/products/pcb-mount-mini-sip/dc-output/dmo-series/.

[134] M. Putignano and C. P. Welsch, “Numerical studies of curtain gas jet generation for beam profile monitoring applications in the ultra low energy storage ring,” in *BIW 2010*, 2010, pp. 243–246.

[135] M. Putignano and C. P. Welsch, “Numerical study on the generation of a planar supersonic gas-jet,” *Nucl. Instruments Methods Phys. Res. Sect. A Accel. Spectrometers, Detect. Assoc. Equip.*, vol. 667, pp. 44–52, Mar. 2012.

[136] M. Putignano and C. P. Welsch, “Optimization studies of planar supersonic gas-jets for beam profile monitor applications,” in *IPAC*, 2010, pp. 1149–1151.

[137] MicroLab Devices Power Supplies, “MicroLab Devices Power Supplies.” [Online]. Available: http://www.microlabdevices.com/home.html.

[138] PHOTONIS microchannel plates, “PHOTONIS microchannel plates.” [Online]. Available: http://www.photonis.com/en/microchannel-plates.

[139] IDS imaging systems, “IDS imaging systems.” [Online]. Available: https://en.ids-imaging.com/.

[140] PSP vacuum, “PSP Vacuum,” *http://www.pspvacuum.com/electron_source_for_aes.html*. [Online]. Available: http://www.pspvacuum.com/electron_source_for_aes.html.

[141] H. Pauly, *Atom, Molecule, and Cluster Beams I*, vol. 28, no. 9. Berlin, Heidelberg: Springer Berlin Heidelberg, 2000.

[142] H. Ashkenaz and F. S. Sherman, *Rarefied gas dynamics: proceedings of the fourth International Symposium on Rarefied Gas Dynamics, held at the Institute for Aerospace Studies, University of Toronto, 1964 edited by J.H. de Leeuw*. New York: Academic Press, 1965-1966., 1966.

[143] J. B. Anderson and J. B. Fenn, "Velocity Distributions in Molecular Beams from Nozzle Sources," *Phys. Fluids*, vol. 8, no. May 2014, p. 780, 1965.

[144] J. Wang *et al.*, "Speed ratios greater than 1000 and temperatures less than 1 mK in a pulsed He beam," *Phys. Rev. Lett.*, vol. 60, no. 8, pp. 696–699, Feb. 1988.

[145] T. K. and H. Knudsen, "Current status of antiproton impact ionization of atoms and molecules: theoretical and experimental perspectives," *J. Phys. B At. Mol. Opt. Phys.*, vol. 44, no. 12, p. 122001, 2011.

[146] T. Kirchner and H. Knudsen, "Current status of antiproton impact ionization of atoms and molecules: theoretical and experimental perspectives," *J. Phys. B At. Mol. Opt. Phys.*, vol. 44, no. 12, p. 122001, 2011.

[147] V. Tzoganis and C. P. Welsch, "Alignment of a nozzle skimmer system for a non-invasive gas jet based beam profile monitor," in *IBIC*, 2013, pp. 803–806.

[148] Leybold Vacuum, "Turbovac SL 700 TMP."

[149] H. Ashkenas S. F. Sherman, "No TitleExperimental Methods in Rarefied Gas Dynamics," in *Proceedings of the 4th International Symposium on Rarefied Gas Dynamics*, 1966, p. 84.

[150] H. Zhang, V. Tzoganis, C. P. Welsch, and K. Widmann, "3D DENSITY SCANS OF A SUPERSONIC GAS JET FOR BEAM PROFILE MONITOR," in *IBIC*, 2016, pp. 8–10.

[151] VACGEN, "Miniax XYZ Manipulator." [Online]. Available: http://www.vacgen.com/pages/miniax-xyz-manipulators.

[152] S. D. Eder, B. Samelin, G. Bracco, K. Ansperger, and B. Holst, "A free jet (supersonic), molecular beam source with automatized, 50 nm precision nozzle-skimmer positioning," *Rev. Sci. Instrum.*, vol. 84, no. 9, pp. 1–10, 2013.

[153] A. Friedman *et al.*, "Computational Methods in the Warp Code Framework for Kinetic Simulations of Particle Beams and Plasmas," *IEEE Trans. Plasma Sci.*, vol. 42, no. 5, pp. 1321–1334, May 2014.

[154] H. Zhang, V. Tzoganis, A. Jeff, A. Alexandrova, and C. P. Welsch, "CHARACTERIZING SUPERSONIC GAS JET-BASED BEAM PROFILE MONITORS also at RIKEN," in *IPAC*, 2016, pp. 357–360.

[155] S. Udrea *et al.*, "PREPARATORY WORK FOR A FLUORESCENCE BASED PROFILE MONITOR FOR AN ELECTRON LENS BIF SETUP FOR TRANSVERSE," in *IBIC*, 2016, pp. 7–10.

[156] G. Fu, A. Menciassi, and P. Dario, "Development of a low-cost active 3D triangulation laser scanner for indoor navigation of miniature mobile robots," *Rob. Auton. Syst.*, vol. 60, no. 10, pp. 1317–1326, Oct. 2012.